l'université nantes angers le mans
COMMUNAUTÉ D'UNIVERSITÉS ET ÉTABLISSEMENTS

UNIVERSITÉ DE NANTES

Thèse de Doctorat

Yi YUAN

Mémoire présenté en vue de l'obtention du
grade de Docteur de l'Université de Nantes
sous le label de l'Université de Nantes Angers Le Mans

École doctorale : 503 (STIM)

Discipline : Électronique et Génie électrique
Spécialité : Génie électrique
Unité de recherche : Institut de Recherche en Énergie Électrique de Nantes Atlantique (IREENA)

Soutenue le 25 mars 2014

Torque Ripple Reduction in a Permanent Magnet Synchronous Machine Using Repetitive Control Techniques (Drift)

JURY

Rapporteurs :	**M. Luc DUGARD**, Directeur de Recherche, CNRS ENSE3 - INP Grenoble
	M. Mickael HILAIRET, Professeur des Universités, Université de Franche Comté
Examinateur :	**M. Maurice FADEL**, Professeur des Universités, Université de Toulouse
Invité :	**M. Stéphane MOISY**, Ingénieur, SKF France - Automotive Division - ADCSI
Directeur de thèse :	**M. François AUGER**, Professeur des Universités, LUNAM - Université de Nantes
Co-directeur de thèse :	**M. Luc LORON**, Professeur des Universités, LUNAM - Université de Nantes

Remerciements

Je tiens tout d'abord à adresser mes plus vifs remerciements à François AUGER, directeur de ma thèse et professeur à l'université de Nantes. Il m'a orienté vers la bonne direction, corrigé les erreurs que j'ai pu faire et donné des conseils importants. J'ai également été impressionné par son attitude envers la science et son travail. Il aura autant contribué que moi à cette thèse : merci à lui.

Je remercie également Luc LORON, co-directeur de cette thèse et professeur à l'université de Nantes, pour sa gentillesse, sa patience, ainsi que pour sa culture scientifique vaste et profonde.

J'adresse tous mes remerciements à Mathieu HUBERT, responsable industriel de ma thèse et ingénieur à SKF France, pour sa préparation du banc d'essai, mais aussi pour son soutien quotidien. Il est un exemple d'ingénieur compétent, j'appris beaucoup à ses cotés pendant ces trois années.

Je remercie également Stéphane MOISY, superviseur de cette thèse et manageur de l'équipe. Il m'a donné toutes les ressources nécessaires pour mener à bien ce sujet de recherche. Il a consacré beaucoup de temps personnel à la correction de mon mÃ©moire. Sans son soutien, je n'aurais sans doute pas pu terminer ma thèse.

Je fais part de ma grande gratitude aux membres de jury de ma thèse, Prof. Luc DUGARD, Prof. Maurice FADEL et Prof. Mickael HILAIRET, pour avoir jugé mon travail précisément et m'avoir apporté des suggestions utiles et justifiées.

Un remerciement particulier à Franck DEBRAILLY, directeur du service Sensor Integration (SKF), pour m'avoir donné sa confiance et avoir permis de réaliser ce sujet de thèse. C'est également lui qui m'a fait découvrir la culture française. J'ai pu, grâce à ses conseils, m'adapter à celle-si facilement tant d'un point de vue professionnel que personnel. Un grand merci aussi à Alberto CARLEVARIS, ancien directeur de notre service. J'ai souvent été touché par son sérieux dans son travail et sa gentillesse envers ses équipes. Je remercie également Adam REEDMAN, directeur de Automotive Development Centre et Edward HOLWEG, directeur de

Product and Development de Automotive Division, pour leur support et encouragements.

Je tiens à remercier Oliver CHEVE et Simon HUBERT, mes collègues de SKF et professeurs de français. Quand je passais les moments difficiles et avait besoin d'aide, ils étaient toujours là pour m'aider et m'encourager. Sans eux, ces trois années auraient été moins cocasses. Je remercie également toute l'équipe de l'ADC-SI.

Je remercie Ouahid DAHMANI et René AUBREE, mes collègues du laboratoire IREENA. Dans le bureau 356 ou la salle de café, nous avons passé beaucoup de temps formidables ensemble. Je remercie également Hao CHEN, Jian ZHANG, Jin JIAN, Wenli KANG et Zhihao SHI: vivre à l'étranger n'est pas facile, mais avec eux, je retournais en Chine le temps d'une conversation. Je tiens également à saluer Mohamed MACHMOUM, directeur de laboratoire, Madame Christine BROHAN, et Monsieur Frank JUDIC.

Prof. Didier TRICHET, Prof. Mohamed-El-Hadi ZAIM, Mr. Brahim RAMDANE, Dr. Guillaume WASSELYNCK, Dr. Salvy BOURGUET et Dr. Luc MOREAU. Leur conseils et soutien m'ont permis de terminer ma thèse avec un bon résultat. Je voudrais partager le même remerciement à tous les professeurs et thésards du laboratoire.

Je salue particulièrement Madame et Monsieur VIGIER, mes propriétaires à St-Nazaire et presque ma demi-famille, et Madame et Monsieur Clavier, mes propriétaires à Saint-Cyr-sur-Loire, pour m'avoir fourni une chambre confortable et aidé à découvrir la culture française. Je remercie aussi mon colocataire Benjamin EMERIAU et mon ami Lipin SHI avec lesquels j'ai eu de nombreuses discussions intéressantes.

Enfin, j'adresse des remerciements spéciaux à mes parents et ma fiancée Na HUO, pour leur soutien inconditionnel et permanent.

Introduction

Preamble

This work has been done in collaboration between SKF France, Automotive Development Centre (ADC), Sensor Integration (SI) department and Nantes University, IREENA laboratory. The aim of this thesis is to develop a smart sensor which is based on the Repetitive Control (RC) technique and is able to achieve the torque ripple reduction in Permanent Magnet Synchronous Machines (PMSMs).

Problem definition

The basic distinction between a PMSM and a synchronous machine without magnet is the way they generate the magnetic field [1]. The former ones use permanent magnets and the latter ones use windings. PMSMs do not need energy to produce the rotor magnetic field, so they have a higher energy efficiency, which, regarding to the growing energy crisis, is a very attractive feature. On the other side, thanks to the development of material science, the reliability of permanent magnets, which once was a major limitation of PMSMs, has been remarkably improved [2]. More significantly, their performances have reached such a level that PMSMs could perform same or even better than their without magnets counterparts, boosting the use of PMSMs in many high performance applications [1]. In addition, since permanent magnets are placed on the rotor instead of windings, it is not necessary to consider the rotor cooling that is always a serious concern for other machines. All these merits explain the increasing popularity of PMSMs. However, there is no denying that the PMSMs equipped with the permanent magnets are more costly than the machines without permanent magnets.

As a coin has two sides, the particular structure of PMSMs brings not only advantages, but also disadvantages. First, the unavoidable imperfection of the permanent magnets interacting with the winding distributions causes magnetic flux harmonics, resulting in harmonic torque ripples. Second, a magnetic field variation arising from the relative movement between the rotor magnets and the stator teeth generates a torque, which is usually called cogging torque. These undesired para-

sitic torque ripples can cause vibrations and noises, so they are considered as the main drawbacks of PMSMs for many applications [1]. This is why the study and the comprehension of the characteristic of the PMSM torque ripple was the first step of this work.

Providing a smooth torque is a common requirement for PMSMs. Therefore, in past decades, a large number of papers were published to accomplish this aim. The proposed solutions can be roughly divided into two families [3, 4]. The first one attempts to reduce the torque ripples through the improvement of the machine design. The second one intends to achieve the torque reduction by using advanced control methods, which can modify the machine currents to compensate for any non-ideal characteristic of the machine. As we know, particular machine designs usually mean more complex structures, so their manufacturing is more complicated and expensive. On the opposite, a controller is a necessary component in a drive system, so integrating an advanced control algorithm into an existing drive requires nearly no extra expense. This is very important for most industrial sectors, especially the automotive one, where the cost is always a significant concern. Hence this Ph.D project supported by an automotive related company naturally needs a suitable and economic solution for the PMSM torque ripple reduction.

Many control methods such as the programmed current waveform control [5], the instantaneous torque control [6] have been reported for the PMSM torque ripple reduction. This Ph.D thesis chooses the RC technique to deal with this problem. The possibility of using the RC technique to reduce the PMSM torque ripples has been reported in many publications [7, 8, 9, 10, 11, 12]. The presented theoretical analysis and experimental results show the disturbance rejection capability of the RC technique. However, they also reveal an unacceptable limitation: the efficiency of this technique is guaranteed only when the machine speed is constant. In practice, most PMSMs are designed for variable speed drive systems. Therefore, developing a new technique, which is able to handle the torque ripple reduction with a varying speed, is mandatory, so it is one of the main challenges of this work.

In addition, the conventional way of applying the RC technique for PMSM drives requires the modification of the system controller [7, 8]. This is almost impossible for industrial applications, since the system controller commonly bought from others, what is inside the controller is unknown for the one who develops the PMSM drive. In order to simplify the use of the RC technique, we propose to integrate the compensation algorithm inside the sensor, instead of inside the controller, to accomplish the torque ripple reduction. Then the desired torque ripple reduction could be simply achieved by adopting a particular sensor instead of a conventional one. The feasibility of this idea is also an important objective of this work.

Contributions

The original contributions of this work can be summarized as the following points:

1. We study the tracking performance of various repetitive controllers, and reveal that their performance suffers from undesired oscillations when the systems need to track a step reference. To get rid of these annoying oscillations, we define a new repetitive controller named non-overshooting step response repetitive controller with an improved tracking behavior and the same reduction capability.

2. We develop a repetitive smart sensor technique to accomplish the torque ripple reduction in a new way. The smart sensor proposed in this work merges the speed sensor and the repetitive controller together, so it is able to feedback a modified speed information to the PMSM control system. Thanks to this repetitive smart sensor, we can achieve the torque ripple reduction without breaking the control system integrity. We study the stability and the performance of this type of system. Accordingly, the feasibility of this new technique is verified through its implementation in the test bench.

3. We propose an angle-based RC technique, which takes the angle as the control algorithm reference. This technique extends the reduction capability of the RC technique to varying speeds, enabling the RC technique to be a really applicable solution for the PMSM torque ripple reduction. To guarantee the efficiency of this technique, the stability condition and the performances of angle-based RC systems are studied. Furthermore, the feasibility and the efficiency of this new technique are verified experimentally after its implementation in a test bench.

This work led to the filing of two international patents and to a recently submitted two-part article.

Outline

This report is organized in four chapters.

To understand the torque ripple issues in PMSMs, one must start with the machine fundamentals. Chapter1 will first provide an elementary introduction of the architecture of PMSMs, its modeling and its driving system as well as the strategy used to control the subsequent drive system. Chapter1 will also give a thorough presentation of PMSM torque ripples. This consists of a classification of the various torque ripples, a description of their specifications and computations. Then, a survey on the current state of PMSM torque ripple reduction technique will be

presented. At the end of this chapter, a description of the test bench and the analysis of the measurements will be accomplished as the basis for further study.

The aim of Chapter 2 is to introduce the RC technique. Hence, this chapter will start with a brief presentation about the origin and the history of the RC technique. This will be followed by an introduction about the basic repetitive controller. Chapter 2 will also offer a comparison between the RC technique and another memory-based RC, called iterative learning control technique, so as to distinguish these techniques from each other. Two other current repetitive controllers, which integrate the current information into the basic repetitive controller, will be also presented. Then to ensure the efficiency of these repetitive controllers, their stability conditions and performance will be studied. Besides, to apply them for the torque ripple reduction, design methodologies used to obtain the desired rejection capabilities will be developed for each controller. Finally, a new repetitive controller, aiming to improve the tracking behavior of the closed-loop system, is proposed at the end of this chapter.

The first part of Chapter 3 will address the repetitive smart sensor technique. Accordingly, a conventional control system using the repetitive smart sensor is called repetitive smart sensor system. The relationship between this system and the conventional RC systems will be studied. Finally, a dedicatedly designed repetitive smart sensor will be applied into the test bench so as to show its effectiveness. In the second part of this chapter, a limitation of the conventional RC technique that it cannot reduce the torque ripple for variable speed machines will be presented and explained. Then according to a fact that the relationship between the torque ripple and mechanical angle is fixed whether the speed is changing or not, the angle-based RC technique will be proposed to liberate the reduction capability of RC technique from this limitation. To guarantee the functionality and the efficiency of the system, the stability condition and the performance of the angle-based controller will be discussed. Besides, with an elaborate design, the performance of the angle-based repetitive controller will be checked in the test bench.

Chapter 4 will present some general conclusions of this work, and will also show several potential ideas for the future research.

Furthermore, an extended abstract written in French will be presented at the end of this report to facilitate the French-speaking people to understand the contribution of this work.

1

PMSMs, Drive Systems and Torque Ripples

The aim of this Ph.D thesis is the torque ripple reduction of PMSMs. To accomplish this, first of all, we need to be able to answer the following questions: what are PMSMs, how to design their drive systems and what are the torque ripples. The goal of this chapter is to answer these questions.

The characteristics of PMSMs depend on their design, which generally consist of the rotor design and the stator design. Therefore, in order to understand PMSMs, we need to study the rotor and the stator first. Thereby, with the acquired machine knowledge, a PMSM model can be established. To build a PMSM drive system, it is necessary to consider three aspects: the system hardware, the control strategy and the controller tuning methodology. A typical PMSM drive system usually includes a sensor, an inverter, a controller and a PMSM. In turn, a good understanding of all these components is something important hence is introduced in this chapter. The vector control, due to its simplicity, is commonly used for many modern PMSM drive systems, therefore it is also chosen to accomplish the drive system in this thesis. Accordingly, the Park transformation and the machine model developed in the d-q reference frame as the basis of the vector control are necessary to be presented together. In addition, the tuning approaches for the controller, to ensure a good system performance, are due to be presented.

On the other hand, there are several kinds of torque ripples in PMSMs. To get the torque ripple reduction, their features should be known first. Lots of methods have been reported that can achieve the PMSM torque ripple reduction. In order to choose an appropriate one, it is useful to show a state of the art of the development

of the torque ripple reduction techniques.

A PMSM vector control system used to verify the theoretical analysis is built in the SKF mechatronic laboratory, consequently, we will give an introduction about this experimental platform.

1.1 Architecture of PMSMs

PMSMs are polyphase synchronous machines equipped with permanent magnet in their rotor [13]. Therefore, compared to conventional synchronous machines, they use permanent magnets instead of field windings to generate the rotor magnetic flux. Like any synchronous machine, in PMSMs, the stator magnetic flux excited by the stator currents and the rotor magnetic flux generated by the permanent magnets need to rotate at the same speed. Consequently, it is necessary to synchronize the phase of the state current with the rotor position. Usually, position sensors, which can capture the rotor position information, are installed close to PMSMs.

1.1.1 The rotor

In PMSMs, permanent magnets are mounted on the rotor shaft. With various configurations of the permanent magnets, the pole pairs can vary from two to much more. The features of the permanent magnets strongly influence the machine performance. To meet several performance requirements and to satisfy cost considerations, various magnetic materials can be chosen for the permanent magnets. Among them, ferrite magnets and rare earth magnets are two common choices. The ferrite magnets are less expensive, however they have the disadvantage of low magnetic density (around $0.4\,\mathrm{T}$) [14]. In contrast, in spite of their higher cost, the rare earth magnets, owing to their higher magnetic density (around $1.2\,\mathrm{T}$), allow to increase the torque to weight ratio of the machine [14].

The permanent magnets can be made in many shapes such as rectangular, radial and breadloaf, and also can be magnetized with different orientations such as radial, parallel, or any others [13]. Besides, PMSMs can be broadly classified into two types, according to their magnetic flux direction: the radial field PMSM and the axial PMSM. The radial one is seizing the market whereas the axial one is gaining the dominant position in a few applications that require high power density, such as the machines used for electric vehicles and boats. This report focuses only on the radial field PMSMs, which, depending on the way of arranging magnets on the rotor, can be separated into many types. This report introduces three popular ones: the surface-mounted PMSM, the surface-inset PMSM and the interior PMSM, which are shown in Fig. 1.1.

In surface-mounted PMSMs, as shown in Fig. 1.1.a, the permanent magnets are

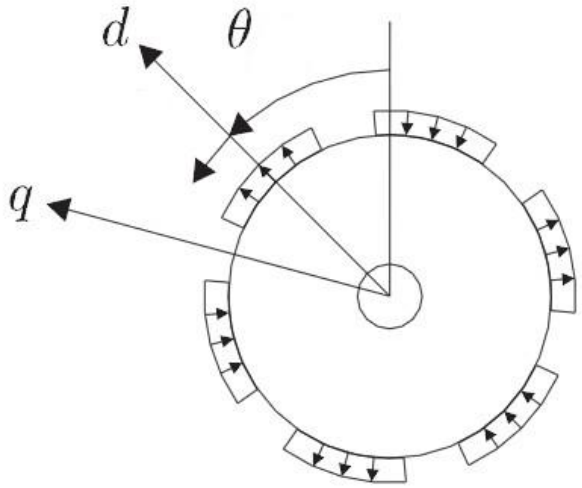

(a) The surface-mounted PMSM

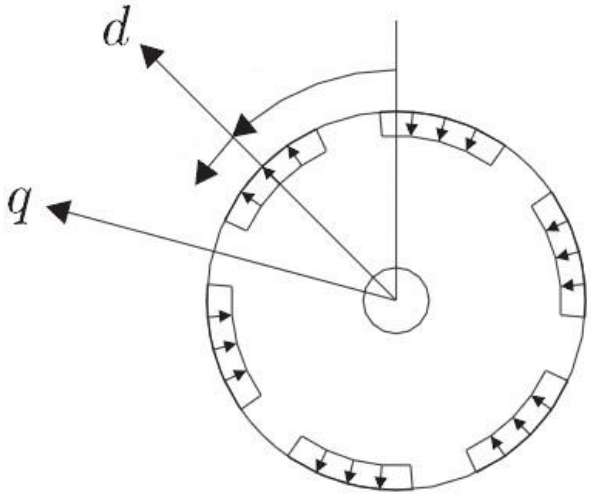

(b) The surface-inset PMSM

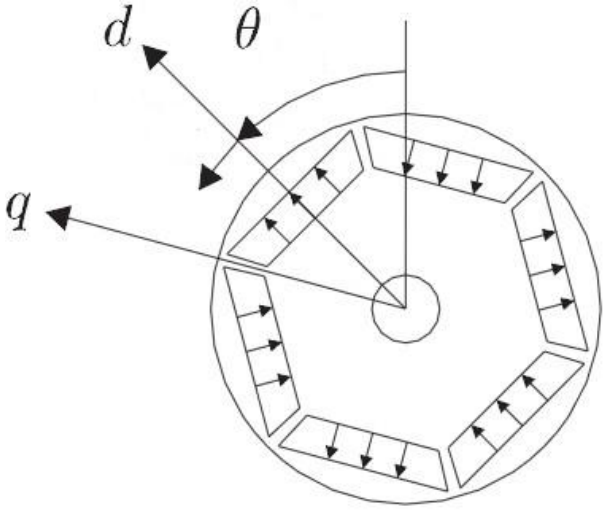

(c) The interior PMSM

Figure 1.1: The rotor design in different types of PMSM (reprinted from [15]).

placed on the outer periphery of rotor laminations [1]. Thanks to their simplicities in the manufacturing, most of the PMSMs are surface-mounted ones. Usually, because of their lower structural integrity and mechanical robustness, they are inappropriate for high speed applications. Fortunately, the efficient use of non-magnetic materials could improve their mechanical robustness, consequently, the use of surface-mounted PMSMs for high speed applications recently became possible. Since the magnetic permeability of the magnets and the air is almost the same, this design possesses very small differences between the direct and quadrature inductances. Hence this type of machine is sometimes called "nonsalient" PMSM [13].

The typical rotor design of the surface-inset PMSMs is shown in Fig. 1.1.b: the permanent magnets are placed in the grooves of the outer periphery of the rotor laminations [1]. Hence this kind of rotor has a uniform cylindrical surface. This structure enhances the mechanical robustness, but also results in "salient" phenomena in the machine. As stated in [13, 16], in this kind of machine, the ratio between the quadrature and direct axis inductances can be as high as 2-2.5.

Fig. 1.1.c is an example of an interior PMSM rotor design, in which the rotor magnets are mounted inside the rotor [1]. This design, due to its particular magnet placement, possesses the best mechanical robustness among three presented designs, therefore are suitable for high speed applications, but it also has the most complicated manufacturing process, therefore is usually relatively expensive. An apparent advantage of this design is that the placement of the magnets inside the rotor magnets can be made in various ways, which offers flexibilities to tailor the expected level of rotor saliency and the desired magnet flux according to the application [14]. In this kind of PMSMs, the ratio between the quadrature and direct inductances generally is around 3, which usually is the highest among three designs [13].

1.1.2 The stator

The stator flux is generated by the conducting windings distributed inside the stator slots. Generally, the stator of PMSMs resembles that of induction machines: coils are placed in slots and they are interconnected to make a winding [14]. Most PMSMs have three stator windings connected in star fashion [14].

In an operating PMSM, the winding current results from an energized voltage from the inverter and an induced voltage known as back Electromotive Force (back EMF) [14]. Back EMF, according to Lenz's Law, is generated by the windings that experience the variation of magnetic flux caused by the moving magnets [1]. If the magnetic flux linkage generated by the permanent magnet ψ_r is sinusoidal, then it can be expressed as [1]

$$\psi_r(t) = \Psi_{rm} \sin(\omega_e t) \tag{1.1}$$

in which Ψ_{rm} is the maximum value of the magnetic flux, ω_e is the electric angular speed and t is the instantaneous time. Provided that the number of coil turns per phase is N_c, then the back EMF e_{back} can be calculated as [1]

$$e_{\text{back}}(t) = -N_c \frac{d\psi_r(t)}{dt} = -N_c\, \omega_e\, \Psi_{rm} \cos(\omega_e t) \tag{1.2}$$

There is another type of PM machines called brushless DC machines, who share many basic characteristics with PMSMs. Compared to PMSMs, which, ideally, require a perfect sinusoidal back EMF, brushless DC machines are designed to provide a trapezoidal back EMF [1]. This notable distinction can be achieved by using a distributed winding in PMSMs and a concentrated winding in brushless DC machines, and it can also be achieved by a particular rotor pole shaping, and sometimes by both of them [17]. In brushless DC machines, the conducting current is rectangular in shape with generally 120 electrical angle wide, in contrast, this current is sinusoidal in PMSMs [14]. Because of the inductance, it is impossible for the stator current to rise and fall instantaneously. So a kind of torque ripple usually called commutation torque appears in brushless DC machines [1]. Thanks to the sinusoidal current, PMSMs are immune to this kind of torque ripple. As a result, the torque output of brushless DC machines is usually less smooth than that of PMSMs. However, it is easier to synthesize the regular current in brushless DC machines compared to the sinusoidal current in PMSMs, resulting in lower requirements of position sensor for brushless DC machines than that for PMSMs, as well as controlling a brushless DC machine is usually less complicated than controlling a PMSM. In addition, for equal resistive losses, the brushless DC machines have $15.4\,\%$ higher power density than PMSMs [1].

1.2 Model of PMSMs

In this section, a typical three-phase PMSM model is presented. To simplify the analysis, the studied machine is assumed to be perfectly balanced and without magnetic saturation.

1.2.1 Magnetic flux analysis

Since the magnetic flux of a PMSM results from the permanent magnets and the winding currents together, to know its distribution, we need to study both the rotor flux generated by the permanent magnets and the stator flux generated by the winding currents.

To analyze the rotor flux, first of all, we need to define the magnetic flux density B, which is the amount of magnetic flux through a unit area [13, 15]. The rotor

flux is related to the magnets and the windings. In this studied machine, both of them are supposed to be distributed ideally, as shown in Fig. 1.2, where circles with cross and point symbols represent the coils with different current directions; A, B, C are the three-phase windings. The rotor axis and the stator axis respectively lie in the center of one permanent magnet and the center of winding-A. θ_r and θ_s are the electrical angles locating the position of a point P in relation to the rotor frame and the stator frame. $\theta_e = \theta_s - \theta_r$ is the electrical angle between the rotor axis and the stator axis, and in this report, it usually represents the electrical angular position of the rotor. As shown in Fig. 1.2, if using θ_r as the reference, the magnetic flux density symmetrically distributes around the rotor axis, therefore it can be expanded into an even Fourier series with only odd harmonic orders [15]

$$B(\theta_r) = \sum_{i=1}^{\infty} B_{2i-1} \cos\left((2i-1)\theta_r\right), \tag{1.3}$$

where the coefficients of the magnetic flux density harmonics B_{2i-1} are strongly dependent on the magnet and rotor design. The magnetic flux of phase-A can be derived as [2]

$$\psi_{ra}(\theta_e) = N_c \int_s B(\theta_r) dS = N_c \int_s B(\theta_s - \theta_e) dS, \quad \text{with} \quad dS = \frac{R_{in} l_{ef}}{n_p} d\theta_s, \tag{1.4}$$

where R_{in} is the inner radius of the stator, l_{ef} is the effective length of the stator, n_p is the number of pole pairs and N_c is defined in Eq. 1.1. Then considering Eq. 1.3 and Eq. 1.4, $\psi_{ra}(\theta_e)$ can be expressed as [15]

$$\begin{aligned}
\psi_{ra}(\theta_e) &= \frac{R_{in} l_{ef} N_c}{n_p} \int_{-\pi/2}^{\pi/2} B(\theta_s - \theta_e) d\theta_s \\
&= \frac{R_{in} l_{ef} N_c}{n_p} \int_{-\pi/2}^{\pi/2} \sum_{i=1}^{\infty} B_{2i-1} \cos\left((2i-1)(\theta_s - \theta_e)\right) d\theta_s \\
&= \frac{2 R_{in} l_{ef} N_c}{n_p} \sum_{i=1}^{\infty} \frac{B_{2i-1}(-1)^{i+1}}{2i-1} \cos((2i-1)\theta_e) \\
&= \sum_{i=1}^{\infty} \psi_{2i-1} \cos((2i-1)\theta_e), \qquad (1.5) \\
\text{with} \quad \psi_{2i-1} &= \frac{2 R_{in} l_{ef} N_c}{n_p} \frac{B_{2i-1}(-1)^{i+1}}{2i-1},
\end{aligned}$$

which reveals that the magnetic flux can be expressed as a sum of cosines functions

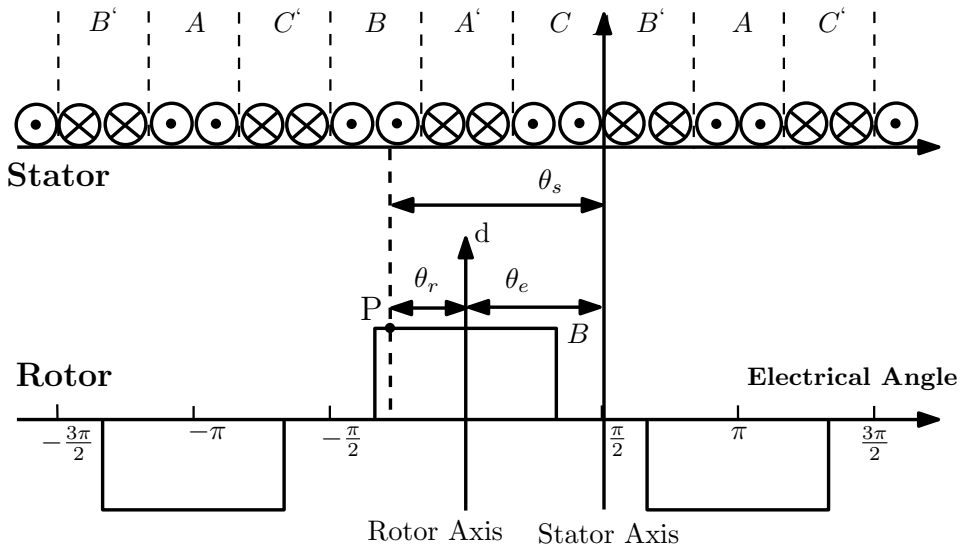

Figure 1.2: The winding distribution and the flux density in a machine.

with odd harmonic orders. Eq. 1.5 is expanded as [2],

$$\begin{aligned}\psi_{ra}(\theta_e) &= \sum_{i=1}^{\infty} \psi_{r,2i-1} \cos((2i-1)\theta_e) \\ &= \psi_{r,1}\cos(\theta_e)+\psi_{r,3}\cos(3\theta_e)+\psi_{r,5}\cos(5\theta_e)+\cdots. \end{aligned} \tag{1.6}$$

Winding-B and winding-C are shifted by ± 120 electrical degrees relatively to phase-A. As a result, the magnetic flux generated from the magnets of three phases can be expressed in a vector form, as [15]

$$\psi_{r,abc} = \begin{bmatrix} \psi_{ra}(\theta_e) \\ \psi_{rb}(\theta_e) \\ \psi_{rc}(\theta_e) \end{bmatrix} = \begin{bmatrix} \psi_{ra}(\theta_e) \\ \psi_{ra}(\theta_e - 2\pi/3) \\ \psi_{ra}(\theta_e + 2\pi/3) \end{bmatrix}. \tag{1.7}$$

On the other hand, the flux excited from the conducting current is associated with the winding inductances, which includes the self-inductance and the mutual inductance. The self-inductance of phase-A without considering the saturation can be expressed as [15]

$$L_{s,aa}(\theta_e) = \sum_{i=0}^{\infty} L_{s,2i}\cos(2i\theta_e) = L_{s,0} + L_{s,2}\cos(2\theta_e)+\cdots. \tag{1.8}$$

Owing to the supposed symmetry, $L_{s,bb}(\theta_e) = L_{s,aa}(\theta_e - 2\pi/3)$ and $L_{s,cc}(\theta_e) =$

$L_{s,aa}(\theta_e+2\pi/3)$, then,

$$L_{s,bb}(\theta_e)=L_{s,aa}\left(\theta_e-\frac{2}{3}\pi\right)=L_{s,0}+L_{s,2}\cos\left(2\theta_e+\frac{2}{3}\pi\right)+\cdots,$$
$$L_{s,cc}(\theta_e)=L_{s,aa}\left(\theta_e+\frac{2}{3}\pi\right)=L_{s,0}+L_{s,2}\cos\left(2\theta_e-\frac{2}{3}\pi\right)+\cdots. \quad (1.9)$$

Similarly, the mutual inductances between phase-B and phase-C is written as [15]

$$L_{m,bc}(\theta_e)=L_{m,cb}(\theta_e)=\sum_{i=0}^{\infty}L_{m,2i}\cos(2i\theta_e)=L_{m,0}+L_{m,2}\cos(2\theta_e)+\cdots. \quad (1.10)$$

Again, the symmetry of the machine ensures that other mutual inductances can be expressed as $L_{m,ab}(\theta_e)=L_{m,ba}(\theta_e)=L_{m,bc}(\theta_e+2\pi/3)$ and $L_{m,ac}(\theta_e)=L_{m,ca}(\theta_e)=L_{m,bc}(\theta_e-2\pi/3)$, then

$$L_{m,ab}(\theta_e)=L_{m,bc}\left(\theta_e+\frac{2}{3}\pi\right)=L_{m,0}+L_{m,2}\cos\left(2\theta_e-\frac{2}{3}\pi\right)+\cdots,$$
$$L_{m,ac}(\theta_e)=L_{m,bc}\left(\theta_e-\frac{2}{3}\pi\right)=L_{m,0}+L_{m,2}\cos\left(2\theta_e+\frac{2}{3}\pi\right)+\cdots.$$

Finally, the self-inductance and the mutual inductance together can be presented as a symmetric matrix L_{abc} that [15]

$$L_{abc}=\begin{bmatrix} L_{s,aa}(\theta_e) & L_{m,ab}(\theta_e) & L_{m,ac}(\theta_e)\\ L_{m,ba}(\theta_e) & L_{s,bb}(\theta_e) & L_{m,bc}(\theta_e)\\ L_{m,ca}(\theta_e) & L_{m,cb}(\theta_e) & L_{s,cc}(\theta_e)\end{bmatrix}. \quad (1.11)$$

Since $\psi_{s,abc}=L_{abc}i_{abc}$, where $i_{abc}=[i_a,\ i_b,\ i_c]^T$ stands for the three-phase current, then the total magnetic flux in PMSMs can be written as

$$\begin{aligned}\psi_{abc}&=\psi_{s,abc}+\psi_{r,abc}=L_{abc}i_{abc}+\psi_{r,abc}\\ &=\begin{bmatrix} L_{s,aa}(\theta_e) & L_{m,ab}(\theta_e) & L_{m,ac}(\theta_e)\\ L_{m,ba}(\theta_e) & L_{s,bb}(\theta_e) & L_{m,bc}(\theta_e)\\ L_{m,ca}(\theta_e) & L_{m,cb}(\theta_e) & L_{s,cc}(\theta_e)\end{bmatrix}\begin{bmatrix} i_a\\ i_b\\ i_c\end{bmatrix}+\begin{bmatrix} \psi_{ra}(\theta_e)\\ \psi_{rb}(\theta_e)\\ \psi_{rc}(\theta_e)\end{bmatrix}. \quad (1.12)\end{aligned}$$

Eq. 1.12 illustrates that the magnetic flux of PMSM consists of two parts: one is the stator magnetic flux $\psi_{s,abc}$ related to the inductances and the winding currents, the other is the rotor magnetic flux $\psi_{r,abc}$ associated with the magnets and the winding.

1.2.2 Electrical, electromagnetic and mechanical connection

The relationship between the stator current and voltage is [15]

$$\begin{aligned} v_{abc} &= R_{abc}\, i_{abc} + \frac{d}{dt}\psi_{abc} = R_{abc}\, i_{abc} + \frac{d}{dt}(\psi_{s,abc} + \psi_{r,abc}) \\ &= R_{abc}\, i_{abc} + \frac{d}{dt}(L_{abc}\, i_{abc} + \psi_{r,abc}) = R_{abc}\, i_{abc} + L_{abc}\frac{di_{abc}}{dt} + \frac{dL_{abc}}{dt} i_{abc} + \frac{\psi_{r,abc}}{dt}, \end{aligned} \tag{1.13}$$

where $v_{abc} = [v_{an},\ v_{bn},\ v_{cn}]^T$ represents the phase voltage. The resistance matrix R_{abc} can be presented as [15]

$$R_{abc} = \begin{bmatrix} R_s & 0 & 0 \\ 0 & R_s & 0 \\ 0 & 0 & R_s \end{bmatrix}, \tag{1.14}$$

where, because of the assumed symmetry, resistances of three phases are equal to R_s. With the supposed linear magnetic condition, the magnetic energy W can be expressed as [15]

$$W = \frac{1}{2} i_{abc}^T\, L_{abc}\, i_{abc} + i_{abc}^T\, \psi_{r,abc}. \tag{1.15}$$

Hence, the electromagnetic torque expression is

$$T_e(\theta_m) = \frac{dW}{d\theta_m} = n_p \frac{dW}{d\theta_e} = n_p \left(\frac{1}{2} i_{abc}^T \frac{dL_{abc}}{d\theta_e} i_{abc} + i_{abc}^T \frac{d\psi_{r,abc}}{d\theta_e} \right), \tag{1.16}$$

where $\theta_e = n_p \theta_m$ and θ_m is the mechanical angular position of the rotor. Then, the mechanical angular speed ω_m and θ_e can be expressed as [18]

$$\frac{d\omega_m}{dt} = \frac{1}{J}(T_e - T_l - T_{\text{fric}}), \tag{1.17}$$

$$\frac{d\theta_e}{dt} = \omega_e = n_p\, \omega_m, \tag{1.18}$$

where J is the inertia of the rotor, T_l is the load torque, T_{fric} is the friction torque usually modeled as $T_{\text{fric}} = k_f\, \omega_m$, where k_f is known as the friction coefficient.

1.3 PMSM drive system

A typical architecture of a PMSM vector control drive is shown in Fig. 1.3, where we can see that this PMSM drive consists of the following parts: a controller, an inverter, sensors and of course a PMSM. This section provides a brief description of the function of each component

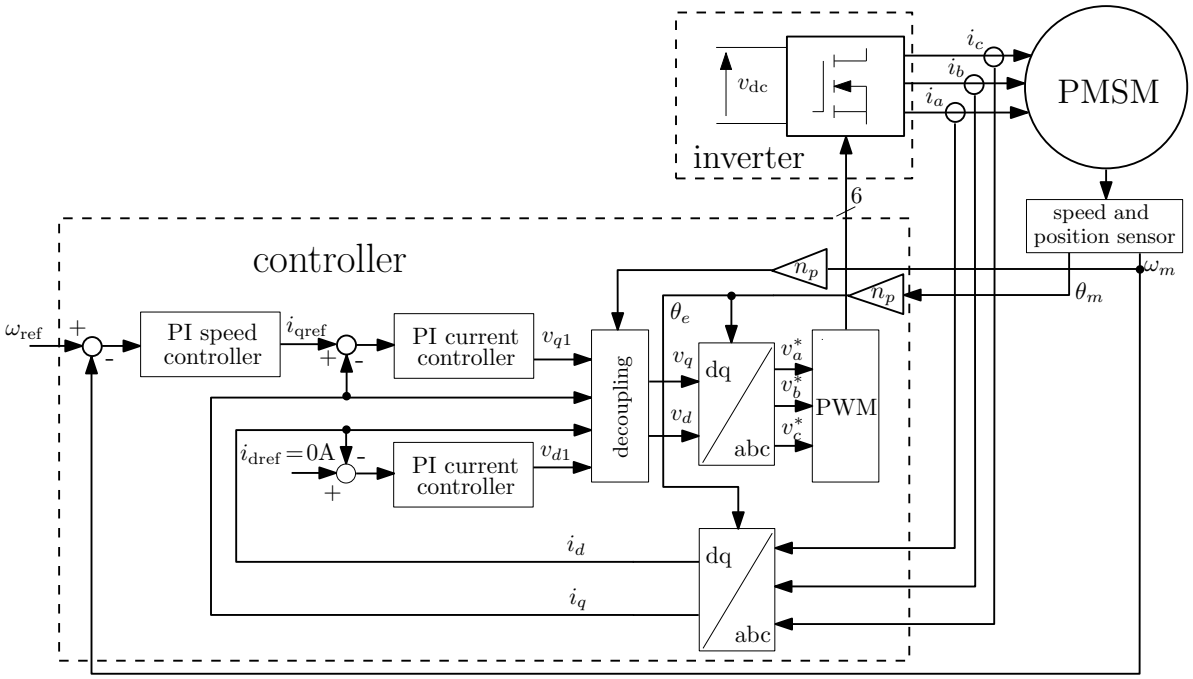

Figure 1.3: The block diagram of a typical PMSM vector control system.

1.3.1 The sensors

Sensors are used to provide the measured information to the controller so as to implement the closed-loop system. As shown in Fig. 1.3, the required feedback information of this system consists of the armature current, the rotor position and the speed. Hence, current sensors, a speed and position sensor are needed for a PMSM drive system.

Since the armature currents generally need to be regulated in a PMSM drive system, the current sensors, which give the instantaneous current information of each phase to the controller, are normally installed inside the inverter. In a balanced three-phase PMSM, at least, the currents of two phases are required for the current control, correspondingly, two current sensors are needed.

In order to synchronize the phase of the stator current with the rotor position, the absolute rotor position information is necessary. In most applications, this information is measured by a position sensor, but in some cases a sensorless scheme can be considered. The position sensors used in PMSM systems generally are: Hall sensors, incremental and absolute encoders or inductive resolvers.

Hall sensors are transducers sensitive to a magnetic field [19]. Hall sensor are usually used in BLDCs. A typical way to use this sensor is to mount three sensors together with filtering and amplification and let those sense the magnetic field of the permanent magnets [20]. A Hall sensor can be made very small and cheap.

Encoders offer angular information as rectangular pulses with a frequency depending on the rotor velocity [19]. Incremental encoders give three rectangular

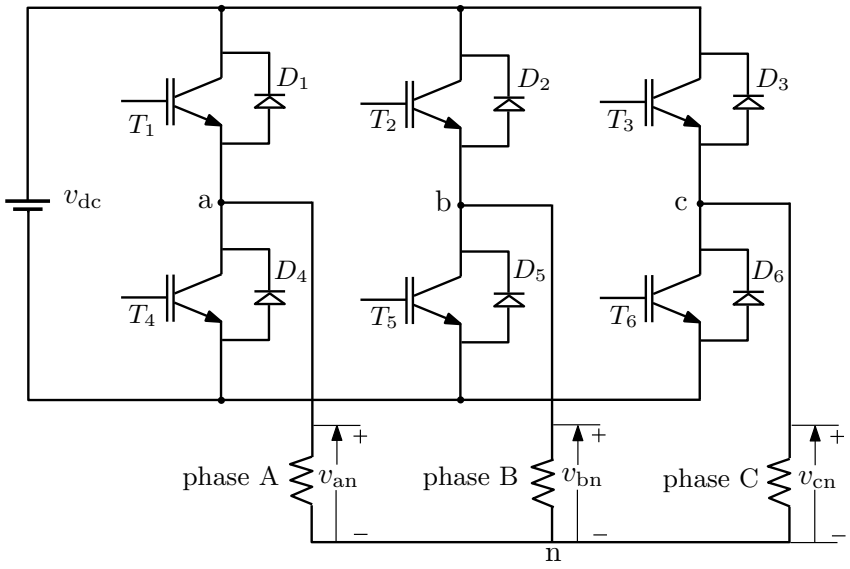

Figure 1.4: Three-phase inverter.

pulse signals, the first two determine the speed and rotation direction due to 90 degrees phase shift between each other, the third one is the index track which gives only one pulse in each rotation so that the incremental encoders can detect the absolute mechanical position [19] For absolute encoders, after enable, can immediately detect an absolute actual position.

Inductive resolvers provide the absolute rotor electrical position with a high accuracy. A resolver mainly consists of three coils: one rotor and two stator coils. Two stator coils are configured at 90 degrees shifted from each other. When the rotor is revolving, the rotor coil is excited with a sinusoidal signal which causes a position-dependent induction signal in the remaining coils. In many high performance applications, resolvers are commonly chosen for PMSM systems [19]. In that case, the resolver and the machine must have the same pole number. The resolver needs a specific demodulation circuit to extract the position and speed information.

1.3.2 The inverter

In PMSM drive systems, inverters, as shown in Fig. 1.3, convert the control action into variable frequency voltages to feed the machine. The inverter requires a DC voltage input, which, in a majority of cases, is obtained from an AC supply by rectification with a diode bridge. Three-phase PMSM drive systems commonly need a three-phase inverter. Its typical structure and connection with machine windings are shown in Fig. 1.4 [13], where v_{dc} is the DC source voltage; v_{an}, v_{bn}, v_{cn} are defined in Eq. 1.13; Two switches (top and bottom) are used in each phase, as a result, six transistors are employed in this inverter; D stands for diodes that are used to avoid the reverse current.

When the inverter is working, its switches are controlled via trigger signals given by the controller. Then the three-phase current shaped by the actions of the switches is able to generate a continuous rotary magnetic field that drives the PMSM.

1.3.3 The controller

In control systems, controllers are used to alter the control object dynamic according to given commands, and also to protect the system by monitoring the system states. Controllers can be classified into two kinds: the analog ones and the digital ones. In PMSM drive systems, analog ones are no longer used, hence contemporary controllers are always implemented in a digital manner. The controller output is calculated at discrete, equally-spaced time instants, and the period between two neighbouring time instants is known as the sampling period. A digital controller can be a digital chip such as a DSP, a micro-controller, a FPGA, system on chip or an entire system such as computers [14].

1.4 Control strategies

Several control strategies are commonly applied for PMSM drive systems [1], for instance the six-step control, the direct torque control and the vector control. The vector control, which is able to reduce the machine control complexity by decoupling the flux and torque generation, is popularly used for high performance drive systems. Hence, it is chosen in this thesis and its operating principle as well as its realization are presented in this section.

1.4.1 The vector control

In the late 1960s, the vector control was firstly proposed for induction machines, then its application was extended to synchronous motor drives [21, 22]. As we know, it is rather difficult to control AC drives because of their complicated dynamic behavior; whereas it is relatively easy to control DC machines owing to the independence between their flux and torque generation. In DC machines, the flux is controlled by the field current, and the torque is generated through the interaction between the flux and the armature current [1]. Since the angle between the excitation flux and the armature current is kept as 90 electrical degrees spatially by use of the brush and the commutator regardless of the rotation of the rotor, the torque of the DC machine is simply the product of the magnitude of the flux and the armature current [1]. If the magnitude of the flux is kept constant, then the torque is solely proportional to the armature current. As a result, one can simply regulate the armature current to control the machine torque. The space orientations of the flux and

the armature current are generally called d-axis and q-axis respectively [1].

The above analysis implies that the possibility of reducing the complexity of AC drive control lies in finding out its equivalent flux-producing current and torque-producing current. The key is to use the space phasor transformation to transfer a three-phase machine into a machine with only one stator winding and one rotor winding, thereby making it to equivalent a DC machine.

The simplicity of controlling a DC machine results from the independence between its flux and torque generation. In fact, it is also possible to get such kind of independence in PMSM drives. Provided that all magnetic flux comes from the permanent magnets, meanwhile, the armature current is intentionally controlled to be shifted from the flux by 90 electrical degrees [22]. Then, as the DC machine, torque controlling in PMSM can be easily achieved by regulating the magnitude of the armature current. It should be noted that in order to ensure that flux is only related to permanent magnets, the d-axis should be aligned with the permanent magnet north pole. Accordingly, the space orientation of the armature current is the q-axis. In DC machine, the armature current is a one-phase constant current, however, in PMSM, the armature current is in fact three-phase sinusoidal currents. Hence to accomplish the PMSM vector control, it is necessary to transfer the three-phase sinusoidal currents into a rotating q-axis constant current.

The Park transformation, which is able to transfer variables from a a-b-c reference frame to a d-q-0 reference frame, is used here to realize the vector control system. This transformation is written as [18, 22]

$$\begin{aligned} [x_d\, x_q\, x_0]^T &= T\,[x_a\, x_b\, x_c]^T\,, \\ \text{with } T &= \frac{2}{3}\begin{bmatrix} \cos(\theta) & \cos(\theta-2\pi/3) & \cos(\theta+2\pi/3) \\ -\sin(\theta) & -\sin(\theta-2\pi/3) & -\sin(\theta+2\pi/3) \\ 1/2 & 1/2 & 1/2 \end{bmatrix}. \end{aligned} \tag{1.19}$$

Inversely, the inverse-Park transformation is

$$\begin{aligned} [x_a\, x_b\, x_c]^T &= T^{-1}\,[x_d\, x_q\, x_0]^T\,, \\ \text{with } T^{-1} &= \begin{bmatrix} \cos(\theta) & -\sin(\theta) & 1 \\ \cos(\theta-2\pi/3) & -\sin(\theta-2\pi/3) & 1 \\ \cos(\theta+2\pi/3) & -\sin(\theta+2\pi/3) & 1 \end{bmatrix}. \end{aligned} \tag{1.20}$$

where x_a, x_b and x_c represent variables, such as current, inductance, voltages and others in the a-b-c reference frame and x_d, x_q and x_0 represent these variables in the d-q-0 reference frame.

Then using the Park transformation, the a-b-c sinusoidal currents can be converted into the d-q-0 constant currents. When d-axis current is equal to zero, the

desired independence between the flux and the torque generation can be achieved in PMSM drive systems.

1.4.2 The PMSM d-q model

With the Park transformation, the a-b-c three-phase PMSM model introduced in section 1.2 can be equivalently changed into a d-q-0 three-phase machine model. First of all, the magnetic flux in the d-q-0 reference frame can be derived as [16, 15]

$$\begin{aligned}
\psi_{abc} &= \psi_{s,abc} + \psi_{r,abc} = L_{abc}\, i_{abc} + \psi_{r,abc} \\
T^{-1}\psi_{dq0} &= L_{abc}\, T^{-1}\, i_{dq0} + T^{-1}\psi_{r,dq0} \\
\psi_{dq0} &= T\, L_{abc}\, T^{-1} i_{dq0} + T\, T^{-1}\psi_{r,dq0} \\
\psi_{dq0} &= T\, L_{abc}\, T^{-1} i_{dq0} + \psi_{r,dq0}, \qquad (1.21)
\end{aligned}$$

where

$$\psi_{dq0} = \begin{bmatrix} \psi_d \\ \psi_q \\ \psi_0 \end{bmatrix}, \quad i_{dq0} = \begin{bmatrix} i_d \\ i_q \\ i_0 \end{bmatrix} \quad \text{and} \quad \psi_{r,dq0} = \begin{bmatrix} \psi_{rd} \\ \psi_{rq} \\ \psi_{r0} \end{bmatrix}.$$

In a balanced operation, the zero sequence component can be ignored [1, 15], then Eq. 1.21 can be simplified as a d-q two-phase model,

$$\psi_{r,dq} = T_{23}\, L_{abc}\, T_{32}^{-1}\, i_{dq} + \psi_{r,dq} = L_{dq}\, i_{dq} + \psi_{r,dq}, \qquad (1.22)$$

where

$$T_{23} = \frac{2}{3}\begin{bmatrix} \cos(\theta) & \cos(\theta - 2\pi/3) & \cos(\theta + 2\pi/3) \\ -\sin(\theta) & -\sin(\theta - 2\pi/3) & -\sin(\theta + 2\pi/3) \end{bmatrix}, \qquad (1.23)$$

$$T_{32}^{-1} = \begin{bmatrix} \cos(\theta) & -\sin(\theta) \\ \cos(\theta - 2\pi/3) & -\sin(\theta - 2\pi/3) \\ \cos(\theta + 2\pi/3) & -\sin(\theta + 2\pi/3) \end{bmatrix} \qquad (1.24)$$

and

$$\psi_{r,dq} = \begin{bmatrix} \psi_{rd} \\ \psi_{rq} \end{bmatrix} = \begin{bmatrix} \psi_m + \sum_{k=1}^{\infty} \psi_{rd,6k} \cos(6k\theta) \\ \sum_{k=1}^{\infty} \psi_{rq,6k} \sin(6k\theta) \end{bmatrix}, \qquad (1.25)$$

where $\psi_m = \psi_{r,1}$ and

$$\begin{aligned}\psi_{rd,6k} &= \psi_{r,6k-1} + \psi_{r,6k+1},\\ \psi_{rq,6k} &= -\psi_{r,6k-1} + \psi_{r,6k+1}.\end{aligned}$$

$\psi_{rd,k}$ and $\psi_{rq,k}$ are coefficients of the flux harmonics, which are defined in Eq. 1.6, and the derivation of Eq. 1.25 can be found in section 6.1.1.

The inductance in the d-q reference frame can be written as [15]

$$L_{dq} = \begin{bmatrix} L_d + \sum_{i=1}^{\infty} L_{6i}\cos(6i\theta_e) & -\sum_{i=1}^{\infty} L_{6i}\sin(6i\theta_e) \\ -\sum_{i=1}^{\infty} L_{6i}\sin(6i\theta_e) & L_q - \sum_{i=1}^{\infty} L_{6i}\cos(6i\theta_e) \end{bmatrix}, \tag{1.26}$$

where

$$\begin{aligned}L_d &= L_{s,0} + \frac{L_{s,2}}{2} - L_{m,0} + L_{m,2},\\ L_q &= L_{s,0} - \frac{L_{s,2}}{2} - L_{m,0} - L_{m,2},\\ L_{6i} &= \frac{L_{s,6i-2}}{2} + L_{m,6i-2}.\end{aligned}$$

$L_{s,i}$ are coefficients of the inductance harmonics defined in Eq. 1.9. The voltage equation in the d-q-0 reference frame is deduced as [15]

$$\begin{aligned}v_{abc} &= R_{abc}\, i_{abc} + \frac{d}{dt}\,\psi_{abc}\\ T^{-1}v_{dq0} &= R_{abc}\, T^{-1}\, i_{dq0} + \frac{d}{dt}\left(T^{-1}\psi_{dq0}\right)\\ v_{dq0} &= T\, R_{abc}\, T^{-1} i_{dq0} + T\,\frac{d}{dt}(T^{-1}\psi_{dq0})\\ v_{dq0} &= T\, R_{abc}\, T^{-1}\, i_{dq0} + T\, T^{-1}\frac{d\psi_{dq0}}{dt} + T\frac{dT^{-1}}{dt}\psi_{dq0}\\ v_{dq0} &= T\, R_{abc}\, T^{-1} i_{dq0} + \frac{d\psi_{dq0}}{dt} + T\frac{dT^{-1}}{dt}\psi_{dq0},\end{aligned} \tag{1.27}$$

where

$$T\frac{dT^{-1}}{dt} = \omega_e \begin{bmatrix} 0 & -1 & 0 \\ 1 & 0 & 0 \\ 0 & 0 & 1 \end{bmatrix}, \tag{1.28}$$

The derivation of Eq. 1.28 can be found in section 6.1.2. Neglecting the zero sequence components, the above equation in the d-q reference frame can be written

as

$$v_{dq} = T_{23}\, R_{abc}\, T_{32}^{-1} i_{dq} + \frac{d\psi_{dq}}{dt} + \omega_e \begin{bmatrix} 0 & -1 \\ 1 & 0 \end{bmatrix} \psi_{dq} \tag{1.29}$$

$$= R_{dq} i_{dq} + \frac{d\psi_{dq}}{dt} + \omega_e \begin{bmatrix} 0 & -1 \\ 1 & 0 \end{bmatrix} \psi_{dq}$$

$$= R_{dq} i_{dq} + \frac{dL_{dq}}{dt} i_{dq} + L_{dq} \frac{di_{dq}}{dt} + \omega_e \begin{bmatrix} 0 & -1 \\ 1 & 0 \end{bmatrix} (L_{dq} i_{dq} + \psi_{r,dq}).$$

where

$$R_{dq} = T_{23} \begin{bmatrix} R_s & 0 & 0 \\ 0 & R_s & 0 \\ 0 & 0 & R_s \end{bmatrix} T_{32}^{-1} = \begin{bmatrix} R_s & 0 \\ 0 & R_s \end{bmatrix}$$

$$\text{and} \quad \frac{dL_{dq}}{dt} = \begin{bmatrix} -6\omega_e \sum_{i=1}^{\infty} L_{6i} \sin(6i\theta_e) & -6\omega_e \sum_{i=1}^{\infty} L_{6i} \cos(6i\theta_e) \\ -6\omega_e \sum_{i=1}^{\infty} L_{6i} \cos(6i\theta_e) & 6\omega_e \sum_{i=1}^{\infty} L_{6i} \sin(6i\theta_e) \end{bmatrix}.$$

If all harmonic components appearing in Eq. 1.25, Eq. 1.27 and Eq. 1.29 are neglected, then Eq. 1.29 can be rewritten as [15]

$$\begin{bmatrix} v_d \\ v_q \end{bmatrix} = \begin{bmatrix} R_s & 0 \\ 0 & R_s \end{bmatrix} \begin{bmatrix} i_d \\ i_q \end{bmatrix} + \begin{bmatrix} L_d & 0 \\ 0 & L_q \end{bmatrix} \frac{d}{dt} \begin{bmatrix} i_d \\ i_q \end{bmatrix}$$
$$+ \omega_e \begin{bmatrix} 0 & -1 \\ 1 & 0 \end{bmatrix} \left(\begin{bmatrix} L_d & 0 \\ 0 & L_q \end{bmatrix} \begin{bmatrix} i_d \\ i_q \end{bmatrix} + \begin{bmatrix} \psi_m \\ 0 \end{bmatrix} \right),$$

which can be equally rewritten as

$$v_d = R_s i_d + L_d \frac{di_d}{dt} - \omega_e L_q i_q,$$

$$v_q = R_s i_q + L_q \frac{di_q}{dt} + \omega_e L_d i_d + \omega_e \psi_m. \tag{1.30}$$

Finally, from Eq. 1.15, the electromagnetic torque expression in the d-q reference frame can be deduced as [15]

$$T_e(\theta_m) = \frac{\partial W}{\partial \theta_m} = n_p \frac{\partial W}{\partial \theta_e} = n_p \left(\frac{1}{2} i_{abc}^T \frac{dL_{abc}}{d\theta_e} i_{abc} + i_{abc}^T \frac{d\psi_{r,abc}}{d\theta_e} \right) \tag{1.31}$$

$$= n_p \left(\frac{1}{2} i_{dq0}^T \left(T^{-1}\right)^T \frac{d(T^{-1} L_{dq0} T)}{d\theta_e} T^{-1} i_{dq0} + i_{dq0}^T \left(T^{-1}\right)^T \frac{dT^{-1}}{d\theta_e} \psi_{r,dq0} \right).$$

According to Eq. 6.9 and Eq. 6.12, if we ignore all the harmonic components and

the zero sequence components [23], we can get

$$(T^{-1})^T \frac{dT^{-1}}{d\theta_e} = \frac{3}{2}\begin{bmatrix} 0 & -1 \\ 1 & 0 \end{bmatrix} \tag{1.32}$$

$$\text{and} \quad (T^{-1})^T \frac{d(T^{-1}L_{dq}T)}{d\theta_e} T^{-1} = \frac{3}{2}(L_d - L_q)\begin{bmatrix} 0 & 1 \\ 1 & 0 \end{bmatrix}. \tag{1.33}$$

Eq. 1.31 without considering the zero sequence components can be rewritten as

$$T_e = \frac{3}{2} n_p (\psi_d \, i_q - \psi_q \, i_d). \tag{1.34}$$

The derivation of Eq. 1.34 can be shown in Eq. 6.13. From this derivation, we find that Eq. 1.34 can also be represented as

$$T_e = \frac{3}{2} n_p (\psi_m i_q - (L_q - L_d) i_d \, i_q), \tag{1.35}$$

In this thesis, the target machine is a surface-mounted PMSM, therefore its L_q is only slightly larger than L_d. To facilitate the analysis, we can assume that $L_d = L_q$, then the reluctance torque disappears, and Eq. 1.35 can be rewritten as [15, 18]

$$T_e = \frac{3}{2} n_p \psi_m i_q. \tag{1.36}$$

From this final equation, we find that this PMSM electromagnetic torque expression has the same form as the torque expression of DC machines.

1.5 PMSM vector control system

As shown in Fig. 1.3, in the PMSM vector control system, one Park transformation (referred as abc-dq) and one inverse Park transformation (referred as dq-abc) are used so that the controllers designed in the d-q reference frame are capable of controlling three-phase machines. As a drive system, the machine speed should be able to track its reference, hence a speed loop managed by a PI controller is used in this system. On the other side, the machine speed as shown in Eq. 1.17 is influenced by the electromagnetic torque that is related to the current, therefore the current control is also widely used in contemporary AC drives to guarantee the performance of the drive system. Besides, in the vector control system, all armature current is expected for the torque generation, therefore, $i_{\text{dref}} = 0$ A. In addition, this system also contains a module called decoupling whose functionality will be explained in the following subsection.

In Fig. 1.3, the current and the speed are controlled by two Proportional-Integral

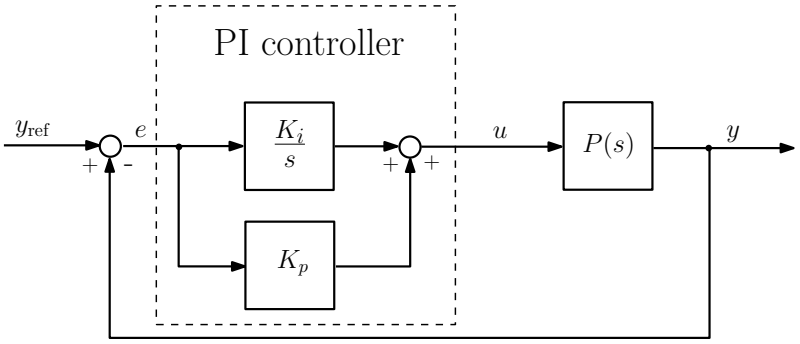

Figure 1.5: The block diagram of the PI control system.

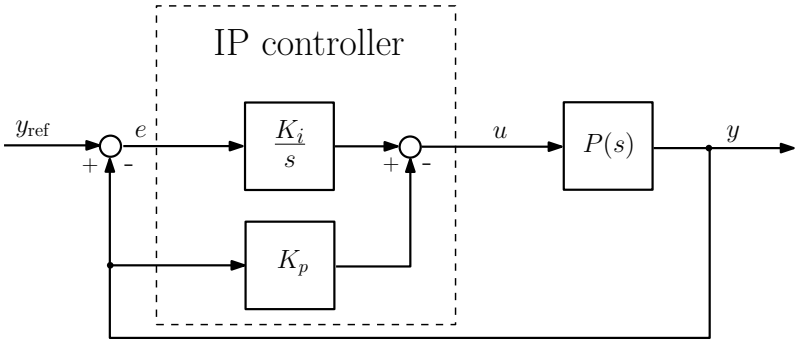

Figure 1.6: The block diagram of the IP control system.

(PI) current controllers and one PI speed controller, respectively. Therefore the tuning of these PI controllers is the key to determine the system performance. Issues about how to appropriately set parameters for both speed and current PI controllers are studied in this section. Since the PI parameter tuning strongly relies on the characteristics of the control processes, the way to model these control processes is also discussed in this section.

1.5.1 PI controller and IP controller

Proportional-Integral-Derivative (PID) controllers chosen for 90% industrial control systems are enjoying their popularity in every corners of the control world [24]. Many PID controllers are commonly implemented in drive systems to improve their dynamic performances. Since a PI controller without derivative component is already enough for PMSM drive control, to simplify the analysis, in this thesis, we focus only on the PI controller. A PI controller is defined as [25]

$$G_{pi} = K_p + \frac{K_i}{s} = K_p\left(1+\frac{1}{sT_i}\right) = K_p\left(1+\frac{\omega_i}{s}\right),$$
$$\text{with } \omega_i = \frac{K_i}{K_p} = \frac{1}{T_i}, \tag{1.37}$$

where K_p is the proportional gain, K_i is the integral gain and ω_i is the integral action. The structure of a closed-loop system using a PI controller is shown in Fig. 1.5, where $P(s)$ represents a control process, u is the control action, y_{ref} and y are the reference input and the system output respectively, and $e = y_{\text{ref}} - y$ is the control error.

In PI controllers, the proportional component can change the magnitude of the error information without changing its phase [24]. In a cascade system, a high K_p can increase the open-loop gain and reduce the steady-state error, however it decreases the system relative stability. Since using the proportional component alone usually cannot eliminate the steady-state error, integral component is added to cooperate with the proportional component in order to remove this error. However, as the integral term responds to accumulated errors from the past, it can result in the present value to overshoot the setpoint value [24]. Sometimes, this overshoot can harm the health of the device. For instance, power semiconductors are sensitive to instantaneous current overshoot [26]. Therefore, it is better to avoid overshoots in the control system. IP controllers are developed from PI controllers. If they are well tuned, they can enable system to avoid this undesired overshoot. The control system using this controller is shown in Fig. 1.6. This IP structure is equivalent to a PI control with a low-pass reference filter [25]:

$$\frac{Y(s)}{Y_{\text{ref}}(s)} = \frac{1}{1+s\frac{K_p}{K_i}} \frac{G_{pi}(s)P(s)}{1+G_{pi}(s)P(s)} = \frac{\frac{K_i}{s}P(s)}{1+G_{pi}(s)P(s)}. \tag{1.38}$$

As a matter of fact, the efficiency of the designed PI system is determined by how well we know the characteristics of its control process as well as which tuning method we chose for the PI parameter selection. The rest of this section focuses on these two problems.

1.5.2 Control system and its modeling

To tune the PI controllers, first, we need to know the characteristics of the controlled process. Therefore, how to model the PMSM vector control system is the main topic of this subsection. To make the discussion more clear, a sophisticated representation of a typical PMSM vector control system is drawn in Fig. 1.7. Compared to the system shown in Fig. 1.3, this new one has the following features: the part of PMSM involving the electrical part is presented in the d-q reference frame. The Park and inverse-Park transformations are no longer useful, hence are omitted. The inverter, the pulse width modulated (PWM) signal generator and the sensors are supposed to be perfect. In turn, their transfer functions are approximated by a unit gain, hence also disappeared in Fig. 1.7. The decoupling shown in Fig. 1.3 is presented in another way in Fig. 1.7. Besides, the torque ripples influencing this

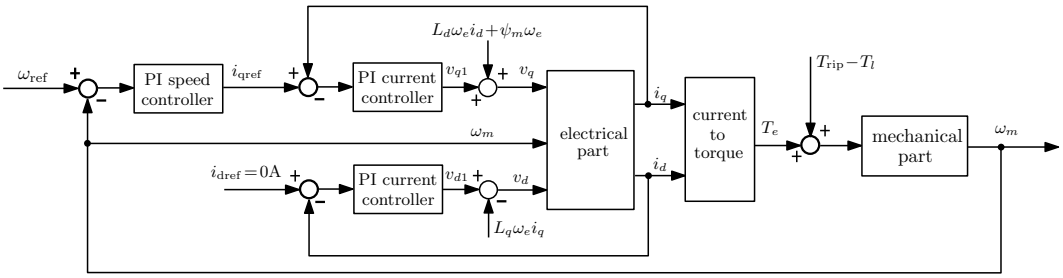

Figure 1.7: Representation of the PMSM vector control system.

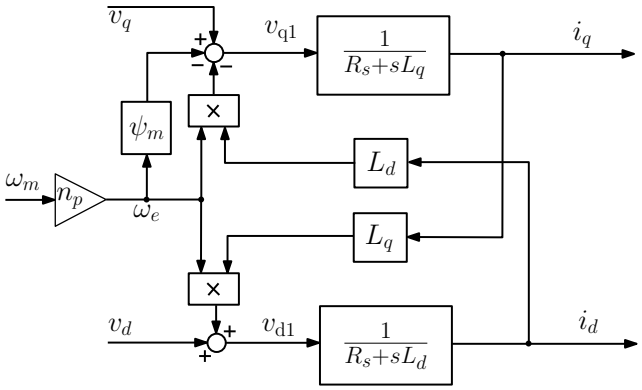

Figure 1.8: The detail of the PMSM electrical part (derived from Eq. 1.30).

system is visualized as T_{rip} in this figure. In addition, ω_{ref} is the speed reference and ω_m is defined in Eq. 1.16.

The aim of the PI current controllers is to make i_{dq} tracks $i_{\text{dq,ref}}$ with a good performance. Therefore, the transfer functions of the electrical part should be considered in the controller tunning.

The mathematical representation of the machine electrical part in the d-q reference frame written in Eq. 1.30 is represented as [27]

$$v_d = R_s i_d + L_d \frac{di_d}{dt} - \omega_e L_q i_q,$$
$$v_q = R_s i_q + L_q \frac{di_q}{dt} + \omega_e L_d i_d + \omega_e \psi_m.$$

Then according to Eq. 1.30, we can get Fig. 1.8, in which the d-axis current and the q-axis current are coupled, creating a control difficulty. To overcome this problem, the decoupling, as shown in Fig. 1.7, is commonly chosen to remove the interconnection between both axis. With the decoupling, the system current-loop based on Eq. 1.30 is drawn in Fig. 1.9, in which K_{pc} and K_{ic} are the proportional gain and the integral gain of the PI controllers. Correspondingly, we can get the following

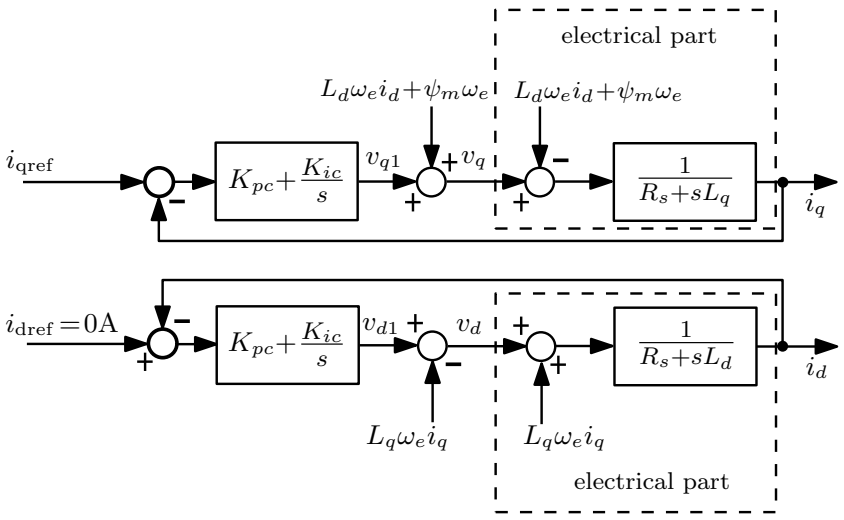

Figure 1.9: The detail of the PMSM current loop with decoupling.

independent equations

$$v_{d1} = R_s i_d + L_d \frac{di_d}{dt},$$
$$v_{q1} = R_s i_q + L_q \frac{di_q}{dt}.$$

As we know, the chosen machine is a surface-mounted one, consequently, we can assume that $L_d = L_q = L$. Then, the control processes for two PI current controllers become the same, hence we can use the same tuning for both. According to Fig. 1.9, the transfer function of the closed-loop is

$$\frac{I_d(s)}{I_{\text{dref}}(s)} = \frac{I_q(s)}{I_{\text{qref}}(s)} = \frac{\frac{K_{ic}+sK_{pc}}{s}\frac{1}{R_s+sL}}{1+\frac{K_{ic}+sK_{pc}}{s}\frac{1}{R_s+sL}}. \tag{1.39}$$

The Pole Cancellation Method (PCM) is popularly used for the PI current controller parameters setting [26]. PCM requires that the zero of the PI controller cancels the dominant pole of the control process. Then based on the principle of PCM and Eq. 1.39, we can obtain the following relation

$$\frac{K_{pc}}{K_{ic}} = \frac{L}{R_s}, \tag{1.40}$$

Accordingly, Eq. 1.39 can be simplified as

$$\frac{I_d(s)}{I_{\text{dref}}(s)} = \frac{I_q(s)}{I_{\text{qref}}(s)} = \frac{1}{1+s\frac{R_s}{K_{ic}}} = \frac{1}{1+sT_d}, \tag{1.41}$$

in which $T_d = R_s/K_{ic}$ is the time constant of this transfer function, and its bandwidth f_b can be calculated through $f_b = 1/(2\pi T_d)$. Meanwhile, for a given band-

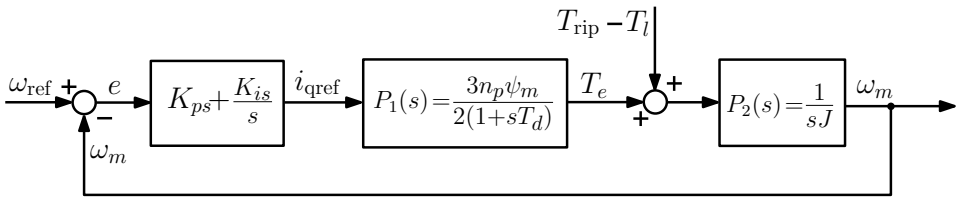

Figure 1.10: Simplified block diagram of the PMSM vector control system.

width f_d, the parameters of this current controller are calculated by

$$K_{ic} = \omega_d R_s = 2\pi f_d R_s \quad \text{and} \quad K_{pc} = K_{ic}\frac{L}{R_s} = 2\pi f_d L. \tag{1.42}$$

Because the PMSM considered in this project is a surface-mounted one, according to the previous analysis, $T_e = 3n_p\psi_m i_q/2$. Therefore, the current-to-torque conversion factor is $3n_p\psi_m/2$. On the other hand, to simplify the problem, the mechanical part considered here ignores the friction, so it can be written as

$$\omega_m(s) = \frac{1}{sJ}(T_e(s) - T_l(s)). \tag{1.43}$$

Then the system presented in Fig. 1.7 taking account of Eq. 1.41 can be deduced as

$$\begin{aligned} \omega_m(s) &= \frac{1}{sJ}\left(\frac{3}{2}n_p\psi_m I_q(s) - T_l(s)\right) \\ &= \frac{1}{sJ}\left(\frac{3}{2}n_p\psi_m \frac{1}{1+sT_d} I_{\text{q ref}}(s) - T_l(s)\right). \end{aligned} \tag{1.44}$$

Finally, the transfer function of the control process $P(s)$ can be expressed

$$\begin{aligned} P(s) &= P_1(s) \times P_2(s) = \frac{K}{sT_d(1+sT_d)}, \\ \text{with} \quad P_1(s) &= \frac{3n_p\psi_m}{2(1+sT_d)}, \quad P_2(s) = \frac{1}{sJ} \quad \text{and} \quad K = \frac{3n_p T_d \psi_m}{2J}. \end{aligned} \tag{1.45}$$

Accordingly, the system shown in Fig. 1.9 can be further simplified as shown in Fig. 1.10, in which K_{ps} and K_{is} are the proportional gain and integral gain of the PI speed controller. Consequently, we will use $P(s)$ to tune the parameters of the PI speed controller. In addition, the design and tunning of repetitive controllers presented in the future chapters will also be based on the system model shown in Fig. 1.10.

1.5.3 PI speed controller tuning

Until now, we already have the model of the control process, but we still need to choose an appropriate method to tune the PI speed controller tunning. Several

methods such as the PCM, the Cohen-Coon tuning method [28] and the Symmetrical Optimum Method (SOM) [29] are currently served for PI speed controller tuning. SOM proposed by Kessler is popularly used in the field of machine drive systems. Since SOM is able to enhance the system robustness and the disturbance rejection, it is chosen to tune the PI speed controller in this thesis.

The objective of the SOM is to obtain an open-loop transfer function of the below formula [29]

$$H_{\mathrm{bo}} = \frac{\omega_Q^2(\frac{\omega_Q}{\eta}+s)}{\sqrt{\eta}s^2(\omega_Q+s)}. \tag{1.46}$$

where ω_Q is the inverse of the system time constant T_d, and η is determined via a given phase margin φ_m as [25]

$$\eta = \left(\frac{1+\sin(\varphi_m)}{\cos(\varphi_m)}\right)^2. \tag{1.47}$$

H_{bo} has three poles and one zero. Two poles reside at the origin and the third one is a real plot locating at ω_Q. The only real zero is ω_Q/η. From Eq. 1.46, we can find that it has two frequency cut-offs: ω_d/η and ω_d, and its crossover frequency is $\omega_c = \omega_d/\sqrt{\eta}$ [1]. At the same time, it is easy to see that the slope of the magnitude response at the crossover is -20 dB/decade, which is the most desirable characteristic for good dynamic behavior. On the other hand, at its crossover frequency, the phase of the system is $\varphi_m - \pi$. As a result, the SOM can not only get a good system performance but also guarantee the desired stability margin.

In order to use the SOM for the model of Eq. 1.45, according to [25], K_{ps} and K_{is} are chosen as [25]

$$K_{ps} = \frac{1}{K\sqrt{\eta}} \quad \text{and} \quad K_{is} = \frac{1}{KT_d\eta^{\frac{3}{2}}}, \tag{1.48}$$

In this report, Eq. 1.48 would be used to tune the PI speed controller.

1.6 Torque ripples

The torque ripples of the PMSM produce speed ripple and seriously degrade machine performances, particularly at low speed. These torque ripples come from various sources, such as the cogging torque, the harmonic torque, the offset torque, the mechanical bias and several others [4, 30]. The origin and the characteristics of various kinds of torque ripples are presented in this section.

1.6.1 The cogging torque

The cogging torque manifests itself by the tendency of the rotor to align several stable positions, even when the machine is unexcited. It is caused by the interaction between the magnet flux and the stator slots. Therefore, only the slotless machines are immune to this kind of torque [18]. In many commercially available machines, the cogging torque has a nominal value of 5%-10% of the rated torque, and sometimes the cogging torque caused by an improper design of the machines might be as high as 25% of the rated torque [1].

Origin of the cogging torque

Fig. 1.11 shows four different positions of a permanent magnet in relation to the stator teeth, providing a clear explanation of the origin of the cogging torque. To simplify the discussion, an assumptive machine with four teeth and one pair of poles is used in this case.

Fig. 1.11.a shows the rotor aligned in position a. which is known as the detent position [1, 31]. A detent position is a position where the resulting cogging torque is zero [31]. In this position, the amount of air gap between the stator and the rotor reach its maximum. Moving the rotor from this position generates the cogging torque, which tries to reduce the air gap reluctance between the stator and the rotor. Since the subsequent torque attempts to “pull” the rotor away from this position, it is an unstable position [31].

When the rotor is rotating in the counterclockwise direction as shown in Fig. 1.11, it can reach position b, where the circumferential attractive forces are maximum. As it is shown in Fig. 1.11.b, position b corresponds to the peak value of the cogging torque. The cogging torque shown in Fig. 1.11.b “pulls" the rotor to a stable detent position [31].

Fig. 1.11.c shows the rotor aligned in a stable detent position. Here, the air gap and the reluctance are minimized. Any displacement of the rotor from position c increases the reluctance, leading to a cogging torque which forces the rotor to return to this position.

When the rotor moves from position c to position d, the cogging torque finishes one cycle as shown in Fig. 1.11.d. During this rotation, the corresponding cogging torque is negative one. As a result, this torque is attempting to “pull” the rotor back to position c.

Modeling of the cogging torque

The mathematical model of the PMSM cogging torque is derived from the magnetic field analysis. To simplify this analysis, several assumptions need to be made

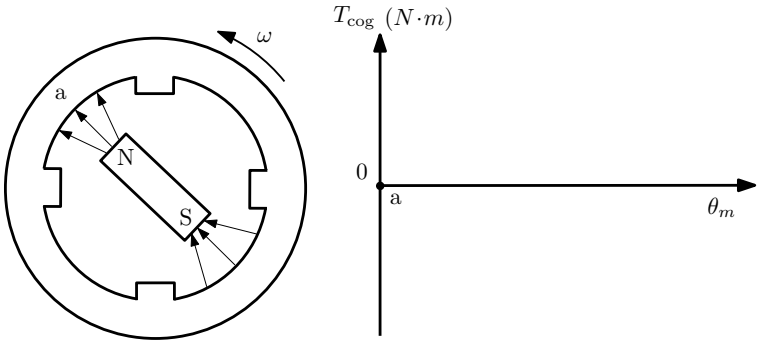

(a) An unstable detent position

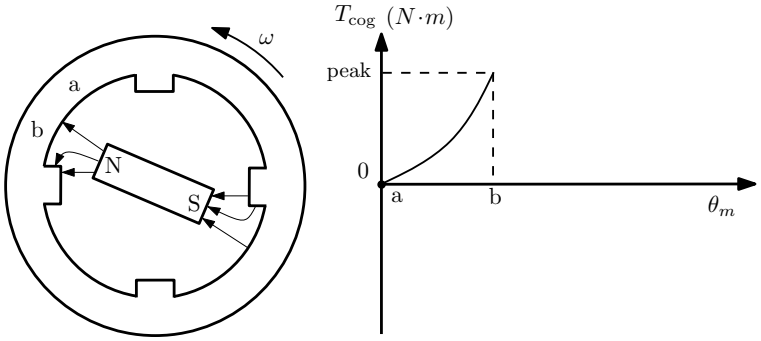

(b) A peak cogging torque position

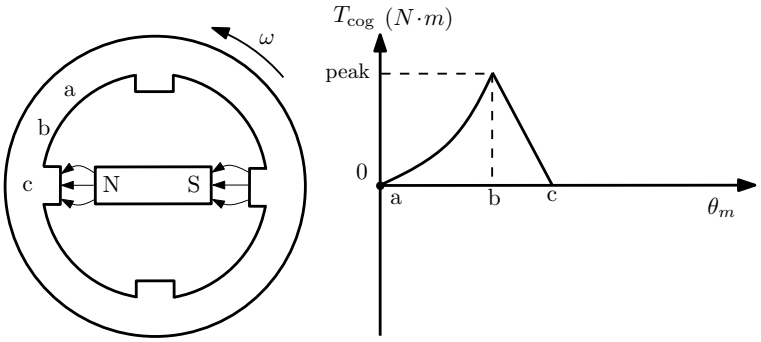

(c) A stable detent position

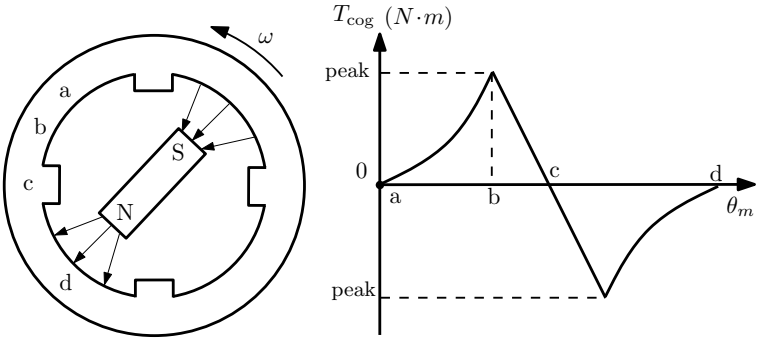

(d) An unstable detent position

Figure 1.11: One period of a typical cogging torque.

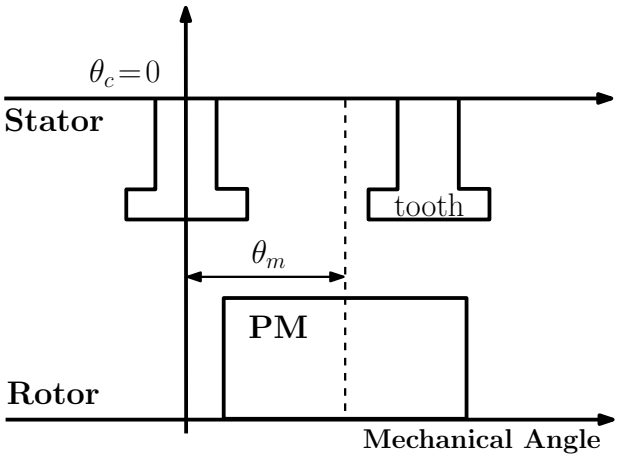

Figure 1.12: The relationship between the permanent magnets and the slots.

first [32]:

1. The magnetic permeability of the iron core is infinite, as $\mu_{\mathrm{Fe}} = \infty$.
2. The magnetic permeability of the permanent magnet μ_{PM} is the same as the magnetic permeability of air μ_0.
3. All the permanent magnets have the same performance, and all the windings also have the same performance.
4. There is no slot skewing and no rotor skewing in the machine.
5. Both the stator slots or the rotor magnets are distributed evenly and symmetrically.

The cogging torque can be defined as the negative partial derivative of the magnetic energy W_{cog} to the mechanic angular position θ_m [32, 33]

$$T_{\mathrm{cog}}(\theta_m) = -\frac{\partial W_{\mathrm{cog}}(\theta_m)}{\partial \theta_m}. \tag{1.49}$$

Therefore, in order to get the cogging torque expression, we need to analyze the magnetic energy first. With the first and the second assumptions, the magnetic energy of the machine can be regarded as the sum of the energy stored in air gap and in the permanent magnets [33],

$$W_{\mathrm{cog}}(\theta_m) \simeq W(\theta_m)_{\mathrm{airgap+PM}} = \frac{1}{2\mu_0}\int_V B(\theta_m)^2 dV, \tag{1.50}$$

where V is the magnetized volume which includes the air gap and the permanent magnet, and θ_m is defined in Eq. 1.16. Then $B(\theta_m)$, as a function of θ_m, presents the magnetic flux density distribution. The relationship between the permanent magnets and the slots in a PMSM is shown in Fig. 1.12, where θ_c is a reference angle, and in this case, $\theta_c = 0$ located the center of one tooth. As a result, θ_m, as shown in Fig. 1.12, is defined as the angle between the center of the chosen tooth and the

center of the chosen permanent magnet. The distribution of magnetic field in the air gap can be presented as the product of air gap relative permeance and air gap flux density in an equivalent slotless machine [33, 34], as

$$B = B(\theta_c, \theta_m) G(\theta_c), \tag{1.51}$$

where $B(\theta_c, \theta_m)$ is the flux density distribution of an equivalent slotless machine, $G(\theta_c)$ is the air gap relative permeance. Note that when $\theta_m = 0$, $B(\theta_c, \theta_m) = B_a(\theta_c)$, and when $\theta_m \neq 0$, $B_a(\theta_c, \theta_m)$ can be expressed as [33]

$$B(\theta_c, \theta_m) = B_a(\theta_c - \theta_m). \tag{1.52}$$

Considering Eq. 1.51, Eq. 1.50 can be rewritten as [33, 34]

$$W(\theta_m) = \frac{1}{2\mu_0} \int_V B_a^2(\theta_c, \theta_m)\, G^2(\theta_c) dV. \tag{1.53}$$

$B^2(\theta_c, \theta_m)$ can be expanded into a Fourier series

$$B^2(\theta_c, \theta_m) = B_{a0} + \sum_{m=1}^{\infty} [B_{a_m 2n_p} \cos(2mn_p(\theta_c - \theta_m)) + B_{b_m 2n_p} \sin(2mn_p(\theta_c - \theta_m))]. \tag{1.54}$$

$G^2(\theta_c)$, due to its symmetry, can be expanded into an even Fourier series

$$G^2(\theta_c) = G_{a0} + \sum_{k=1}^{\infty} G_{a_k z} \cos(kz\theta_c), \tag{1.55}$$

where z is the slot number. As shown in [33], the Fourier series coefficients B_{a0}, $B_{a_m 2n_p}$ and $B_{b_m 2n_p}$ are related to the slot opening, and G_{a0} and $G_{a_k z}$ are associated with the ratio between the pole-arc and the pole-pitch.

Considering Eq. 1.54 and Eq. 1.55, Eq. 1.53 becomes

$$W(\theta_m) = \frac{l_{ef}(R_2^2 - R_1^2)}{4\mu_0} \int_0^{2\pi} \sum_{m=0}^{\infty} B_m^2(\theta_c, \theta_m) \times \sum_{k=0}^{\infty} G_k^2(\theta_c) d\theta_c, \tag{1.56}$$

where R_1 and R_2 are the inner and outer radius of the air gap. Then according to Eq. 1.49 and Eq. 1.56, the cogging torque finally can be expressed as [35]

$$T_{\text{cog}}(\theta_m) = -\frac{\pi\, l_{ef} N_l}{4\mu_0} (R_2^2 - R_1^2) \sum_{n=1}^{\infty} n B_{a_n N_l} G_{a_n N_l} \sin(nN_l\theta_m), \tag{1.57}$$

where N_l is the least common multiple of z and $2n_p$,

$$N_l = \text{LCM}(z, 2n_p). \tag{1.58}$$

More detail about the mathematical deduction of the cogging torque expression can be found in [33]. Form Eq. 1.57, we can find that the cogging torque is a periodic function of the rotor position.

1.6.2 The harmonic torque

Another significant torque ripple is called harmonic torque in this report. In several other publications, it is also called ripple torque [4] or flux harmonics [36]. As implied by its name, this torque ripple comes from the harmonic components of the magnetic flux. As analyzed in section 1.2, the magnetic flux harmonic components appear since the permanent magnets and the inductances do not have the perfect sinusoidal shape. As a matter of fact, this kind of torque ripple is unavoidable for any practical PMSM.

To investigate the characteristics of the harmonic torque, we should first take a look at the electromagnetic torque equation, which is rewritten as

$$T_e = \frac{3}{2} n_p \psi_m i_q,$$

where the harmonic components of the magnetic flux have been intentionally ignored. To highlight the effect of the harmonic torque, these harmonic components are reconsidered, and according to Eq. 1.25, the electromagnetic torque equation can be changed as

$$T_e(\theta_e) = \frac{3}{2} n_p \left(\psi_m + \sum_{i=1}^{\infty} \psi_{rd,6i} \cos\left(6i\theta_e\right) \right) i_q. \tag{1.59}$$

To distinguish the harmonic torque from the total electromagnetic torque, Eq. 1.59 can be rewritten as

$$T_e(\theta_e) = T_{\mathrm{e,dc}} + T_{\mathrm{e,harm}}(\theta_e), \tag{1.60}$$

$$\text{with } T_{\mathrm{e,dc}} = \frac{3}{2} n_p \psi_m i_q$$

$$\text{and } T_{\mathrm{e,harm}}(\theta_e) = \frac{3}{2} n_p \left(\sum_{i=1}^{\infty} \psi_{rd,6i} \cos(6i\theta_e) \right) i_q. \tag{1.61}$$

Eq. 1.60 clearly shows that the electromagnetic torque contains a DC component and harmonic components. The characteristics of the harmonic torque are demonstrated in Eq. 1.61, where the harmonic torque is a function of the electrical angle. Since $\theta_e = n_p \theta_m$, the harmonic torque, as the cogging torque, is also a function of the mechanical angle.

1.6.3 Other torque ripples

As the cogging torque and the harmonic torque, several others sources can also lead to the torque ripple. In this subsection, we give a brief description of them.

1. The current offset torque.
   The current offset, which arises from the imperfection of the current sensors and other analog devices in the stator current measurement path, leads to a supplementary torque ripple, which is usually called DC offset torque [36, 37]. Because the DC offset currents are superimposed on the real phase currents, the measured phase currents can be expressed as [36]

$$\begin{aligned} i_{a,AD} = i_a + \Delta i_a, \quad i_{b,AD} = i_b + \Delta i_b \\ \text{and} \quad i_{c,AD} = -(i_{a,AD} + i_{b,AD}), \end{aligned} \tag{1.62}$$

   where $i_{k,\,AD}$ with $k = a, b, c$ presents the measured current and Δi presents the offset current. Consequently, i_d and i_q also contain the offset component, thus they can be written as [36]

$$i_{d,AD} = i_d + \Delta i_d \quad \text{and} \quad i_{q,AD} = i_q + \Delta i_q. \tag{1.63}$$

   According to the analysis in [36, 37], Δi_q can be calculated as

$$\begin{aligned} \Delta i_q &= \frac{2}{\sqrt{3}} \cos(\theta_e + \kappa) \sqrt{\Delta i_a^2 + \Delta i_a \Delta i_b + \Delta i_b^2}, \\ \text{with} \quad \kappa &= \tan^{-1}\left(\frac{\sqrt{3}\Delta i_a}{\Delta i_a + 2\Delta i_b}\right). \end{aligned} \tag{1.64}$$

   Then with Eq. 1.36, this current offset torque can expressed as

$$\Delta T_{\text{off}} = \sqrt{3} n_p \psi_m \cos(\theta_e + \kappa) \sqrt{\Delta i_a^2 + \Delta i_a \Delta i_b + \Delta i_b^2}. \tag{1.65}$$

   Note that this torque ripple is a function of the machine electrical angle, hence it is also the function of the mechanical angle.

2. The scaling error torque
   Current scaling error, as another type of current measurement error, results in another torque ripple, which is generally called scaling error torque [36]. Scaling error appears when the output of a current sensor must be scaled to fit the input range of an A/D converter, or a current controller rescales the value of the A/D converter output to get the actual value of a current [37]. Consequently, scaling errors of the currents always happen in digital

controller [37]. In this case, the measured currents can be presented as [36]

$$i_{a,AD} = \frac{I_s \cos(\theta_e)}{K_{as}}, \quad i_{b,AD} = \frac{I_s \cos(\theta_e - \frac{2}{3}\pi)}{K_{bs}}$$
$$\text{and } i_{c,AD} = -(i_{a,AD} + i_{b,AD}). \tag{1.66}$$

In Eq. 1.66, I_s is the nominal value of the current, $K_{as} \approx 1$ and $K_{bs} \approx 1$ are the scaling factors of phase-a and phase-b. Then the scale error of i_q, as derived in [37], is

$$\Delta i_q = i_q - i_{q,AD} = \frac{I_s}{\sqrt{3}} \left(\frac{K_{as} - K_{bs}}{K_{as} K_{bs}} \right) \left(\cos\left(2\theta_e + \frac{\pi}{3}\right) + \frac{1}{2} \right). \tag{1.67}$$

From Eq. 1.36 and Eq. 1.67, this scaling error torque is

$$\Delta T_{\text{scale}} = \frac{\sqrt{3} n_p \psi_m I_s}{2} \left(\frac{K_{as} - K_{bs}}{K_{as} K_{bs}} \right) \left(\cos\left(2\theta_e + \frac{\pi}{3}\right) + \frac{1}{2} \right), \tag{1.68}$$

which shows that the torque ripple caused by the scaling error is also a function of the machine electrical angle.

3. The mechanical default
   Several mechanical default such as the mechanical bias and the unequal distribution of friction in the bearing also can cause torque ripples. These torque ripples are naturally functions of the machine mechanical angle and their periods are usually equal to one mechanical rotation.

Summarizing the above analysis, we can reach the essential conclusion that the torque ripples of PMSM are functions of the mechanical angle, correspondingly their reduction can be considered as a periodic disturbance rejection problem.

1.7 Torque ripple reduction overview

A smooth torque is usually an important requirement for PMSMs. For instance, in electronic power steering (EPS) systems, the vibrations and noises caused by machine torque ripples seriously deteriorate the comfortability of the driver and the passengers. During the past thirty years, a considerable number of techniques have been dedicated to the reduction of the PMSM torque ripples. Broadly speaking, these proposed techniques can be classified into two major categories. The first one involves the design-based methods, which, focusing on the machine itself, aim to provide a smooth torque by optimizing the machine structure. The other includes the control-based methods, which, with the use of advanced control methods, modify the excitation current to actively reduce the torque ripples. A brief state-of-art of both kinds of techniques is given in this section.

1.7.1 Design-based techniques

Owing to the fact that the cogging torque is the main torque ripple component in PMSMs, most design-based techniques concentrate their attention on the connections between the cogging torque reduction and the machine structure optimization. As shown in section 1.6.1 and Eq. 1.57, the cogging torque is associated with the stator and the rotor design, as well as with the slot and pole number combination. A large number of papers have shown that the cogging torque can be effectively reduced by machine structure optimizations.

Moreover, the analysis in section 1.6.2 and Eq. 1.61 shows that the harmonic torque is related to the magnetic flux, which is determined by both the winding distribution and the rotor magnet design. Thus, it is also possible to reduce the harmonic torque through an improvement of the design of the windings and the magnets.

Slot number and pole number combination

The amplitude of the cogging torque decreases with the rise of its frequency [1, 4], therefore its reduction can be realized by purposely increasing the frequency of the cogging torque. According to Eq. 1.58, this frequency is related to the combination number of poles and slots. Hence to reduce the torque ripple, one needs to deliberately choose this combination number [38]. For example, for a 4 poles PMSM, with a 15 slots structure, the cogging torque of the corresponding machine has a higher frequency, hence a smaller amplitude than with 12 slots.

Stator design

Cogging torque, as a resultant of stator slots and rotor magnets, can be minimized by several particular stator designs. First, dummy slots and dummy teeth, adding some false slots and teeth in the machine, are two of these particular designs [39]. These additional slots and teeth are able to increase the frequency of the cogging torque, then reduce its amplitude correspondingly. On the other hand, as the cogging torque is related to the slot openings, it can be reduced through an optimization of the slot opening [40, 41]. In addition, as shown in [32], using the unevenly distributed slots is also a possible solution to minimize the cogging torque.

Winding design

As shown in Eq. 1.4 and Eq. 1.61, the ameliorations of the winding distribution and the magnetic flux density can possibly reduce the harmonic components of the magnetic flux, leading to a smaller harmonic torque. Meanwhile, the particular winding designs influencing the magnetic field are able to influence the cogging

torque. Short-pitched windings [42] and fractional number of slots per pole [43] are two popular techniques, which are developed to reduce the high-order harmonic component of the magnetic flux. Besides, the air gap winding technique, which is commonly used in axial-flux disk drive motors and high-speed machine tools, is able to compensate the stator teeth effect, and then to reduce the cogging torque [44].

Magnet design

Eq. 1.57 and Eq. 1.61 show that magnet design can affect not only the specifications of the cogging torque but also the amplitude of the harmonic torque. More sophisticated magnet arc designs can be used to minimize the cogging torque, and the realization of these methods is commonly achieved by using the finite-element method (FEM) [45]. For instance, [46] states that the 6 th harmonic torque can be effectively eliminated by choosing a particular magnet with approximately 150° arc. Another approach to reduce the cogging torque is to shift one pair of magnet poles with respect to the other [3]. Since the cogging torque arises from the interaction between the slots and the magnets, shifting one set of magnets, for example $1/4$ slot pitch can cancel the second-order harmonic component of the cogging torque [4].

Skewing

Skewing is phase shifting of the stator laminations or PMs along the axial direction in radial flux machines [1]. This technique, including the slot skewing and the magnet skewing, is one of the most popular techniques to reduce pulsating torque [32, 47]. Skewing accomplishes the cogging torque minimization by reducing the variation of magnetic reluctance seen by the rotor magnets. Skewing has also the effect of improving the stator windings distribution, so that the higher order magnetic flux can be reduced, hence the use of skewing technique can also bring the harmonic torque reduction.

However, as a coin has two sides, we cannot deny a fact that, despite certain particular designs are able to alleviate the torque ripple problem, almost all the techniques presented in this section would more or less specialize machine structure, in turn, causing additional design difficulties and the extra manufacturing costs. Moreover, some of them, such as the skewing, gain the reduction at a cost of losing a few efficiency [4].

1.7.2 Control-based techniques

As shown in Eq. 1.36, the electromagnetic torque is generated from the interaction between the magnetic field and the exciting current. Therefore, it is possible to reduce the torque ripple through a modification of the current shape. In a conventional PMSM drive system, PI controllers, owing to their bandwidth limitation, are not a good candidate to handle the torque ripple rejection problem. As a result, many advanced approaches have been studied for the PMSM torque ripple reduction. For instance, special filter techniques such as the passive filters [48], the hybrid filter [49] and the adaptive filter [50] have been already used to reduce the harmonic components for the current so as to achieve the torque ripple reduction. On the other hand, many more sophisticated control methods such as the adaptive control [51], the fuzzy control [52], the neural control [53] have been also reported on the torque ripple reduction. Since it is impossible to cover them all, in this section, we only focus on three popular ones: the programmed current waveform control, the instantaneous torque control and the memory-based control.

Programmed current waveform control

One of the most popular approaches for actively reducing the torque ripples is to use programmed excitation current waveforms. This approach comes from a straightforward idea that the torque ripple can be neutralized by adding a supplementary torque, which has the same amplitude and frequency as the target torque ripple, but its phase has an opposite-sign. Hence, to achieve this idea, the system needs an additional current, called compensating current, to produce the desired supplementary torque.

This approach generally can be realized in two manners, the time-based one and the frequency-based one. The time-based technique uses the time domain relationship between the current and the electromagnetic torque to calculate the compensating current [54]. The frequency-based technique usually referred as the harmonic injection method derives the compensation current according to the frequency features of the torque ripple. These desired features are usually obtained from the Fourier analysis of the torque [5].

Considering the number of related publications [33, 43, 55, 56, 57, 58], the frequency-based techniques obviously wins more attention from researchers than their time-based counterparts. The harmonic rejection method is a kind of off-line method [5], because to perform the desired torque ripple cancellation, the relationship between the compensating current and the target torque ripple needed to be found from tests and be programed into the controller in advance. Consequently, the reduction capability of this method definitely counts on the knowledge of the machine model and the accuracy of the measurement. As we know, these require-

ments can hardly be satisfied in a common PMSM drive. Several on-line estimation approaches are introduced to overcome this problem. For example, in [59], a Kalman filter was used to identify the harmonic components in flux in real-time so as to achieve the torque ripple minimization. However, an estimator usually consumes lots of calculation capability of the controller, increasing the requirement of the system. In a word, this kind of method is not well-suited for PMSM torque ripple reduction.

Instantaneous torque control

In most PMSM control systems, torque, in fact, cannot be considered as a direct controlled object, because the system can only indirectly control the torque by controlling the current. Consequently, it is rather complicated to achieve the torque ripple reduction with such a kind of control process. However, with the rapid development of torque sensors and torque estimation techniques, the instantaneous torque control [31], which takes torque as the direct controlled object, gradually comes from theory to reality in PMSM control systems. This new coming trend provides the possibility to reduce the torque ripple by directly controlling the torque.

The PMSM instantaneous torque control system, different from other conventional control systems, uses the torque control loop instead of the current loop [6] to achieve its control task. In turn, the torque controller, according to the measured rotor position and the torque value, chooses directly the corresponding voltage vectors to generate the desired torque output. Naturally, the efficiency of this system is determined by two factors, one is the accuracy and the rapidity of the torque information provided by the sensors or the estimators, and the other one is the performance of the torque controller.

Since a torque measuring mechanism is very expensive and bulky, efforts are mainly made to improve the torque estimator. In the early stage, the torque estimator, based on a simple system model, use the armature current alone to calculate the torque [6]. To improve the accuracy, the torque estimator developed from the Least-Square Method (LSM) was proposed in [60] and becomes a welcome solution in this field. Unfortunately, it is very difficult to implement LSM in practical systems, because it requires the differentiation of the current. To avoid this annoying problem, [61] proposed another estimator that uses the estimated flux and the measured current together to compute the torque. Since the model reference adaptive system technique is adopted for the flux estimation, the current differentiation is no longer an obstruction for the torque control system.

On the other hand, the bandwidth of the PI controllers constrains the torque ripple minimization. Consequently, in several publications [6, 62], the variable structure control, was chosen to enhance the torque control system. Though the use of

the variable structure control shows an interesting efficiency in the torque ripple reduction, it still has several practical problems, such as the unavoidable steady-state error, to be solved. For this, the integral variable structure control was proposed in [61], where a new controller, taking an integral action into the variable structure controller, was proposed to remove this steady-state error.

Though the capability of the torque control in the torque ripple reduction has been shown in many publications, the obvious distinction between the structure of this torque control system and that of other conventional PMSM control systems still strongly limits its popularity in industrial applications.

Memory-based control

The family of memory-based control techniques usually includes, the Iterative Learning Control (ILC), the Repetitive Control (RC) and the Run-to-Run control (R2R) [63]. This kind of methods is able to learn the "experience" from past executions to improve its current performance. The efficiency of this kind of method is definitely determined by the availability of the "experience", which requires the strictly repetitiveness of the control task. As analyzed in section 1.6, the torque ripple of PMSM is a function of the machine mechanical angle, so torque ripple reduction can be considered as a periodical disturbance rejection problem, which is perfectly welcomed by the memory-based control techniques. Many publications have reported the possibility to use the ILC and the RC for the PMSM torque ripple reduction.

The RC technique was firstly used for induction machines to improve their performances by alleviating the torque ripple problem [9, 10, 64]. With almost ten years of delay, the use of the RC for the PMSM torque ripple reduction problem was firstly appeared in [11], where a basic repetitive controller was applied to reduce the torque ripple. Some developments were made in [12], where a smoother torque output could be achieved by using a plug-in repetitive controller to suppress the harmonic current. Compared to the basic repetitive controller, the plug-in one gives a better tracking performance. An improved version of this idea was presented in [65], in which an high-pass filter was integrated into the repetitive controller to get a better system stability and a faster disturbance convergence speed. In [7], a new control system, in which a repetitive controller and a PI speed controller work together by a parallel connection, was used for the PMSM torque ripple reduction. The realization of this proposed system shows that it is possible to add the RC technique to a conventional PMSM vector control system. Several useful design rules were also offered in this paper.

Besides, the first application of the ILC technique on the PMSM torque ripple reduction was appeared in [66], where the process was controlled by a basic itera-

tive learning controller and a torque sensor was used for the direct torque control. To facilitate the implementation of the ILC, the plug-in iterative learning controller was chosen in [67], and accordingly, the tracking performance of this ILC system is superior to the basic ILC one. The improvement was made in [36], where the frequency-domain ILC algorithm instead of the time-domain ILC algorithm was chosen to get a better rejection capability, and a forgetting factor was also introduced to enhance the system robustness. Several progresses appeared recently. For example, in [68], a PI controller and an iterative learning controller work cooperatively to reduce the torque ripple. In [69], the iterative learning controller was integrated within the sensor to guarantee the integrality of the original system, as a result, the control object of the iterative learning controller is no longer the current but the measurement speed.

Therefore, according to the above analysis, we can conclude that both the RC technique and the ILC technique can provide a good torque ripple reduction capability. Moreover, the use of the memory-based control techniques needs only the memories of the controller, hence is relatively simple compared to other presented methods [11, 63]. Therefore, we consider the memory-based control technique to achieve the PMSM torque ripple reduction. Among these two candidates, we choose the RC technique, and the reason of this choice will be explained in section 2.1.3.

1.8 Test bench introduction

A dSPACE-based test bench shown in Fig. 1.13 was built in the SKF Automotive Development Center (ADC), Sensor Integration (SI) department, mechatronic laboratory. This test bench is used to implement not only the PMSM vector system but also various repetitive control systems, which will be presented in the following chapters.

This test bench, as shown in Fig. 1.13, consists of the following hardware: a surface-mounted PMSM, chosen as the experimental object; a dSPACE DS1005 processor board connected to a dSPACE DS5202 FPGA board and associated with a host PC; a dSPACE RapidPro power unit is used as inverter. A Magtrol hysteresis brake dynamometer HD705 is used as a load and it is controlled by the DSP 7000 dynamometer controller. In addition, a Meamwell PSP600 is used as a power supply.

On the other hand, two softwares are used to realize this practical implementation. One is Matlab&Simulink 2010a, which is used to do numerical simulations before the experiments and also to prepare and compile the Simulink scheme of the controllers. The other one is dSPACE Control Desk 4.3, which is able to down-

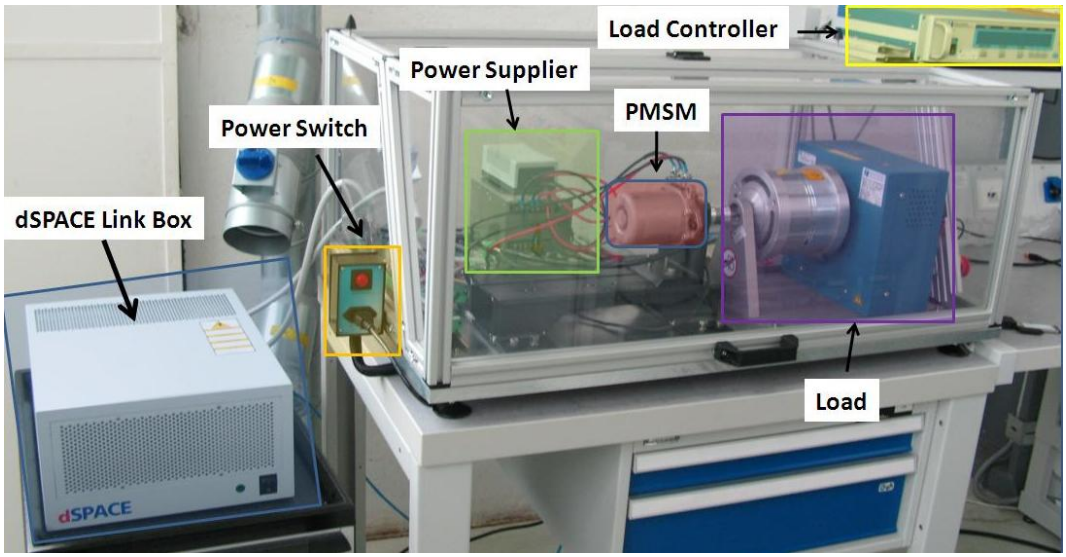

Figure 1.13: The SKF electric machine test bench.

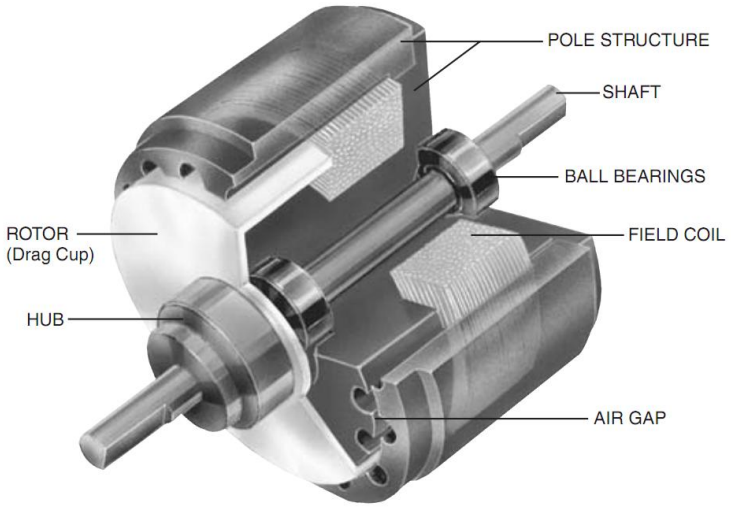

Figure 1.14: The structure diagram of the Hysteresis Dynamometer (reprinted from [70]).

load the corresponding code into the dSPACE FPGA, and can also provide a visual interface for users to manage the experiments.

In this section, a short presentation of the characteristics of the machine, the hysteresis brake dynamometer and the dSPACE board are shown first. Then the performance of a classical PMSM vector control system is verified through a simple test. Finally, the characteristics of the torque ripple of this system is shown, based on a frequency analysis of a speed measurement.

1.8.1 Experimental system introduction

The control plant chosen in this project is a surface-mounted PMSM designed for the Renault Mégane EPS system. Through several simple measurements and

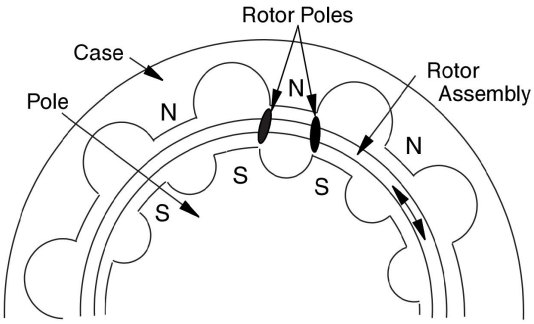

Figure 1.15: The cross-section of the Hysteresis Dynamometer (reprinted from [70]).

observations, the main parameters of this machine are determined and shown in Table. 1.1. A resolver used as a position sensor is embedded inside this machine to offer the position and speed information to the controller. At the same time, a position encoder set up outside the machine is used to verify the correctness of the information from the resolver.

Table 1.1: Parameters of PMSM

Stator resistance	0.013Ω
Stator inductance	0.07 mH
Magnetic flux linkage	0.017 Wb
Number of poles	8
Number of slots	12
Nominal power	1 kW
Machine+load inertia	0.012 kg.m^2

The load is a Magtrol hysteresis brake dynamometer. As shown in Fig. 1.14, it consists of a stator and a rotor, which are assembled together but not in physical contact. When the field coil is energized, a magnetic field proportional to the current is established. Then the rotor, located within the air gap, becomes magnetized, and the magnetic attractive force between the rotor and the stator generates a torque [70]. A cross-section presented in Fig. 1.15 shows the particular structure of this device, in which we can find that this hysteresis brake has the slots structure in both stators and slots. This brake can lead to cogging torque as PMSMs [70]. For the model we chose, the rate torque of this device is $6.2\,\mathrm{N{\cdot}m}$ and its rate power is $300\,\mathrm{W}$ [70]. Through a DSP-based controller, we can easily enable this device to provide the desired load. Besides, the PMSM and the hysteresis brake dynamometer are connected via a flexible coupling.

As mentioned at the beginning of this section, the dSPACE hardware in this experimental system is used for the controller and the inverter. The dSPACE controller consists of a DS1005 processor board and a DS5202 FPGA board [71]. The control program developed by the user is executed on the DS1005. The low-level signal processing is carried on the FPGA of the DS5202. It contains for example

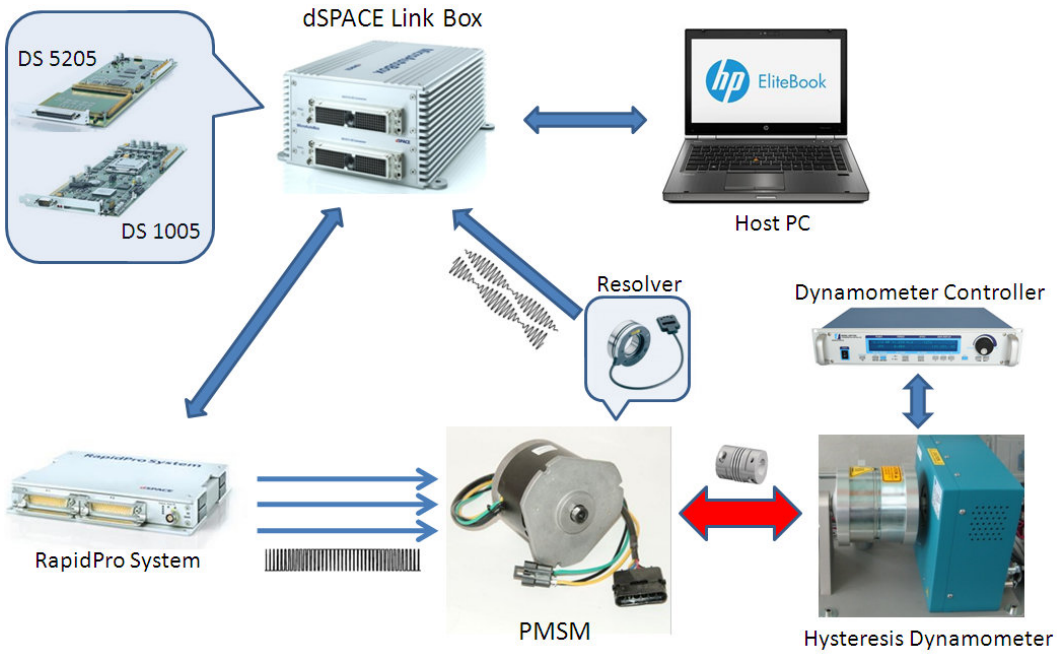

Figure 1.16: The architecture of the test system.

the processing of the rotor velocity and position for several types of rotary sensors (Hall encoders, incremental encoders, resolvers, SSI or EnDat encoders), processing of data from analog-digital-converters and the generation of PWM signals for 3-phase-motor control [71]. The DS5202 is connected to the DS1005 via a PHS bus [19]. The I/O EV1048 board placed on the DS5202 is the interface between the FPGA board and the motor and the sensors. On the other side, a RapidPro power unit is used to provide the prototyping system with the necessary power stages [71]. Because of its perfect compatibility with dSPACE controllers, it was chosen as the inverter in this system.

The working principle of this test bench is demonstrated by Fig. 1.16 and is explained as follows: before the test, the model of the system controllers established in the Matlab/Simulink should be downloaded into the dSPACE controller memory, and a visual operational interface should be created in the Control Desk so that a user can directly use a host PC to give orders to the dSPACE controller, and then control the PMSM. Then, when we begin to manipulate the system, the DS1005 processor, according to the given orders from the host PC and the acquired machine current and position information, is able to execute the programs stored in its memory to generate the control outputs. The DS 5202 converts these control outputs into PWM trigger signals and sends them to the RapidPro power unit. Then RapidPro power unit feeds the three-phase currents to the PMSM, making it run as expected. Besides, we can use the dynamometer controller to control the hysteresis brake dynamometer so as to get the desired load.

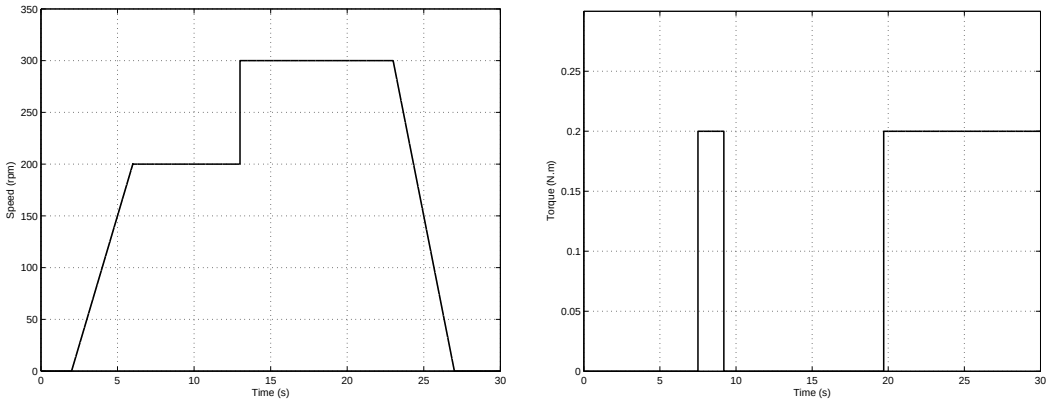

(a) The speed reference

(b) The torque disturbance

Figure 1.17: Profile of the reference speed and the torque disturbance.

1.8.2 The speed test and the torque ripple identification

The PI controllers tuning presented in section 1.5 are used here to set the PI current controllers and the PI speed controller parameters. The expected bandwidth of the speed loop is around 10 Hz, therefore the current response is chosen 10 times faster than the speed response, hence the bandwidth of the current loop is chosen as 100 Hz in this test bench. Then according to the parameters shown in Table. 1.1 and the PCM, the parameters of PI current controllers are chosen as: $K_{pc} = 0.044$ V/A and $K_{ic} = 7.54$ V·rad/s/A. In oder to get a 50 degrees phase margin, we can use SOM to get the PI speed controller parameters, which are: $K_{ps} = 26.90$ A·s/rad and $K_{is} = 2.24 \times 10^3$ A.

A simple test with a variable speed reference and a variable load was performed to check the performance of the designed system. The profile of the speed reference and the load torque are shown Fig. 1.17, and the system speed output is shown in Fig. 1.18. An analysis of this system behavior under various speed and load conditions is given as follows:

- The speed reference changed from 0 to 200 rpm between 3 and 6 s as a ramp, at the same time the load was zero. At the end of this transient, a very small overshoot happened. Therefore, Fig. 1.18 shows that the system could correctly follow a speed reference ramp.
- Between 6 and 13 s, the speed reference was 200 rpm, and the system could track this reference without any steady-state error. A 0.2 N·m load torque considered as a disturbance affected the system between 7.5 and 9 s. Fig. 1.18 shows that the occurrence of this load caused a -9 rpm speed error, whereas its extinction resulted in a 11 rpm speed ripple. Besides, these speed ripples faded within 0.3 s, proving that the designed system has an acceptable disturbance rejection capability.
- The speed reference changed as a step from 200 rpm to 300 rpm at 13 s, while

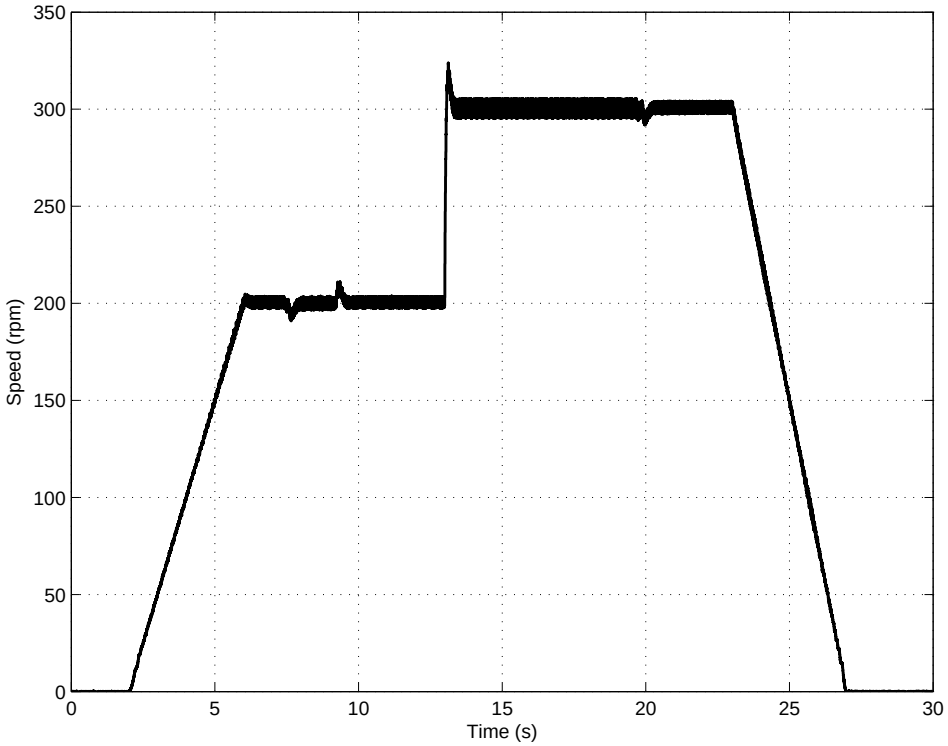

Figure 1.18: The measured speed obtained from the PMSM drive with the designed PI controllers.

the load torque was zero. As shown in Fig. 1.18, an overshoot whose absolute value is 25 rpm appeared just after this speed variation. Meanwhile, this overshoot disappeared within 0.3 s. Hence, in this system, the step response can reach the reference value with an overshoot of 25 % of the magnitude of the step.

– The speed reference decreased from 300 to 0 rpm between 23 and 27 s as a ramp while the load was 0.2 N·m. Under these conditions, the system can still track the speed reference, which is confirmed by Fig. 1.18.

The results and analysis above confirms the efficiency of the designed PMSM vector control system.

Since the torque ripples in PMSM cause the speed ripples, the frequency spectrum of the torque ripple can be known from the the spectrum of speed ripples. Fig. 1.19 shows the amplitude spectrum of the measured speed obtained in steady-state with tuned PI controllers. This test was achieved at 60 rpm and with a 1 N·m load torque. As shown in this figure, the 24 Hz is the biggest speed ripple, at the same time, 1, 4, 8, 16 and 35 Hz ones are also relatively important. Therefore, this PMSM drive contains 1, 4, 8, 16, 24 and 35 th speed ripples. Since our machine has 8 poles and 12 slots, according to Eq. 1.57, this 24 th speed ripple is the fundamental of the cogging torque. Meanwhile, from Eq. 1.61, this torque ripple component is also the fundamental of the harmonic torque. On the other hand, the 1 th probably comes from the mechanical bias, and the 4 th and the 8 th, according to Eq. 1.68

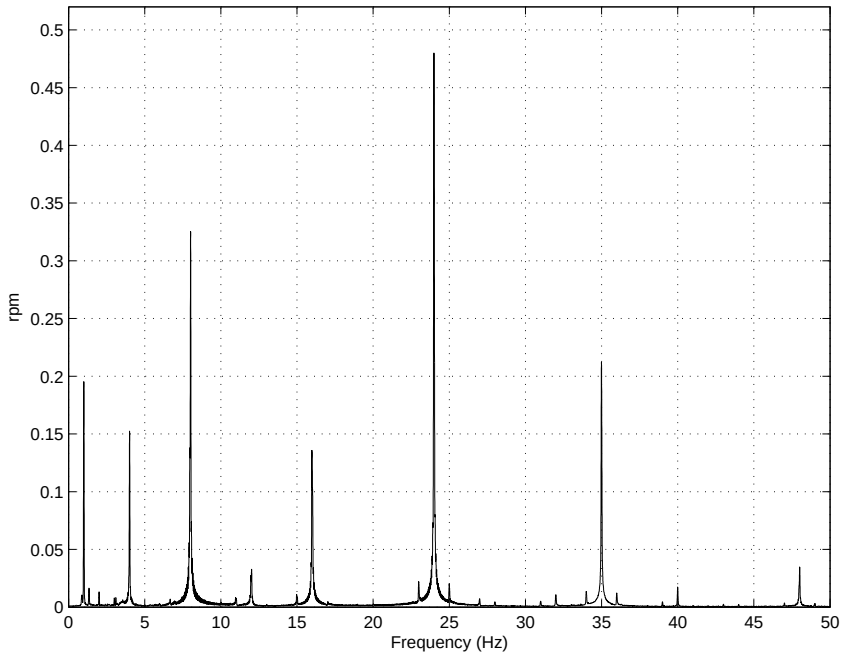

Figure 1.19: The frequency spectrum of the speed ripple measured from the test bench. The reference speed is $\omega_m = 2\pi$ rad/s (60 rpm) and the load torque is $T_l =$ 1N·m.

and Eq. 1.65, correspond to the DC offset and the scaling error. Besides, the 16 th might be the second order of scaling error. In addition, with a simple test and observation, we confirm that the 35 th component stems from the cogging torque of the hysteresis brake dynamomete.The above analysis shows that the measured results can coincide with the theoretical analysis.

1.9 Conclusion

The background presented in this chapter is the necessary basis of this PhD thesis. At the beginning of this chapter, we describe some general knowledge of PMSMs, their basic modeling, a PMSM drive system architecture, the vector control conception and the PI controller tuning methodology in order to build a PMSM drive system. Second, to minimize the torque ripple, we provide a classification and also an analysis of the PMSM torque ripples, which reveal that most of the torque ripples can be considered as periodical disturbances, hence the torque ripple reduction in PMSMs can be considered as a periodic disturbance rejection problem. This is followed by a survey about the existing approaches used for torque ripple reduction, showing that the repetitive control is a good candidate for this issue. Finally, with the knowledge mentioned above, we implemented a PMSM drive system in a dSPACE based test bench. The measurements carried on this experimental platform confirm the efficiency of system design, and also show the periodic characteristics of the torque ripple.

2

Repetitive Control

The Repetitive Control (RC) technique, because of its high capability in periodic disturbance rejection, is chosen in this Ph.D thesis to achieve the PMSM torque ripple reduction. The success of the use of the RC technique is mainly determined by how well we know it. Hence, establishing a deep and sound understanding of this technique is the theme of this chapter. In addition, several original contributions, such as providing controller design methodologies and developing a new repetitive controller, are also presented in this chapter.

The theoretical background and the development history of the RC technique should be given at first in order to offer a general idea about it. The Iterative Learning Control (ILC), as another memory-based control technique, is very similar to the RC, so it is necessary to distinguish the ILC technique from the RC technique. A more technical study should start from the basic repetitive control controller, since it is the simplest one and is also the basis of repetitive control controllers. The simplicity of this basic structure will make the presentation of stability and performance indicator easier, although we will quickly show that this controller is not suitable for the torque ripple reduction in PMSM drive. The stability and the performance of the basic RC system, regarding to their importance, must be studied carefully. A design methodology that can balance the stability and the performance should be given to guarantee the system efficiency. The same study should be done for current repetitive controllers, because they are also important members in the RC family. According to popularity and importance, the current iteration repetitive controller and the current feedback repetitive controller will be considered for the PMSM torque ripple reduction problem. The tracking performance of all these studied RC systems is impaired by large overshoots and oscillations. To overcome

this problem, one has to give a reasonable interpretation first, and then provide a feasible solution that can improve the RC system tracking behavior while keeping the reduction capability.

2.1 Overview of the repetitive control

The repetitive control, based on the Internal Model Principle (IMP), is an effective approach used for periodic reference tracking or for periodic disturbance rejection [72]. Since the torque ripple reduction of PMSM, as analyzed in section 1.6, can be regarded as a periodic disturbance rejection problem, the repetitive control technique is naturally a good choice to deal with this problem. Before going into a more technical discussion, a brief historical overview of the RC technique is given at the beginning of this section. Then, the operating principle of the repetitive controller and the basic repetitive controller are introduced together. In order to differentiate the RC technique from another similar technique, a description of their relationship is also provided in this section.

2.1.1 Brief historical overview

The IMP proposed by Francis and Wonham [73] is the theoretical foundation of the RC technique [72]. The IMP states that in a stable closed-loop system, in order to track or reject a repetitive signal without steady-state error, an autonomous generator, which is able to regenerate this target signal, should be contained within this control system. Such kind of autonomous generator can be achieved through a time-delay positive feedback system. A control system adopting this scheme to achieve its control task is considered as a RC system [63].

The RC was initially developed for continuous-time SISO LTI systems in [74] in order to track a periodic reference input with a high accuracy. In the same paper, the authors also proved that the stability of repetitive controllers could be determined by a BIBO condition. However, [75] pointed out that the availability of this BIBO condition could be guaranteed only when the transfer function of the control object were proper but not strictly proper. Then, another general RC stability condition derived from the Phragmen-Lindelof theorem was proposed in [76]. Several years later, the connection between the RC stability and the small gain theorem was reported in [77], in which the authors treated the learning control system as an infinite-dimensional system, which facilitates the analysis. This publication concluded that the sufficient stability condition of RC systems could be deduced from the small gain theorem.

Efforts have been made to improve the robustness and the performance of RC systems. Hara et al in [75] proposed that the stability robustness could be improved

by introducing low-pass filters in RC systems, but they also confessed that the use of the filter would impair the tracking performance. On the other hand, [78] expanded this modified repetitive controller from SISO to MIMO cases, and also offered an exponential stability condition. A new type of repetitive controller called plug-in repetitive controller was first proposed in [75], where the repetitive controller could be added into an existing system without breaking its integrity [79]. Further, [80] revealed that the plug-in repetitive controller could offer RC systems a better transient response.

The performance of RC systems is usually analyzed in the frequency domain. For example, in [81], some authors introduced a so-called regeneration spectrum, which is a useful tool to evaluate the performance of the SISO continuous-time RC system. By carefully tuning the regeneration spectrum, one could balance the stability and performance. Meanwhile, several synthesis approaches were also proposed to achieve RC system designs, for instance, the state-space approach [78], the factorization approach [75], and the $\mathcal{H}_\infty$ optimal design approach [82].

Implementing the repetitive controller in a discrete-time manner was first reported in [83], where the RC technique was chosen to reduce the periodic error caused by the discretization of continuous-time systems. M. Tomizuka studied the stability condition of the discrete-time repetitive controller in [84], showing that the asymptotic stability of the discrete-time repetitive controller could be ensured by solving a Diophantine equation. A typical problem that needs to be considered in the discrete-time repetitive controller design is that the target exogenous periodic signals cannot always be synchronized exactly as an integer multiple of the sampling period, which seriously limits the performance of the repetitive controllers. To overcome this, M. Steinbuch [85] provided a novel repetitive controller structure, which uses multiple memory-loops within a certain feedback configuration. Another possible solution was presented in [86], where an on-line tuning delay filter was used to reconstruct non-synchronized signals by optimally interpolating signals between samples.

At the early stage of the RC research, the emphasis of its development mainly laid in how to use this technique to achieve the periodic reference tracking without steady-state error. The initial objects of this kind of applications were servo systems [78] and robot systems [87, 88], and then its application expanded towards peristaltic pumps [89], disc drives [90, 91] or satellite trajectory control systems [92]. Thereby, more and more scientists turned their attention to the disturbance rejection capability of the RC technique. The use of the RC for the periodic disturbance rejection stems originally from the machine control area, because the nature of this technique is well-suited to reduce the torque and the speed oscillations in rotating machines. In the past decades, a lot of papers, as already shown in section 1.7.2, were devoted to this kind of application. Another typical application of

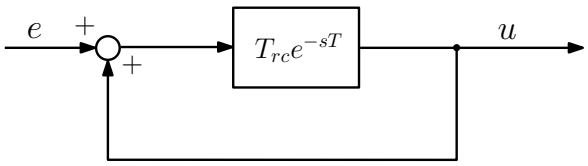

Figure 2.1: A periodic signal generator derived from the IMP.

the RC is the rejection of the current harmonics of the PWM inverters [93, 94, 95]. Meanwhile, this kind of application also spreads to many other areas, such as friction compensations [96], photovoltaic generation systems [97] and so on.

Two surveys on the RC technique were written by C.Y. Li [72] and Y.Q. Wang [63] respectively. The former one focused on the theoretical basis of various repetitive controllers, as well as offered a classification of different RC techniques. The latter one distinguished the RC technique from two other memory-based techniques by presenting the characteristics of the RC technique, and it also provided an introduction about the practical applications of this technique.

Recently, applying the RC technique for the aperiodic disturbance rejection is gaining popularity, and several papers [98, 99] have made their contribution to this subject. Wu et al [98] proposed to use an estimator-based repetitive controller to handle the disturbance with varying periods, and in [99], Lu et al suggested to integrate a sliding-mode technique with the RC technique so as to bring the system aperiodic disturbance rejection capability. On the other hand, an increasing number of scientists consider using the adaptive RC technique to remove varying frequency disturbance [100] and enhance the system stability robustness [101]. Besides, developing the RC technique for nonlinear system currently becomes a booming topic in this field, and the model predictive based RC technique is a welcome solution for this kind of problem [102, 103].

2.1.2 Basic repetitive controller

The functionality of the RC, according to the IMP, is established on a time-delay positive feedback system, whose typical realization is shown in Fig. 2.1 [63]. In this figure, e^{-sT} is a time-delay, T_{rc} is a transfer function used to manage the system performance, e is the input of this generator and u is its output. The relationship between e and u, regarding the Fig. 2.1, is derived as

$$U_{rc}(s) = \frac{T_{rc}(s)e^{-sT}}{1 - T_{rc}(s)e^{-sT}} E(s), \tag{2.1}$$

which indicates that this signal generator can be possibly represented by another structure as shown in Fig. 2.2. This new representation uses two delay components

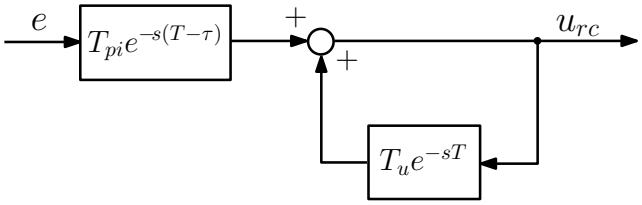

Figure 2.2: Another realization of the periodic signal generator.

and two tunable transfer functions, T_u and T_{pi}. When $T_u = T_{pi} = T_{rc}$ and $\tau = 0$, it has the same transfer function as the structure shown in Fig. 2.1. Note that the subscript "pi" used here stands for previous iteration. Compared to the first structure, the new one with an additional parameter and τ can bring more design freedom. In fact, the generator shown in Fig. 2.2 is a basic repetitive controller [63], and this repetitive controller is written as

$$U_{rc}(s) = T_u(s)\, e^{-sT} U_{rc}(s) + T_{pi}(s)\, e^{-s(T-\tau)} E(s), \tag{2.2}$$

where τ is usually called leading-time component [7, 104] and is introduced in this basic repetitive controller owing to its ability of changing the system behavior. From Eq. 2.2, we can see that the repetitive controller generates its output information with its output information delayed of T and the error information delayed of $T-\tau$. It is not difficult to get an idea that to guarantee the functionality of the repetitive controller, T should be equal or an integer multiple of the period of the reference or the disturbance. This matching between T and the period of the disturbance will be discussed again in Chapter 3 with a deeper analysis.

To know more about this controller, its time domain expression obtained with the inverse Laplace transform is

$$u_{rc}(t) = \mathcal{L}^{-1}\{T_u(s)\} * u_{rc}(t-T) + \mathcal{L}^{-1}\{T_{pi}(s)\} * e(t-(T-\tau)), \tag{2.3}$$

where $\mathcal{L}^{-1}\{\ \}$ is the inverse Laplace transform operator and $*$ is the convolution operator. Since the repetitive controller is implemented in a digital controller, it is also interesting to introduce its discrete-time expression. Provided that T_s is the sampling period of this discrete-time repetitive controller, $N = T/T_s$ and $N_\tau = \tau/T_s$, Eq. 2.3 can be changed as

$$u_{rc}[k] = \mathcal{Z}^{-1}\{T_u(z)\} * u_{rc}[k-N] + \mathcal{Z}^{-1}\{T_{pi}(z)\} * e[k-(N-N_\tau)], \tag{2.4}$$

where $\mathcal{Z}^{-1}\{\ \}$ is the inverse Z-transform operator and $k = 0, 1, 2 \ldots$ is the discrete

time index. Finally with the Z-transform, Eq. 2.4 in the z-domain can be written as

$$U_{rc}(z) = T_u(z) z^{-N} U_{rc}(z) + T_{pi}(z) z^{-(N-N_\tau)} E(z), \tag{2.5}$$

where z^{-N} represents the delay in the z-domain. Note that in the digital controller, the controller delay is accomplished by a memory, so N is also the length of these memories.

The simplest continuous-time RC system includes a basic repetitive controller and a process connected in a series way. This system is usually called basic RC system and its typical realization is shown in Fig. 2.3 [72]. Since the subject of this work is to use the RC technique to reduce PMSM torque ripple, the process considered here comes from the PMSM model presented in section 1.5.2, and is rewritten as

$$P(s) = P_1(s)P_2(s) = \frac{K}{sT_d(1+sT_d)},$$
$$\text{with } P_1(s) = \frac{3n_p\psi_m}{2(1+sT_d)}, \quad P_2(s) = \frac{1}{sJ} \text{ and } K = \frac{3n_pT_d\psi_m}{2J}.$$

$P(s)$ is a linear time-invariant process with a single input and a single output. In a PMSM control system, the exogenous disturbance d usually consists of two components: one is the load torque, which is a DC component; the other one, including the different kinds of torque ripples, is a periodic disturbance. The period of this disturbance, according to section 1.6, is equal to the duration of one mechanical rotation. As a result, $T = 2\pi/\omega_m$ is chosen for this repetitive controller in order to ensure that its rejection capability can cover all possible torque ripples. It should be noted that ω_m discussed in this section represents a nominal speed.

The study of the modeling of the PMSM presented in section 1.5.2 deliberately ignored the friction. If we reconsider it, then $P_2 = 1/(k_f+sJ)$ and the process model is changed as

$$P(s) = P_1(s)P_2(s) = \frac{3n_p\psi}{2(1+sT_d)} \frac{1}{k_f+sJ} = \frac{K}{T_d(k_f/J+s)(1+sT_d)}, \tag{2.6}$$

in which $k_f = 1.2\times10^{-4}$ N·m·s/rad is the friction coefficient. It should be noted that this model will be specifically considered when studying the stability and load-torque error of the basic repetitive controller.

Henceforward, to make the report more clear, we will drop (s) or $(j\omega)$ in most equations. According to Eq. 2.2 and Fig. 2.3, the transfer function of the basic

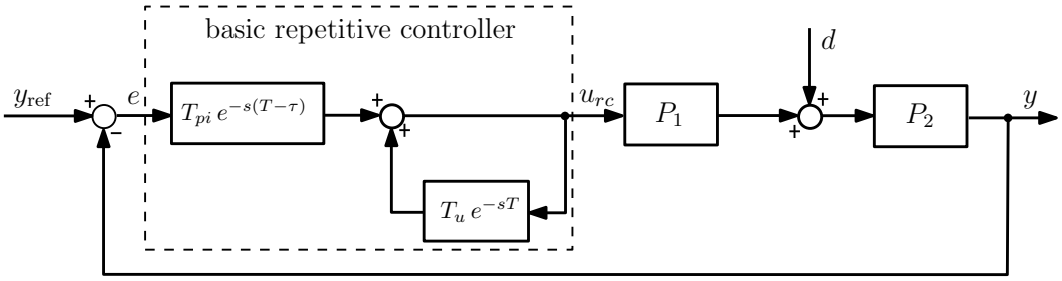

Figure 2.3: Block diagram of the process controlled by a basic repetitive controller (in our case, $y_{\text{ref}} = \omega_{\text{ref}}$, $y = \omega_m$, $u_{rc} = i_{\text{qref}}$, $d = T_{\text{cog}} - T_l$, P_1 and P_2 are defined in Eq. 1.45).

repetitive controller between its input e and output u_{rc} can be deduced as

$$\begin{aligned} U_{rc}(s) &= T_u(s)\, e^{-sT} U_{rc}(s) + T_{pi}(s)\, e^{-s(T-\tau)} E(s) \\ \left(1 - T_u(s)\, e^{-sT}\right) U_{rc}(s) &= T_{pi}(s)\, e^{-s(T-\tau)} E(s), \end{aligned}$$

therefore,

$$C_{rc}(s) = \frac{U_{rc}(s)}{E(s)} = \frac{T_{pi}(s)\, e^{-s(T-\tau)}}{1 - T_u(s)\, e^{-sT}}. \tag{2.7}$$

From Eq. 2.7, the relationship between the system output y, the reference input y_{ref} and the disturbance d is

$$\begin{aligned} Y &= \frac{T_{pi} P e^{-s(T-\tau)} Y_{\text{ref}} + (1 - T_u e^{-sT}) P_2 D}{1 - T_u e^{-sT} + T_{pi} P e^{-s(T-\tau)}} \\ Y &= \frac{T_{pi} P e^{-s(T-\tau)}}{1 - (T_u - T_{pi} P e^{s\tau}) e^{-sT}} Y_{\text{ref}} + \frac{1 - T_u e^{-sT}}{1 - (T_u - T_{pi} P e^{s\tau}) e^{-sT}} P_2 D \\ Y &= H_{\text{rcr}}\, Y_{\text{ref}} + H_{\text{rcd}}\, P_2 D, \end{aligned} \tag{2.8}$$

$$\text{with } H_{\text{rcr}} = \frac{T_{pi} P e^{-s(T-\tau)}}{1 - G_{rc} e^{-sT}}, \quad H_{\text{rcd}} = \frac{1 - T_u e^{-sT}}{1 - G_{rc} e^{-sT}},$$

$$G_{rc} = T_u - T_{pi} P e^{s\tau} = T_u (1 - T_{pi2} P e^{s\tau}) \text{ and } T_{pi2} = T_{pi}/T_u.$$

Similarly, from Eq. 2.7, the relationship between the error signal e, the reference input y_{ref} and the disturbance d is

$$\begin{aligned} E &= \frac{1 - T_u e^{-sT}}{1 - T_u e^{-sT} + T_{pi} P e^{-s(T-\tau)}} Y_{\text{ref}} - \frac{1 - T_u e^{-sT}}{1 - T_u e^{-sT} + T_{pi} P e^{-s(T-\tau)}} P_2 D \\ E &= \frac{1 - T_u e^{-sT}}{1 - G_{rc} e^{-sT}} (Y_{\text{ref}} - P_2 D) \\ E &= H_{\text{rcd}}\, (Y_{\text{ref}} - P_2 D)\,. \end{aligned} \tag{2.9}$$

The further study of this system, involving the stability and the performance analy-

sis is based on Eq. 2.8 and Eq. 2.9.

2.1.3 The iterative learning control

The ILC technique, as one of the memory-based control technique, is perhaps the most similar one to the RC technique, so it is necessary to distinguish the RC from its "twin brother". The ILC stems from a commonsense that human being can improve himself through repetitive trainings, so for the machines which execute same tasks repeatedly, their performance can also be improved by learning the experience from their previous tasks.

In 1978, the original idea of the ILC was first presented in Japanese by M. Uchiyama [105] for a mechanical arm control system. The first introduction of the ILC in English was done in 1984 by another Japanese scientist, S. Arimoto, for a robot control system [106]. After thirty years of rapid development, the ILC has become an important branch in the control family and is currently used in many applications. A widely used ILC algorithm in the z-domain is written as [107]

$$U_i(z) = Q(z)\left(U_{i-1}(z) + zL(z)\,E_{i-1}(z)\right), \tag{2.10}$$

where i is the iteration index, $Q(z)$ and $L(z)$ are called the Q-filter and the learning function respectively. The error information $E(z)$ is the input of the iterative learning controller and the control information $U(z)$ is its output. Correspondingly, its time domain equation is

$$u_i[k] = \mathcal{Z}^{-1}\{Q(z)\} * \left(u_{i-1}[k] + \mathcal{Z}^{-1}\{L(z)\} * e_{i-1}[k+1]\right), \tag{2.11}$$

where $k = 0, \ldots N-1$ is a relative time index to the beginning of the current iteration and N is the length of an iteration.

The comparison between Eq. 2.5 and Eq. 2.11 shows the similarity and the distinction between the ILC and the RC. On one side, the output of the ILC is formulated with its output of the last iteration and the error information of the last iteration, which is very close to how RC works. On the other side, Eq. 2.5, which uses a the time-delay, indicates that the RC is fit to handle continuous operations, such as the disc drive system [90, 91]; on the opposite side, Eq. 2.11, using the iteration index, implies that the ILC is good when dealing with batch operations, such as the robot trajectory control [108, 109]. Besides, for a ILC system, a perfect reset, which ensures that the system can repeatedly operate on the same task under the same condition, must be done after each iteration (trail, execution, run), showing that it is usually applied to discontinuous (batch) applications [110]. As a result, the RC technique is more suitable than the ILC technique for the torque ripple reduction in PMSMs. Besides, without the reset, the study and the realization of this

technique is relatively more simple than the ILC.

However, for several kinds of operations whose initial state of a new iteration closely follows their final state of the last iteration, so the reset is no longer absolutely required or could be directly considered as an automatic process, in which the use of the RC and the ILC are nearly the same. More importantly, the no-reset technique [111] helps the ILC to get rid of the initial condition without influencing its functionality, leading to an unclear boundary between these techniques.

Provided that the reset is not mandatory for the iterative learning controller, then the operation of the ILC can be regarded as a continuous process, and Eq. 2.11 can be changed as

$$\begin{aligned} u_i[k] &= \mathcal{Z}^{-1}\{Q(z)\} * \left(u_{i-1}[k] + \mathcal{Z}^{-1}\{L(z)\} * e_{i-1}[k+1]\right) \\ u[iN+k] &= \mathcal{Z}^{-1}\{Q(z)\} * \left(u[(i-1)N+k] + \mathcal{Z}^{-1}\{L(z)\} * e[(i-1)N+k+1]\right) \\ u[iN+k] &= \mathcal{Z}^{-1}\{Q(z)\} * \left(u[iN+k-N] + \mathcal{Z}^{-1}\{L(z)\} * e[iN+k-(N-1)]\right). \end{aligned}$$

Suppose that the sampling period of this discrete-time ILC algorithm is T_s. The current time t is $(iN+k)\cdot T_s$, the duration of one iteration is $T = N \cdot T_s$ and τ is equal to T_s. By replacing Q by T_u, and $Q*L$ by T_{pi}, the discrete-time ILC algorithm can be written as

$$u[n] = \mathcal{Z}^{-1}\{T_u(z)\} * u(n-N) + \mathcal{Z}^{-1}\{T_{pi}(z)\} * e(n-(N-N_\tau)), \tag{2.12}$$

with $n = iN + k$. The comparison between Eq. 2.3 and Eq. 2.12 shows that without the reset, the distinction between the ILC and the RC vanishes. This is the reason why Wang et al claimed in [63] that there is no essential difference between the two techniques. In my personal opinion, although they are quite similar, owing to the reset of the ILC, we still have sufficient reasons to define them as two different control techniques.

2.2 Stability analysis

Stability is a general and important concern for any control system. This section is dedicated to seeking the stability condition of the basic RC system. At the beginning of this chapter, a preliminary result is presented to help understand the stability condition of the basic RC system. Then the small gain theorem, which is an effective approach to deal with the stability issue of time-delay systems, is introduced. At last, a sufficient stability condition of the basic RC system is derived from the small gain theorem.

2.2.1 Preliminary results

Before introducing the small gain theorem, the analysis of the particular case where $T_u = 1$ and $\tau = 0\,\mathrm{s}$ in a basic RC system will be the starting point of the study of the RC system stability condition. With these assumptions, Eq. 2.9 can be rewritten as

$$E = \frac{1-e^{-sT}}{1-(1-T_{pi}P)e^{-sT}}Y_{\text{ref}} - \frac{(1-e^{-sT})}{1-(1-T_{pi}P)e^{-sT}}P_2D,$$
$$\text{then} \quad \left(1-(1-T_{pi}P)e^{-sT}\right)E = (1-e^{-sT})Y_{\text{ref}} - (1-e^{-sT})P_2D. \tag{2.13}$$

Suppose that the reference signal Y_{ref}, the disturbance D and the error E are a complex sinusoids of frequency k/T, where k is a positive integer, then we can get

$$y_{\text{ref}}(t) = A_{\text{ref}}e^{j\frac{2\pi kt}{T}}, \quad d(t) = A_d e^{j\frac{2\pi kt}{T}}, \quad \text{and} \quad e(t) = A_e e^{j\frac{2\pi kt}{T}}, \tag{2.14}$$

where A_{ref}, A_d and A_e represent the magnitude of the reference, the disturbance and the error respectively. So for a LTI system, Eq. 2.13 can be changed as

$$(1-(1-T_{pi}P)e^{-j2\pi k})e(t) = (1-e^{-j2\pi k})(y_{\text{ref}}(t) - P_2d(t)).$$

Since $e^{-j2\pi\,k} = 1$, $(1-e^{-j2\pi k})(y_{\text{ref}} - P_2d) = 0$, therefore

$$(1-(1-T_{pi}P)e^{-j2\pi k})e(t) = 0. \tag{2.15}$$

e is expected to be zero, which would be realized if

$$1-(1-T_{pi}P) \neq 0, \quad \text{then} \;\; 1-T_{pi}P \neq 1.$$

This condition will be satisfied if

$$|1-T_{pi}(j\omega_k)P(j\omega_k)| < 1, \quad \forall \omega_k = k\omega_1 = k2\pi/T, \tag{2.16}$$

where k is positive integer. The above analysis shows that if the condition presented in Eq. 2.16 is fulfilled, the error caused by the disturbance in this control system can be eventually reduced to zero, therefore, it gives a condition when $T_u = 1$ to judge the stability of the basic RC system. In fact, Eq. 2.16 has been considered as the stability condition of the basic RC system in several publications [107, 110, 112]. Note that the deduction of this condition indicates that it is only a sufficient stability condition. Furthermore, this conclusion is obtained with an assumption that $T_u = 1$, which, in fact, is very limited. As a result, it is really necessary to know the stability condition of the basic RC system when $T_u \neq 1$.

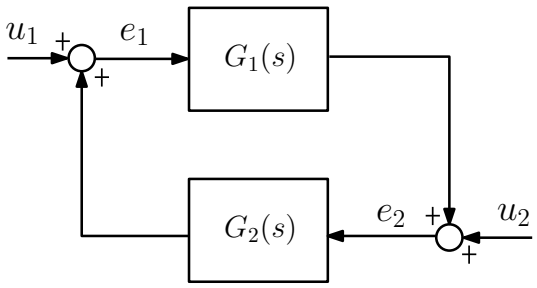

Figure 2.4: A simple feedback system.

2.2.2 The small gain theorem

In order to use the small gain theorem, the basis of this theorem is reviewed in this subsection. The small gain theorem, which gives a sufficient stability condition for the feedback connection, is a useful result for the system stability robustness analysis [113]. This theorem states that if a feedback loop consists of stable systems and the loop-gain product is less than unity, then the feedback loop is internally stable [24, 114]. To understand the small gain theorem, a LTI feedback system shown in Fig. 2.4 [24] is used here as an example to illustrate this theorem. Provided that $G_1(s)$ and $G_2(s)$ are stable transfer functions, in Fig. 2.4, the small gain condition considered for this SISO case can be written as [24]

$$| G_1(j\omega)G_2(j\omega) | < 1, \quad \forall\omega \in [0, +\infty[\tag{2.17}$$

Proof: First of all, the system shown in Fig. 2.4 can be written as

$$\begin{cases} E_1 = U_1 + G_2E_2 \\ E_2 = U_2 + G_1E_1 \end{cases} \Longrightarrow \begin{bmatrix} E_1 \\ E_2 \end{bmatrix} = \frac{1}{1 - G_1(s)G_2(s)} \begin{bmatrix} I & G_2(s) \\ G_1(s) & I \end{bmatrix} \begin{bmatrix} U_1 \\ U_2 \end{bmatrix}.$$

It is clear that only when $1-G_1(s)G_2(s)$ has no zero in the whole closed right-half s-plane, this system can be stable. Therefore, to get a stable system, $|1–G_1(s)G_2(s)|$ should be always larger than zero in the closed right-half s-plane.

According to the triangular inequality, we derive that

$$|1-G_1(s)G_2(s)| \geq 1-|G_1(s)G_2(s)|\,. \tag{2.18}$$

Since $G_1(s)$ and $G_2(s)$ are stable, they are analytic in the closed right-half s-plane. According to the maximum modulus theorem [115], the maximum of $|G_1(s)G_2(s)|$ should appear at the boundary of the closed right-half s-plane, which is the imaginary axis, so

$$|G_1(s)G_2(s)| < \mathrm{Max}|G_1(j\omega)G_2(j\omega)|. \tag{2.19}$$

Considering Eq. 2.18 and Eq. 2.19 together, we can get

$$|1-G_1(s)G_2(s)| \geq 1-|G_1(s)G_2(s)| > 1-\mathrm{Max}|G_1(j\omega)G_2(j\omega)|. \tag{2.20}$$

Then if

$$|\,G_1(j\omega)G_2(j\omega)\,| < 1, \quad \forall\omega \in [0,+\infty[$$

is satisfied, we can get $\mathrm{Max}|G_1(j\omega)G_2(j\omega)| < 1$. Therefore, $|1-G_1(s)G_2(s)| > 0$ can be fulfilled for all s in the closed right-half s-plane, so this system is stable.

Therefore, the small gain theorem is a condition that can guarantee the stability of this system. However, it is only a sufficient stability condition, because even when $\mathrm{Max}|\,G_1(j\omega)G_2(j\omega)\,| > 1$, it is still possible to get $|1-G_1(s)G_2(s)| > 0$ for all s in the closed right-half s-plane.

In fact, the small gain theorem is only a derivation of the Nyquist stability criterion [24], where the stability of a closed-loop system can be determined by drawing the Nyquist plot of its open-loop transfer function. To explain the relation between the small gain theorem and the Nyquist stability criterion, the closed-loop system shown in Fig. 2.4 is used again as an example. This figure shows that the open-loop transfer function of this system is $G_1(j\omega)G_2(j\omega)$. According to the Nyquist stability criterion [24], in a positive feedback system, if and only if the net number of positive clockwise encirclements (or negative counterclockwise encirclements) of the point $-1+j0$ in the s-plane by the Nyquist plot of $-G_1(j\omega)G_2(j\omega)$ plus the number of unstable poles (the poles located in right side of s-plane) of $-G_1(j\omega)G_2(j\omega)$ is zero, the system is stable. As it has been assumed that G_1 and G_2 are two stable transfer functions, which means that $-G_1(j\omega)G_2(j\omega)$ is stable hence has no unstable pole. Considering the Nyquist stability criterion, in order to guarantee the system stability, the Nyquist plot of $-G_1(j\omega)G_2(j\omega)$ cannot encircle the point $-1+j0$, which can be assured only when its Nyquist plot lies strictly inside the unit circle for any frequency, expressed as

$$|\,G_1(j\omega)G_2(j\omega)\,| < 1, \quad \forall\omega \in [0,+\infty[$$

which is the same as Eq. 2.17. This equation shows the connection between the small gain theorem and the Nyquist stability criterion, and implies that Eq. 2.17 derived from the small gain theorem is only a sufficient stability condition.

2.2.3 Stability condition of the basic RC system

After presenting the basic RC system and introducing the small gain theorem, a sufficient stability condition of a general basic RC system is derived with the help

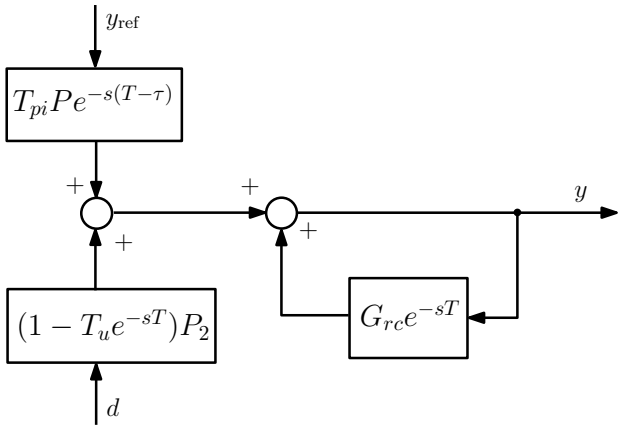

Figure 2.5: Alternative block diagram of the basic RC system.

of the small gain theorem.

Comparing the basic RC system shown in Fig. 2.3 to the system shown in Fig. 2.4, one cannot directly use the small gain theorem for this system. The basic RC system presented in Eq. 2.8 can be rewritten as

$$\begin{aligned}\left(1-G_{rc}e^{-sT}\right)Y &= T_{pi}Pe^{-s(T-\tau)}Y_{\text{ref}} + (1-T_ue^{-sT})P_2D \\ Y &= G_{rc}e^{-sT}Y + T_{pi}Pe^{-s(T-\tau)}Y_{\text{ref}} + (1-T_ue^{-sT})P_2D,\end{aligned} \tag{2.21}$$

Based on this equation, an equivalent representation of the basic RC system is shown in Fig. 2.5 [116], which shows that a basic RC system consists of three parts: $T_{pi}Pe^{-s(T-\tau)}$, $(1-T_ue^{-sT})P_2$ and a closed-loop containing a time-delay component $G_{rc}e^{-sT}$. It is easy to find that the third part is a particular case of the structure shown in Fig. 2.4, thus its stability can possibly be studied through the small gain theorem.

Since the stability of this system is a combined result of these three parts, before seeking the stability condition of the third part, we should first check the stability of the other two parts. Because the time-delay cannot change the stability, the stability of $T_{pi}Pe^{-s(T-\tau)}$ is determined by $T_{pi}P$ only, and the stability of $(1-T_ue^{-sT})P_2$, since

$$(1-T_ue^{-sT})P_2 = (1-e^{-sT})P_2 + (1-T_u)P_2e^{-sT} \tag{2.22}$$

relies on $(1-e^{-sT})P_2$ and $(1-T_u)P_2$. If considering the P_2 presented in Eq. 1.45, P_2 is not stable, however, if using Eq. 2.6, this term is stable. Therefore, the stability of $(1-T_ue^{-sT})P_2$ is only associated with the stability of $(1-T_u)P_2$. Meanwhile, before using the small gain theorem, one also need to check the stability of G_{rc}. Provided G_{rc} is stable, then according to the small gain theorem, a sufficient stability

condition of this closed-loop can be deduced as

$$\left|G_{rc}(j\omega)e^{-j\omega T}\right| = \left|(T_u(j\omega) - T_{pi}(j\omega)P(j\omega)e^{j\omega\tau})e^{-j\omega T}\right| < 1, \ \forall\omega \in [0, +\infty[$$

since $|e^{-j\omega T}| = 1$, this equation can be simplified as

$$|G_{rc}(j\omega)| = \left|T_u(j\omega) - T_{pi}(j\omega)P(j\omega)e^{j\omega\tau}\right| < 1, \ \ \forall\omega \in [0, +\infty[\tag{2.23}$$

Provided that $(1-e^{-sT})P_2$, $(1-T_u)P_2$, $T_{pi}P$ and G_{rc} do not have any pole in the right-side of the s-plane, then the inequality shown in Eq. 2.23 is considered as a sufficient stability condition that can guarantee the stability of the basic RC system. Although only sufficient, this condition advantageously provides a stability condition that only involves G_{rc}, called the regeneration spectrum in [117], regardless of the disturbance period T.

2.3 System performances

After obtaining the sufficient stability condition, we turn our attention to the performance of the basic RC system. The performance study consists of the reference tracking and the disturbance rejection. The step and the ramp signal tracking behaviors are used to evaluate its tracking capability. On the other hand, not only how much but also how fast the achieved disturbance reduction is reached are used for the evaluation of the disturbance rejection capability. To facilitate the discussion, hereafter, the first performance is referred to as the rejection ratio and the second one is referred to as the convergence speed.

2.3.1 Reference tracking

In order to know the reference tracking ability of a general RC system, we should investigate its tracking error when $t \to \infty$. Then, to calculate the steady-state reference tracking error, we use the final value theorem [118], which states that if $f(t)$ is a function of time, and if $\lim_{t\to\infty} f(t)$ exists, then

$$\lim_{t\to\infty} f(t) = \lim_{s\to 0} sF(s) \tag{2.24}$$

where $F(s)$ is the Laplace transform of $f(t)$.

From Eq. 2.9, the error caused by the reference tracking, E_r, can be calculated by

$$E_r(s) = H_{\text{rcd}}(s)\, Y_{\text{ref}}(s) = \frac{1 - T_u(s)e^{-sT}}{1 - G_{rc}(s)e^{-sT}} Y_{\text{ref}}(s) \tag{2.25}$$

The first test input signal is a step signal $A \cdot \Gamma(t)$, whose Laplace transform is A/s.

Provided that the stability of RC system is guaranteed, so $G_{rc}(0)$ and $T_u(0)$ exist. Then from Eq. 2.24 and Eq. 2.25, as well as considering $\lim_{s\to 0} e^{sT} = 1$, we can derive

$$e_{\text{step}}(\infty) = \lim_{t\to+\infty} e_{\text{step}}(t) = \lim_{s\to 0} sH_{\text{rcd}}(s)\frac{A}{s} = H_{\text{rcd}}(0)A = \frac{1-T_u(0)}{1-G_{rc}(0)}A. \quad (2.26)$$

Hence when $T_u(0) = 1$, the system could have no steady-state tracking error for the step signal.

The second test input signal is a ramp signal $B\cdot t\cdot\Gamma(t)$ whose Laplace transform is B/s^2. For a stable system, according to Eq. 2.24, we can deduce

$$e_{\text{ramp}}(\infty) = \lim_{t\to+\infty} e_{\text{ramp}}(t) = \lim_{s\to 0} sH_{\text{rcd}}(s)\frac{B}{s^2} = \lim_{s\to 0}\frac{1-T_u(s)e^{-sT}}{s\left(1-G_{rc}(s)e^{-sT}\right)}B, \quad (2.27)$$

which shows that for a basic RC system, tracking a ramp signal will lead to a steady-state error. This error, when $\lim_{s\to 0} T_u(s) = 1$, will be equal to $T/(1-G_{rc}(0))$, and in other situations, will continuously increase with the time.

2.3.2 Rejection ratio

From Eq. 2.9, the error caused by the periodic disturbance is

$$E_d(s) = -H_{\text{rcd}}(s)\,P_2(s)D(s) = -\frac{1-T_u e^{-sT}}{1-G_{rc}e^{-sT}}P_2(s)D(s). \quad (2.28)$$

At a frequency $\omega_k = k\omega_1 = 2\pi k/T$, the amplitude of E_d can be calculated as

$$|E_d(j\omega_k)| = \left|\frac{1-T_u(j\omega_k)}{1-G_{rc}(j\omega_k)}\right| |P_2(j\omega_k)D(j\omega_k)| = |H_{\text{rcd}}(j\omega_k)P_2(j\omega_k)D(j\omega_k)|, \quad (2.29)$$

in which k is a positive integer. Eq. 2.29 shows that the amplitude of the error resulting from the periodic disturbance is $|H_{\text{rcd}}(j\omega_k)P_2(j\omega_k)D(j\omega_k)|$, and only when $|H_{\text{rcd}}(j\omega_k)| < 1$, this system is able to reduce these periodic disturbances. Eq. 2.29 also shows that the goal of eliminating this disturbance can be achieved only when $|H_{\text{rcd}}(j\omega_k)| = 0$, which can be achieved by $T_u = 1$ with $G_{rc}(j\omega_k) \neq 1$.

2.3.3 Constant load torque rejection

The load torque, as a kind of constant disturbance, also needs to be considered to evaluate the system disturbance rejection capability. Suppose that the magnitude of the load torque is B_d and the system is stable. According to Eq. 2.24, the steady-

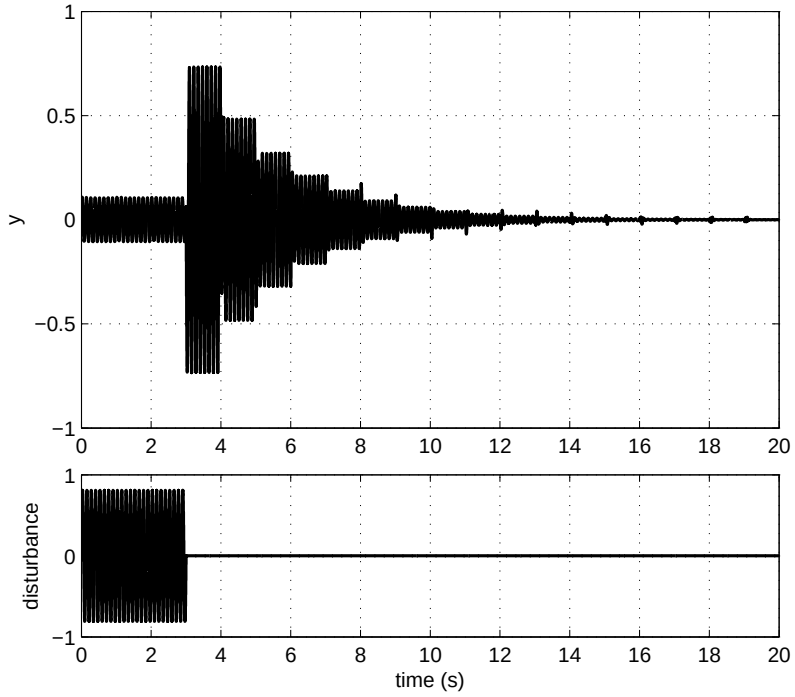

Figure 2.6: The convergence speed of the 8 Hz harmonic in the designed basic RC system.

state error resulting from this load torque can be computed as

$$e_{\text{load}}(\infty) = \lim_{t\to+\infty} e_{\text{load}}(t) = \lim_{s\to 0} sH_{\text{rcd}}(s)P_2(s)\frac{B_d}{s} = \lim_{s\to 0}\frac{1-T_u(s)e^{-sT}}{1-G_{rc}(s)e^{-sT}}P_2(s)B_d.$$

where using the model presented in Eq. 2.6, leads to

$$e_{\text{load}}(\infty) = \frac{1-T_u(0)}{1-G_{rc}(0)}P_2(0)B_d \tag{2.30}$$

This shows that, only when $T_u(0) = 1$, $e_{\text{load}}(\infty)$ will be removed completely, and when $T_u(0) \neq 1$, $e_{\text{load}}(\infty)$ will be finite but unbounded.

2.3.4 Convergence speed

In RC systems, as shown in [7, 11, 119], the disturbance rejection cannot be accomplished instantly but needs a convergence period. Hence, the convergence speed of the disturbance reduction is also an important performance. To investigate this convergence speed, we need to suppose a particular situation: $Y_{\text{ref}} = 0$ and a sinusoidal disturbance affects the system. At a given moment, the disturbance

abruptly vanishes, then from this moment, Eq. 2.8 leads in steady-state to

$$y(t) = |G_{rc}(j\omega)|\, y\left(t - T + \frac{\Phi}{\omega}\right), \text{ with } \Phi = \mathrm{Arg}(G_{rc}(j\omega)). \tag{2.31}$$

This shows that $|G_{cf}(j\omega)|$ is the convergence speed at which a sinusoidal disturbance of angular frequency ω that suddenly appears at a given time will go to zero.

A simple simulation, which visualizes the convergence behavior of a periodic disturbance, is used to confirm the analysis above. The basic RC system considered in this simulation will be presented in section 2.4. The result is shown in Fig. 2.6, where the input reference is zero ($y_{\text{ref}} = 0$). Before 3 s, the system was in a steady-state, where a 8 Hz disturbance was affecting the system and the basic repetitive controller was providing a 8 Hz compensation signal to neutralize part of this disturbance, hence the amplitude of the the process output (y) was relatively small. Then, the disturbance suddenly stops at 3 s, so at this moment, the process output, in fact, is only due to the compensation signal. Owing to the delay, the convergence of process output starts from 4 s. As shown in this figure, the convergence is accomplished in a step-by-step geometric progression, and the duration of each step is equal to the delay (in section 2.4, $T = 1$ s). This convergence behavior coincides with Eq. 2.31. On the other hand, between two neighbouring steps, the convergence (reduction) rate is 0.660 (ex: at the step starting from 4 s, the peak-to-peak amplitude of y is 1.446, and from 5 s, this value is 0.967, and from 6 s, it is 0.638), which corresponds to $|G_{rc}(j16\pi)| = 0.660$ (as will be confirmed in Fig. 2.9). Therefore, $|G_{rc}|$ indeed can determine the convergence speed of the periodic disturbance.

2.4 Controller design methodology

In this section, a basic repetitive controller that can guarantee the system stability and the required periodic disturbance performance for our PMSM drive is designed. Then from the analysis of this basic RC system, we will confirm that, as mentioned in section 2.2.3, section 2.3.3 and section 2.3, the basic repetitive controller is not suitable for the torque ripple reduction in PMSM drives. Despite this repetitive controller will not be applied to a real system, the results and the analysis shown here are able to deepen our understanding of the RC technique, and the approach chosen here will also be used to study other repetitive controllers.

The design methodology presented in this section is based on the machine model presented in Eq. 1.45. The parameters of the PMSM come from section 1.8 and three disturbance harmonic components namely the 8 th, 16 th and 24 th are considered in this design. Among these components, the 24 th is the most important one. In addition, this design is based on a nominal speed of 60 rpm, leading to $T = 1$ s.

The parameters of PMSM, the disturbance harmonics as well as the nominal speed used for the basic repetitive controller design will be also used for all the following repetitive controllers.

In this case, we do not use a leading component (τ), so it is set to zero. Then we need to tune T_u and T_{pi} to obtain a stable basic RC system with a desired performance. First of all, we discuss how to choose T_u. According to Eq. 2.9 and the analysis presented in section 2.2.1, the periodic disturbance rejection of this basic repetitive controller is due to the term $1-T_u e^{-sT}$. If T_u is a constant approaching to one, then $e^{-sT}=1$ when $\omega=2k\pi/T$, and this term will be close to zero. Consequently, the periodic disturbances with frequencies $\omega=2k\pi/T$ can be largely reduced. In the opposite, if T_u is a transfer function, the term $1-T_u(s)e^{-sT}$ can be written as $1-|T_u(j\omega)|e^{j\phi(\omega)-\omega T}$, in which $\phi(\omega)$ is the phase brought from $T_u(s)$. Only when

$$\omega-\frac{\phi(\omega)}{T}=\frac{2\pi k}{T},$$

the controller can provide a good rejection capability. However, these frequencies are no longer integer multiple of the fundamental frequency of the disturbance ($2\pi/T$). Therefore, T_u should be chosen as a constant close to one. In the following part of this report, T_u will be always used as a constant.

Since T_u is a constant and $T_{pi2}=T_{pi}/T_u$, then, considering the model presented in Eq. 1.45, T_{pi2} can be designed as a kind of second order high-pass filter

$$T_{pi2}(s)=\frac{K_{hp}}{T_d}\frac{s(1+sT_d)}{s^2+2z_n\omega_n s+\omega_n^2}, \tag{2.32}$$

to meet the design requirements. Eq. 2.32 shows that most of the numerator of T_{pi2} is intentionally chosen to be equal to the denominator of the process. In this manner, the chosen T_{pi2} in fact has only three free parameters, where ω_n is the natural frequency, z_n is the damping factor and K_{hp} is the high frequency gain of this filter. Then $T_{pi2}P$ can be written as

$$\begin{aligned} T_{pi2}(s)P(s)&=\frac{K_{hp}}{T_d}\frac{s(1+sT_d)}{s^2+2z_n\omega_n s+\omega_n^2}\frac{K}{sT_d(1+sT_d)}=\frac{K_{hp}K}{\omega_n^2T_d^2}\frac{\omega_n^2}{s^2+2z_n\omega_n s+\omega_n^2}\\ &=\frac{\alpha\omega_n^2}{s^2+2z_n\omega_n s+\omega_n^2},\quad \text{with}\quad \alpha=\frac{K_{hp}K}{\omega_n^2T_d^2}. \end{aligned} \tag{2.33}$$

where α is the static gain of $T_{pi2}P$. Eq. 2.33 shows that $T_{pi2}P$ is a second-order low-pass filter. Then according to Eq. 2.23 and Eq. 2.33, G_{rc} is

$$G_{rc}(s)=T_u\left(1-T_{pi2}(s)P(s)\right)=T_u\left(\frac{s^2+2z_n\omega_n s+(1-\alpha)\omega_n^2}{s^2+2z_n\omega_n s+\omega_n^2}\right), \tag{2.34}$$

which implies that

$$G_{rc}(0)=T_u\,(1-\alpha),\ \lim_{\omega\to+\infty} G_{rc}(j\omega)=T_u\ \text{ and }\ G_{rc}(j\omega_n)=T_u\left(1+j\frac{\alpha}{2z_n}\right). \tag{2.35}$$

To choose these parameters, first of all, we need to consider the system stability. From Eq. 2.35, we can easily get

$$|T_u|\ <\ 1\ \text{ and }\ |T_u\,(1-\alpha)|<1. \tag{2.36}$$

Since $|T_u|\ <\ 1$, according to Eq. 2.26 and Eq. 2.27, this RC system will track a step reference with an unavoidable steady-state error and track a ramp reference with a continuously increasing error. For the same reason, the load torque will bring the steady-state error to this system. To fulfill $|G_{rc}(\omega_n)|\ <\ 1$, we can deduce

$$z_n > \frac{\alpha\,T_u}{2\sqrt{1-T_u^2}}. \tag{2.37}$$

Therefore, to ensure the system stability, the conditions presented in Eq. 2.36 and Eq. 2.37 should be fulfilled simultaneously.

As analyzed in section 2.3.1, the tracking performance of the basic RC system is related to $H_{\mathrm{rcd}}(0)$. Undoubtedly, we need to consider $H_{\mathrm{rcd}}(0)$ so as to control the magnitude of the steady-state error to an acceptable level. The system tracking capability derived from Eq. 2.26 is written as

$$H_{\mathrm{rcd}}(0)=\frac{1-T_u}{1-G_{rc}(0)}=\frac{1-T_u}{1+(\alpha-1)T_u}. \tag{2.38}$$

Once T_u is settled for the robust stability, to get a desired $H_{\mathrm{rcd}}(0)$, according to Eq. 2.38, α can be calculated from

$$\alpha=\frac{(1-T_u)\,(1-H_{\mathrm{rcd}}(0))}{T_u\,H_{\mathrm{rcd}}(0)}. \tag{2.39}$$

Since $\alpha>0$ and $|T_u(1-\alpha)|<1$, from Eq. 2.38, we can deduce the chosen $|H_{\mathrm{rcd}}(0)|$ must satisfy

$$\frac{1-T_u}{2}<H_{\mathrm{rcd}}(0)<1. \tag{2.40}$$

This equation shows that the range of possible $H_{\mathrm{rcd}}(0)$ is related to the choice of T_u. To get a smaller steady-state error, T_u should be close to one.

In the report, the rejection ratio of the main harmonic component is used to indicate the system reduction capability. ω_n is chosen as

$$\omega_n=2\pi f_d,\ \text{ with }\ f_d=\frac{k_d}{T}=k_d\frac{V}{60}. \tag{2.41}$$

in which k_d is the order of the main harmonic component and V is the rotor speed (in rpm). The reduction ratio of the main harmonic component can be deduced from

$$H_{\mathrm{rcd}}(j\omega_n)=\frac{1-T_u}{1-T_u(1+j\frac{\alpha}{2z_n})}=\frac{1}{1-j\frac{\alpha T_u}{2z_n(1-T_u)}}. \tag{2.42}$$

This allows to derive z as

$$z=\frac{\alpha T_u|H_{\mathrm{rcd}}(j\omega_n)|}{2(1-T_u)\sqrt{1-|H_{\mathrm{rcd}}(j\omega_n)|^2}}=\frac{(1-H_{\mathrm{rcd}}(0))|H_{\mathrm{rcd}}(j\omega_n)|}{2H_{\mathrm{rcd}}(0)\sqrt{1-|H_{\mathrm{rcd}}(j\omega_n)|^2}}. \tag{2.43}$$

From Eq. 2.37 and Eq. 2.43, we can get the following inequality

$$z=\frac{\alpha T_u|H_{\mathrm{rcd}}(j\omega_n)|}{2(1-T_u)\sqrt{1-|H_{\mathrm{rcd}}(j\omega_n)|^2}}>\frac{\alpha T_u}{2\sqrt{1-T_u^2}} \tag{2.44}$$

which leads to

$$\frac{1-T_u}{2}<|H_{\mathrm{rcd}}(j\omega_n)|^2<1. \tag{2.45}$$

which shows that for a given T_u, the chosen rejection ratio has a lower limit.

Then according to the above analysis, we tune the controller parameters. First, according to Eq. 2.40, we choose $T_u=0.9$ as so to get a small $H_{\mathrm{rcd}}(0)$. Then we can choose $H_{\mathrm{rcd}}(0)=0.1$, and according to Eq. 2.39, $\alpha=1$. If $V=60$ rpm, $f_d=24$ Hz, and from Eq. 2.41, $\omega_n=150.8$ rad/s and $K_{hp}=0.0068$ A rad/s. $H_{\mathrm{rcd}}(j\omega_n)=0.3$ (-10.45 dB), and this reduction target is achievable since it satisfies Eq. 2.45. Then to meet the rejection requirement, we can get $z=1.415$ through Eq. 2.44, and this result obeys the condition presented in Eq. 2.37.

We need to make sure that the designed controller can lead to a stable system. According to the previous analysis, the stability of this system is determined by $(1-T_u)P_2$, $T_{pi}P$ and the closed-loop containing $G_{rc}e^{-sT}$ together. Since T_u is only a constant, then according to Eq. 2.6, the term $(1-T_u)P_2$ is stable. On the other hand, with the chosen T_{pi} has two roots: $-364.41+j0$ and $-62.40+j0$, hence the term $T_{pi}P$ is stable. The stability of the closed-loop is judged by the small gain theorem, but before doing it, we should first check the stability of G_{rc}. Thanks to the stable $T_{pi}P$ and a constant T_u, G_{rc} is also stable. Then a Nyquist plot of G_{rc} shown in Fig. 2.7 is used to indicate the stability of this closed-loop. The maximum value of $|G_{rc}|$ ($Max|G_{rc}|$), as shown in this figure, is 0.9775, hence this closed-loop is stable as well. Then the proposed basic repetitive controller can ensure the system stability. $Max|G_{rc}|$ is located at 38.54 Hz, and this location $f_{\max}$ can be calculated

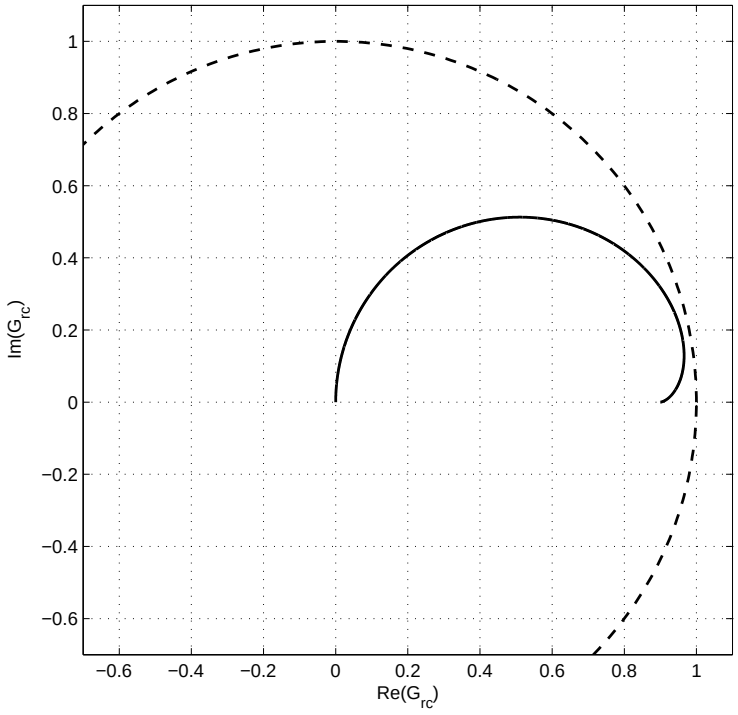

Figure 2.7: Nyquist plot of G_{rc} (solid line) compared to the unit circle (dotted line). The maximum value of $|G_{rc}|$ is 0.97 appearing at 38.45 Hz.

through

$$f_{\max} = \frac{\omega_n}{2\pi}\sqrt{\frac{2-\alpha-\sqrt{\alpha^2+16z^2}}{2}}. \tag{2.46}$$

The reference tracking and disturbance rejection behavior of the designed system are shown in Fig. 2.8. The first Bode plot derived from H_{rcr} shows, from 1 to 100 Hz, that $|H_{\text{rcr}}(j\omega)|$ has lots of resonances whose values are obviously higher than 0 dB, indicating that the tracking behavior of this system may be impaired by overshoots and oscillations. On the other side, the second Bode plot derived from H_{rcd} shows that $|H_{\text{rcd}}(j48\pi)|$ is almost -10.45 dB, so the desired rejection ratio is achieved. More importantly, this figure shows the rejection behavior of a basic RC system. This repetitive controller provides a good rejection only for the sinusoidal disturbance with frequency $f_k = \omega_k/(2\pi)$. For other frequencies, the controller cannot offer an effective rejection, on the contrary, it can lead to amplification of some harmonic components (especially between 10 and 100 Hz). This means that the use of the basic repetitive controller perhaps cause the amplification of the noise. Besides, as shown in this figure, for the low harmonic components (from 1 to 10 Hz), this system has a quite good rejection capability (ex: $H_{\text{rcd}}(j16\pi) = -18$ dB), and then the rejection capability attenuates with a rising frequency (ex: $H_{\text{rcd}}(j32\pi) = -16$ dB).

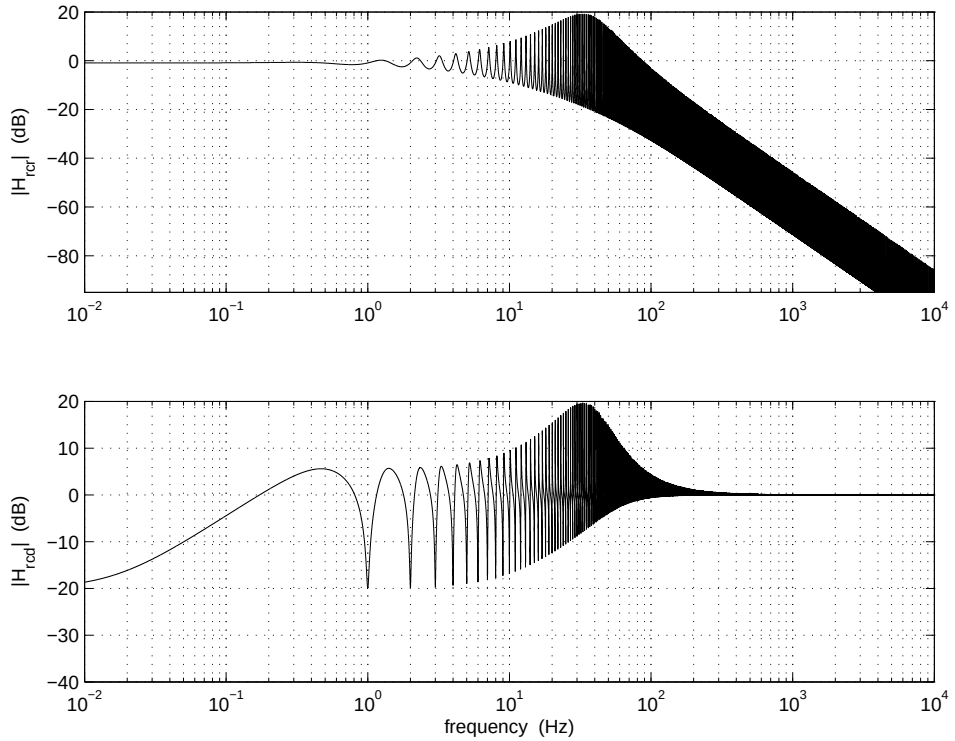

Figure 2.8: Bode magnitude plots of H_{rcr} (in figure above) and H_{rcd} (in figure below).

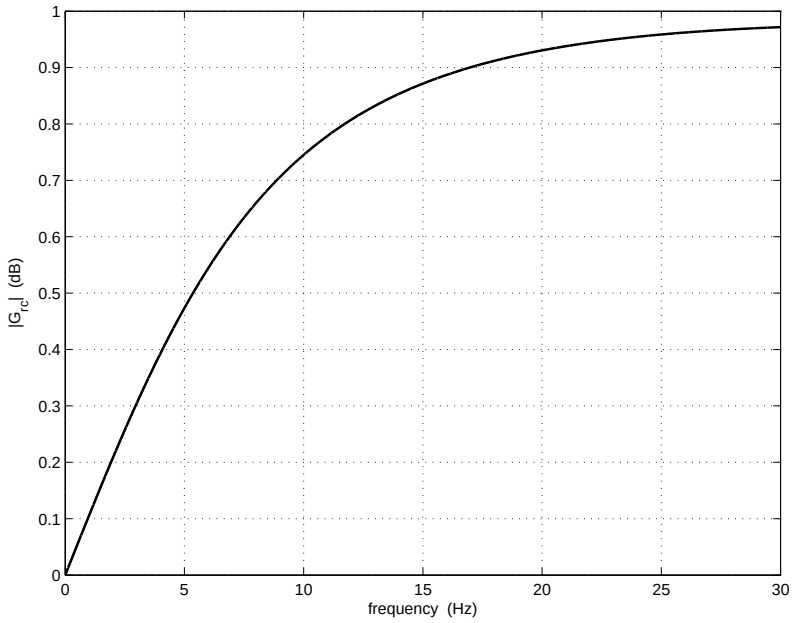

Figure 2.9: Plot of $|G_{rc}(j2\pi f)|$ indicating the convergence speed of sinusoidal disturbances with the designed basic repetitive controller.

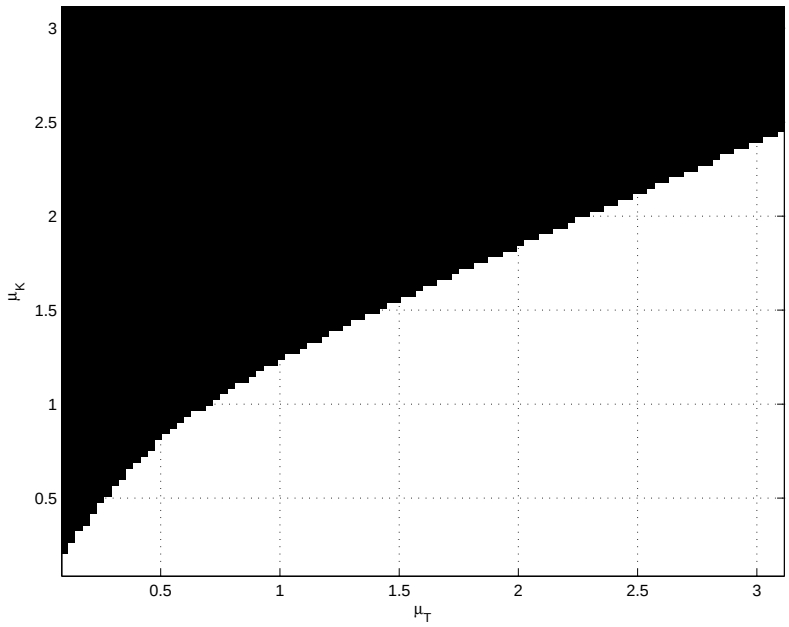

Figure 2.10: Stability robustness analysis of the designed basic RC system.

Though the convergence speed of the periodic disturbance has not been considered in this design, it is still necessary to check it. The analysis presented in section 2.3.4 has shown that $|G_{rc}(j\omega)|$ determines this convergence speed, hence a plot of $|G_{rc}(j\omega)|$ from 0 to 30 Hz is shown in Fig. 2.9 to indicate the convergence speed of the different disturbance components. As shown in this figure, $|G_{rc}(j16\pi)|$, $|G_{rc}(j32\pi)|$ and $|G_{rc}(j48\pi)|$ are around 0.660, 0.887 and 0.955 respectively, therefore the 8 th harmonic components will be reduced to its steady-state in several iterations (as already shown in Fig. 2.6), whereas, the 16 th and the 24 th components, obviously need much more time to complete their convergence.

The variation of the parameters will change the system stability. Hence, a stability robustness analysis of this system is done, and the corresponding result is shown in Fig. 2.10. For a controller whose parameters are derived from the supposed values of the process parameters, this figure shows whether the stability of the closed-loop system is guaranteed (white areas) or not (black areas) when the parameters diverges from their supposed values. To achieve this analysis, primarily, we define $K^{\text{real}} = \mu_K K$ and $T_d^{\text{real}} = \mu_T T_d$ (superscripts "real" indicates the real value of the parameters). K and T_d are the supposed values of the process parameters used to tune the PI speed controller and repetitive controller. With μ_k and μ_T, Eq. 2.34 can be changed as

$$G_{rc}^{\text{real}}(j\omega) = T_u \left(1 - T_{pi2}(j\omega) P^{\text{real}}(j\omega)\right), \tag{2.47}$$

$$\text{with} \quad P^{\text{real}}(j\omega) = \frac{\mu_K K}{j\omega\mu_T T_d(1 + j\omega\mu_T T_d)}, \tag{2.48}$$

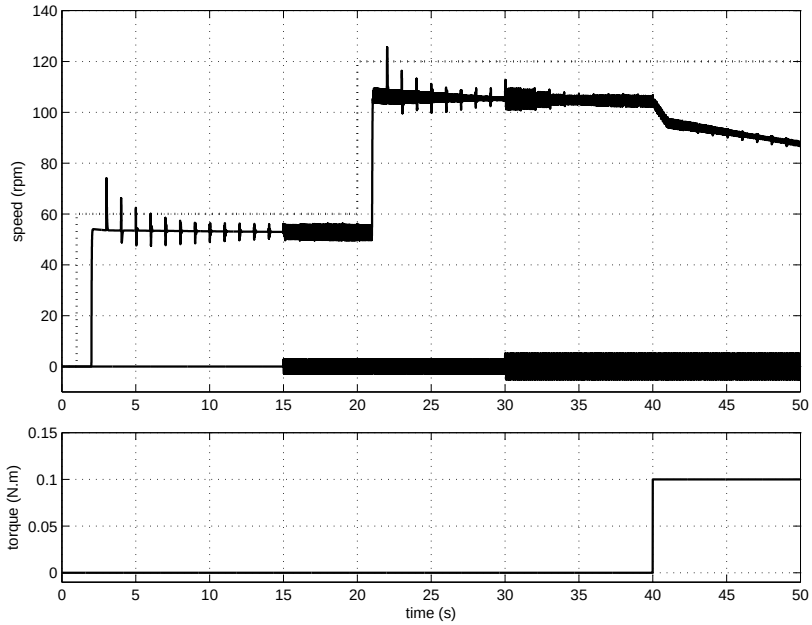

Figure 2.11: Simulation results showing how a closed-loop system using a basic repetitive controller behaves when the system contains periodical disturbances with variable speed reference (in figure above, dotted line) and variable load torque (in figure below). The magnitude of $|P_2 D|$ is also visualized (in figure above).

which reveals that

$$\lim_{\mu_k \to +0} G_{rc}^{\text{real}}(j\omega) = \lim_{\mu_T \to \infty} G_{rc}^{\text{real}}(j\omega) = T_u. \tag{2.49}$$

This equation shows that the choice of T_u directly influences the stability robustness of this system. The result presented in Fig. 2.10 illustrates that overestimating T_d and underestimating K simultaneously will quite easily break the system stability. On the opposite, the underestimation of T_d and overestimation of K will not be a problem for the system stability. In a word, this system remains stable with nearly a $\pm 20\%$ uncertainty on K and T_d. Therefore, to use this controller, one needs a rather good knowledge about the machine parameters.

The time response of this basic RC system is tested through a simulation. During a 50-second simulation, the input reference changes twice as step, respectively at 1 s from 0 to 60 rpm and at 12 s from 60 to 120 rpm. Besides, a 0.1 N.m load torque starts at 40 s and lasts until the end of this simulation. The periodic disturbance begins at 15 s, and before 30 s, it contains only a 5 N·m 24 th harmonic (as a 24 Hz sinusoidal signal), and afterward, a 2.5 N·m 8 th harmonic is also added (as a 8 Hz sinusoidal signal). In this case, it should be noted that despite the variation of the speed, the frequency of the disturbances remains unchanged.

The result obtained from this simulation is shown in Fig. 2.11, in which $|P_2D|$ and y_{ref} are also visualized so as to facilitate the analysis. From Fig. 2.11, first a $10\,\%$ steady-state error can be observed while the system is tracking a constant reference, which coincides with the theoretical analysis and meets the design requirement. Second, this system tracks the input signal with an inevitable delay whose value (1 s) is equal to the controller delay. Third, the step signal, owing to the chosen T_{pi2}, leads to an important overshoot whose value is $33\,\%$ of the step amplitude. Further, due to the delay and the closed-loop, additional damped oscillations inherited from the overshoot continuously influence the system until being overshadowed by the speed ripple. It is obvious that this overshoot and oscillations seriously degrades the system tracking behavior. In addition, the controller can efficiently reduce the 8 th or the 24 th harmonic components, but the convergence speed of the 24 th is much slower than the 8 th. Finally, the load torque, despite is a very small one, leads to a continuously increasing tracking error. This, in fact, is also due to $T_u \neq 1$. We can use Eq. 2.30 to calculate its steady-state value. To do it, first, with the P shown in Eq. 2.6, $T_{pi2}P$ can be written as

$$\begin{aligned} T_{pi2}(s)P(s) &= \frac{K_{hp}}{T_d}\frac{s(1+sT_d)}{s^2+2z_n\omega_n s+\omega_n^2}\frac{K}{T_d(s+k_f/J)(1+sT_d)} \\ &= \frac{K_{hp}K}{\omega_n^2 T_d^2}\frac{s}{s+k_f/J}\frac{\omega_n^2}{s^2+2z_n\omega_n s+\omega_n^2}, \end{aligned} \tag{2.50}$$

then, we can deduce that $T_{pi2}(0)P(0)=0$, and then $G_{\text{rc}}(0)=T_u$. Therefore, according to Eq. 2.30 and Eq. 2.6,

$$\lim_{t\to\infty} e_{\text{load}} = \frac{1-T_u}{1-G_{rc}(0)}P_2(0)B_d = \frac{B_d}{k_f}. \tag{2.51}$$

With $B_d = 0.1$N·m and $k_f = 1.2\times10^{-4}$ N·m·s/rad, the steady-state value of this error is 833 rpm, which, of course, is absolutely unacceptable. Therefore, the basic RC system, because of the inevitable time-delay and steady-state error, as well as the extreme weak constant disturbance rejection capability, is not fit for the PMSM torque ripple reduction.

2.5 Current feedback repetitive controller

The previous analysis shows that the use of the basic RC system will be seriously hindered by the bad tracking behaviors, such as the delay and the steady-state error, and also by the bad load-torque rejection capability. As explained in [110], the absence of the current information should be responsible for these problems. Consequently, the wish to improve the tracking performance lies in adding the current information into the repetitive controller. This can be realized by integrating a

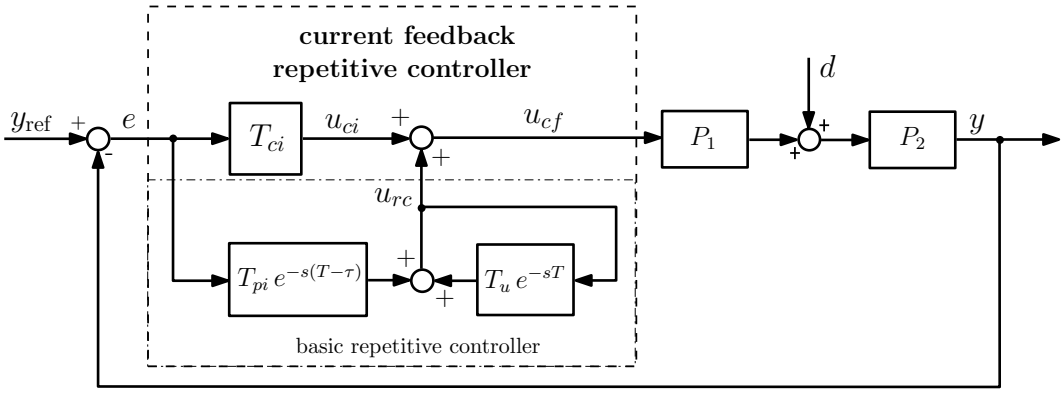

Figure 2.12: Block diagram of the plant controlled by a current feedback repetitive controller (in our case, $T_{ci} = K_{ps} + K_{is}/s$, $u_{cf} = i_{\text{qref}}$, $T = 2\pi/\omega_m$ and y_{ref}, y, d as well as P_1 and P_2 are defined in Eq. 1.45).

conventional controller into a RC controller. On the other hand, we generally hope that the use of the RC technique in control systems will not break their existing structure. This requires that the repetitive controller does not replace these existing controllers, but works together with them. As a result, a new kind of repetitive controller, which includes a basic repetitive controller and a conventional controller, is studied in this report. Owing to the integration of the conventional controller, the output of this new repetitive controller contains not only the past information, but also the current information, hence it is called current repetitive controller.

There are lots of possibilities to form a current repetitive controller [107]. However, considering the real need of this thesis, as well as importance and popularity of these current controllers, two current repetitive controllers, the current feedback repetitive controller and the current iteration repetitive controller are considered and studied. Their names, in fact, borrow from the ILC research [107].

First, we present the current feedback repetitive controller and its control system. This controller was first studied by C. Rech et al in [120], where a basic repetitive controller and a predictive PID controller work together to achieve the minimization of the periodic disturbance in a PWM inverter. In [7], P. Mattavelli et al applied this controller to a PMSM drive to attenuate its torque ripple problem. According to these publications, a basic structure of the current feedback RC system is shown in Fig. 2.12, in which a basic repetitive controller linked with a conventional controller (PI speed controller) with a parallel connection forms a current feedback repetitive controller. Then, the transfer function of the current feedback

repetitive controller is

$$
\begin{aligned}
U_{cf}(s) &= T_{ci}(s)E(s)+U_{rc}(s)=T_{ci}(s)E(s)+\frac{T_{pi}(s)e^{-s(T-\tau)}}{1-T_u e^{-sT}}E(s),\\
\text{then } C_{cf}(s) &= \frac{U_{cf}(s)}{E(s)}=\frac{T_{ci}(s)(1-T_u e^{-sT})+T_{pi}(s)e^{-s(T-\tau)}}{1-T_u e^{-sT}}.
\end{aligned}
\tag{2.52}
$$

where the subscript "cf" used here indicates the current feedback controller and "ci" stands for the conventional controller that can provide the current iteration information. From Eq. 2.52, the relationship between the system output y, the reference input y_{ref} and the disturbance d is

$$
\begin{aligned}
Y &= \frac{(T_{ci}P-(T_uT_{ci}-T_{pi}e^{s\tau})Pe^{-sT})Y_{\text{ref}}+(1-T_ue^{-sT})P_2D}{(1+T_{ci}P)-((1+T_{ci}P)T_u-T_{pi}Pe^{s\tau})e^{-sT}}\\
Y &= \frac{(T_{ci}-(T_uT_{ci}-T_{pi}e^{s\tau})e^{-sT})PY_{\text{ref}}+(1-T_ue^{-sT})P_2D}{(1+T_{ci}P)\left(1-(T_u-\frac{T_{pi}Pe^{s\tau}}{1+T_{ci}P})e^{-sT}\right)}\\
Y &= H_{\text{cfr}}Y_{\text{ref}}+H_{\text{cfd}}P_2D,\\
\text{with } H_{\text{cfr}} &= S_{ci}\frac{\left(T_{ci}-(T_uT_{ci}-T_{pi}e^{s\tau})e^{-sT}\right)P}{1-G_{cf}e^{-sT}},\quad H_{\text{cfd}}=S_{ci}\,H_{\text{cfd2}},\\
H_{\text{cfd2}} &= \frac{1-T_ue^{-sT}}{1-G_{cf}e^{-sT}},\quad G_{cf}=T_u(1-T_{pi2}S_{ci}Pe^{s\tau})\ \text{ and }\ S_{ci}=\frac{1}{1+T_{ci}P},
\end{aligned}
\tag{2.53}
$$

where $T_{pi2}=T_{pi}/T_u$ is defined as in Eq. 2.8 and S_{ci} is the sensitivity function of closed-loop system when using the conventional controller only ($H_{\text{cfd}}=S_{ci}$ when $T_u=T_{pi}=0$). From Eq. 2.53, the relationship between the error signal e, the reference input y_{ref} and the disturbance d is

$$
\begin{aligned}
E &= \frac{1-T_ue^{-sT}}{(1+T_{ci}P)-((1+T_{ci}P)T_u-T_{pi}Pe^{s\tau})e^{-sT}}(Y_{\text{ref}}-P_2D)\\
E &= \frac{1-T_ue^{-sT}}{(1+T_{ci}P)(1-G_{cf}e^{-sT})}(Y_{\text{ref}}-P_2D)\\
E &= H_{\text{cfd}}(Y_{\text{ref}}-P_2D).
\end{aligned}
\tag{2.54}
$$

Eq. 2.53 and Eq. 2.54 are the basis of the further study of the current feedback repetitive controller and its control system.

2.5.1 Stability

As the basic RC system, to simplify the analysis and to facilitate the use of the small gain theorem, Eq. 2.53 is first changed as

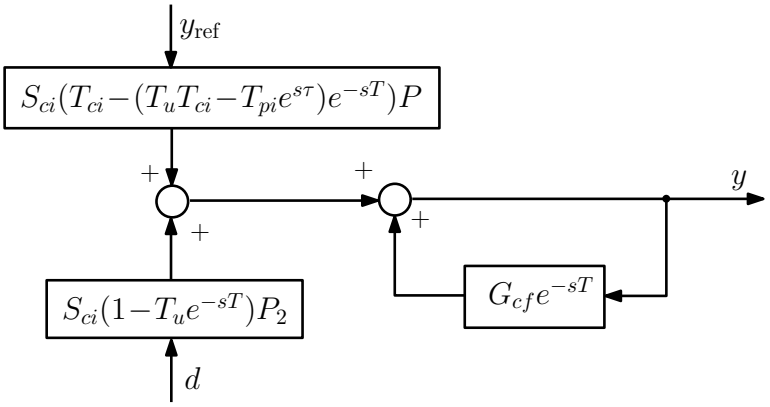

Figure 2.13: Alternative diagram of the current feedback RC system.

$$\left(1-G_{cf}e^{-sT}\right)Y=S_{ci}(T_{ci}-(T_uT_{ci}-T_{pi}e^{s\tau})e^{-sT})PY_{\text{ref}}+S_{ci}(1-T_ue^{-sT})P_2D$$
$$Y=G_{cf}e^{-sT}Y+S_{ci}(T_{ci}-(T_uT_{ci}-T_{pi}e^{s\tau})e^{-sT})PY_{\text{ref}}+S_{ci}(1-T_ue^{-sT})P_2D. \quad (2.55)$$

From this equation, an equivalent representation of the current feedback RC system can be pictured as Fig. 2.13, which shows that this current RC system, as its basic counterpart, is also made of three parts: $(1-T_ue^{-sT})S_{ci}P_2$, $(T_{ci}-(T_uT_{ci}-T_{pi}e^{s\tau})e^{-sT})S_{ci}P$, and one closed-loop containing $G_{cf}e^{-sT}$. Only when all these parts are stable, the current feedback RC system can be stable. Since T_u is a constant and T_{ci} is a PI controller, then

$$S_{ci}(s)=\frac{s^2T_d(1+sT_d)}{T_d^2s^3+T_ds^2+KK_{ps}s+KK_{is}}, \quad (2.56)$$

and the stability of $(1-T_ue^{-sT})S_{ci}P_2$ results from the cancellation of the zero pole of P_2 by one zero root of S_{ci}. On the other hand,

$$S_{ci}(T_{ci}-(T_uT_{ci}-T_{pi}e^{s\tau})e^{-sT})P=$$
$$(1-e^{-sT})T_{ci}PS_{ci}+(1-T_u)T_{ci}PS_{ci}e^{-sT}+T_{pi}PS_{ci}e^{-s(T-\tau)},$$

hence the stability of $S_{ci}(T_{ci}-(T_uT_{ci}-T_{pi}e^{s\tau})e^{-sT})P$ is a result of $(1-e^{-sT})T_{ci}PS_{ci}$, $(1-T_u)T_{ci}PS_{ci}$ and $T_{pi}PS_{ci}$ together. From Eq. 1.45 and Eq. 2.56, we can deduce that the stability of both $(1-e^{-sT})T_{ci}PS_{ci}$ and $(1-T_u)T_{ci}PS_{ci}$ can be guaranteed by a stable S_{ci}. Hence, once both S_{ci} and $T_{pi}PS_{ci}$ are stable, $S_{ci}(T_{ci}-(T_uT_{ci}-T_{pi}e^{s\tau})e^{-sT})P$ will be stable. Meanwhile, in order to be able to use the small gain theorem for this closed-loop, we should assure the stability of G_{cf}, which, according to Eq. 2.53, is also related to $T_{pi}PS_{ci}$. The stability of S_{ci} and $T_{pi}PS_{ci}$ can be known by checking whether they have unstable poles or not. Then provided G_{cf} is stable,

a sufficient stability condition of this closed-loop can be written as

$$|G_{cf}(j\omega)| = \left| T_u - \frac{T_{pi}(j\omega)P(j\omega)e^{j\omega\tau}}{1+T_{ci}(j\omega)P(j\omega)} \right| = \left| T_u - S_{ci}(j\omega)T_{pi}(j\omega)P(j\omega)e^{j\omega\tau} \right| < 1, \quad \forall\omega \in [0, +\infty[\tag{2.57}$$

Therefore, if S_{ci} and $T_{pi}PS_{ci}$ are stable, Eq. 2.57 becomes a sufficient stability condition of the stability of the current feedback RC system.

2.5.2 Performance

As the basic RC system, the reference tracking and the disturbance rejection are two important factors to judge the performance of a current feedback RC system.

Reference tracking

As the basic RC system, the reference tracking capability of the step signal and the ramp signal of the current feedback RC system are studied here. According to the analysis in section 2.3.1 and Eq. 2.54, and provided that the system is stable ($|G_{cf}(s)| < 1$ and $G_{cf}(0)$ exists), then when the system is tracking a step signal with amplitude A, the subsequent steady-state error is

$$e_{\text{step}}(\infty) \;=\; S_{ci}(0)\frac{1-T_u}{1-G_{cf}(0)}A, \tag{2.58}$$

which shows that $S_{ci}(0) = 0$ or $T_u = 1$ can enable this RC system to track a step signal without any state-state error. The steady-state error resulting from a ramp signal $B \cdot t \cdot \Gamma(t)$ is deduced as

$$e_{\text{ramp}}(\infty) = \lim_{s\to 0} \frac{S_{ci}(s)}{s} \frac{1-T_u e^{-sT}}{1-G_{cf}(s)e^{-sT}} B \tag{2.59}$$

which shows two possibilities to get the no steady-state tracking error. The first one is $\lim_{s\to 0} S_{ci}(s)/s = 0$. The other one is $T_u = 1$ that can also lead to no steady-state tracking error.

Disturbance rejection

According to section 2.3.2 and Eq. 2.54, we can get the following equation

$$|E_d(j\omega_k)| = |S_{ci}(j\omega_k)H_{\text{cfd2}}(j\omega_k)|\,|P_2(j\omega_k)D(j\omega_k)|, \tag{2.60}$$

in which ω_k is defined in Eq. 2.29. Therefore, $|S_{ci}(j\omega_k)H_{\text{cfd2}}(j\omega_k)|$ is the periodic disturbance rejection ratio of the current feedback RC system. At the same time,

$|S_{ci}(j\omega_k)|$ is the sensitivity function of the system with the T_{ci} controller only, so $|H_{\text{cfd2}}(j\omega_k)|$ reflects the rejection capability difference between the current feedback RC system and its conventional counterpart. Only when $|H_{\text{cfd2}}(j\omega_k)|<1$, the repetitive controller can provide a better periodic disturbance rejection capability than its conventional counterpart. Meanwhile, according to the analysis presented in section 2.3.4, the convergence speed of the disturbance is determined by $|G_{cf}(j\omega)|$.

On the other hand, we should also consider the rejection of the load torque. Assume that the magnitude of the load torque is B_d and this system is stable, from Eq. 2.54, we can deduce that

$$\begin{aligned} e_{\text{load}}(\infty) = \lim_{t\to+\infty} e_{\text{load}}(t) &= \lim_{s\to 0} sS_{ci}(s)\frac{1-T_u e^{-sT}}{1-G_{cf}(s)e^{-sT}}P_2(s)\frac{B_d}{s}. \\ &= \left(\lim_{s\to 0} S_{ci}(s)P_2(s)\right)\frac{1-T_u}{1-G_{cf}(0)}B_d. \end{aligned} \tag{2.61}$$

This equation shows that when $\lim_{s\to 0} S_{ci}(s)P_2(s)=0$ or $T_u=1$, a load-torque will not lead to steady-state error in this RC system.

2.5.3 Design methodology 1

In this subsection, we present a design methodology for the current feedback repetitive controller so as to provide a trade-off among the stability robustness, the disturbance rejection and the convergence speed in our PMSM drive. The parameters of the PI controller (T_{ci}), as shown in section 1.8, are $K_{ps}=26.90$ A·s/rad and $K_{is}=2.24\times 10^3$ A.

We start our discussion from the stability condition. The comparison between Eq. 2.57 and Eq. 2.34 shows the similarities and differences between both stability conditions. In the basic RC system, to ensure the stability and the performance, the choice of T_{pi2} is based on P, whereas in the current feedback RC system, $S_{ci}P$ instead of P should be considered for the choice of T_{pi2}. As a result, to find out a suitable T_{pi2}, primarily, we need to know the features of $S_{ci}P$ from its transfer function

$$S_{ci}(s)P(s)=\frac{P(s)}{1+T_{ci}(s)P(s)}=\frac{sK}{s^3T_d^2+s^2T_d+sKK_{ps}+KK_{is}} \tag{2.62}$$

which shows that $S_{ci}P$ is a band-pass filter. On the other hand, Eq. 2.62 can be represented as

$$\begin{aligned} S_{ci}(s)P(s) &= \frac{sK}{T_d^2}\frac{1}{(r_1+s)(s^2+2z_s\omega_s s+\omega_s^2)} \\ &= \frac{K}{\omega_s^2T_d^2}\frac{s}{r_1+s}\frac{\omega_s^2}{s^2+2z_s\omega_s s+\omega_s^2}, \end{aligned} \tag{2.63}$$

where r_1 is the real root of the denominator of $S_{ci}P$, and $s^2+2z_s\omega_s s+\omega_s^2$ has two complex conjugated roots. $S_{ci}P$ is made of three parts: a gain, a high-pass filter and a low-pass filter. T_{pi2} is chosen as

$$T_{pi2}(s)=K_{pi}\frac{s^2+2z_0\omega_0 s+\omega_0^2}{s^2+2z_n\omega_n s+\omega_n^2}, \tag{2.64}$$

where K_{pi} is the high frequency gain. It seems that T_{pi2} has five parameters, however, with $z_0=z_s$ and $\omega_0=\omega_s$, its numerator is used to cancel the low-pass filter in $S_{ci}P$, therefore, only three parameters, in fact, need to be tuned. With this intentional cancellation, $T_{pi2}S_{ci}P$ can be changed as

$$\begin{aligned} T_{pi2}(s)S_{ci}(s)P(s) &= \frac{KK_{pi}}{w_s^2T_d^2}\frac{w_s^2 s}{(r_1+s)(s^2+2z_n\omega_n s+\omega_n^2)} \\ &= \alpha\frac{s}{r_1+s}\frac{w_s^2}{s^2+2z_n\omega_n s+\omega_n^2}, \quad \text{with } \alpha=\frac{KK_{pi}}{w_s^2T_d^2}. \end{aligned} \tag{2.65}$$

From this equation, we can deduct that

$$\begin{aligned} &\lim_{s\to 0}T_{pi2}(s)S_{ci}(s)P(s)=0 \ \text{ and } \ \lim_{s\to+\infty}T_{pi2}(s)S_{ci}(s)P(s)=0, \\ &\text{then } \ G_{cf}(0)=T_u \ \text{ and } \ \lim_{s\to+\infty}G_{cf}(s)=T_u, \end{aligned} \tag{2.66}$$

which shows that T_u has a strong influence on the system stability. Eq. 2.65 also shows that this tuning problem can now be considered as taking a user defined low-pass filter $w_n^2/(s^2+2z_n\omega_n s+\omega_n^2)$ to adapt the characteristics of an unchangeable high-pass filter $s/(r_1+s)$ so as to get a stable system with desired performances. Note that for this changeable low-pass filter, its cut-off frequency ω_c, according to Eq. 2.65, can be computed as

$$\omega_n = \omega_c\sqrt{2z_n^2-1+\sqrt{(2z_n^2-1)^2+1}}. \tag{2.67}$$

The main harmonic component considered in this case is the 24 th, and its frequency at a speed of 60 rpm is 24 Hz. In the design, we wish to reduce this harmonic to a desired level within a short time. In order to get the possible fastest convergence, the minimum value of $|G_{cf}(j\omega)|$ should appear at 24 Hz, which can be achieved by tuning ω_n and z_n together. Note that when the value of z_n is chosen between 4 and 12, the system performance is not sensitive to this parameter, so $z_n=6$ is first settled here. Then with the help of Matlab, we can find that when $\omega_c=100$ rad/s, and the minimum value of $|G_{cf}(j\omega)|$ is located at 24 Hz. Hence, from Eq. 2.67, $\omega_n=1192$ rad/s.

Further, T_u, regarding to the stability robustness and the rejection performance,

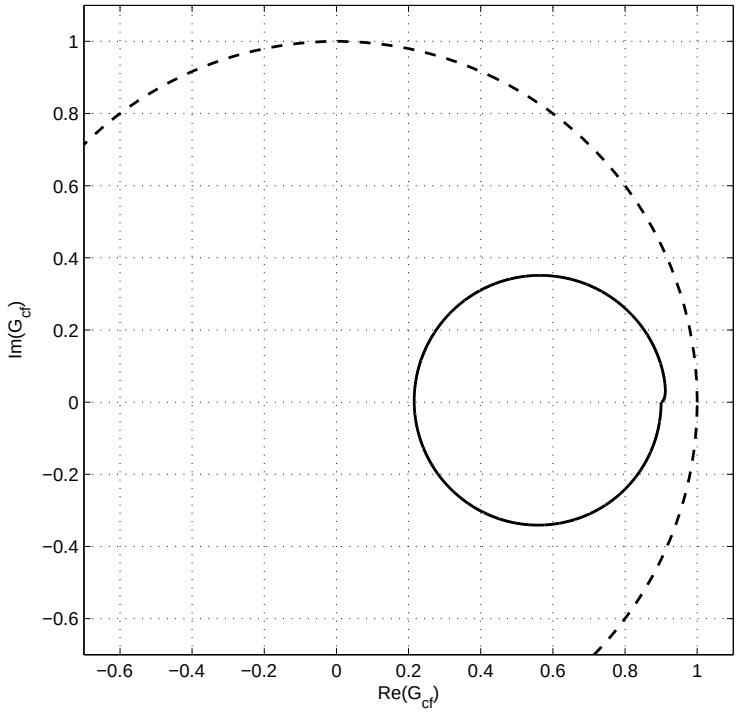

Figure 2.14: Nyquist plot of G_{cf} (solid line) compared to the unit circle (dash dotted line).

is chosen as 0.9. Once, T_u, z_n and ω_n are already chosen, from Eq. 2.54, the desired reduction capability can be achieved by choosing α. In this case, we hope that 90% of the 24 Hz harmonic can be removed, which means

$$|H_{\text{cfd}}(j48\pi)| = |S_{ci}(j48\pi)|\frac{|1-T_u|}{|1-G_{cf}(j48\pi)|} = 0.1. \tag{2.68}$$

To meet this requirement, with the help of Matlab, α is chosen as 2.5. According to Eq. 2.65, $K_{pi} = 1.058$ A·s/rad.

First of all, we check the reference tracking performance and the load rejection capability of this current feedback repetitive controller. According to Eq. 2.56, we can deduce that

$$S_{ci}(0) = 0 \quad \text{and} \quad \lim_{s\to 0}\frac{S_{ci}(s)}{s} = 0. \tag{2.69}$$

From Eq. 2.59 and Eq. 2.58, we can conclude that for this system, no matter tracking a step or a ramp reference, it will not have any steady-state error. Meanwhile, $S_{ci}(s)P_2(s)$ goes to zero when s goes to zero, then according to Eq. 2.61, a load torque also will not lead to any steady-state error in this system.

Then we check the stability of the resulting system. According to Eq. 2.5.1, we need to examine whether S_{ci} and $S_{ci}T_{pi}P$ are stable or not. First, SOM ensures the stability of S_{ci}. On the other hand, $S_{ci}T_{pi}P$ with the chosen parameters has three

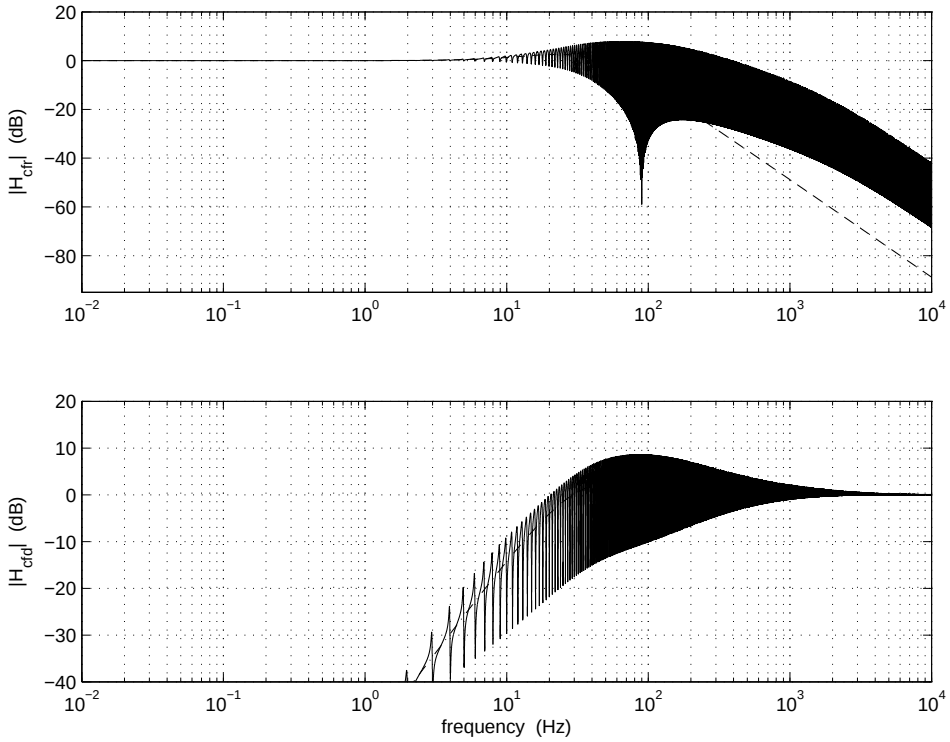

Figure 2.15: Bode magnitude plots of H_{cfr} (above, solid line) and H_{cfd} (below, solid line), compared to those obtained with an PI controller only (dash lines).

roots: $-228+j0$, $-100+j0$ and $-1.42\times10^4+j0$. They are all located in the left-side of the s-plane, hence it is stable. As a result, to guarantee the stability of this system, we need to check the stability of the closed-loop. Fig. 2.14 shows a plot of G_{cf} whose maximum value is 0.906. Then according to the small gain theorem, this closed-loop is stable, so as this current feedback RC system.

The tracking and the rejection capability of this system are shown in Fig. 2.15. In order to highlight the advantage of the repetitive controller, the performances of the system controlled with the PI speed controller alone are also visualized in this figure. Note that both systems use the same PI speed controller. Hereafter, this kind of PI system will always accompany the other studied RC system to provide comparative results.

As shown in Fig. 2.15, $H_{\text{cfr}}(j\omega)$ at low frequencies (below 10 Hz) is quite similar to its conventional counterpart (PI control system), but at high frequencies, it has, as the basic RC system, lots of periodic resonances occurring at ω_k. Owing to these resonances, $H_{\text{cfr}}(j\omega)$ is frequently higher than 0 dB, indicating that overshoots and damped oscillations may happen during the tracking transient. Meanwhile, the noises of the speed sensor will be amplified, if they locate at these frequencies, in which $|H_{\text{cir}}|$ is higher than one. The second Bode plot shows that the desired rejection $|H_{\text{cfd}}(j48\pi)|=-20$ dB is achieved by the proposed current feedback repetitive controller. The rejection capability obtained with the current feedback repetitive

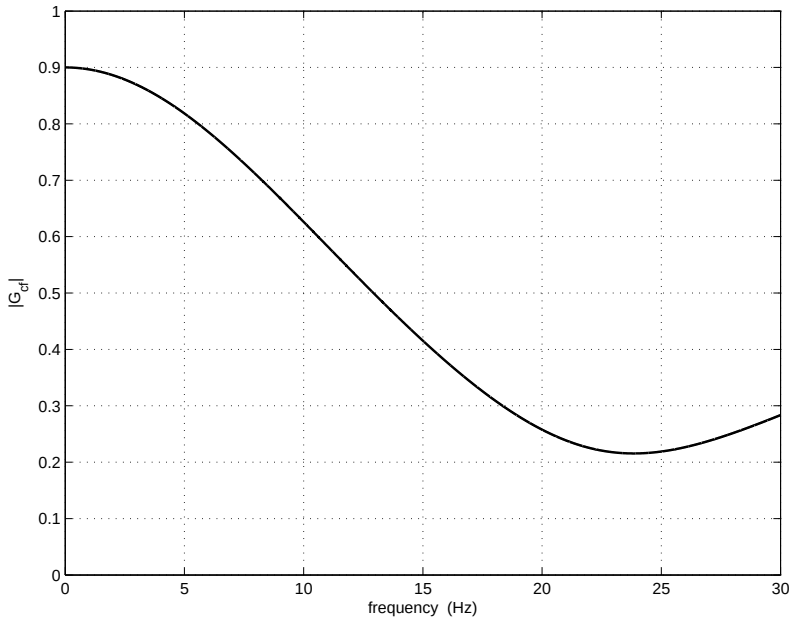

Figure 2.16: Plot of $|G_{cf}(j2\pi f)|$ indicating the convergence speed of sinusoidal disturbances with the designed basic repetitive controller.

controller, as with the basic repetitive controller, is also a periodic rejection capability. Only at ω_k, the rejection capability of this system is much better than its conventional counterpart (ex: $|S_{ci}(j48\pi)| = -2$ dB), at others frequencies, the rejection is not much better and even worse than its conventional counterpart. This requires that the target disturbance should be exactly located at ω_k, otherwise, the system rejection will not benefit from the use of the repetitive controller (the Chapter 3 will provide a deeper analysis to this). Besides, thanks to $S_{ci}(0) = 0$, $H_{\mathrm{cfd}}(0) = 0$, then at low frequencies, $|H_{\mathrm{cfd}}|$ is much smaller than $|H_{\mathrm{rcd}}|$, correspondingly the rejection is much better, this is another advantage obtained from the conventional controller (ex: $|H_{\mathrm{cfd}}(j16\pi)| = -32$ dB and $|H_{\mathrm{cfd}}(j24\pi)| = -16$ dB).

To check the convergence speed of the periodic disturbance, a plot of $|G_{cf}(j\omega)|$ between 0 and 30 Hz is shown in Fig. 2.16. This figure shows that the minimum value of $|G_{cf}(j\omega)|$, just as expected, is precisely located at 24 Hz with a small value 0.22. Theoretically, the main harmonic component can converge to its steady-state in very few iterations. At the same time, $|G_{cf}(j16\pi)|$ and $|G_{cf}(j32\pi)|$ are equal to 0.71 and 0.38 respectively, indicating that the 16 th harmonic component can reach its steady-state within several iterations, but the 8 th harmonic component theoretically needs more time.

For the current feedback RC system, we not only evaluate the influence of the variation of the machine parameters to the system stability, but also to the system performances. Its stability robustness is studied first. Since the variation of the parameters will change the stability of S_{ci} (conventional part) and the closed-loop

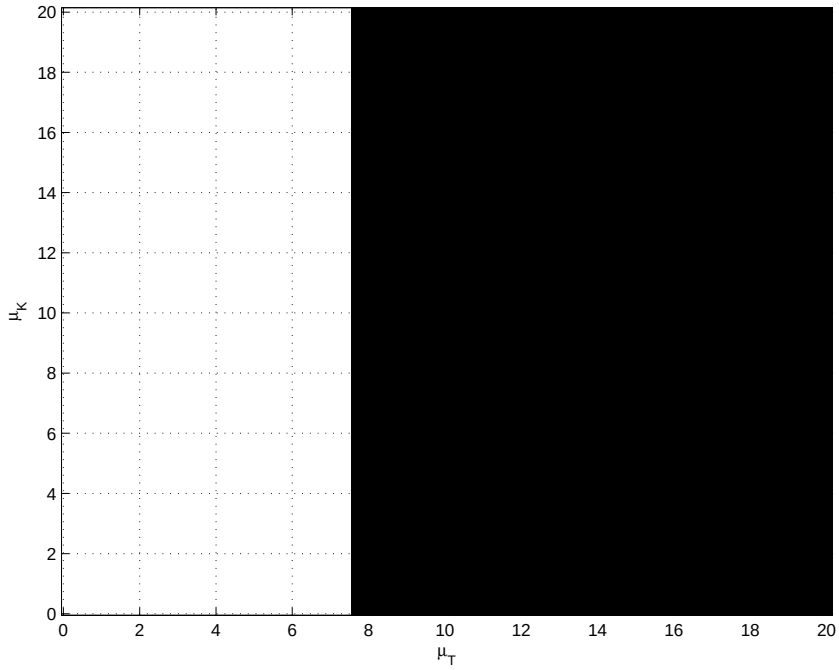

Figure 2.17: Stability robustness analysis of S_{ci} in the current feedback RC system. As shown in Fig. 2.7, $\mu_K = K^{\text{real}}/K$ and $\mu_T = T_d^{\text{real}}/T_d$.

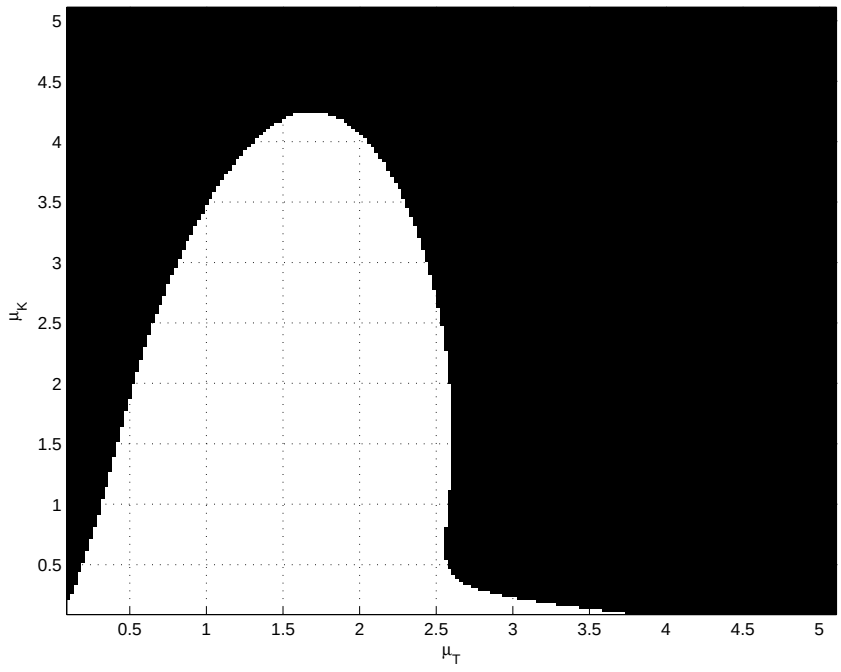

Figure 2.18: Stability robustness analysis of G_{cf} in the current feedback RC system. As shown in Fig. 2.7, $\mu_K = K^{\text{real}}/K$ and $\mu_T = T_d^{\text{real}}/T_d$.

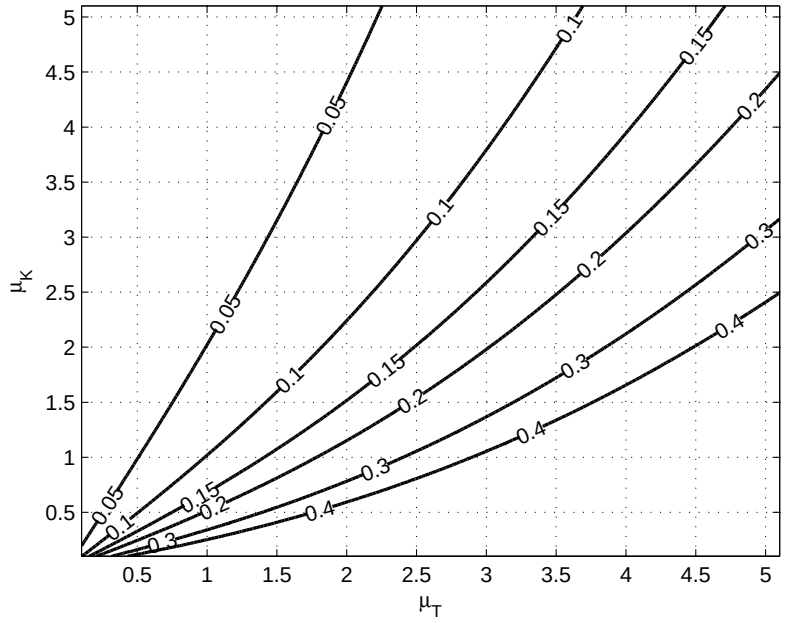

Figure 2.19: Main disturbance rejection robustness analysis of the current feedback repetitive controller. As shown in Fig. 2.7, $\mu_K = K^{\text{real}}/K$ and $\mu_T = T_d^{\text{real}}/T_d$.

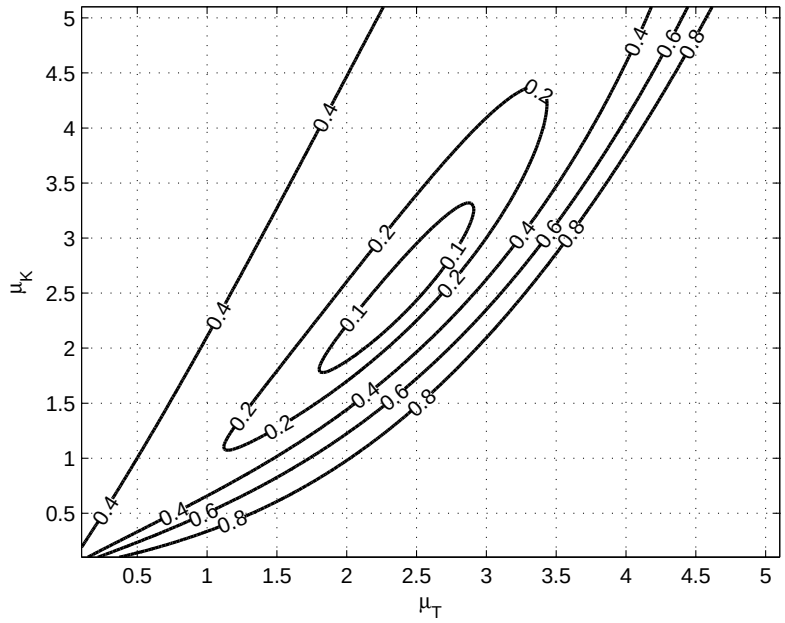

Figure 2.20: Main disturbance convergence speed robustness analysis of the current feedback repetitive controller. As shown in Fig. 2.7, $\mu_K = K^{\text{real}}/K$ and $\mu_T = T_d^{\text{real}}/T_d$.

containing G_{cf} (RC part), both of them need to be considered in this stability robustness analysis. The result of this stability robustness analysis of S_{ci} and the closed-loop are presented in Fig. 2.17 and Fig. 2.18 respectively. The stability robustness of S_{ci} is deduced from checking whether $1/(1+T_{ci}P_{\text{real}})$ has unstable poles or not, in which P_{real} is defined in Eq. 2.48. Meanwhile, the result of the closed-loop is obtained from Eq. 2.57 with the P_{real}. In both figures, the color, μ_K and μ_T have the same meaning as the basic RC case. The first figure shows that only when μ_T is larger than 7.6, S_{ci} will have an unstable pole. This second one shows that overestimating T_d and underestimating K simultaneously is more problematic than any other situation. However, even with $\mu_T = 0.5$ and $\mu_K = 1.5$, the system does not lose its stability. The comparison between both figures shows that the conventional controller (PI controller) has much better stability robustness than its RC counterpart, therefore, the stability robustness of this system is determined by the repetitive controller (G_{cf}). According to the results shown in Fig. 2.18, the current feedback repetitive controller with the proposed design offers a good stability robustness.

Then we need to study the performance robustness of this system, which involve two aspects: the rejection robustness and the convergence robustness. With μ_K and μ_T, we can get following equations

$$|G_{cf}^{\text{real}}(j48\pi)| = |T_u| \left|1 - S_{ci}^{\text{real}}(j48\pi)T_{pi2}(j48\pi)P^{\text{real}}(j48\pi)\right| \tag{2.70}$$

$$\text{with } S_{ci}^{\text{real}}(j48\pi) = \frac{1}{1 + T_{ci}(j48\pi)P^{\text{real}}(j48\pi)} \tag{2.71}$$

Then we can get

$$|H_{\text{cfd}}^{\text{real}}(j48\pi)| = |S_{ci}^{\text{real}}(j48\pi)| \frac{|1 - T_u|}{|1 - G_{cf}^{\text{real}}(j48\pi)|}. \tag{2.72}$$

Then, Eq. 2.72 and Eq. 2.70 can be used to measure the influence of the parameter variation to the rejection and convergence of the main harmonic component. The corresponding results are shown in Fig. 2.19 and Fig. 2.20. From Fig. 2.19, we can find that underestimating T_d and overestimating K at the same time will lead to a relatively important rejection capability degradation (ex: when $\mu_T = 1.5$ and $\mu_K = 0.5$, $|H_{\text{cfd}}(j48\pi)|$ will be around 0.3). Otherwise, with 50 % uncertainty of the parameters, the subsequent reduction capability is acceptable. On the other hand, Fig. 2.20 shows that the convergence speed is rather sensitive to the variation of the machine parameters. Both underestimating T_d and overestimating K simultaneously or overestimating T_d and underestimating K simultaneously will cause a serious loss of the convergence speed (ex: when $\mu_T = 1.5$ and $\mu_K = 0.5$, $|G_{\text{cf}}(j48\pi)|$ will even be higher around 0.8). From the above analysis, we can conclude that this system can keep its stability and provide an acceptable rejection capability with

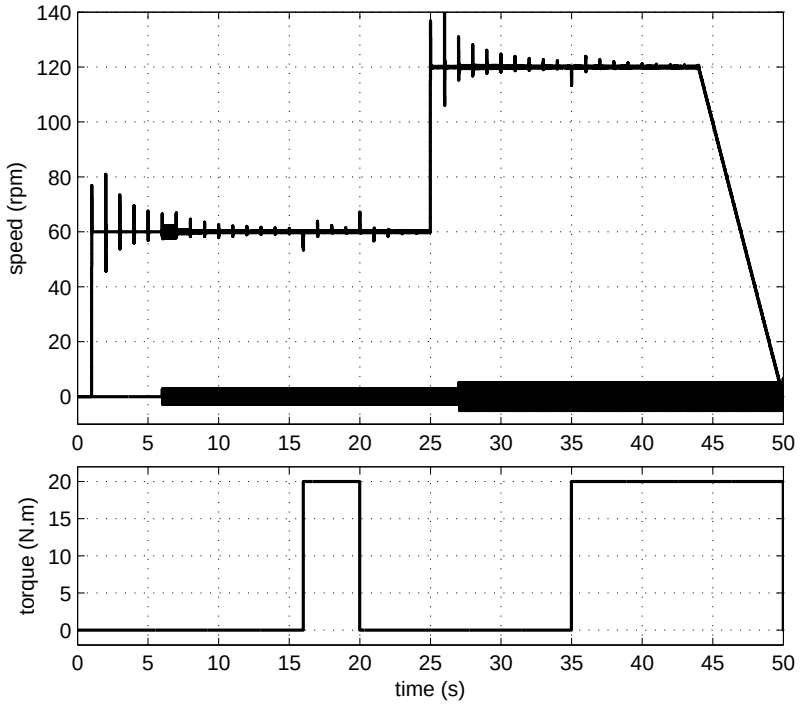

Figure 2.21: Simulation results showing how the closed loop system using a current feedback repetitive controller behaves when the system contains periodic disturbances, with variable speed reference (shown in figure above) and variable load torque (shown in figure below). The magnitude of $|P_2 D|$ is also visualized in the above figure.

$50\,\%$ uncertainty of the machine parameters, but the convergence of the main harmonic components may become very long.

This current iteration RC system is tested through a simulation in order to know its time response. During the 50-second simulation, the input reference changes three times, respectively at 1 and at $25\,$s as a step, and from 44 to $50\,$s as a ramp. Meanwhile a $20\,$N·m load torque influences this system in two time intervals between 16 and 20 s and between 35 and 50 s. The periodic disturbance starts at $6\,$s and at first is only made of a $5\,$N·m $24\,$th harmonic (as a $24\,$Hz sinusoidal signal), then after $27\,$s, a $2.5\,$N·m $8\,$th harmonic (as a $8\,$Hz sinusoidal signal) is also added. As the basic RC case, the frequency of disturbance is independent of the speed.

The time response of the current feedback RC system is shown in Fig. 2.21. To obtain a comparative result, the time response of the conventional PI system is shown in Fig. 2.22. Fig. 2.21 confirms that this current feedback RC system is able to track a constant reference without any steady-state error and also without the delay occurred in the basic RC case. Owing to the PI controller, the step signal can result in the same overshoot in both systems. Unfortunately, in this RC system, the chosen T_{pi2}, as a high-pass filter, also causes an overshoot, then because of the

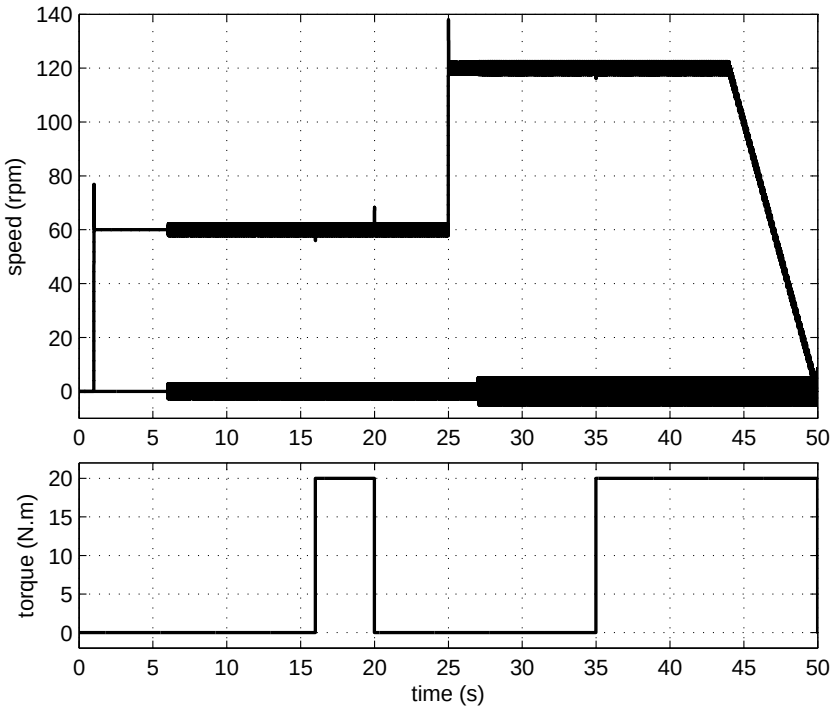

Figure 2.22: Simulation results showing how the closed loop system using a conventional controller behaves, with the same process, the same disturbances and the same reference as Fig. 2.21.

delay and the closed-loop, this overshoot leads to a series of oscillations that has a gradually decreasing magnitude reappearing between each T interval (1 s) until its visibility is finally covered by the speed ripple. This is quite similar to the basic RC system. The magnitude of the first few oscillations are larger or equal to the overshoot caused by the PI controller (ex: the magnitude of the overshoot is 16.84 rpm and the first and second oscillations are respectively 20.90 and 13.44 rpm), so they strongly impair the system tracking behavior. Meanwhile, as shown in Fig. 2.21, the peak-to-peak value of the speed ripple caused by the 24 th harmonic changed from 4.416 to 0.602 rpm in only 4 s, hence 86.4 % of this error can be removed within a short period, proving a good rejection ratio and a fast convergence speed of the main harmonic component. In addition, after 27 s, due to the emergence of the 8 th harmonic, the disturbance convergence becomes slower than that of the 24 th harmonic alone. However, after 8 s, the peak-to-peak value changed from 4.98 to 0.712 rpm, so 85.7 % of the disturbance containing the 8 th and the 24 th together is still successfully removed from the system, confirming a good reduction of the 8 th harmonic. Compared with Fig. 2.22, the periodic disturbance rejection of this system is obviously superior to the conventional PI system. At the same time, thanks to the conventional controller, the delay and the steady-state error resulting from

tracking a constant reference or rejecting a load torque no longer exists. Therefore, the use of the current information indeed improves the reference tracking and disturbance rejection performance. However, there is no denying that its tracking behavior suffering from the damped oscillations is still far from acceptable.

2.5.4 Design methodology 2

The analysis above presents an efficient methodology that designs T_{pi2} as a second order transfer function to get the satisfying stability and performance. In this section, we show that choosing T_{pi2} as a simple constant K_{pi} as well as using the leading component is another possible way to achieve an efficient current feedback repetitive controller.

Before presenting this design methodology, we first provide a simple example to show the possibility of using this method. If we chose $T_u = 0.9$ and $K_{pi} = 0.02$, the resulting maximum $|G_{cf}|$ is 0.985, so this system is stable. The subsequent reduction capability of the main disturbance (24 Hz) is -17.4 dB, showing that using a constant T_{pi2} can also offer an important reduction. If such kind of performance meets the requirement, this method, thanks to its simplicity, is quite efficient, hence is very attractive. However, if the desired reduction capability is -20 dB, using Eq. 2.54, we compute that $K_{pi} = 0.028$, which cannot guarantee the system stability anymore, since the corresponding Max$|G_{cf}|$ is 1.02. This implies a serious performance limitation of this design methodology. This maximum occurs at around 80 Hz, where $|S_{ci}P|$ is 10.7 hence $|K_{pi}S_{ci}P| = 0.32$, and the phase of $S_{ci}P$ is -110 degrees. There are two possible solutions that can reduce this maximum. The first one is to use a smaller K_{pi} and the second one is to use the leading-time component τ. The first one earns the system stability at the cost of impairing the reduction capability, just as mentioned above. In the second method, the use of τ adds only a positive angle $j\omega\tau$ into $S_{ci}P$, hence τ with an appropriate value can reduce the Max$|G_{cf}|$ without weakening the performance. This is the reason why we provide a design methodology that chooses a constant T_{pi2} and uses τ in this section.

Owing to the introduction of τ, we have three parameters to tune. To design a useful current feedback controller, first of all, the stability condition of this system with this design methodology can be rewritten as

$$|G_{cf}(j\omega)| = |T_u| \left|1 - K_{pi}S_{ci}(j\omega)P(j\omega)e^{j\omega\tau}\right| < 1, \quad \forall\omega \in [0, +\infty[\tag{2.73}$$

From Eq. 2.73, one can show that

$$G_{cf}(0) = T_u \text{ and } \lim_{\omega\to+\infty} G_{cf}(j\omega) = T_u, \tag{2.74}$$

which implies that to ensure the stability, at least $|T_u| < 1$.

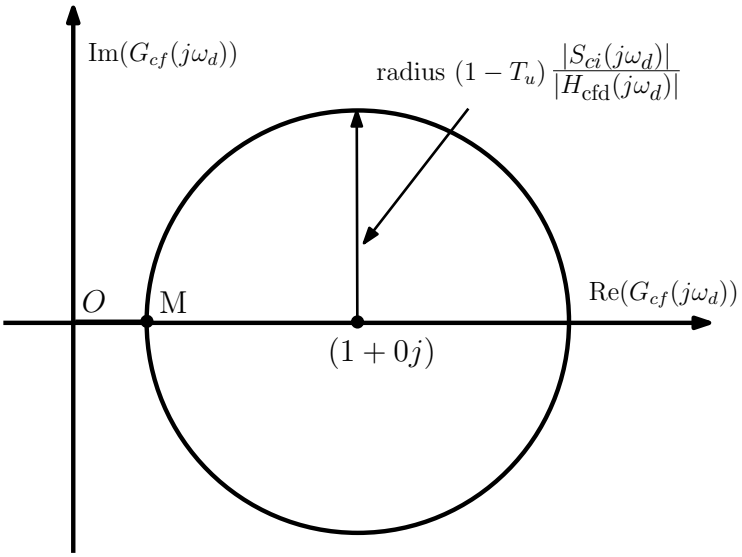

Figure 2.23: The relationship between $|G_{cf}(j\omega_d)|$ and $|H_{\text{cfd}}(j\omega_d)|$.

Provided that k_d is the order of the main disturbance component, then its angular frequency is $\omega_d = 2\pi k_d/T$. Therefore, the magnitude of the disturbance rejection ratio of this component can be written as

$$|H_{\text{cfd}}(j\omega_d)| = (1-T_u)\frac{|S_{ci}(j\omega_d)|}{|1-G_{cf}(j\omega_d)|}, \tag{2.75}$$

$$\text{thus } |1-G_{cf}(j\omega_d)| = (1-T_u)\left|\frac{S_{ci}(j\omega_d)}{H_{\text{cfd}}(j\omega_d)}\right|. \tag{2.76}$$

Eq. 2.76 shows that the set of complex values resulting from chosen values of T_u and $|H_{\text{cfd}}(j\omega_d)|$ is a circle centered on $(1+j0)$ with a radius $(1–T_u)|S_{ci}(j\omega_d)|/|H_{\text{cfd}}(j\omega_d)|$, as shown in Fig. 2.23. The fastest convergence speed will be achieved if $|G_{cf}(j\omega_d)|$ is the smallest, which corresponds to the M point located on the real axis in Fig. 2.23. This leads to the requirement

$$G_{cf}(j\omega_d) = 1-(1-T_u)\frac{|S_{ci}(j\omega_d)|}{|H_{\text{cfd}}(j\omega_d)|} \tag{2.77}$$

$$\text{with } G_{cf}(j\omega_d) = T_u(1-K_{pi}e^{j\omega_d\tau}S_{ci}(j\omega_d)P(j\omega_d)).$$

This will be possible if K_{pi} and τ are chosen as

$$K_{pi} = |Z|, \text{ and } \tau = \frac{1}{\omega_d}\text{Arg}(Z), \tag{2.78}$$

$$\text{with } Z = K_{pi}e^{j\omega_d\tau} = \frac{1}{S_{ci}(j\omega_d)P(j\omega_d)}\left(1-\frac{G_{ci}(j\omega_d)}{T_u}\right),$$

For such a design rule, $|H_{\text{rcd}}(j\omega_d)|$ cannot be chosen too small, since the condition

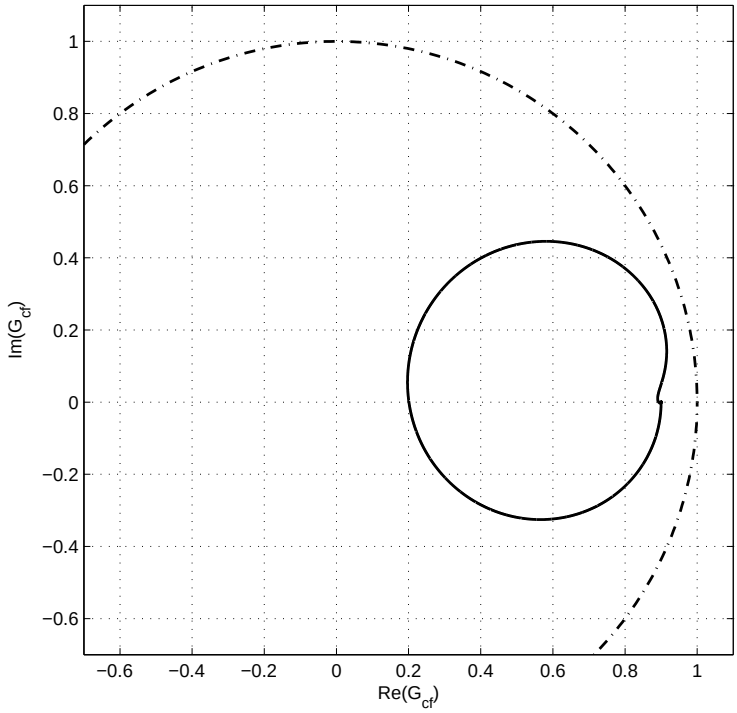

Figure 2.24: Nyquist plot of G_{cf} (solid line) compared to the unit circle (dash dotted line). The maximum value of $|G_{ci}|$ is 0.93.

$|G_{cf}(j\omega_d)| < 1$ leads to

$$|H_{\text{cfd}}(j\omega_d)| > \frac{1-T_u}{2}|S_{ci}(j\omega_d)|. \tag{2.79}$$

The proposed design methodology is applied to the system used in the previous cases and based on a nominal speed of 60 rpm. To balance between robust stability and performance, we chose $T_u = 0.9$. The main disturbance component is the 24 th harmonic ($\omega_d = 48\pi$) and we wish to remove 90 % of this component ($|H_{\text{cfd}}(48\pi)| = 0.1$). From Eq. 2.78, this leads to $K_{pi} = 17.74$ A·s/rad and $\tau = 841\ \mu$s. The choice of K_{pi} and τ satisfies Eq. 2.79, hence they can be used in this repetitive controller.

First, with the chosen T_{ci}, T_u and T_{pi}, we can easily confirm that this system is able to track a step or a ramp reference without any steady-state error. Meanwhile, a load-torque will not lead to steady-state error.

Since S_{ci} is stable, and with constant T_u and T_{pi}, $S_{ci}T_{pi}P$ is stable as well. The closed-loop, as shown in Fig. 2.24, is also stable. Therefore, this current feedback RC system with the proposed controller is stable. Comparing Fig. 2.24 with Fig. 2.14, one can find that the Nyquist plot of G_{cf} obtained from both tuning methods are quite similar. However, the maximum of G_{cf} obtained in this case is slightly larger than its previous counterpart, therefore, the use of the second tuning method relatively attenuates the stability margin.

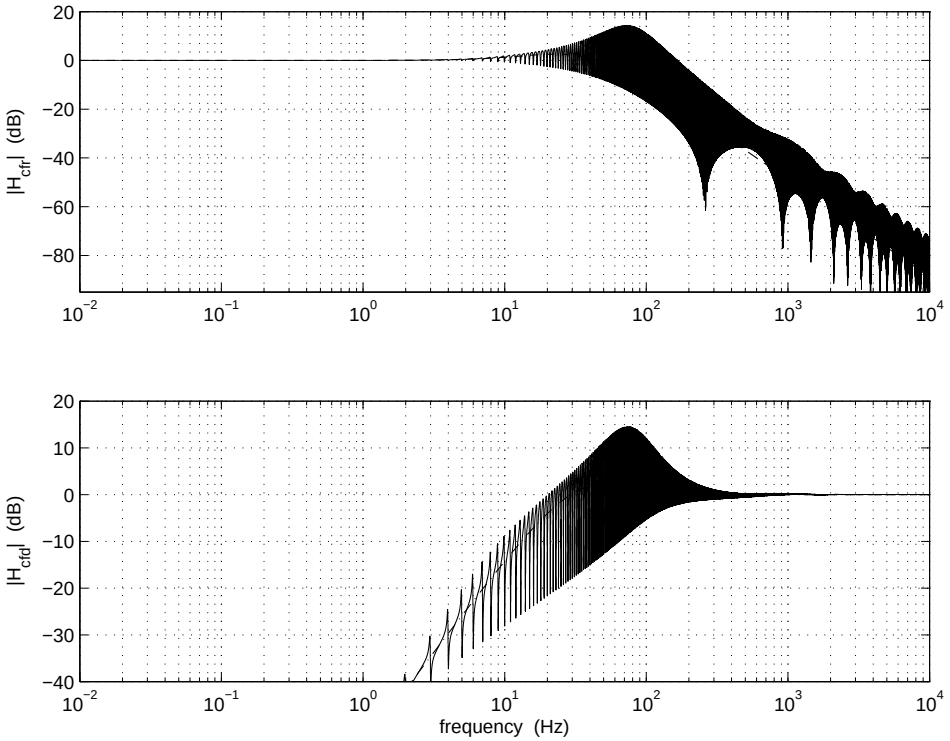

Figure 2.25: Bode magnitude plots of H_{cfr} (above, solid) and H_{cfd} (below, solid), compared to those obtained with an PI controller only (dash lines).

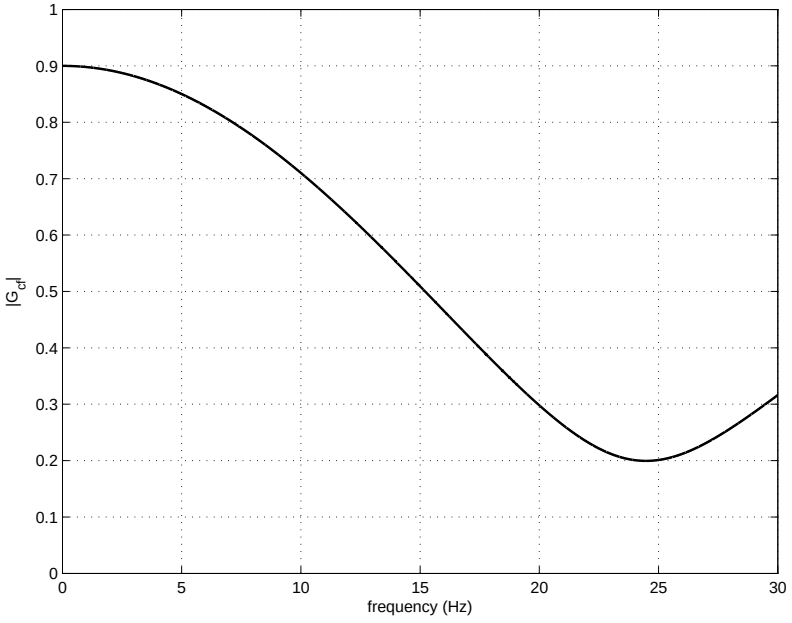

Figure 2.26: Plot of $|G_{cf}(j2\pi f)|$ indicating the convergence speed of sinusoidal disturbances with the designed basic repetitive controller

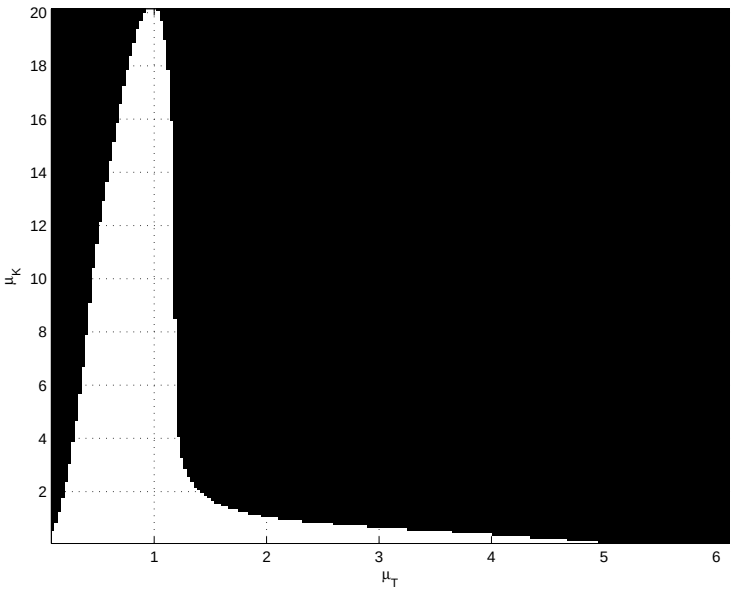

Figure 2.27: The stability robustness analysis of the designed current feedback RC system. As shown in Fig. 2.7, $\mu_K = K^{\text{real}}/K$ and $\mu_T = T_d^{\text{real}}/T_d$.

The reference tracking and disturbance rejection performances are shown in Fig. 2.25 by two Bode plots. The comparison between Fig. 2.15 and Fig. 2.25 clearly shows that $|H_{\text{cfr}}(j\omega)|$ are similar in both cases, especially below 150 Hz. Above this frequency, the $|H_{\text{cfr}}(j\omega)|$ obtained with the second tuning method is smaller than the first one, implying that the second design might provide a better transient behavior (smaller overshoots and oscillations). On the other hand, the figure shows that the goal $|H_{\text{cfd}}(j48\pi)| = -20$ dB is reached. $|H_{\text{cfd}}(j\omega)|$ obtained with the second tuning, in the low frequencies (below 100 Hz) and in high frequencies (beyond 1000 Hz), is very close to the first one. However, in the middle frequencies, the current feedback repetitive controller obtained with the second tuning provides less rejections at ω_k than the first one.

As in the previous cases, a plot of $|G_{cf}(j\omega)|$ between 0 and 30 Hz is shown in Fig. 2.26 to illustrate the convergence speed of different harmonic components. This figure shows that $|G_{cf}(j48\pi)|$ is 0.2, indicating that the main harmonic component converges to its steady-state a little faster than in the last case. Besides, $|G_{cf}(j16\pi)|$ and $|G_{cf}(j32\pi)|$ are 0.74 and 0.44, which are nearly the same as the last tuning. Consequently, the convergence speeds obtained from both current feedback RC systems are similar.

To determine the stability and performance robustness of this proposed design, the robustness analysis is made with the same conditions as the previous cases. The result of the stability robustness of this system is shown in Fig. 2.27. As is the last case, the RC part is the key of this stability robustness analysis. The result of this RC part is rather different from the result presented in Fig. 2.18. In this case, if

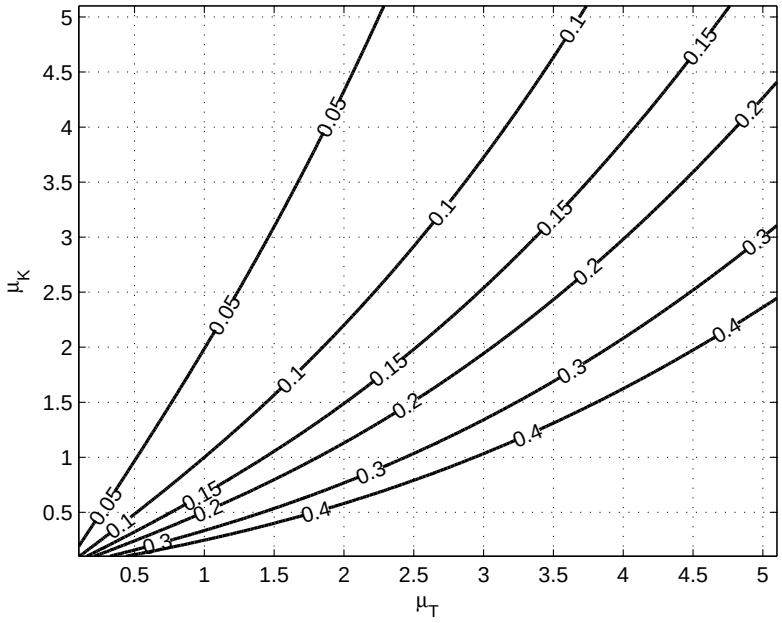

Figure 2.28: Main disturbance rejection robustness analysis of the current feedback repetitive controller. As shown in Fig. 2.7, $\mu_K = K^{\text{real}}/K$ and $\mu_T = T_d^{\text{real}}/T_d$.

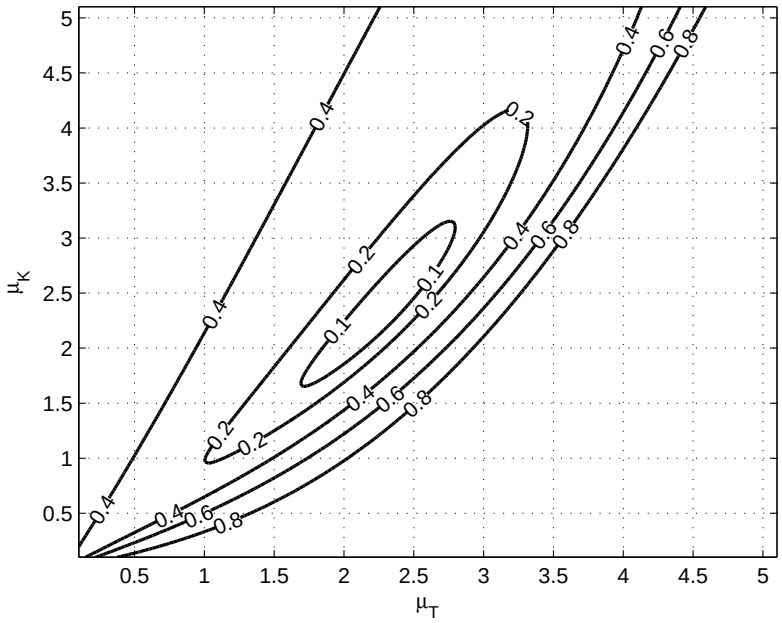

Figure 2.29: Main disturbance convergence speed robustness analysis of the current feedback repetitive controller. As shown in Fig. 2.7, $\mu_K = K^{\text{real}}/K$ and $\mu_T = T_d^{\text{real}}/T_d$.

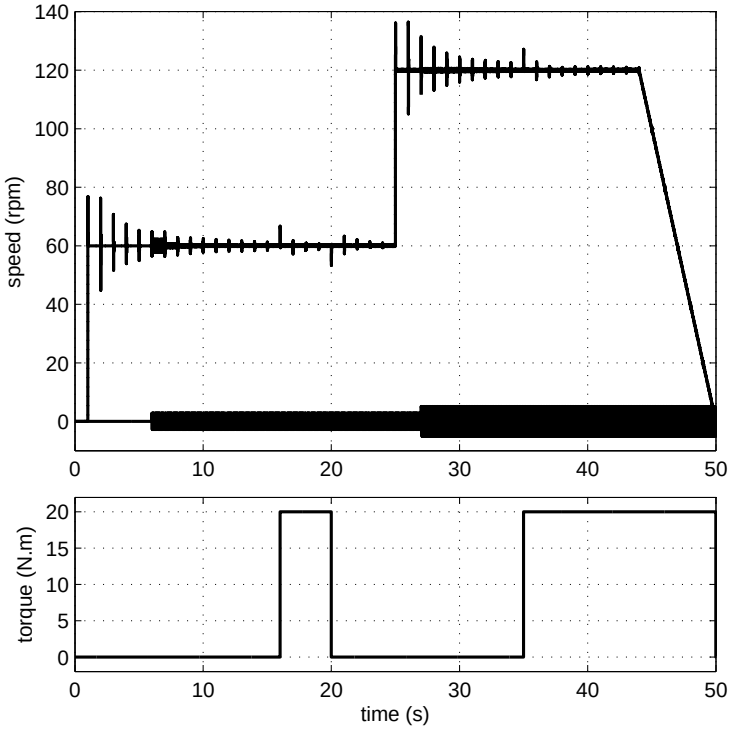

Figure 2.30: Simulation results showing how the closed loop system using a current feedback repetitive controller behaves with the same process, the same disturbances and the same reference as Fig. 2.21.

the variation between the T_d^{real} and the supposed one is less than $\pm 25\,\%$ ($0.75 < \mu_T < 1.25$), a large range of μ_k (from 0 to 10) cannot break the system stability. On the other side, a large underestimation of T_d ($\mu_T > 2$) is evidently troublesome to the system stability. The results presented in Fig. 2.28 and Fig. 2.29 show that this design methodology can provide nearly the same performance robustness as the last one. As a result, with less than $50\,\%$ variation of parameters, the system can also remains stable and offer an adequate rejection while convergence speed may be degrade seriously.

This designed current feedback RC system is tested through the same simulation as the last case and the corresponding results are shown in Fig. 2.30. This figure shows that with this new tuning, the system tracking still suffers from damped oscillations. Fortunately, the amplitude of these oscillations in this system is almost $20\,\%$ less than the first one (ex: the magnitude of the first and the second oscillation are 16.28 and $10.73\,$rpm in this system versus 20.90 and $13.44\,$rpm in the last system), confirming the previous analysis. This figure also shows that the rejection ratio and speed of the $24\,$th harmonic component are the same as the last one, and for the $8\,$th, the rejection is slightly worse than the last one ($84.1\,\%$ of the $8\,$th and the 24 the harmonic components are removed in $10\,$s). Hence, this current feedback

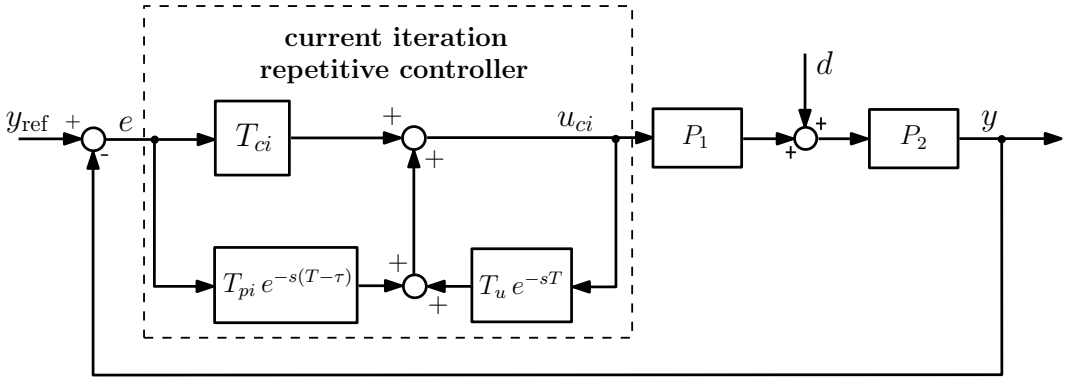

Figure 2.31: Block diagram of the plant controlled by a current iteration repetitive controller (in our case, $u_{ci} = i_{\text{qref}}$ and other symbols have the same definition as in Fig. 2.12.

repetitive controller with this tuning method can provide almost the same periodic rejection capability as the first tuning method with a better tracking behavior.

If considering the robustness and rejection capability, there is no obvious distinction between two tuning methods. However, the second one, thanks to its simplicity, will be considered in the practical applications. Further, it is relatively easier to design an angle-based current feedback controller based on the second tuning, because it has less parameters, which will be discussed in Chapter 3.

2.6 Current iteration repetitive controller

This section is devoted to presenting another important current repetitive controller: the current iteration repetitive controller [107]. The typical structure of a closed-loop system controlled by a current iteration repetitive controller is shown in Fig. 2.31, which shows that the realization of a current iteration RC system is quite similar to that of a current feedback RC system. The distinction between them is that the input of a current iteration repetitive controller includes the output of T_{ci}; on the other hand, the input of a current feedback repetitive controller does not contain this output, resulting in different characteristics between both current RC systems.

The reason of studying this controller is that it is developed on the basis of another widely used repetitive controller: the plug-in repetitive controller. The basic structure of a plug-in repetitive controller and its control system is shown in Fig. 2.32 [75, 79, 80]. To show more clearly the relationship between these two repetitive controllers, the plug-in RC system can be equivalently represented in Fig. 2.33. Then the comparison between Fig. 2.31 and Fig. 2.33 illustrates that the plug-in repetitive controller is only a particular case ($T_{pi} = 0$ and $T_{ci} = 1$) of the current iteration one. Consequently, the conclusions obtained from the current iteration RC system generally are also effective for the plug-in RC system.

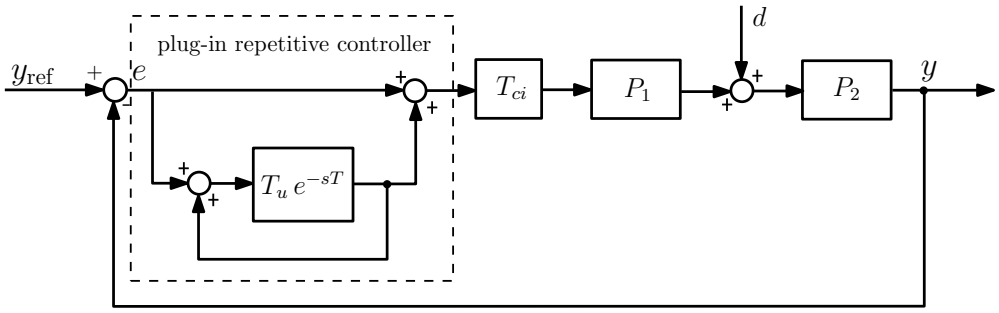

Figure 2.32: Block diagram of the system using the plug-in repetitive controller.

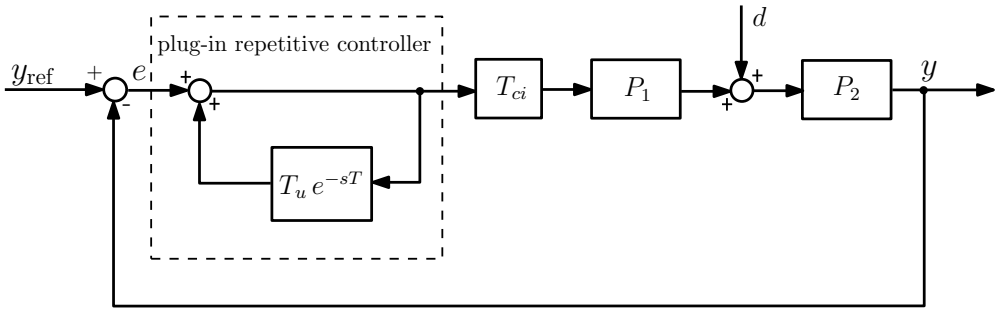

Figure 2.33: Another representation of the plug-in RC system.

To study the current iteration repetitive controller, first of all, from Fig. 2.31, its transfer function can be written as [107]

$$\begin{aligned} U_{ci}(s) &= T_u e^{-sT} U_{ci}(s) + T_{pi}(s) e^{-s(T-\tau)} E(s) + T_{ci}(s) E(s), \\ \text{then } C_{ci}(s) &= \frac{U_{ci}(s)}{E(s)} = \frac{T_{pi}(s) e^{-s(T-\tau)} + T_{ci}(s)}{1 - T_u e^{-sT}}. \end{aligned} \tag{2.80}$$

From Eq. 2.80 and Fig. 2.31, the relationship between the system output y, the reference input y_{ref} and the disturbance d is

$$\begin{aligned} Y &= \frac{(T_{ci} + T_{pi} e^{-s(T-\tau)}) P Y_{\text{ref}} + (1 - T_u e^{-sT}) P_2 D}{(1 + T_{ci} P)\left(1 - \frac{T_u - T_{pi} P e^{s\tau}}{1 + T_{ci} P} e^{-sT}\right)} \\ Y &= H_{\text{cir}}\, Y_{\text{ref}} + H_{\text{cid}}\, P_2 D, \\ \text{with } H_{\text{cir}} &= S_{ci} \frac{(T_{ci} + T_{pi}\, e^{-s(T-\tau)}) P}{1 - G_{ci}\, e^{-sT}}, \quad H_{\text{cid}} = S_{ci} H_{\text{cid2}}, \\ H_{\text{cid2}} &= \frac{1 - T_u e^{-sT}}{1 - G_{ci} e^{-sT}}, \quad \text{and } G_{ci} = S_{ci}\, G_{rc}. \end{aligned} \tag{2.81}$$

where G_{rc} is defined in Eq. 2.8 and S_{ci} is defined in Eq. 2.53. The above equations show that S_{ci} and H_{cid2} can mutually improve themselves: if $S_{ci}(0) = 0$, then $H_{\text{cid}}(0) = 0$ and if $|H_{\text{cid2}}(j\omega_d)|$ is small, then $|H_{\text{cid}}(j\omega_d)|$ will be small.

From Eq. 2.81, the relationship between the error e, the reference input y_{ref} and the disturbance d is

$$\begin{aligned} E &= \frac{1-T_u e^{-sT}}{(1+T_{ci}P)(1-G_{ci}e^{-sT})} Y_{\text{ref}} - \frac{1-T_u e^{-sT}}{(1+T_{ci}P)(1-G_{ci}e^{-sT})} P_2 D \\ E &= H_{\text{cid}}\,(Y_{\text{ref}} - P_2 D). \end{aligned} \tag{2.82}$$

Eq. 2.81 and Eq. 2.82 are the basis for the stability and performance investigation of this current iteration RC system.

2.6.1 Relationship between the two current RC systems

The similarity between the current iteration and the current feedback RC system has been mentioned at the head of this section, and this subsection is dedicated to unveiling their underlying relationship.

To simplify the problem, several assumptions need to be made first. Since both repetitive controllers are applied to the same plant, P is the same in both systems, accordingly, the conventional controller T_{ci} is same as well. Besides, T_u and τ, for the sake of simplicity, are also set to be the same. Therefore, T_{pi} is the only different parameter between two systems. So as to differentiate T_{pi} of the two systems, T_{pi} of the current iteration controller is marked as T_{pi}^{ci} and in the current feedback one, it is remarked as T_{pi}^{cf}. Consequently, the closed-loop transfer function of the current iteration system is

$$H_{\text{cir}} = S_{ci} \frac{(T_{ci} + T_{pi}^{ci} e^{-s(T-\tau)})P}{1 - G_{ci}e^{-sT}}, \tag{2.83}$$

and the closed-loop transfer function of the current feedback system is

$$H_{\text{cfr}} = S_{ci} \frac{(T_{ci} - (T_u T_{ci} - T_{pi}^{cf} e^{s\tau})e^{-sT})P}{1 - G_{cf}e^{-sT}}, \tag{2.84}$$

The comparison between Eq. 2.83 and Eq. 2.84 shows that both systems generally have different denominators and numerators. Since the denominator determines the system stability, it is interesting to know whether the denominators of both transfer functions could be equal under certain conditions. The denominator of Eq. 2.83 is $1-G_{ci}e^{-sT}$ and that of Eq. 2.84 is $1-G_{cf}e^{-sT}$, and if they are same, we can get

$$\frac{T_u - T_{pi}^{ci} P e^{s\tau}}{1+T_{ci}P} = T_u - \frac{T_{pi}^{cf} P e^{s\tau}}{1+T_{ci}P}. \tag{2.85}$$

To get Eq. 2.85, the T_{pi} from both systems should fulfill the following relationship

$$T_{pi}^{ci} = T_{pi}^{cf} - T_{ci} T_u e^{-s\tau}. \tag{2.86}$$

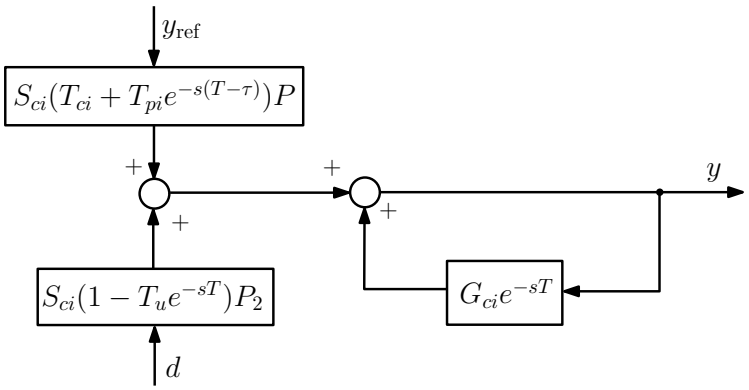

Figure 2.34: Alternative diagram of the current iteration RC system.

Eq. 2.86 enables Eq. 2.83 and Eq. 2.84 to have the same denominator, and one can also deduce that $G_{ci} = G_{cf}$, $H_{\text{cid}} = H_{\text{cfd}}$ and $H_{\text{cir}} = H_{\text{cfr}}$. Then with Eq. 2.86 and the previous assumptions, the current iteration repetitive controller and the current feedback one can provide the same stability robustness, the same tracking and the same rejection capability. Therefore, Eq. 2.86 is the condition that can equalize the current iteration RC system and the current feedback RC system.

It seems not necessary to specially provide a design method for the current iteration repetitive controller, because by using Eq. 2.86, we can easily obtain a current iteration controller from the current feedback controllers presented in section 2.5. However, according to Eq. 2.86, it is easy to know that these deduced current iteration controllers will be much more complicated than their current feedback counterparts, hence it is difficult to apply them in practical systems. As a result, in this section, we will seek another design methodology for the current iteration repetitive controller so as to gain a balance among the controller simplicity, the system stability and the performances.

2.6.2 Stability and performance

Stability

As the current feedback RC system, an equivalent representation of the current iteration RC system derived from Eq. 2.81 is written as

$$\begin{aligned}\left(1-G_{ci}e^{-sT}\right)Y &= S_{ci}(T_{ci}+T_{pi}e^{-s(T-\tau)})PY_{\text{ref}}+S_{ci}(1-T_ue^{-sT})P_2D\\ Y &= G_{ci}e^{-sT}Y+S_{ci}(T_{ci}+T_{pi}e^{-s(T-\tau)})PY_{\text{ref}}+S_{ci}(1-T_ue^{-sT})P_2D. \end{aligned} \tag{2.87}$$

Following Eq. 2.87, the current iteration system can be reformulated as in Fig. 2.34, which shows that the stability of this current iteration RC system, as other RC systems, is determined by three parts: $S_{ci}(T_{ci}+T_{pi}e^{-s(T-\tau)})P$, $S_{ci}(1-T_ue^{-sT})P_2$ and

one closed-loop containing $G_{ci}e^{-sT}$. According to the analysis presented in section 2.5.1, the stability of both $S_{ci}(T_{ci}+T_{pi}e^{-s(T-\tau)})P$ and G_{ci} is determined by S_{ci} and $T_{pi}P$, and the stability of $S_{ci}(1-T_ue^{-sT})P_2$ is only related to S_{ci}. Provided that S_{ci} and $T_{pi}P$ are stable, a sufficient stability condition of this system derived from the small gain theorem can be written as

$$|G_{ci}(j\omega)|=\left|\frac{T_u-T_{pi}(j\omega)P(j\omega)e^{j\omega\tau}}{1+T_{ci}(j\omega)P(j\omega)}\right|=|S_{ci}(j\omega)G_{rc}(j\omega)|<1,\quad\forall\omega\in[0,+\infty[\tag{2.88}$$

Reference tracking

As other RC systems, the tracking capability of the current iteration system are tested by a step reference and a ramp one. For a stable system, when this it is tracking a step signal $A\cdot\Gamma(t)$, the subsequent steady-state error is

$$e_{\text{step}}(\infty)=S_{ci}(0)\frac{1-T_u}{1-G_{ci}(0)}A. \tag{2.89}$$

Hence, when $S_{ci}(0)=0$ or $T_u=1$, this system is able to track a step signal without any steady-state error. When tracking a ramp signal $B\cdot t\cdot\Gamma(t)$, the subsequent steady-state error is

$$e_{\text{ramp}}(\infty)=\lim_{s\to0}\frac{S_{ci}(s)}{s}\frac{1-T_u}{1-G_{ci}(s)e^{-sT}}B \tag{2.90}$$

Then both $\lim_{s\to0}S_{ci}(s)/s=0$ and $T_u=1$ can lead to no steady-state tracking error.

Disturbance rejection

From Eq. 2.82 and the analysis presented in section 2.5.2, the periodic disturbance rejection ratio of this system is $|H_{\text{cid}}(j\omega_k)|$ and the rejection difference between this RC system and its conventional counterpart (controlled by T_{ci} alone) is determined by $|H_{\text{cid2}}(j\omega_k)|$. Meanwhile, the convergence speed of disturbance in this system is determined by $|G_{cf}(j\omega)|$. Further, the steady-state error resulting from the load torque can be written as

$$\begin{aligned}e_{\text{load}}(\infty)=\lim_{t\to+\infty}e_{\text{load}}(t)&=\lim_{s\to0}sS_{ci}(s)\frac{1-T_ue^{-sT}}{1-G_{ci}(s)e^{-sT}}P_2(s)\frac{B_d}{s}.\\&=\left(\lim_{s\to0}S_{ci}(s)P_2(s)\right)\frac{1-T_u}{1-G_{ci}(0)}B_d.\end{aligned} \tag{2.91}$$

This equation shows that when $\lim_{s\to0}S_{ci}(s)P_2(s)=0$ or $T_u=1$, a load-torque will not lead to any steady-state error in this RC system.

2.6.3 Design methodology 1

As the current feedback repetitive controller, in this subsection, we first study the possibility to chose the current iteration repetitive controller as a second order filter to obtain a stable system with the required performances. As the previous cases, the T_{ci} is chosen as a PI controller, the speed is 60 rpm and the 24 th harmonic is the main disturbance component.

First of all, from Eq. 2.69, Eq. 2.89, Eq. 2.90 and Eq. 2.91, it is obvious that this current iteration RC system, as its current feedback counterpart, is able to track a step and a ramp reference, as well as to reject a load-torque without any steady-state error.

Then, we turn to discuss the system stability. The sufficient stability condition of this system shown in Eq. 2.88 is,

$$|G_{ci}(j\omega)| = |S_{ci}(j\omega)G_{rc}(j\omega)| < 1, \quad \forall \omega \in [0, +\infty[$$

which evidently shows similarities and distinctions between the stability condition of the basic system and this one. Considering their likeness, it is reasonable to choose the same T_{pi2} used in the basic system for this system. Meanwhile, in this case, $\tau = 0$. Therefore, the T_{pi2} chosen in Eq. 2.32,

$$T_{pi2}(s) = \frac{T_{pi}(s)}{T_u(s)} = \frac{K_{hp}}{T_d} \frac{s(1+sT_d)}{s^2 + 2z_n\omega_n s + \omega_n^2},$$

is reused here. This choice of T_{pi2} together with T_u, brings four parameters in this tuning. Comparing to the basic RC system, the stability condition of the current iteration RC system contains $S_{ci}(j\omega)$, hence another tuning methodology that can take S_{ci} into account needs to be provided. To do so, the features of S_{ci} should be known first. According to Eq. 2.56, its magnitude can be shown in Fig. 2.35, which shows that S_{ci} can be considered as a high-pass filter, and its maximum is 1.44 located at 58 Hz. Around this maximum, its value is greater than 1. At low frequencies, its value starts from zero, but soars with the rising frequency, and finally exceeds one around 30 Hz. Whereas, at high frequencies (above 200 Hz), its value is only slightly larger than one.

To achieve the T_{pi2} tuning, we also need to consider G_{rc}, and its transfer function is

$$G_{rc}(s) = T_u \frac{s^2 + 2z_n\omega_n s + (1-\alpha)\omega_n^2}{s^2 + 2z_n\omega_n s + \omega_n^2}, \quad \text{with} \quad \alpha = \frac{K_{hp}K}{\omega_n^2}, \tag{2.92}$$

which shows that G_{rc} with the chosen T_{pi2} also looks like a high-pass filter, and

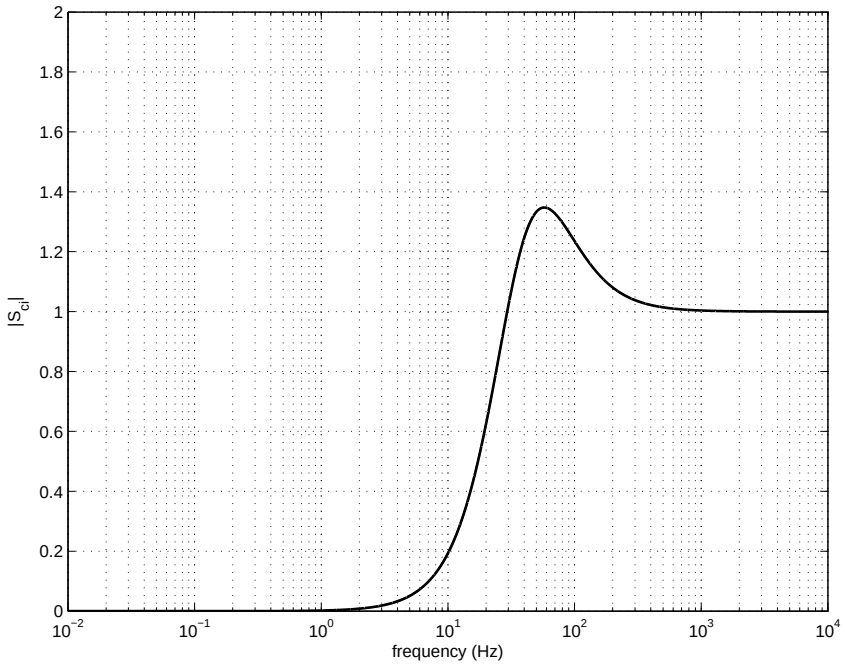

Figure 2.35: Plot of $|S_{ci}|$.

from Eq. 2.92, we can derive that

$$G_{rc}(0) = T_u(1-\alpha) \quad \text{and} \quad \lim_{\omega \to +\infty} G_{rc}(j\omega) = T_u. \tag{2.93}$$

Meanwhile, we can notice that $|G_{rc}|$ has a resonance occurring at a high frequency, and its magnitude can be reduced by choosing a larger z_n. In this case, when z_n is larger than 5, its influence on the magnitude of the resonance is negligible, therefore to get a relative small resonance, $z_n = 5$ is chosen.

The stability condition requires that $|S_{ci}G_{rc}| < 1$ ($|G_{ci}| < 1$). Since $|S_{ci}|$ is large at the area around $58\,\text{Hz}$, then for the sake of the stability, $|G_{rc}|$ should be small in the same area. This can be achieved by choosing a high cut-off frequency for G_{rc}, because it is a high-pass filter [24]. Owing to the fact that above $200\,\text{Hz}$, $|S_{ci}|$ approaches one, it is reasonable to choose the cut-off frequency $f_c = 200\,\text{Hz}$. Then according to the chosen f_c and z_n, from Eq. 2.92, ω_n can be computed through the following equation

$$\omega_n = \omega_c \sqrt{\frac{2}{\sqrt{(4z_n^2+2)^2+4} - (4z_n^2+2)}}, \quad \text{with } \omega_c = 2\pi f_c. \tag{2.94}$$

On the other hand, the main disturbance ($24\,\text{Hz}$) needs to be reduced in a short time, requiring a small $|G_{ci}(j48\pi)|$. Since S_{ci} is already fixed, a small $|G_{ci}(j48\pi)|$ can only be achieved by tuning G_{rc}. At low frequencies, this value is strongly influenced by its low frequency gain, which, as shown in Eq. 2.93, is $(1-\alpha)T_u$.

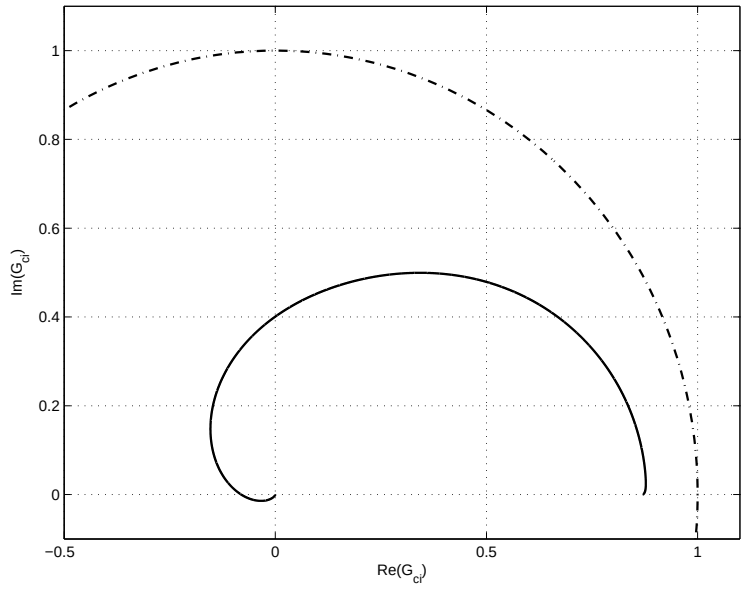

Figure 2.36: Nyquist plot of G_{ci} (solid line) compared to the unit circle (dash dotted line). The maximum value of $|G_{ci}|$ is 0.877.

The frequency of the main disturbance (24 Hz) is located at this area, so as to get a fast disturbance convergence speed, $(1-\alpha)T_u = 0$ is probably the best choice. Consequently, $\alpha = 1$, and then

$$K_{hp} = \frac{\omega_n^2}{K} \tag{2.95}$$

Furthermore, we hope to obtain a -20 dB reduction of the main harmonic component, which means

$$|H_{\text{cid}}(j48\pi)| = |S_{ci}(j48\pi)|\frac{|1-T_u|}{|1-G_{ci}(j48\pi)|} = 0.1. \tag{2.96}$$

Since z_n, ω_n and K_{hp} have been chosen, $T_u = 0.87$ can be calculated from Eq. 2.96.

With the SOM, we can confirm first that the used S_{ci} is stable. On the other hand, $T_{pi}P$ has too stable poles that $-6.08 \times 10^4 + j0$ and $2.6 \times 10^3 + j0$, so this term is stable as well. Therefore, the stability of this system can be presented by a Nyquist plot of G_{ci} as shown in Fig. 2.36, where the maximum $|G_{rc}|$ is 0.877, hence this designed system is stable.

Fig. 2.37 presents the reference tracking and the disturbance rejection performance of the designed system. The first Bode plot derived from $|H_{\text{cir}}|$ shows that the tracking behavior of this current iteration RC system is very close to its current feedback counterpart. Hence, tracking a step signal will probably lead to overshoots and oscillations. Besides, $|H_{\text{cir}}|$ in high frequencies (above 1000 Hz) is higher than $|H_{\text{cfr}}|$ shown in Fig. 2.15, indicating that this controller may result in a

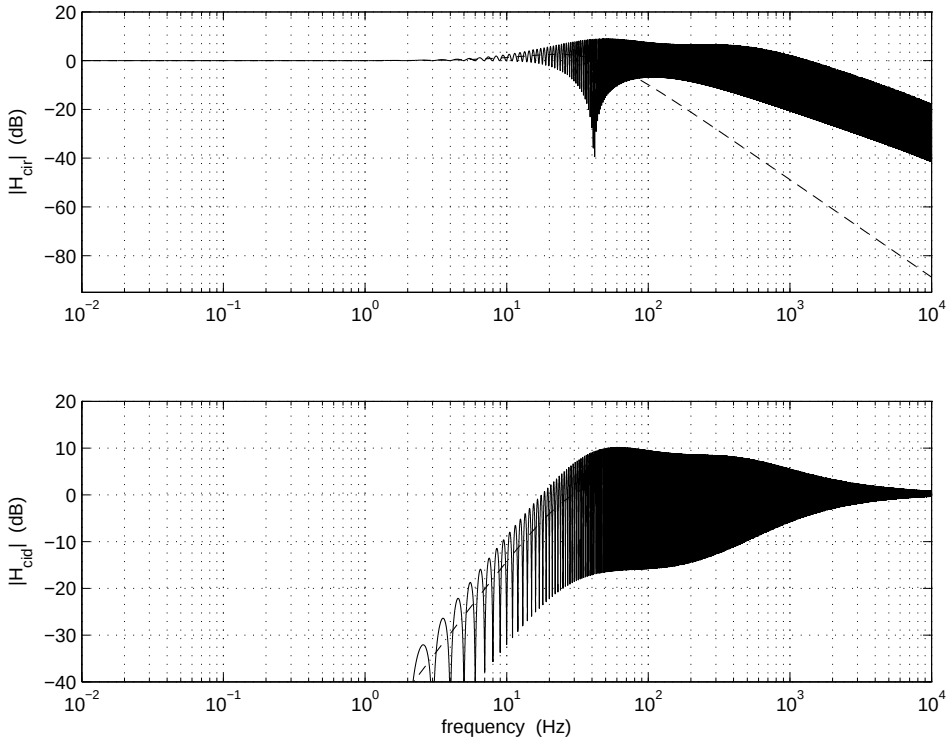

Figure 2.37: Bode magnitude plots of H_{cir} (in figure above, solid line) and H_{cid} (in figure below, solid line), compared to those obtained with an PI controller only (dash lines).

more serious oscillation problem. The second Bode plot derived from $|H_{\text{cid}}|$ shows $|H_{\text{cid}}(j48\pi)| = -20\,\text{dB}$, so the proposed controller is able to fulfill the required rejection. At the same time, we observe that the rejection obtained with this controller, as the current feedback one, is also a kind of periodic disturbance rejection. Hence, as the feedback repetitive controller, the current iteration repetitive controller significantly improves the system periodic disturbance rejection capability, however, it also degrades the tracking behavior and brings the risk of amplification of the noise.

A plot of $|G_{ci}(j\omega)|$ between 0 and $30\,\text{Hz}$ is shown in Fig. 2.38 to present the convergence speed. From this figure, we see that $|G_{ci}(j\omega)|$ in this area is not bigger than 0.2, therefore, all disturbance components considered in this case can converge to their steady-states in a very short time. Compared with the result obtained from the current feedback RC system, the current iteration repetitive controller with the proposed design is able to provide a much faster convergence speed than the current feedback one shown in section 2.5. This is another proof that it is not interesting to directly use Eq. 2.86 to get a current iteration controller. The stability robustness of this controller is also associated with S_{ci} and the closed-loop containing G_{ci}. S_{ci} is the same as previous ones, hence it can provide a quite good stability robustness. Consequently, the stability robustness of this proposed system is mainly determined by the RC part, and its robustness analysis is shown in Fig. 2.39. This result is

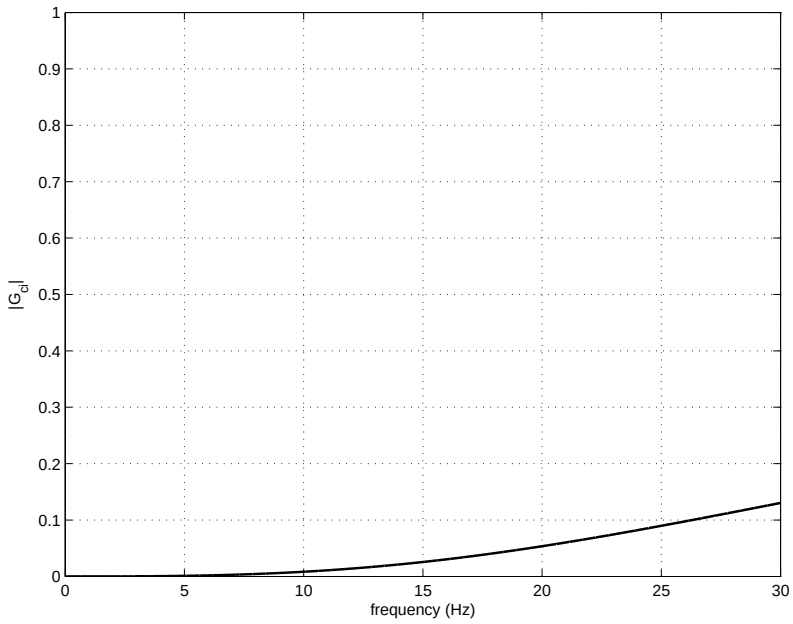

Figure 2.38: Plot of $|G_{ci}(j2\pi f)|$ indicating the convergence speed of sinusoidal disturbances with the designed basic repetitive controller.

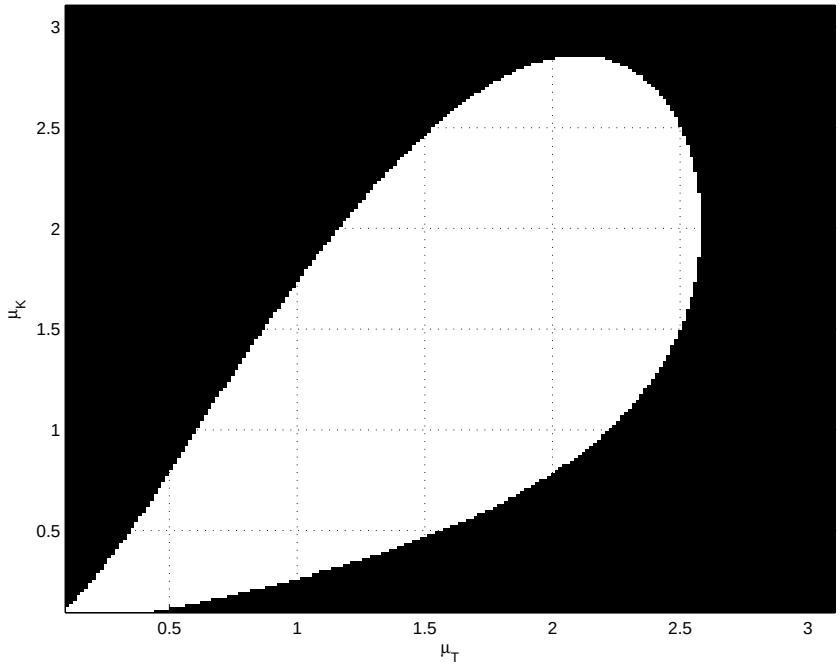

Figure 2.39: Stability robustness analysis of the current iteration RC system. As shown in Fig. 2.7, $\mu_K = K^{\text{real}}/K$ and $\mu_T = T_d^{\text{real}}/T_d$.

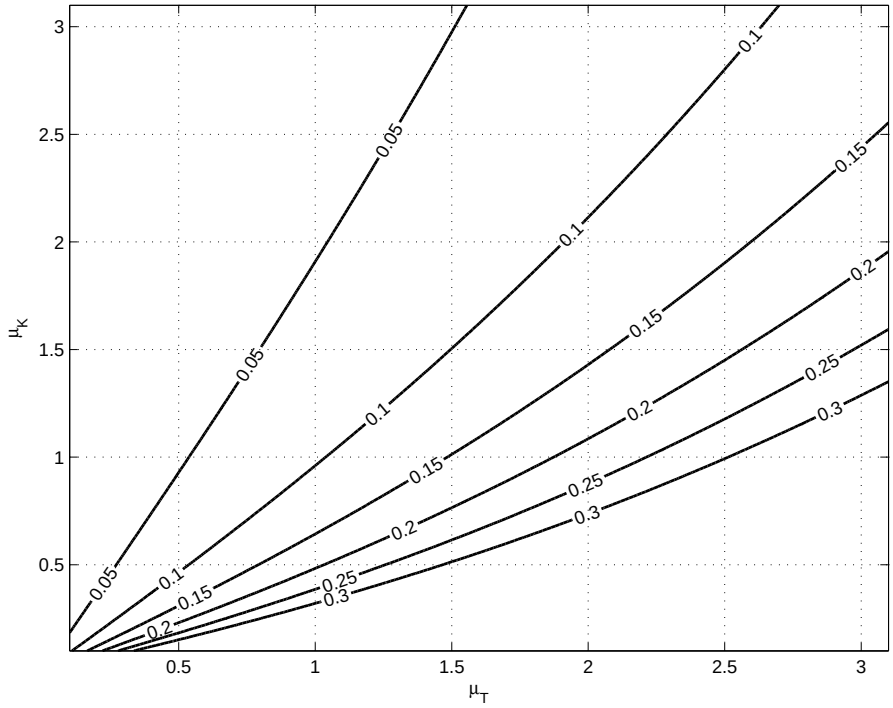

Figure 2.40: Main disturbance rejection robustness analysis of the current iteration RC system. As shown in Fig. 2.7, $\mu_K = K^{\text{real}}/K$ and $\mu_T = T_d^{\text{real}}/T_d$.

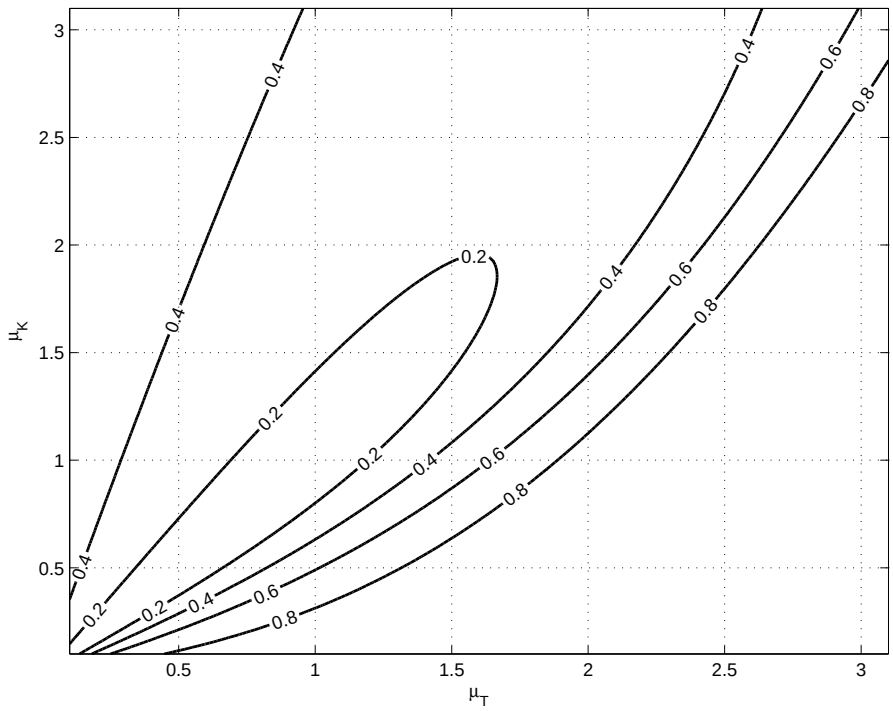

Figure 2.41: Main disturbance convergence speed robustness analysis of the current iteration RC system. As shown in Fig. 2.7, $\mu_K = K^{\text{real}}/K$ and $\mu_T = T_d^{\text{real}}/T_d$.

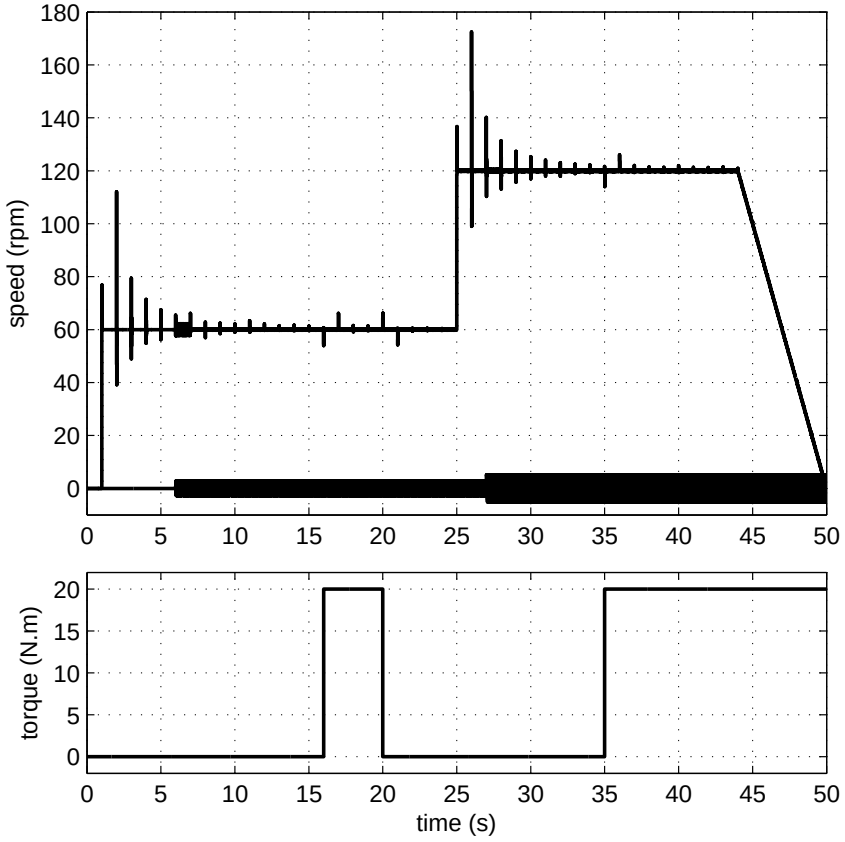

Figure 2.42: Simulation results showing how closed-loop system using a current iteration repetitive controller behaves with the same process, the same disturbances and the same reference as Fig. 2.21.

derived from Eq. 2.88 with considering the uncertain model P_{real}, which is defined in Eq. 2.48. As shown in Fig. 2.39, this system remains stable even with a $\pm 40\,\%$ uncertainty on K or T_d.

On the other hand, the performance robustness analysis of this system is shown in Fig. 2.40 and Fig. 2.41, which are derived from

$$|G_{ci}(j48\pi)| = \left|S_{ci}(j48\pi)T_u(1-T_{pi2}(j48\pi)P^{\text{real}}(j48\pi))\right| < 1, \tag{2.97}$$

$$|H_{cid}(j48\pi)| = |S_{ci}^{\text{real}}(j48\pi)|\frac{|1-T_u|}{|1-G_{cf}(j48\pi)|} \tag{2.98}$$

in which, S_{ci}^{real} is already defined in Eq. 2.70. From these figures, we can find that underestimating μ_T and overestimating μ_K at the same time will cause the largest rejection capability and reduction speed loss. In a word, with a variation smaller than $40\,\%$, this system will be still able to keep its stability and provide an adequate rejection capability, however, its convergence speed will be seriously reduced.

The time response of this designed current iteration RC system tested in the

same simulation used for the current iteration RC system is shown in Fig. 2.42. As its current feedback counterpart, for this system, tracking a step reference does not cause a steady-state error. Meanwhile, tracking a step reference, as shown in Fig. 2.42, leads to the overshoot and the damped oscillations, as the current feedback RC system. On the other hand, Fig. 2.42 shows that the proposed controller provides a quite good disturbance rejection ratio. When the disturbance contains the 24 th harmonic alone, the peak-to-peak value of the speed ripple of the current iteration system decreases from 6.2 to 0.8 rpm, and when the disturbance is made of the 8 th and the 24 th harmonic together, the peak-to-peak value of speed ripple reduces from 8.4 to 1 rpm. So in both situations, thanks to the current iteration repetitive controller, more than $85\,\%$ of speed ripple is removed. Besides, both reductions are accomplished in only two iterations, showing an impressive convergence speed. The analysis and results above draw a conclusion that the designed current iteration repetitive controller offers a much better disturbance rejection capability than its PI controller, at the same time, brings annoying overshoots that will limit its use for the PMSM torque ripple reduction. Hence, admittedly, there is lot of space available for the improvement of its tracking behavior.

2.6.4 Design methodology 2

In section 2.5.4, we have shown that choosing T_{pi2} as a constant is a simple solution to design a current feedback repetitive controller. In this section, we will show that using T_{pi2} as a constant is also a possible way to design a current iteration repetitive controller, but this kind of controller cannot provide the required performance.

First of all, when choosing T_{pi2} as a constant K_{pi} and using the leading-time component τ, the stability condition presented in Eq. 2.88 can be rewritten as

$$|G_{ci}(j\omega)| = \left|T_u S_{ci}(j\omega)(1-K_{pi}P(j\omega)e^{j\omega\tau})\right| < 1, \quad \forall\omega \in [0,+\infty[\tag{2.99}$$

Then following the design methodology presented in section 2.5.4, and from Eq. 2.81 and Eq. 2.82, we can first derive

$$|H_{\text{cid}}(j\omega_d)| = (1-T_u)\frac{|S_{ci}(j\omega_d)|}{|1-G_{ci}(j\omega_d)|}, \tag{2.100}$$

$$\text{thus} \quad |1-G_{ci}(j\omega_d)| = (1-T_u)\left|\frac{S_{ci}(j\omega_d)}{H_{\text{cid}}(j\omega_d)}\right|. \tag{2.101}$$

Then from a given $|H_{\text{cid}}(j\omega)|$ and a fixed T_u, according to the analysis in sec-

tion 2.5.4, we can deduce that

$$G_{ci}(j\omega_d) = 1-(1-T_u)\frac{|S_{ci}(j\omega_d)|}{|H_{\text{cid}}(j\omega_d)|} \tag{2.102}$$

$$\text{with } G_{ci}(j\omega_d) = T_u S_{ci}(j\omega_d)(1-K_{pi}e^{j\omega_d\tau}P(j\omega_d)). \tag{2.103}$$

To enable this choice, K_{pi} and τ should be chosen as

$$K_{pi}=|Z|, \text{ and } \tau=\frac{1}{\omega_d}\text{Arg}(Z), \tag{2.104}$$

$$\text{with } Z=K_{pi}e^{j\omega_d\tau}=\frac{1}{P(j\omega_d)}\left(1-\frac{1}{T_u(j\omega_d)S_{ci}(j\omega_d)}\left(1-(1-T_u)\frac{S_{ci}(j\omega_d)}{H_{cid}(j\omega_d)}\right)\right),$$

Finally, from Eq. 2.101, we find that $|H_{\text{rcd}}(j\omega_d)|$ cannot be chosen too small, since the condition $|G_{cf}(j\omega_d)|<1$ leads to

$$|H_{\text{rcd}}(j\omega_d)| > \frac{1-T_u}{2}|S_{ci}(j\omega_d)|. \tag{2.105}$$

Then, as in section 2.5.4, we first try $T_u=0.9$ and $|H_{\text{cid}}(j\omega_d)|=0.1$. The subsequent maximum value of $|G_{ci}|$ computed from Eq. 2.99 is 1.682, hence the stability of the system is not guaranteed. In order to get a stable system, we have to choose a smaller T_u. With the help of the Matlab, we find that only when T_u is ranged from 0.750 to 0.775, the system can provide the required reduction without losing its stability. As a result, we choose $T_u = 0.76$ (the resulting maximum value of $|G_{ci}|$ is 0.940), then from Eq. 2.104, we can compute that $K_{pi} = 34.91$ A·/rad and $\tau = 4.5$ ms. With these chosen parameters, a plot of $|G_{ci}(j\omega)|$ in Fig. 2.43 is used to show the convergence speed of different harmonic components. As shown in this figure, $|G_{cf}(j48\pi f)| = 0.9179$, hence the convergence of the main harmonic component will be very slow. Therefore, choosing T_{pi2} as a constant is not a good way to get an efficient current iteration repetitive controller.

2.7 Non-overshooting step response repetitive controller

The previous results show that, no matter in the basic RC system or in the current RC systems, a reference step can lead to overshoots and damped oscillations, which are unacceptable for many applications. Therefore, in this section, we propose a new repetitive controller that enables the RC system to be able to track a step reference without a large overshoot while still keeping the disturbance rejection capability as other RC systems. Before presenting this new controller and its control system, first, we need to review why these RC systems suffer from the bad transient tracking behavior.

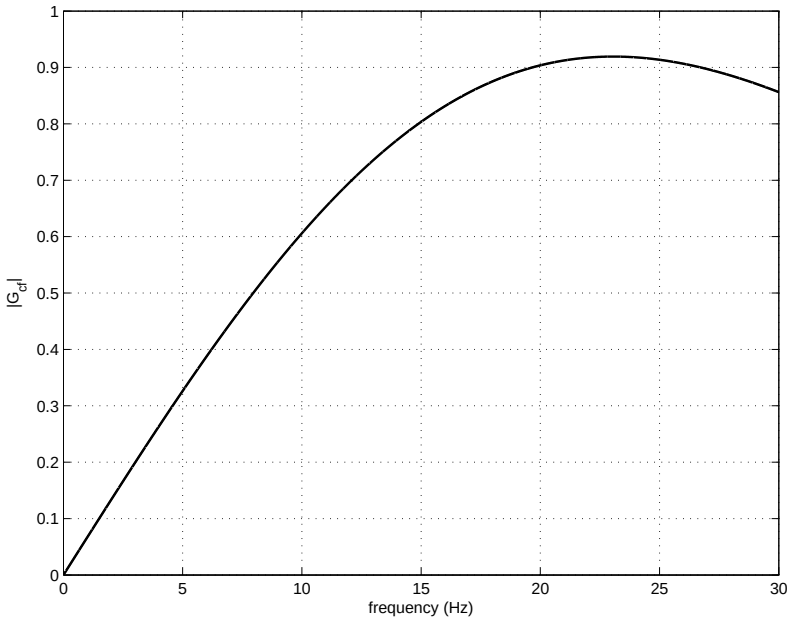

Figure 2.43: Plot of $|G_{ci}(j2\pi f)|$ indicating the convergence speed of sinusoidal disturbances with the designed basic repetitive controller.

The overshoot appearing in Fig. 2.21, Fig. 2.30 and Fig. 2.42, in fact, results from the zero of T_{ci} (T_{ci} was chosen as a PI controller in the previous cases), and the oscillations occurring in these cases are due to the direct transmission of the reference to T_{pi} and the closed-loop. As a result, to avoid them, one can first choose an IP controller, instead of a PI controller, as the conventional controller (relocating the proportional action from the direct path into the feedback loop [26]) and secondly connect T_{pi} to the process output only. Fig. 2.44 shows the system of the resulting controller, where the input of T_{pi} changes from e to y, but the input of T_u is unchanged. At the same time, a IP controller is used as its conventional controller. Since the goal of this controller is to provide a similar disturbance rejection capability with non-overshooting step response, this new repetitive controller is called non-overshooting step response (NOSR) repetitive controller.

From Fig. 2.44, the relationship between the system output y, the reference input $y_{\rm ref}$ and the disturbance d is

$$
\begin{aligned}
Y &= \frac{K_{is}s^{-1}PY_{\rm ref}+(1-T_u e^{-sT})P_2 D}{(1+K_{ps}P+K_{is}s^{-1}P)-(T_u-T_{pi}Pe^{s\tau})e^{-sT}} \\
Y &= H_{\rm nor}\,Y_{\rm ref}+H_{\rm nod}\,P_2\,D, \qquad (2.106)\\
\text{with } H_{\rm nor} &= \frac{S_{ci}\,K_{is}\,P}{s}\,\frac{1}{1-G_{no}\,e^{-sT}},\quad H_{\rm nod}=S_{ci}H_{\rm nod2},\\
H_{\rm nod2} &= \frac{1-T_u\,e^{-sT}}{1-G_{no}\,e^{-sT}},\quad G_{no}=G_{ci}=S_{ci}G_{rc},
\end{aligned}
$$

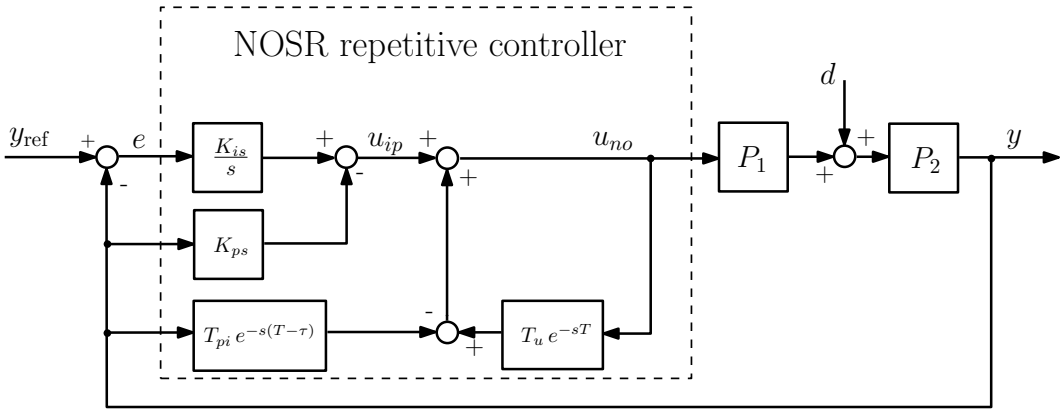

Figure 2.44: Block diagram of the plant controlled by the proposed NOSR repetitive controller (in our case, $u_{no} = i_{\text{qref}}$ and other symbols have the same definition as in Fig. 2.31).

which indicates that $S_{ci}(0) = 0$. From Eq. 2.53, the relationship between the error signal e, the reference input y_{ref} and the disturbance d is

$$\begin{aligned} E &= \frac{(1+K_{ps}P-(T_u-T_{pi}Pe^{s\tau})e^{-sT})Y_{\text{ref}}-(1-T_ue^{-sT})P_2D}{(1+T_{ci}P)-(T_u-T_{pi}Pe^{s\tau})e^{-sT}} \\ &= \frac{(1+K_{ps}P)S_{ci}-S_{ci}(T_u-T_{pi}Pe^{s\tau})e^{-sT}}{1-G_{no}e^{-sT}}Y_{\text{ref}}-\frac{1-T_ue^{-sT}}{1-G_{no}e^{-sT}}S_{ci}P_2D \\ &= \frac{(1+K_{ps}P)S_{ci}-G_{no}e^{-sT}}{1-G_{no}e^{-sT}}Y_{\text{ref}}-\frac{1-T_ue^{-sT}}{1-G_{no}e^{-sT}}S_{ci}P_2D \\ &= H_{\text{nod}}\,(Y_{\text{ref}}-P_2\,D)+H_{\text{noe}}\,Y_{\text{ref}}, \end{aligned} \tag{2.107}$$

$$\text{with}\;\; H_{\text{noe}} = S_{ci}\,\frac{(K_{ps}+T_{pi}\,e^{-s(T-\tau)})\,P}{1-G_{no}\,e^{-sT}}.$$

The subscript "no" used here represents the NOSR repetitive controller, and G_{rc} is defined in Eq. 2.8. The above equations show that $H_{\text{nod}} = H_{\text{cid}}$ and $G_{no} = G_{ci}$. As a result, this proposed NOSR system in fact has the same disturbance rejection capability as the current iteration RC system using a PI controller as T_{ci}.

According to Eq. 2.106, the proposed control system can similarly be presented as in Fig. 2.45, where the process is controlled by an IP controller and receives the filtered reference and disturbance. This figure shows that the closed-loop system will behave as with a conventional IP controller at low frequencies, since $G_{no} \approx 0$. But if T_u is chosen close to one, the first harmonics of the disturbance will additionally be reduced by the $1-T_ue^{-sT}$ term.

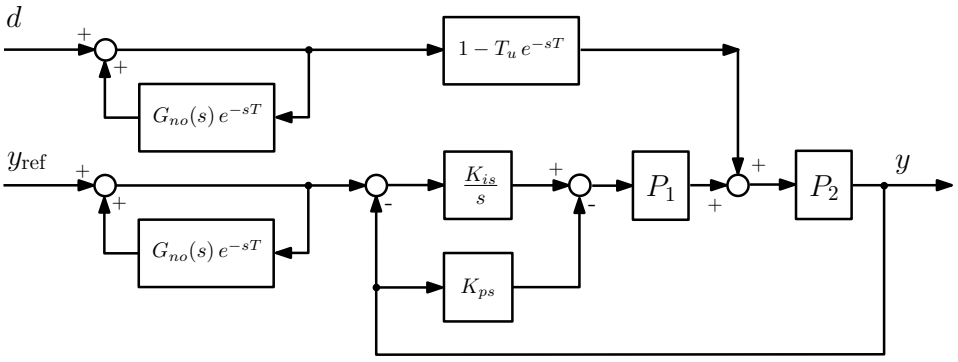

Figure 2.45: An alternative presentation of the NOSR RC system.

2.7.1 Stability and performance

Stability

Fig. 2.45 shows that the stability of the NOSR RC system is determined by three parts. The first one is a conventional IP control system, the second one is $1-T_u e^{-sT}$ and the third one is a closed-loop containing $G_{no}e^{-sT}$. Generally, an appropriate PI tuning method, such as SOM, can ensure the stability of the conventional IP control system and a constant T_u can lead to a stable $1-T_u e^{-sT}$. The stability of G_{no} is related to the choice of T_{pi2}. Provided that the IP conventional system, $1-T_u e^{-sT}$ and G_{no} are stable, according to the small gain theorem, the stability of this system can be guaranteed by

$$|G_{no}(j\omega)| = |S_{ci}(j\omega)G_{rc}(j\omega)| < 1, \quad \forall \omega \in [0, +\infty[\tag{2.108}$$

Reference tracking

Provided that the stability of this system is guaranteed, and the magnitude of a step signal is A and of a ramp signal is B, then from Eq. 2.107 and the final gain theorem, the error resulting from tracking a step signal is

$$e_{\text{step}}(\infty) = -\frac{G_{no}(0)}{1-G_{no}(0)}A. \tag{2.109}$$

Hence, only when $G_{no}(0) = 0$, tracking a step reference will not cause any steady-state error. On the other hand, the error arising from this ramp reference is

$$e_{\text{ramp}}(\infty) = \lim_{s\to 0} \frac{G_{no}(s)}{s(1-G_{no}(s))}B. \tag{2.110}$$

Therefore, only if $\lim_{s\to 0} G_{no}(s)/s = 0$, this system is able to track a ramp reference without any steady-state error.

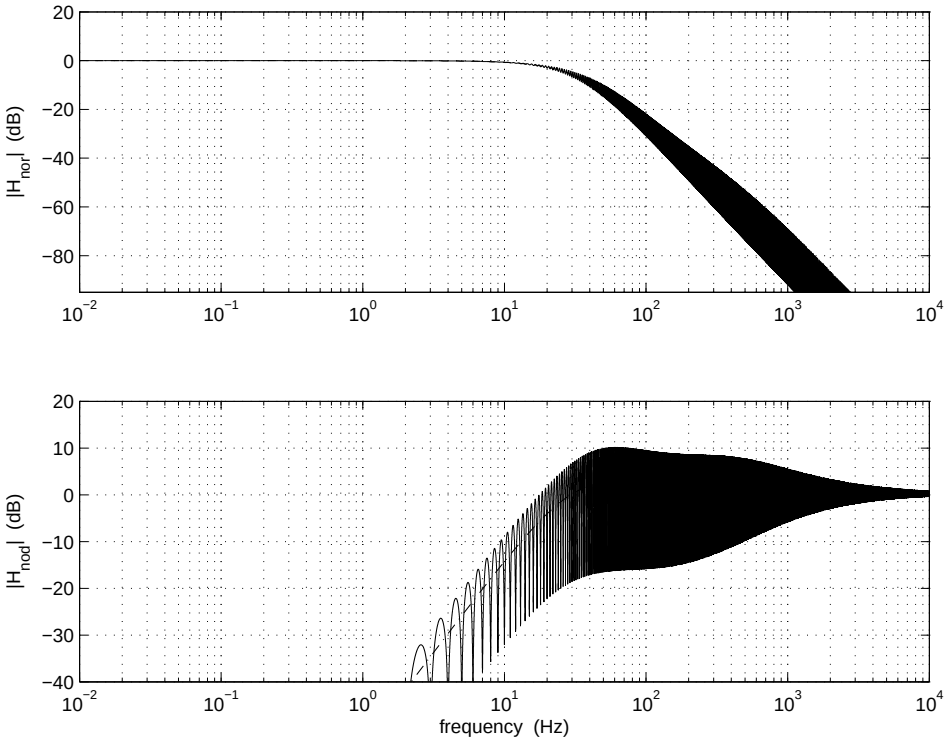

Figure 2.46: Bode magnitude plots of H_{nor} (above, solid line) and H_{nod} (below, solid line), compared to those obtained with an IP controller only (dash lines).

Disturbance rejection

The periodic disturbance rejection ratio and the convergence speed of a NOSR RC system are determined by $|H_{\mathrm{nod}}(j\omega_k)|$ and $|G_{no}(j\omega)|$ respectively. Besides, the load rejection capability of this system can be computed as

$$e_{\mathrm{load}}(\infty) = \left(\lim_{s\to 0} S_{ci}(s)P_2(s)\right) \frac{1-T_u}{1-G_{no}(0)} B_d. \tag{2.111}$$

Therefore, $\lim_{s\to 0} S_{ci}(s)P_2(s) = 0$ and $T_u = 1$ are two conditions that can enable this system to reject a load torque without any steady-state error.

2.7.2 Design methodology

In section 2.6, the proposed current iteration repetitive controller chose T_{ci} as a PI controller. Hence, based on the previous analysis, K_{ps}, K_{is}, T_u and T_{pi2} chosen for the current iteration system can be reused in this NOSR RC system. As a result, both systems will have exactly the stability and rejection capability. In section 2.6, we considered two kinds of controller design. The first one obviously provides much better performance than the second one, so it is chosen for the NOSR repetitive controller. Correspondingly, the result presented in Fig. 2.36, Fig. 2.38 and Fig. 2.39 derived from the current iteration RC system are still useful for this NOSR

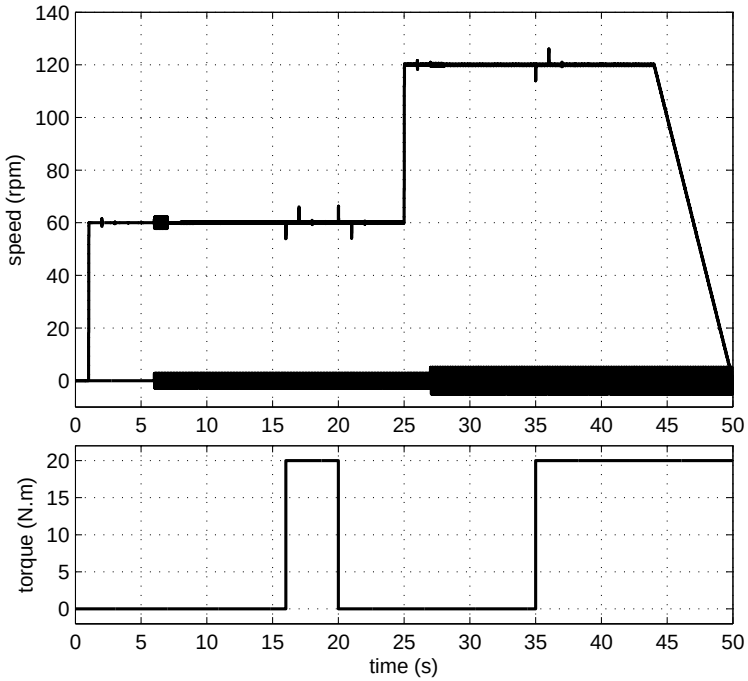

Figure 2.47: Simulation results showing how the closed-loop system using a NOSR repetitive controller behaves when the system contains periodic disturbances with the same process, the same reference and the same disturbance as in Fig. 2.21.

system to show its stability, its robustness and its periodic disturbance convergence speed. Therefore, it is not necessary to present these results and corresponding analysis again in this section. However, we still need to study its tracking performance in order to highlight the advantage of this controller.

To do this, primarily, the Bode plots of this new system with the proposed design shown in Fig. 2.46 are used to present its tracking performance. At the same time, the result derived from a conventional IP system with the same IP tuning is also shown in this figure as a reference. Fig. 2.46 shows that $|H_{\text{nor}}|$ is very close to one at low frequencies (since $H_{\text{nor}}(0) = 1$ and $H_{\text{nod}}(0) = H_{\text{noe}}(0) = 0$), does not have a resonance at low frequencies, and because the first term of H_{nor} in Eq. 2.106 has no zero and a third-order denominator, it decreases outside its bandwidth with a general trend of -60 dB/decade. Consequently, very few $|H_{\text{nor}}(j\omega)|$ are higher than 0 dB, indicating that this system probably can track a step signal without overshoots and oscillations. Fig. 2.46 also illustrates that at low frequencies, H_{nor} is very close to $S_{ci}K_iP/s$, the frequency response of the closed-loop system when using an IP controller only, since G_{no}, as shown in Fig. 2.38, increases very slowly as a function of the frequency. On the other hand, the comparison between Fig. 2.37 and Fig. 2.46 confirms that both systems have the same rejection capability. Therefore, the analysis above shows that the use of NOSR repetitive controller significantly improves

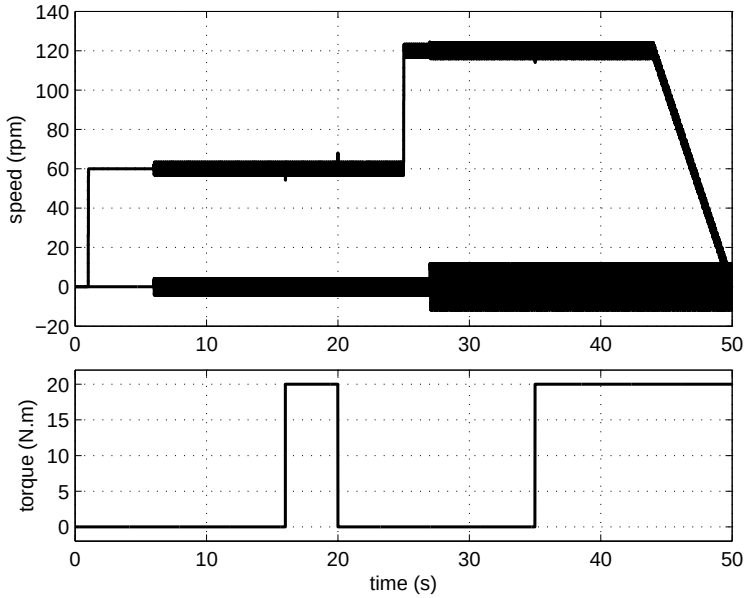

Figure 2.48: Simulation results showing how the closed-loop system using a IP controller behaves when the system contains periodic disturbances with the same process, the same reference and the same disturbance as in Fig. 2.21.

the reference tracking performance of the RC system, and it does not impair the disturbance rejection capability.

Fig. 2.47 shows a simulation of this system with the same reference and the same disturbance as in Fig. 2.42. Meanwhile, its IP counterpart is tested by the same simulation to provide comparative results. The comparison between Fig. 2.47 and Fig. 2.48 (showing the behavior of the closed-loop system when using an IP controller only) shows that the NOSR repetitive controller provides nearly the same responses to reference steps as its IP counterpart, but with a much better disturbance rejection. Meanwhile, the comparison between Fig. 2.47 and Fig. 2.42 shows that this new controller can offer a same rejection as its current iteration counterpart, but its tracking is much better. As a result, the NOSR repetitive controller is able to guarantee the tracking and rejection at the same time.

2.8 Conclusion

This chapter was dedicated to building a deep and comprehensive understanding of the RC technique, especially its particular disturbance reduction capability. At the same time, this chapter also made several original contributions that expand the scope of the RC technique. The beginning of this chapter presents the theoretical basis and a brief history of this technique, and shows the essential distinction between this technique and the ILC technique. Then the small gain theorem is pre-

Table 2.1: Characteristics of repetitive controllers

controller	reference tracking		
performance	steady-state error	delay	transient
basic	yes	yes	bad
current feedback	no	no	bad
current iteration	no	no	worst
NOSR	no	no	good
controller	disturbance rejection		
performance	load torque	convergence speed	rejection
basic	bad	bad	bad
current feedback	good	good	good
current iteration	good	best	good
NOSR	good	best	good

sented as a useful approach to derive a sufficient stability condition of RC systems. This chapter introduces two kinds of the repetitive controllers, the basic one and the current one. The analysis shows that the basic repetitive controller can provide an acceptable rejection capability, but owing to the absence of the current information, it brings an unavoidable delay and steady-state error, as well as an extremely weak constant disturbance rejection. Hence, we concluded that this basic repetitive controller cannot be chosen for the PMSM torque ripple reduction. According to this, two existing current repetitive controllers, the current feedback one and the current iteration one, are studied in this chapter. Both of them are developed from adding the current information into the basic repetitive controller. With the proposed designs, both current repetitive controllers are able to provide an impressive periodic disturbance rejection capability without the unwilling delay and steady-state error, as well as to improve the load-torque rejection capability. Several original design methodologies are proposed for these current repetitive controllers so as to gain a balance among the controller simplicity, the stability and the performance. However, these controllers are responsible for annoying oscillations that seriously impair the tracking behavior, lowering the interest of these controllers for the PMSM torque ripple reduction. In order to handle this problem, we proposed a new repetitive controller called the NOSR repetitive controller, which was developed from the current iteration repetitive controller. The corresponding theoretical analysis and the simulation show that the NOSR repetitive controller provides the desired disturbance rejection capability while offering a more delightful reference tracking behavior. The main characteristic of the studied repetitive controller are shown in Table. 2.1.

3

Repetitive Smart Sensor and Angle-based RC Technique

In this chapter, two original techniques, the repetitive smart sensor technique and the angle-based RC technique are introduced together in order to make the RC technique become a really applicable technique for common PMSM drives.

Both this report and the existing publications [7, 8, 11, 12] have shown that the success of using the RC technique in a PMSM drive is based on the modification of an existing controller. This, unfortunately, is hardly achievable for commercial systems. Therefore, the repetitive smart sensor, which adds a repetitive process into a conventional speed sensor, is proposed to reduce the difficulty of using of the RC technique. This sensor, using an integrated repetitive process, modifies the feedback information given by the conventional speed sensor, so it should be able to achieve the ripple reduction as a conventional repetitive controller. Thanks to this technique, the application of the RC technique in PMSM drives only needs a replacement of a conventional speed sensor by a repetitive smart one. Therefore, the first part of this chapter is devoted to introducing and studying this novel technique.

The potential of using the RC technique for the PMSM torque ripple reduction has been verified through the previous analysis. However, all successful reduction is achieved at a constant speed only. This is because the functionality of the RC technique requires the strict matching between the delay of the repetitive controller and the period of the target disturbance. This period is related to the rotor speed, so with a varying speed, this critical matching can hardly be maintained, resulting in the failure of the reduction. In almost all cases, PMSMs are designed for variable speed applications, so this feature of the RC technique is a serious problem that

makes its use for rotating machines somehow meaningless. To free its periodic disturbance reduction capability from a fixed speed, we propose a new RC technique called angle-based RC technique, which uses the mechanical angle instead of the time as the RC running variable. As concluded in the first chapter, torque ripples of PMSM are functions of the rotor position, hence no matter how the speed changes, the relationship between the torque ripple and the mechanical angle is always unchanged. Consequently, it is possible to use the angle-based technique to unlock the reduction capability of the RC from constant speeds. The second part of this chapter is dedicated to transferring this technique from an idea to a feasible solution.

3.1 Repetitive smart sensor technique

In the previous chapter, we have studied the basic repetitive controller and three current repetitive controllers, and then we concluded that to apply these repetitive controllers, the existing conventional controllers must be changed, or at least be modified. Unfortunately, in most cases, especially in commercial PMSM drives, the controller of PMSM drive is usually bought from other companies as well as configured in advance, hence altering the controller is already out of the question, and modifying the controller is also a tedious and complicated work. Therefore, it may be difficult to apply the RC technique for practical PMSM drives.

The repetitive smart sensor technique is proposed to provide a simpler way of using the RC technique in conventional PMSM drives. To pave the way to this technique, this section is organized as follows. The discussion starts from investigating the possibility to achieve this technique for the desired reduction and seeking a feasible approach to integrate the repetitive controller into a conventional speed sensor. Then, a comparison between the repetitive smart sensor and the current feedback repetitive controller is made to unveil its underlying connection with other RC techniques. Further, due to an inherent shortcoming of the proposed smart sensor technique, we provide an improved version of the repetitive smart sensor, analyzing its stability and performance. Finally, the design methodology of this repetitive smart sensor is offered, and its stability and performance robustness analysis are achieved at the end of this section.

3.1.1 The basis of the repetitive smart sensor

In conventional RC systems, repetitive controllers are used to take place of a conventional controller, so the reduction, in fact, is achieved by a modification of the controller output. For instance, in the current feedback RC system, due to the use of the current feedback repetitive controller, the controller output is no longer the output of the conventional controller u_{ci}, but is u_{cf}, as shown in Fig. 3.1, in which

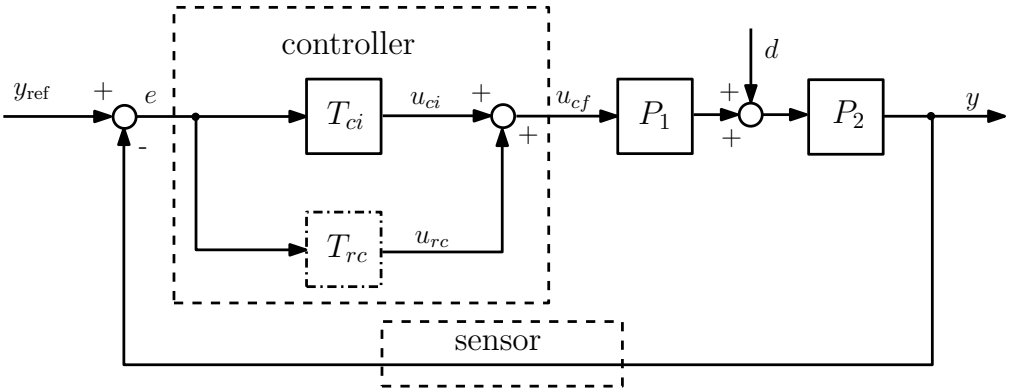

Figure 3.1: The simplified block diagram of the current feedback structure. Signals and blocks have the same meaning as in Fig. 2.12.

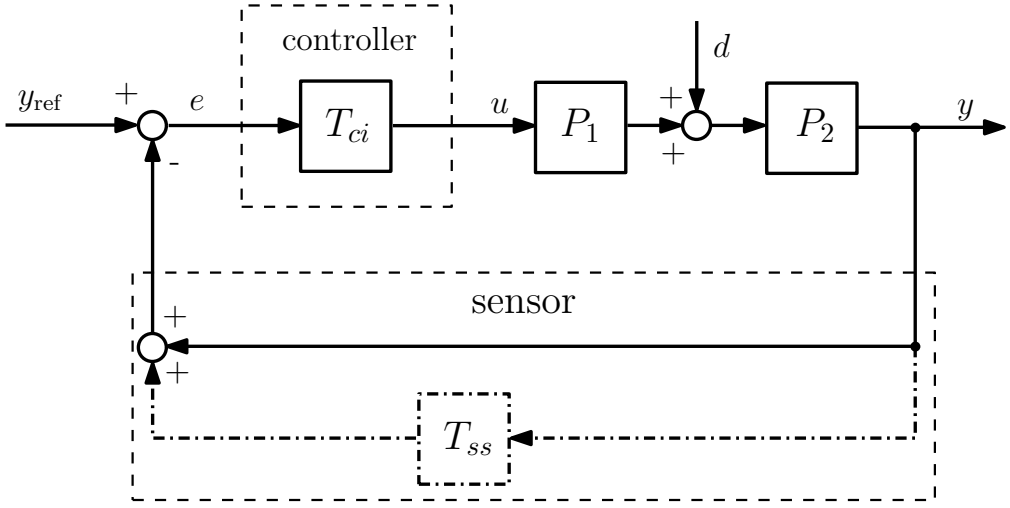

Figure 3.2: The block diagram of a PMSM drive installed with a repetitive smart sensor. Signals and blocks have the same meaning as in Fig. 2.12.

u_{cf} is the sum of u_{ci} and the output of the basic repetitive process (controller) u_{rc}.

In PMSM drives, the output of the conventional controller is usually deduced from the speed error, hence the modification of the controller output can be achieved not only through a modification of the conventional controller, but also by providing a modified feedback speed to the conventional controller. According to this, putting a repetitive process (a repetitive controller) into a speed sensor, is proposed to avoid the complicated controller modification. The structure of such kind of system is shown in Fig. 3.2. Then, this particular speed sensor developed by integrating a repetitive process into a conventional speed sensor is called repetitive smart sensor. Once the efficiency of this repetitive smart sensor is guaranteed, without changing or adjusting the existing controller, the torque ripple reduction can be easily achieved by using a repetitive smart sensor.

Naturally, we expect that the system using the repetitive smart sensor could

provide the same reduction capability as its conventional counterpart. To check the possibility of achieving this idea, firstly, from Fig. 3.1, we can deduce that

$$Y = \frac{(T_{ci}+T_{rc})P}{1+(T_{ci}+T_{rc})P}Y_{\text{ref}} + \frac{1}{1+(T_{ci}+T_{rc})P}P_2D \tag{3.1}$$

On the other side, from Fig. 3.2, we can derive that

$$Y = \frac{T_{ci}P}{1+(1+T_{ss})T_{ci}P}Y_{\text{ref}} + \frac{1}{1+(1+T_{ss})T_{ci}P}P_2D \tag{3.2}$$

Then, according to Eq. 3.1 and Eq. 3.2, two systems can provide the identical reduction once

$$(1+T_{ss})T_{ci} = T_{ci}+T_{rc} \tag{3.3}$$

is satisfied. This requires that T_{ss} should be chosen as

$$T_{ss} = T_{rc}/T_{ci} \tag{3.4}$$

This is the condition that can enable a smart sensor to offer the same reduction capability as its current feedback counterpart. With this condition, the design methodology proposed for the current feedback controller can probably be reused for this smart sensor. Furthermore, with this condition, Eq. 3.2 can be changed as

$$\begin{aligned} Y &= \frac{(T_{ci}+T_{rc}-T_{rc})P}{1+(T_{ci}+T_{rc})P}Y_{\text{ref}} + \frac{1}{1+(T_{ci}+T_{rc})P}P_2D \\ &= \left(\frac{(T_{ci}+T_{rc})P}{1+(T_{ci}+T_{rc})P} - \frac{T_{rc}P}{1+(T_{ci}+T_{rc})P}\right)Y_{\text{ref}} + \frac{1}{1+(T_{ci}+T_{rc})P}P_2D \end{aligned} \tag{3.5}$$

This equation shows that once T_{ss} is chosen as Eq. 3.4, the tracking behavior of the deduced smart sensor system would be different to its conventional analogue, because of the term $-T_{rc}P/(1+(T_{ci}+T_{rc})P)$.

As we know, to get the reduction, the input of the repetitive process (controller) must contain the disturbance (speed ripple) information, which, in conventional RC systems, comes from the difference between the given reference input (reference speed) and the measured process output (measured speed). Thus, to ensure the functionality of the repetitive smart sensor, this useful information (speed ripple) can be obtained with the same manner. Then following this idea, the structure of a closed-loop control system using a repetitive smart sensor is shown in Fig. 3.3, and correspondingly, this system is called repetitive smart sensor system [69]. It should be noted that this repetitive smart sensor is only the first version of this technique. The introduction and study of this smart sensor will be helpful to present

and understand another advanced repetitive smart sensor, which will be presented in section 3.1.2.

As shown in this figure, the proposed repetitive smart sensor consists of two parts, a conventional sensor and a repetitive process, and they are linked together with a quasi series connection. In this case, the repetitive process, in fact, is a basic repetitive controller. The input of the repetitive process (disturbance information) is directly deduced from $e = y_{\text{ref}} - y$, e_r is its output, and $y_f = y - e_r$ is the output of the repetitive smart sensor as well as $e_f = y_{\text{ref}} - y_f$ is the input of the conventional controller T_{ci}. From Fig. 3.3, we learn that to implement this repetitive smart sensor into a control system, first, a connection should be built between the reference input and the smart sensor; second, a digital chip, which is able to realize the function of the repetitive process, needs to be added into the conventional sensor (speed sensor) unit.

From Fig. 3.3, the relationship between the system output y, the reference input y_{ref} and the disturbance d

$$
\begin{aligned}
Y &= \frac{T_{ci}P(1-(T_u-T_{pi}e^{s\tau})e^{-sT})Y_{\text{ref}}+(1-T_ue^{-sT})P_2D}{(1+T_{ci}P)-(T_u(1+T_{ci}P)-T_{pi}T_{hp}T_{ci}Pe^{s\tau})e^{-sT}} \\
Y &= \frac{T_{ci}P(1-(T_u-T_{pi}e^{s\tau})e^{-sT})Y_{\text{ref}}+(1-T_ue^{-sT})P_2D}{(1+T_{ci}P)\left(1-\left(T_u-\frac{T_{pi}T_{hp}T_{ci}Pe^{s\tau}}{1+T_{ci}P}\right)e^{-sT}\right)} \\
Y &= H_{\text{ssr}}Y_{\text{ref}}+H_{\text{ssd}}P_2D, \qquad (3.6) \\
\text{with } H_{\text{ssr}} &= H_{ci}\frac{1-(T_u-T_{pi}\,e^{s\tau})e^{-sT}}{1-G_{ss}e^{-sT}}, \quad H_{\text{ssd}} = S_{ci}\,H_{\text{ssd2}}, \\
H_{\text{ssd2}} &= \frac{1-T_ue^{-sT}}{1-G_{ss}e^{-sT}}, \quad G_{ss} = T_u(1-H_{ci}T_{pi2}\,e^{s\tau}) \text{ and } H_{ci} = S_{ci}T_{ci}P,
\end{aligned}
$$

where the "ss" subscript means smart sensor, H_{ci} is the feedback loop transfer function when using the T_{ci} controller alone and S_{ci} is defined in Eq. 2.81. From Eq. 3.6 and Fig. 3.3, the relationship between the error signal e, the reference input y_{ref} and the disturbance d is

$$E = H_{\text{ssd}}(Y - P_2D). \qquad (3.7)$$

Since in the repetitive smart sensor system, the repetitive process merged inside a smart sensor is used in the feedback loop, the structure of this repetitive smart sensor system looks quite different from other RC systems. But the truth is that this control system is only a kind of current RC system. To better understand this, first of all, the smart sensor system presented in Fig. 3.3 can be rearranged as shown in Fig. 3.4, where the structure of the repetitive smart sensor system already looks like a current RC system. However, it uses the feedback information y twice, leading to

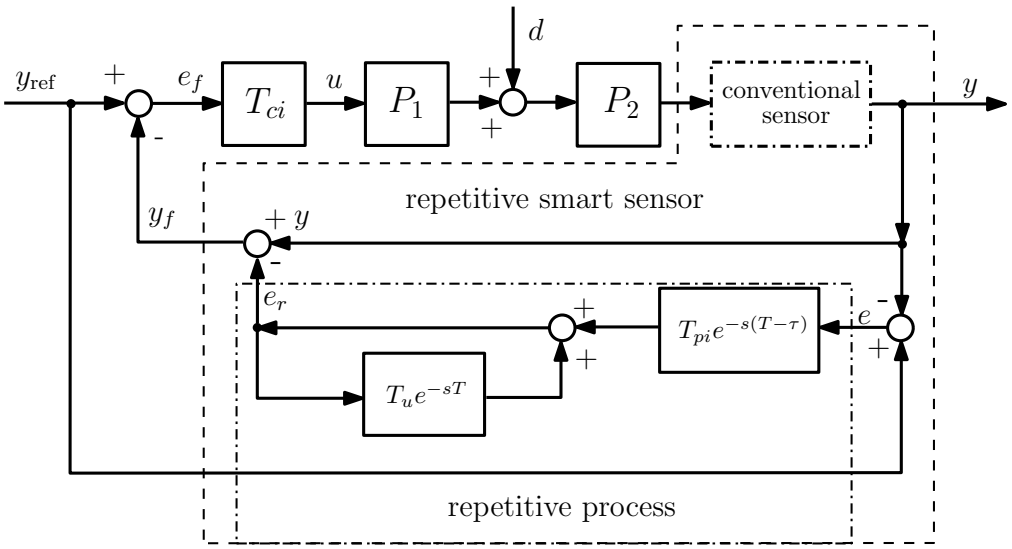

Figure 3.3: The block diagram of the repetitive smart sensor system. The repetitive process and the conventional sensor are shown in the dotted dash line box, and the repetitive smart sensor is shown in the dash line box. Signals and blocks have the same meaning as in Fig. 2.12.

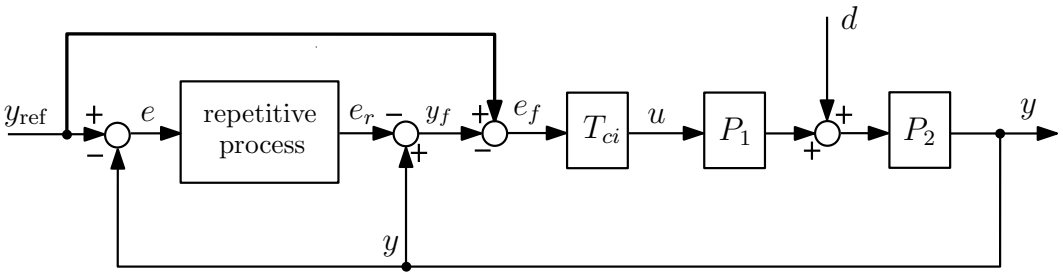

Figure 3.4: An equivalent block diagram of repetitive smart sensor system reorganized from Fig. 3.3

its particularity. Since

$$e_f = y_{\text{ref}} - y_f, \quad y_f = y - e_r \quad \text{and} \quad e = y_{\text{ref}} - y,$$

$$\text{thus,} \quad e_f = y_{\text{ref}} - y + e_r = e + e_r. \tag{3.8}$$

According to this equation, another equivalent presentation of this repetitive smart sensor system is shown in Fig. 3.5, in which the proposed repetitive smart sensor system is no more than a current RC system. Besides, the comparisons between Eq. 2.53 and Eq. 3.6, Eq. 2.54 and Eq. 3.7 show that, once $T_{ci} = 1$ in both systems, $G_{ss} = G_{cf}$, $H_{\text{ssd}} = H_{\text{cfd}}$ and $H_{\text{ssr}} = H_{\text{cfr}}$, indicating the similarity between this repetitive smart sensor system and the current feedback RC system.

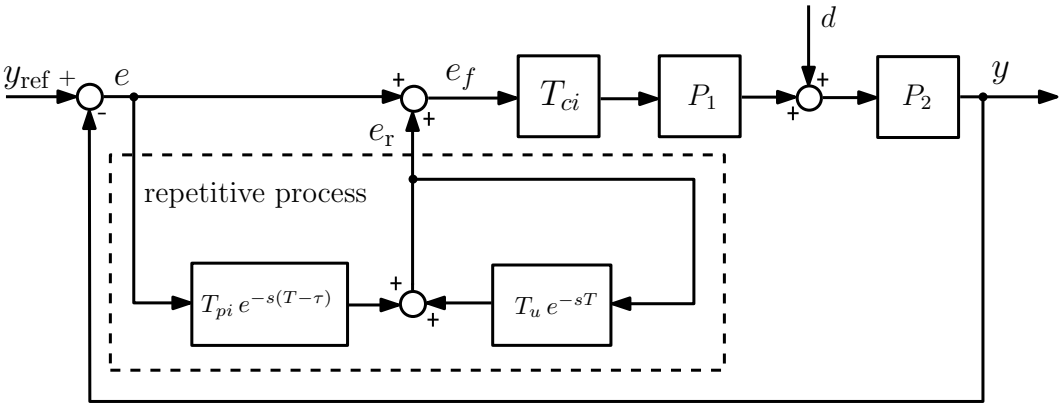

Figure 3.5: Another equivalent block diagram of repetitive smart sensor system changed from Fig. 3.4 and by Eq. 3.8, showing the detail of the repetitive smart process (in the dash line box).

3.1.2 Practical repetitive smart sensor

In the proposed repetitive smart sensor system, the repetitive process gets the speed ripple information from $y_{\text{ref}} - y$ directly. This means that to use the repetitive smart controller, a direct connection between this smart sensor and the reference input is necessary. However, in a commercial PMSM drive, such kind of connection generally cannot be given, so it seems almost impossible to apply this repetitive smart sensor for the PMSM torque ripple reduction. In order to avoid this annoying connection, we propose an improved repetitive smart sensor that is able to obtain the torque ripple information from the measured system output directly.

Basis of the practical repetitive smart sensor

As we know, when a PMSM system tracks a speed reference without steady-state error, the measured speed at steady-state generally consists of two components: the first one is a constant component that should be equal to the speed reference, and the other one is an oscillation (ripple) caused by the torque ripple. According to this, the speed ripple information can be obtained with a high-pass filter. The smart sensor equipped with a high-pass filter is able to keep its functionality without that direct connection, so it can be easily implemented in PMSM drives.

The typical structure of the control system using this smart sensor is shown in Fig. 3.6, in which T_{hp} stands for the high-pass filter. This figure shows that this new smart sensor is made of three parts: a conventional (speed) sensor, a high-pass filter and a repetitive process (a basic repetitive controller). In this smart sensor, the high-pass filter is able to extract an approximated disturbance (speed ripple) information y_{hp} from the captured feedback information (process output) y. Then, the output of the repetitive process e_r is deduced from y_{hp}. Then the output of this smart

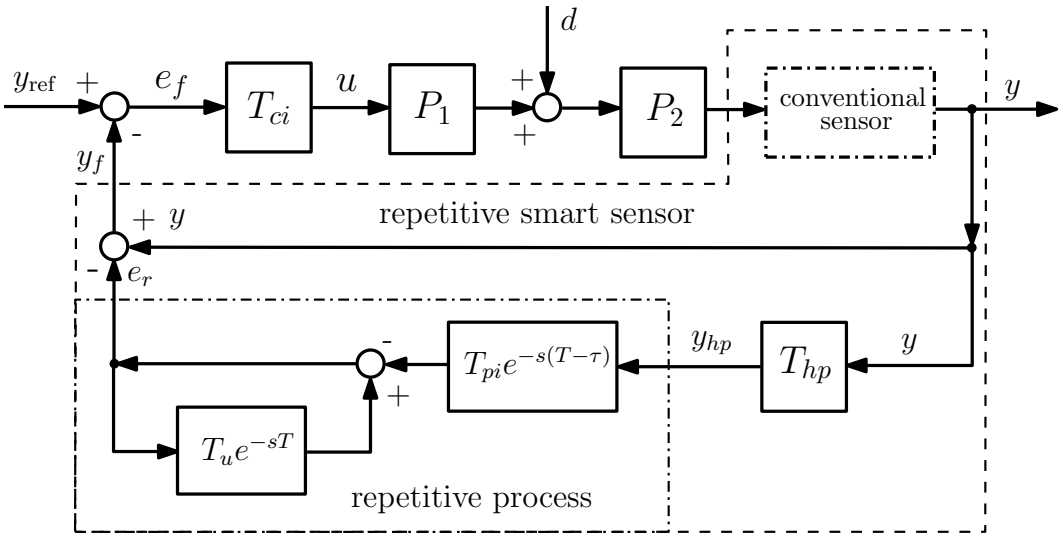

Figure 3.6: Another block diagram of a closed-loop system. The repetitive process and the conventional sensor are shown in the dotted dash line box, and the repetitive smart sensor is shown in the dash line box. In this case, signals and blocks have the same meaning as in Fig. 3.3).

sensor y_f consists of e_r and the raw process output. In order to distinguish this new version of the repetitive smart sensor from the former one, it is temporarily called practical smart sensor. The comparison between Fig. 3.3 and Fig. 3.6 shows that the main distinction between both repetitive smart sensors is their ways of getting the disturbance information. From Fig. 3.6, we can also observe that with this new repetitive smart sensor, the application of the RC technique will no more require any modification of the existing system, but will only need a simple replacement of the conventional speed sensor by a repetitive smart one. However, as the last one, the realization of this repetitive smart sensor requires also a digital chip to execute the function of both the high-pass filter and the repetitive process.

From Fig. 3.6, we can get the relationship between the system output y, the system reference input y_{ref} and the disturbance d

$$Y = \frac{(1-T_u e^{-sT})(T_{ci}PY_{\text{ref}}+P_2D)}{(1+T_{ci}P)-(T_u(1+T_{ci}P)-T_{pi}T_{hp}T_{ci}Pe^{s\tau})e^{-sT}}$$

$$Y = \frac{1-T_u e^{-sT}}{(1+T_{ci}P)\left(1-\left(T_u-\frac{T_{pi}T_{hp}T_{ci}Pe^{s\tau}}{1+T_{ci}P}\right)e^{-sT}\right)}(T_{ci}PY_{\text{ref}}+P_2D)$$

$$Y = H_{\text{psd}}\,(T_{ci}PY_{\text{ref}}+P_2D) = H_{\text{psr}}Y_{\text{ref}}+H_{\text{psd}}P_2D, \tag{3.9}$$

$$\text{with}\;\; H_{\text{psr}} = H_{ci}H_{\text{psd2}},\;\; H_{\text{psd}} = S_{ci}H_{\text{psd2}},\;\; H_{\text{psd2}} = \frac{1-T_u e^{-sT}}{1-G_{ps}e^{-sT}}$$

$$\text{and}\;\; G_{ps} = T_u - H_{ci}\,T_{pi}\,T_{hp}\,e^{s\tau},$$

where the "ps" subscript stands for the repetitive practical smart sensor and H_{ci} is defined in Eq. 3.6. Comparing G_{ps} with G_{ss}, we can find that the difference between them stems from the use of the high-pass (T_{hp}) in the practical smart sensor. The relationship between the error signal e, the reference input y_{ref} and the disturbance d is

$$\begin{aligned} E &= \frac{(1-T_u e^{-sT}+T_{pi}\,T_{hp}\,T_{ci}P\,e^{-s(T-\tau)})Y_{\text{ref}}-(1-T_u e^{-sT})P_2 D}{(1+T_{ci}P)(1-G_{ps}e^{-sT})} \\ E &= \frac{1-T_u e^{-sT}}{(1+T_{ci}P)(1-G_{ps}e^{-sT})}(Y_{\text{ref}}-P_2 D)+\frac{T_{pi}\,T_{hp}\,T_{ci}\,Pe^{-s(T-\tau)}}{1-G_{ps}e^{-sT}}Y_{\text{ref}} \\ E &= H_{\text{psd}}(Y_{\text{ref}}-P_2 D)+\frac{H_{\text{psr}}\,T_{pi}\,T_{hp}\,e^{-s(T-\tau)}}{1-T_u e^{-sT}}Y_{\text{ref}}. \end{aligned} \tag{3.10}$$

As a kind of RC system, the stability and performance of this system can be obtained as before. Hence, provided that S_{ci} and G_{ps} are stable, a sufficient stability condition for this system derived from the small gain theorem is

$$|G_{ps}(j\omega)|<1,\ \ \forall\omega\in[0,+\infty[\tag{3.11}$$

Provided that the system is stable, then from Eq. 3.10, the steady-state errors of this system caused by tracking a step $A\cdot\Gamma(t)$ and a ramp signal $B\cdot t\cdot\Gamma(t)$ are calculated by

$$\begin{aligned} &e_{\text{step}}(\infty)= \\ &\qquad\left(S_{ci}(0)(1-T_u)+\lim_{s\to 0}T_{hp}(s)T_{ci}(s)T_{pi}(s)S_{ci}(s)P(s)\right)\frac{A}{1-G_{ps}(0)}, \end{aligned} \tag{3.12}$$

and

$$\begin{aligned} &e_{\text{ramp}}(\infty)= \\ &\left((1-T_u)\left(\lim_{s\to 0}\frac{S_{ci}(s)}{s}\right)+\left(\lim_{s\to 0}\frac{T_{hp}(s)T_{ci}(s)T_{pi}(s)S_{ci}(s)P(s)}{s}\right)\right)\frac{B}{1-G_{ps}(0)} \end{aligned} \tag{3.13}$$

Besides, as a kind of the RC system, the periodic disturbance rejection ratio of this system is $|H_{\text{psd}}(j\omega_k)|$ and its convergence speed is $|G_{ps}(j\omega)|$. In addition, provided that the magnitude of the load torque is B_d, the steady-state error resulting from this load torque is computed as

$$e_{\text{load}}(\infty)=H_{\text{psd}}(0)=\left(\lim_{s\to 0}S_{ci}(s)P_2(s)\right)\frac{1-T_u}{1-G_{ps}(0)}B_d. \tag{3.14}$$

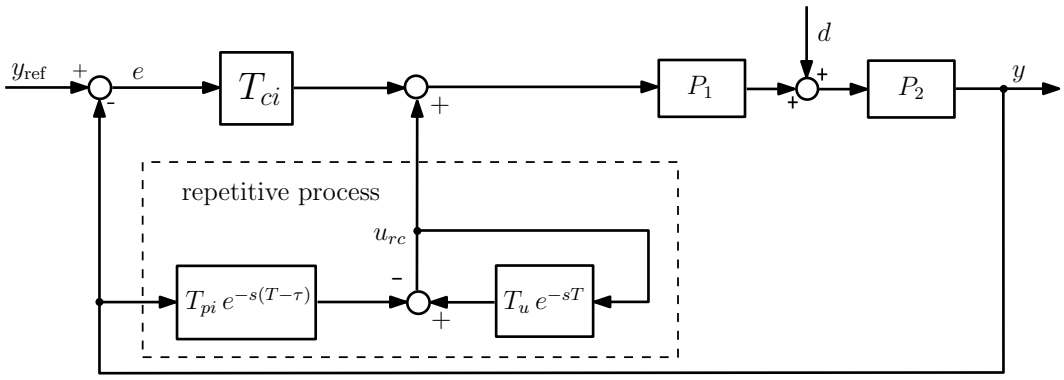

Figure 3.7: The block diagram of a closed-loop system controlled with a particular repetitive controller.

Repetitive smart sensor design

In this thesis, this smart sensor is deemed to provide the same the reduction capability as its current feedback counterpart. To achieve this aim, according to the analysis presented at the head of this section, we need $T_{ss} = T_{rc}/T_{ci}$ for the systems shown in Fig. 3.1 and Fig. 3.2. The comparison between Fig. 2.12 and Fig. 3.1 shows $T_{rc} = T_{pi}e^{-(T-\tau)}/(1 - T_u e^{-sT})$ in a current feedback system. On the other hand, the comparison between Fig. 3.2 and Fig. 3.6 shows $T_{ss} = T_{hp}T_{rc}$ in a practical smart sensor. Then according to Eq. 3.4, we can deduce that with $T_{hp} = 1/T_{ci}$, H_{cdf} becomes equal to H_{psd}. As a result, the design methodology chosen for the current feedback controller probably can be also applied for the practical repetitive smart sensor. In Chapter 2, two design methodologies were proposed for the current feedback repetitive controller. For the sake of simplicity, the second design methodology is reused here to design the practical repetitive smart sensor. Since in chapter 2, T_{ci} is a PI controller, then to make $T_{hp} = 1/T_{ci}$, T_{hp} should be

$$T_{hp} = \frac{s}{K_{is} + sK_{ps}}. \tag{3.15}$$

Here also, T_u and T_{pi} are chosen as constants, $K_{pi} = T_{pi}/T_u$ and τ are derived from a desired value of $|H_{\text{psd}}(j\omega_d)|$ by Eq. 2.78. If the same process and the same rejection target used in the current feedback RC system are also considered for this system, the repetitive process parameters should be the same as those of the last one.

However, even if $T_{hp}T_{ci} = 1$ is satisfied, H_{cfr} and H_{psr} as indicated at the beginning of this section will still be different, so these systems will have different tracking behaviors. According to Eq. 3.12 and Eq. 3.14, it is not difficult to deduce that this repetitive smart sensor system, as its current feedback counterpart, can track a step and reject a load torque without any steady-state error. On the other hand, when its tracks the ramp signal $B \cdot t \cdot \Gamma(t)$, according to Eq. 3.13, the

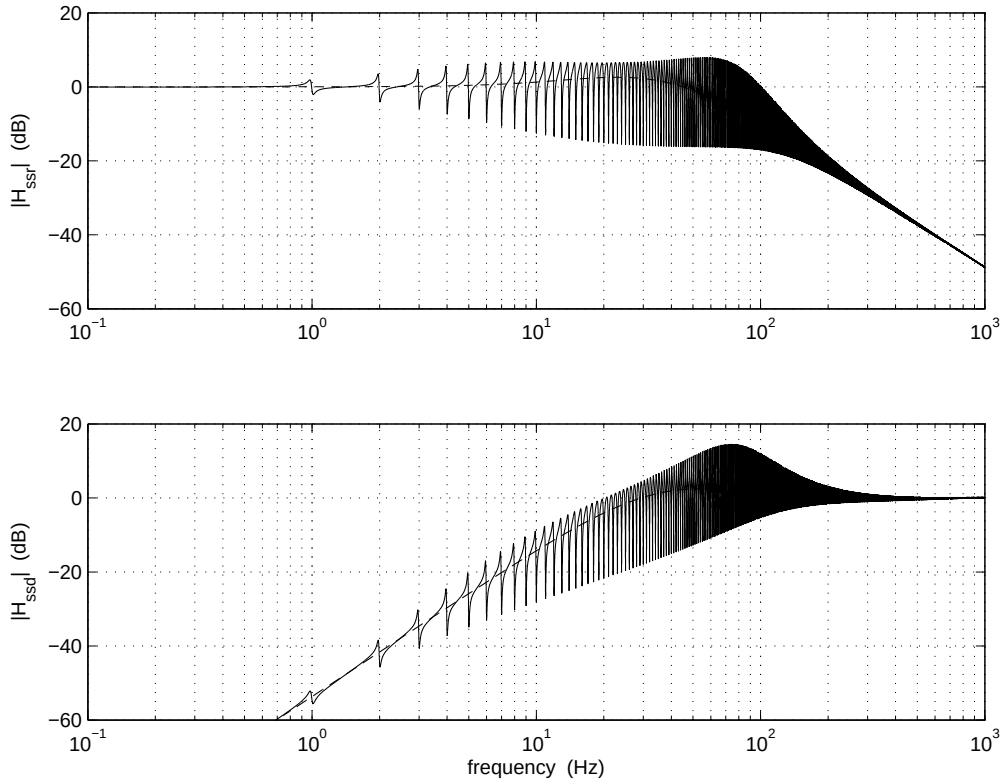

Figure 3.8: Bode magnitude plots of $H_{\rm psr}$ (in figure above, solid line) and $H_{\rm psd}$ (in figure below, solid line), compared to those obtained with a PI controller only (dash dotted lines).

subsequent steady-state error will be $K_{pi}B/K_{is}/(1-T_u)$.

In order to investigate the tracking capability of the proposed smart sensor system, the Bode magnitude plots of $H_{\rm psr}$ and $H_{\rm psd}$ based on the chosen parameters are shown in Fig. 3.8. From Eq. 3.9, one can deduce that

$$H_{\rm psd2}(0)=1 \;\text{ and }\; \lim_{\omega\to+\infty} H_{\rm psd2}(j\omega)=1. \tag{3.16}$$

Therefore, $H_{\rm psr}$ and H_{ci} have the same magnitude plots at low and high frequencies, as clearly illustrated by this figure. Additional resonances appear between 1 and 200 Hz, that may cause overshoots during transients.

The time response of the designed system using the repetitive smart sensor with the same simulation used in Chapter 2 is shown in Fig. 3.9, where we can see that the rejection behavior of this system is exactly the same as the current feedback controller. However, these systems obviously have different transient responses. This may be justified by a relationship between $H_{\rm psr}$ and $H_{\rm cfr}$ when $G_{cf}=G_{ps}$,

$$H_{\rm psr}=H_{\rm cfr}-\frac{S_{ci}T_{pi}e^{-s(T-\tau)}P}{1-G_{cf}e^{-sT}}. \tag{3.17}$$

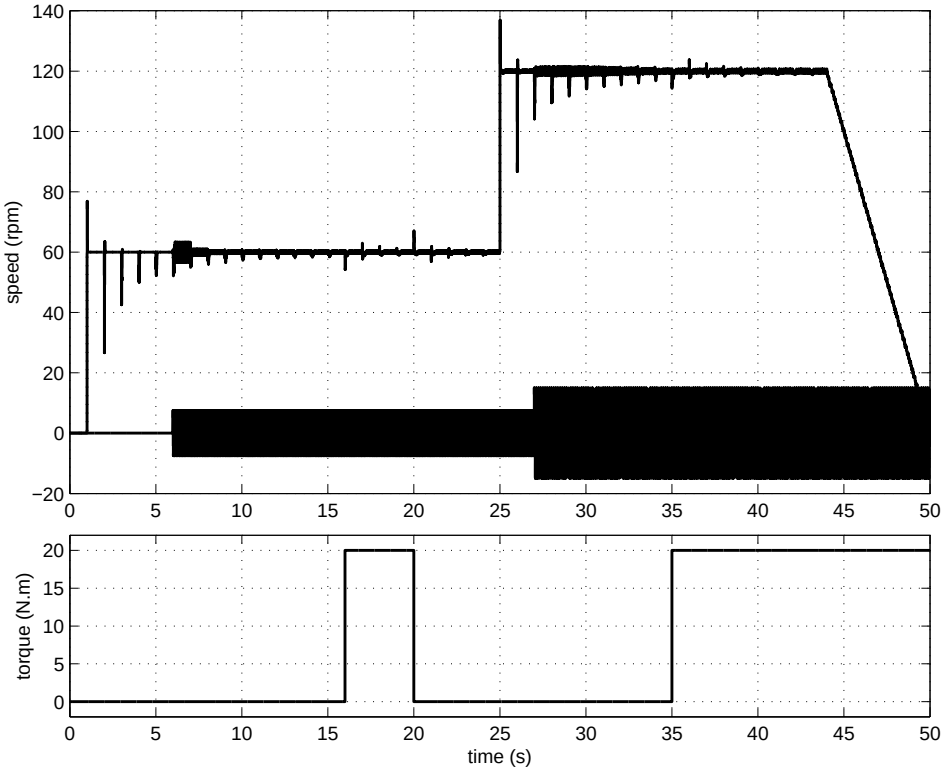

Figure 3.9: Simulation results showing how the closed loop system using a practical repetitive smart sensor behaves, with the same process, the same disturbances and the same reference as in Fig. 2.42.

The complementary term $H_{\text{psr}} - H_{\text{cfr}}$ is responsible for the negative overshoots appearing in Fig. 3.9.

With the proposed repetitive smart sensor technique, the use of the RC technique in PMSM drive no longer requires the modification of the existing controller. However, according to this proposed design, one still needs to know the conventional controller (T_{ci}, in our case, is a PI controller) so as to guarantee the stability and the efficiency of the repetitive smart sensor. Such kind of information might be learned from the controller manufacturer (supplier), but the errors between the real value of the controller parameters and the given ones may happen. As a result, it is important to know whether the proposed repetitive smart sensor can ensure the stability and provide the desired disturbance reduction with an uncertain T_{ci}. These two questions can be answered by a stability and a performance robustness analysis respectively.

To study the robustness analysis, first of all, an uncertain PI controller T_{ci} can be presented as

$$T_{ci}^{\text{real}}(j\omega) = K_{ps}^{\text{real}} + \frac{K_{is}^{\text{real}}}{j\omega}, \quad \text{with} \quad K_{ps}^{\text{real}} = \mu_{\text{Kps}} K_{ps} \quad \text{and} \quad K_{is}^{\text{real}} = \mu_{\text{Kis}} K_{is}, \quad (3.18)$$

in which the superscript “real” indicates the real value of the parameters, K_{ps} and

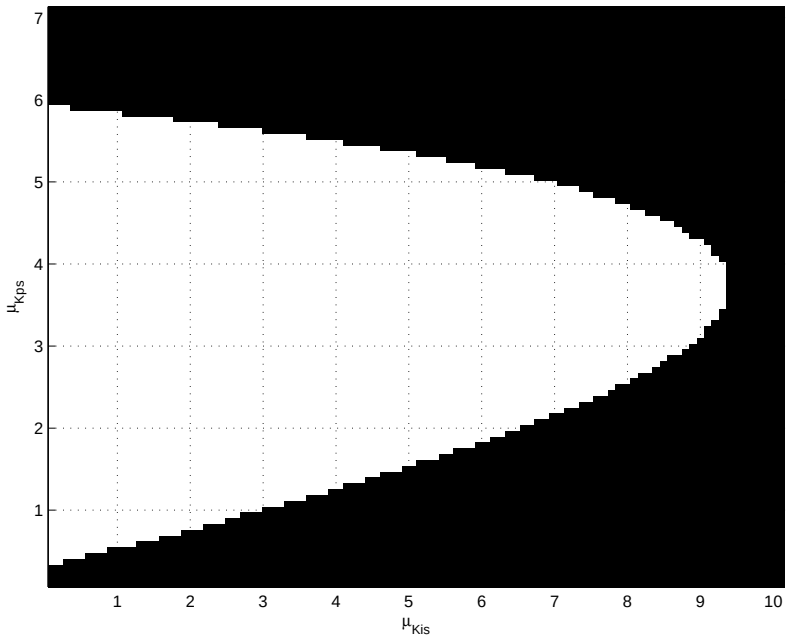

Figure 3.10: Stability robustness analysis of the practical smart sensor system.

K_{is} are the given values, which are used to calculate the high-pass filter and the parameters of the repetitive process. μ_{Kps} and μ_{Kis} indicate the divergence between the real and supposed values.

Then from Eq. 3.11 and Eq. 3.18, the stability condition of the system with an uncertain T_{ci} can be presented as

$$|G_{ps}^{\text{real}}(j\omega)| = |T_u \left(1 - K_{pi} H_{ss}^{\text{real}}(j\omega) e^{j\omega\tau}\right)|, \tag{3.19}$$

$$\text{with} \;\; H_{ss}^{\text{real}}(j\omega) = S_{ci}^{\text{real}}(j\omega) T_{ci}^{\text{real}}(j\omega) P(j\omega)$$

$$\text{and} \;\; S_{ci}^{\text{real}}(j\omega) = \frac{1}{1 + T_{ci}^{\text{real}}(j\omega) P(j\omega)}.$$

The stability robustness of this system deduced from Eq. 3.19 is shown in Fig. 3.10, in which $|G_{ps}^{\text{real}}| < 1$ is represented by a white color and $|G_{ps}^{\text{real}}| \geq 1$ is represented by black color. As shown in Fig. 3.19, overestimation of K_{is} and underestimation of K_{ps} simultaneously will be the main threat to the stability, but generally speaking, with $50\,\%$ uncertainty of K_{ps} and K_{is}, the system can still remain stable, showing an acceptable stability robustness.

On the other hand, to study the performance robustness analysis, according to Eq. 3.18 and Eq. 3.19, we can deduce that

$$|H_{\text{psd}}(j\omega_d)| = \left| S_{ci}^{\text{real}}(j\omega_d) H_{\text{psd2}}^{\text{real}}(j\omega_d) \right|, \tag{3.20}$$

$$\text{with} \;\; H_{\text{psd2}}^{\text{real}}(j\omega_d) = \frac{1 - T_u}{1 - G_{ps}^{\text{real}}(j\omega_d)}.$$

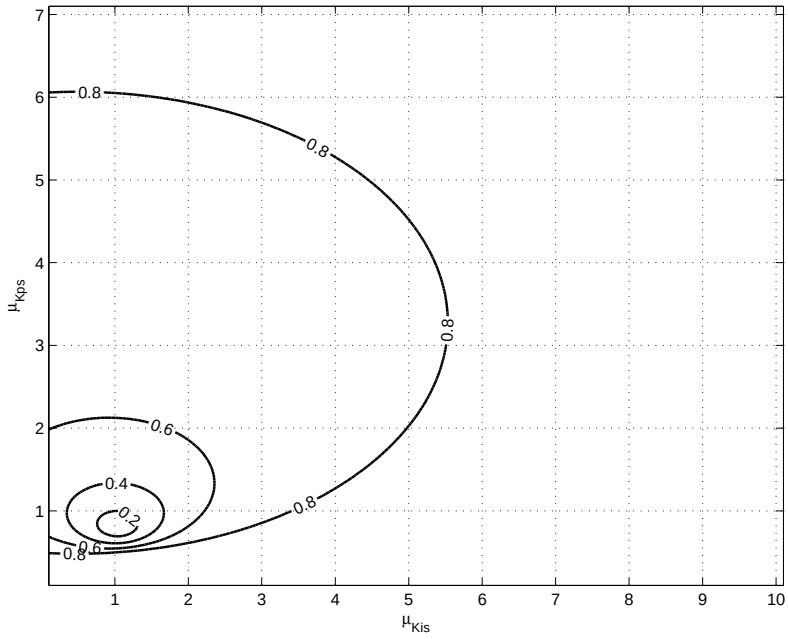

Figure 3.11: Main disturbance convergence speed robustness analysis of the practical smart sensor system.

As the previous cases, the variation of the convergence speed $|G_{ps}(j\omega_d)|$ and the reduction $|H_{\mathrm{psd}}(j\omega_d)|$ are considered here to judge the performance robustness of the proposed repetitive smart sensor. The results about the convergence speed deduced also from Eq. 3.19 are shown in Fig. 3.11, which illustrates that the convergence speed is rather sensitive to the variation of the PI parameters. With almost 50% divergence, $|G_{cf}(h\omega_d)|$ will increase from 0.2 to 0.6, leading to an important loss of the convergence speed. On the other hand, the result of the main harmonic component reduction derived from Eq. 3.20 is shown in Fig. 3.12. From this figure, we can observe that in the stable area (shown in Fig. 3.10), the rejection capability obtained with this repetitive smart sensor remains at a very good level. Since the convergence speed determines only the duration of the transient, once the harmonic has been reduced to its steady-state, the convergence speed is not important any more. Then, considering its good main disturbance rejection robustness, we can say that this system is able to keep its stability while providing an interesting disturbance rejection capability with a $50\,\%$ variation of K_{ps} and K_{is}. As a result, the application of this proposed repetitive smart sensor does not need a very precise knowledge about the conventional controller (PI controller).

Summarizing the above analysis, we conclude that the repetitive smart sensor with the proposed design and the high-pass filter is a useful technique that offers an easier way to use the RC technique for the PMSM torque ripple reduction. Besides, since only the practical repetitive smart sensor can really be applied in PMSM drives, hereafter, without any particular indication, the repetitive smart sensor is re-

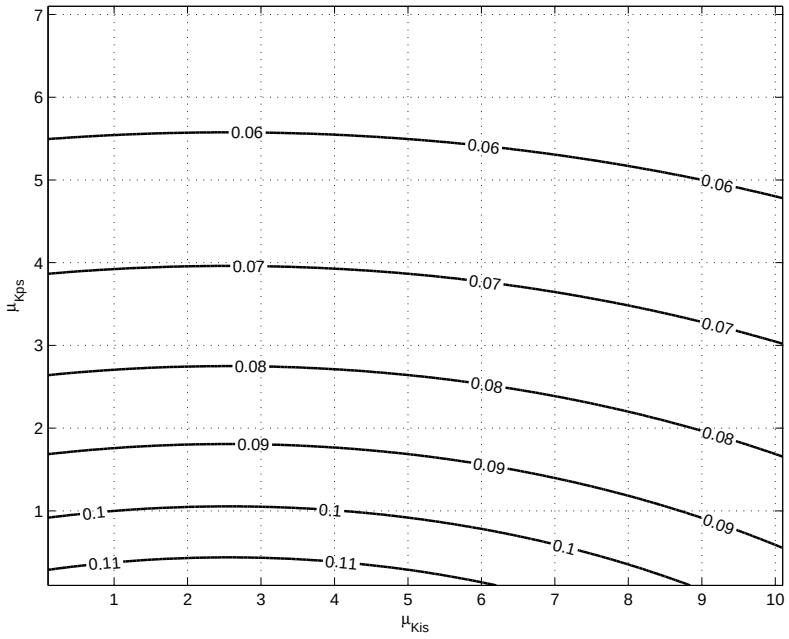

Figure 3.12: Main disturbance reduction robustness analysis of the practical smart sensor system.

ferred to the practical one.

3.2 Angle-based RC technique

The head of this chapter has mentioned that the varying speed is a vital hindrance that excludes nearly all possibilities of using the RC technique for common PMSM drives. The angle-based RC technique, which is able to awake the potential of the reduction capability of the RC technique from a fixed speed, is proposed to change the landscape of the RC technique applications. To put this technique into practice, the rest of this section is organized as follows. First, the answer to why the existing RC techniques are not able to handle the torque ripple reduction in varying speeds is given by an analysis of the basic working principle of the repetitive controller. Second, the feasibility of the angle-based RC technique is presented, regarding to the fixed relationship between the torque ripples and the rotor position. Third, the way of implementing the angle-based RC technique into a control system is introduced. Fourth, to guarantee the availability of this technique, the stability condition and the performance of the angle-based repetitive controller are analyzed, meanwhile a speed-based design methodology is also proposed for an angle-based repetitive controller. Finally, two simple solutions are proposed to improve the tacking behavior of angle-based RC systems.

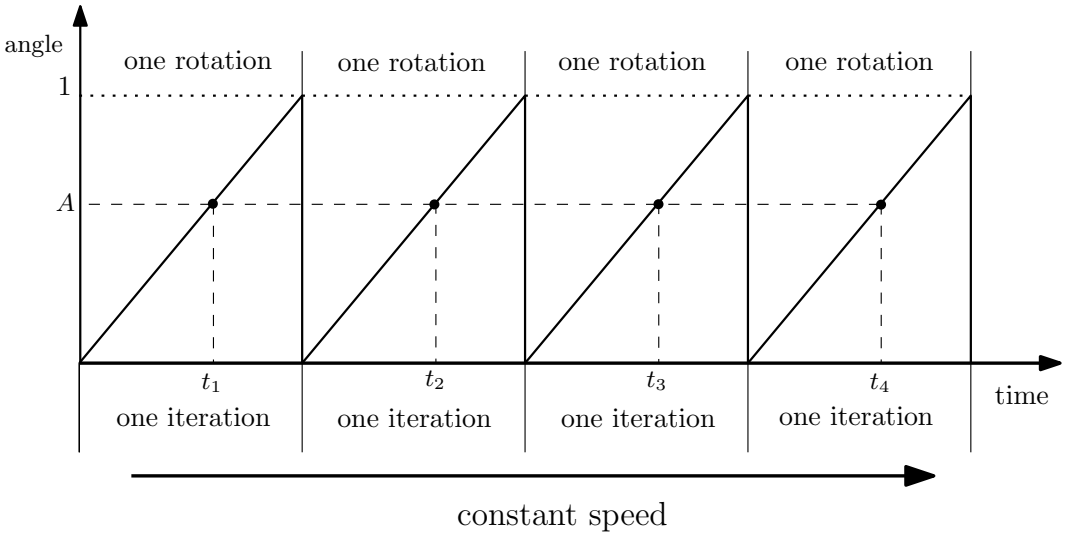

Figure 3.13: The relation between the repetitive controller delay and the mechanical rotation with a constant speed.

3.2.1 Working principle of the repetitive controller

Before presenting the angle-based RC technique, primarily, we need to figure out why existing RC techniques cannot be applied for variable speed machines. The expression of the basic repetitive controller presented in Eq. 2.3 is first rewritten here

$$u_{rc}(t) = \mathcal{L}^{-1}\{T_u(s)\} * u_{rc}(t-T) + \mathcal{L}^{-1}\{T_{pi}(s)\} * e(t-(T-\tau)).$$

This equation shows that the repetitive controller containing two time delays uses the past control and the past error information to compute its current output. The use of the past information is the essential difference between the RC technique and most other control techniques.

The periodic disturbance rejection capability of the repetitive controller has been studied and verified in the previous analysis. This inherent capability is due to the use of the time delays. For a periodic disturbance, the same disturbance reappears in each period, so the disturbance information obtained from the previous periods is surely valuable for the current control. Thanks to the delay, the previous information can be used for the current task in the repetitive controller. Besides, to guarantee the usefulness of the past information, the information from one period ago and the ongoing task must correspond to each other exactly, requiring that the delay should be accurately equal or an integer multiple of the disturbance period. Then the analysis above shows that the strict matching between the delay and the disturbance period is the key to ensure the rejection capability of the RC technique.

Then considering the PMSM torque ripple reduction problem, Fig. 3.13 and Fig. 3.14 are used here to give a vivid explanation why the repetitive controller can achieve the desired torque ripple reduction at constant speeds, but cannot at varying

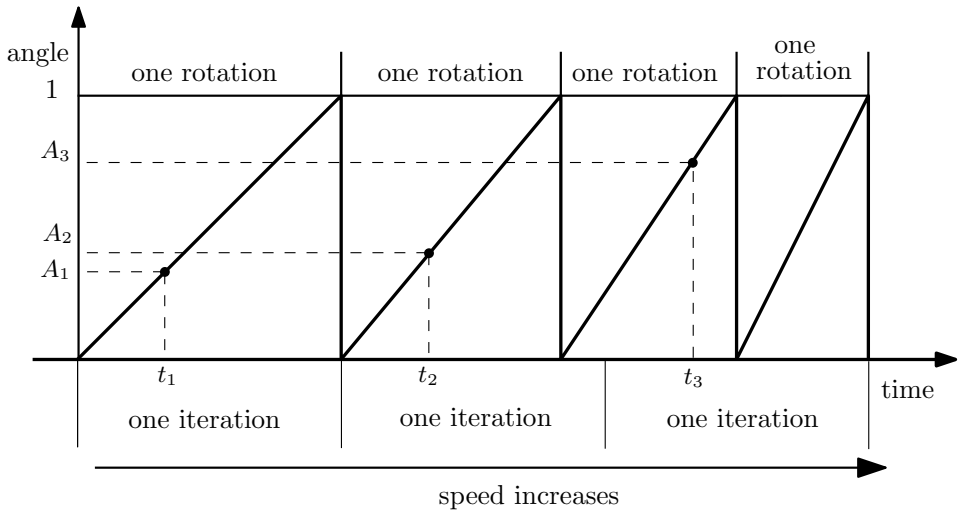

Figure 3.14: The relation between the repetitive controller delay and the mechanical rotation with an increasing speed.

speeds. In both figures, the rotation means the machine mechanical rotation, hence the angle is the mechanical angle. One iteration corresponds to the length of the delay, and the x-axis is the time.

Fig. 3.13 presents what happens when the rotor speed is constant. At constant speed, the duration of each rotation is the same. According to Chapter 2, the delay should be equal to the time needed for one mechanical rotation in order to ensure that the rejection capability can cover all possible torque ripples. Hence, in Fig. 3.13, one iteration is intentionally chosen to be the same as one rotation. In this figure, points like t_1, t_2, t_3, t_4, which are located at different iterations but in the same relative position, are called counterpart points [121]. Owing to the constant speed and the achieved matching, these counterpart points appear at the same mechanical angle, which means that the control and the error information obtained one delay ago should be useful for the current control. As a result, the repetitive controller is capable of reducing the PMSM torque ripple at constant speeds.

Fig. 3.14 presents what happens when the rotor speed is increasing. Because of the rising speed, the duration of the rotations shortens. The delay, which is deliberately designed to be equal to the first rotation, is no longer equal to others, breaking the required matching. Consequently, these counterpart points appear at different mechanical angles, and the information stored in the repetitive controller loses its usefulness, resulting in the failure of the reduction. This is the reason why the RC technique cannot be used for variable speed PMSM drives.

To show more clearly the performance limitation of a conventional repetitive controller, the disturbance rejection capability of the current feedback repetitive controller presented in section 2.5.4 is tested in Simulink with a varying rotor speed V (in rpm). Only the 24 th harmonic component is considered in this test and its

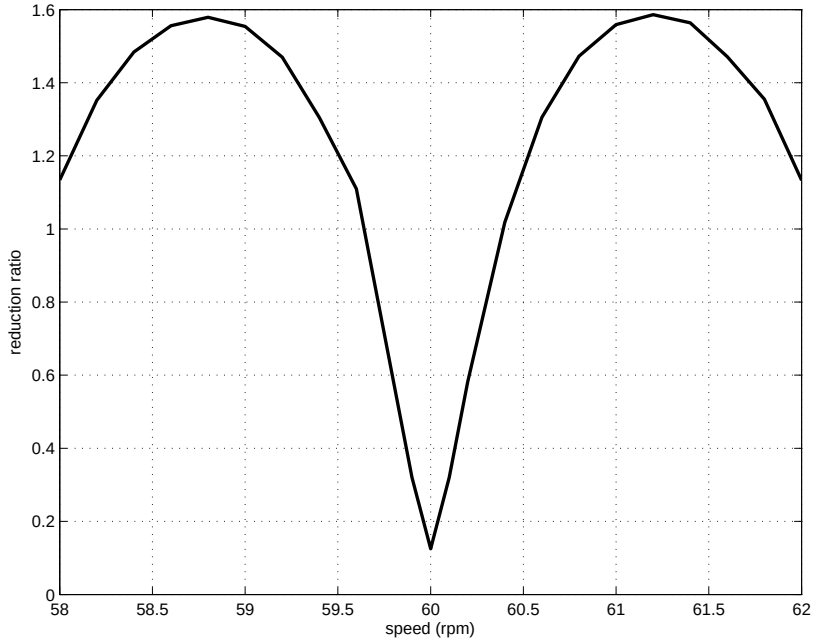

Figure 3.15: The variation of the reduction with the varying speed.

frequency can be computed as $f_d = 24V/60$. In order to judge the performance more fairly, we define that Reduction Ratio (RR) is

$$\mathrm{RR} = \frac{\Delta\,\omega_{\mathrm{RC}}}{\Delta\,\omega_{\mathrm{PI}}} \tag{3.21}$$

where $\Delta\omega_{\mathrm{RC}}$ is the peak-to-peak speed variation obtained with the current feedback repetitive controller and $\Delta\omega_{\mathrm{PI}}$ is the peak-to-peak speed variation obtained with the PI controller only. Hence, RR reflects the rejection capability difference between the current feedback controller and the PI controller. Since the chosen controller is designed for 60 rpm, the speed ranged from 58 to 62 rpm is used here and the result is shown in Fig. 3.15. According to this figure, only when the speed is exactly 60 rpm, the current feedback controller can provide a much better disturbance rejection than its PI counterpart. Then, with only a ± 0.2 rpm divergence, RR increases rapidly from 0.125 (at 60 rpm) to around 0.583. When the divergence is larger than 0.4 rpm, RR will exceed 1 and this repetitive controller will lost its advantage in the periodic disturbance rejection. As we can see, the rejection capability of the repetitive controller is rather sensitive to the speed. This result, in fact, completely coincides with $|H_{\mathrm{cfd}}|$ in Fig. 2.25 (between 23 and 25 Hz). The above results and analysis confirm again that the repetitive controller is only fit for constant speed applications.

3.2.2 Basic principle of the angle-based RC technique

The analysis above implies that, theoretically, the reduction capability of the RC technique can be guaranteed only if the disturbance is strictly periodic in time domain. Practically, this perfect periodicity is rarely met in many applications, such as the PMSM torque ripple reduction.

In fact, the periodicity and the repetitiveness treated in the RC technique are not limited to a time conception only, but can also be state, angle or trajectory conceptions. On the other hand, the torque ripples of PMSM, only when the speed is constant, can be considered as functions of time. According to section 1.6, essentially, they are functions of the mechanical angle. More importantly, the speed variation cannot change the relationship between the angle and the torque ripple. Correspondingly, to use the RC technique for the PMSM torque ripple reduction, this technique should be considered as an angle-dependent control method. This means that the repetitiveness of this controller is no longer a time conception but an angle one. To get an angle-dependent controller, the repetitive controller should choose the mechanical angle as its running variable, and it is called angle-based RC technique. On the other side, the conventional RC technique, which takes time as its running variable, is called time-based RC technique.

To show clearly how to get an angle-based repetitive controller, we take a PMSM running at a constant speed ω_m as an example. For this machine, we can assume that $\theta_m = \omega_m\, t$, then

$$t = \frac{\theta_m}{\omega_m} \text{ and } T = \frac{2\pi}{\omega_m},$$

and the time-based basic repetitive controller with constant T_u and T_{pi} can be rewritten as

$$u_{rc}\left(\frac{\theta_m}{\omega_m}\right) = T_u u_{rc}\left(\frac{\theta_m - 2\pi}{\omega_m}\right) + T_{pi} e\left(\frac{\theta_m + \omega_m \tau - 2\pi}{\omega_m}\right). \tag{3.22}$$

Provided that

$$u_a(\theta_m) = u_{rc}\left(\frac{\theta_m}{\omega_m}\right),\ e_a(\theta_m) = e\left(\frac{\theta_m}{\omega_m}\right) \text{ and } \theta_\tau = \omega_m \tau,$$

then the angle-based repetitive controller can be written as

$$u_a(\theta_m) = T_u u_a\left(\theta_m - 2\pi\right) + T_{pi}\, e_a\left(\theta_m + \theta_\tau - 2\pi\right). \tag{3.23}$$

which shows that the period of this angle-based controller is 2π. The deduction of Eq. 3.23 shows similarities between the angle-based and the time-based RC technique. Therefore, the angle-based repetitive controller, as its time-based counterpart, should be able to handle the periodic disturbance rejection. It is important to

note that, since the angle is now the controller running variable, the input of the angle-based repetitive controller should include the mechanical angle.

To store u_a and e_a in arrays (memories), the angular position is quantized as

$$n = \text{round}\left(\frac{N\theta_m}{2\pi}\right) \bmod N, \tag{3.24}$$

where N is the length of the arrays, which should be smaller or equal to the resolution of the position sensor. There will be no skipped index in the arrays if the rotor speed satisfies

$$V_{\max} < \frac{60F_s}{N}, \tag{3.25}$$

where $V_{\max}$ (in rpm) is the largest rotor speed and F_s is the sampling rate of the digital controller. When the speed exceeds this $V_{\max}$, a linear interpolation technique can be used to maintain the functionality of the angle-based RC technique. Eq. 3.25 indicates that a larger F_s with a fixed N leads to a higher $V_{\max}$.

On the other hand, provided that $k_{\max}$ is the order of the highest torque ripple component, then to avoid aliasing, according to the Nyquist-Shannon sampling theorem, N should satisfy

$$N \geq 2k_{\max}. \tag{3.26}$$

Therefore, only if the choice of N satisfies Eq. 3.25 and Eq. 3.26 simultaneously, the angle-based repetitive controller can correctly perform the torque ripple reduction in a PMSM drive.

It is interesting to know for all presented RC systems, whether their periodic rejection capability can benefit from the use of the angle-based technique. To answer this, we first consider the basic RC system. The result presented in Fig. 2.11 has shown that in a time-based basic RC system, there is a time delay between the basic repetitive controller input and output. For an angle-based basic RC system, this delay is not a time interval anymore, but an angle interval (2π). As a result, the basic angle-based repetitive controller cannot output a control signal until the completion of the first mechanical rotation. However, without the controller output, in the basic RC system, the machine cannot finish its first rotation. Therefore, owing to this obvious paradox, it is impossible to apply the angle-based technique to the basic repetitive controller.

On the opposite, for the current RC systems, thanks to the direct connection between the reference and the process, in the first rotation, the machine can start and run solely with the conventional controller. Then in the following rotations, with the information recorded from the first rotation, the repetitive process can offer the control action to perform the torque ripple reduction. The analysis above draws a conclusion that the angle-based technique can only be applied for current repetitive controllers.

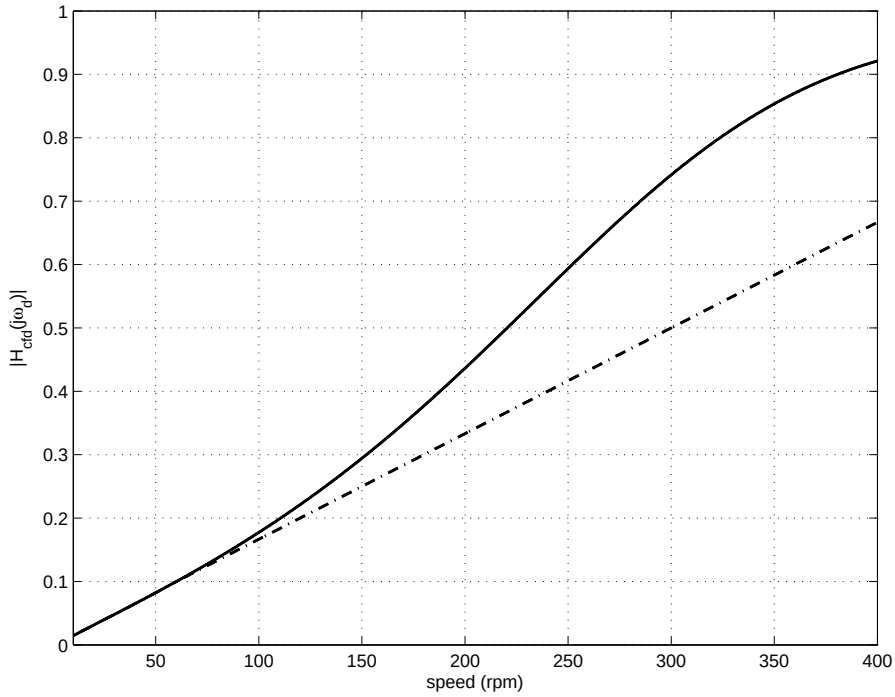

Figure 3.16: Rejection ratio of the main harmonic component of angle-based repetitive controller with fixed parameters (solid line) and with variable parameters (dash dotted line) at different speeds.

3.2.3 Stability, performance and design

To keep the efficiency of the angle-based controller at different speeds, first of all, the stability and the performance of the angle-based repetitive controller need to be investigated. Then, a controller that can adjust its parameters to maintain a good performance at different speeds should be developed for the angle-based technique.

Eq. 3.23 shows that an angle-based repetitive controller at steady-state has an equivalent time-based repetitive controller. As a result, the stability condition and the performance determination equations of this time-based RC system are still available for its angle-based counterpart. With a varying rotor speed V (in rpm), a series of equivalent time-based repetitive controllers can be deduced, and the only distinction among them is their delay length ($T = 60/V$). Since the stability condition derived from the small gain theorem is regardless to the delay, it does not rely on the speed either. Hence, these equivalent time-based RC systems, in fact, share the same stability condition. However, the disturbance rejection ratio and the convergence speed are functions of the frequency. Consequently, the disturbance rejection ratio of the main disturbance component and its convergence speed will change with the variation of the rotor speed, since

$$\omega_d = k_d\,\omega_m = k_d\frac{\pi}{30}V, \tag{3.27}$$

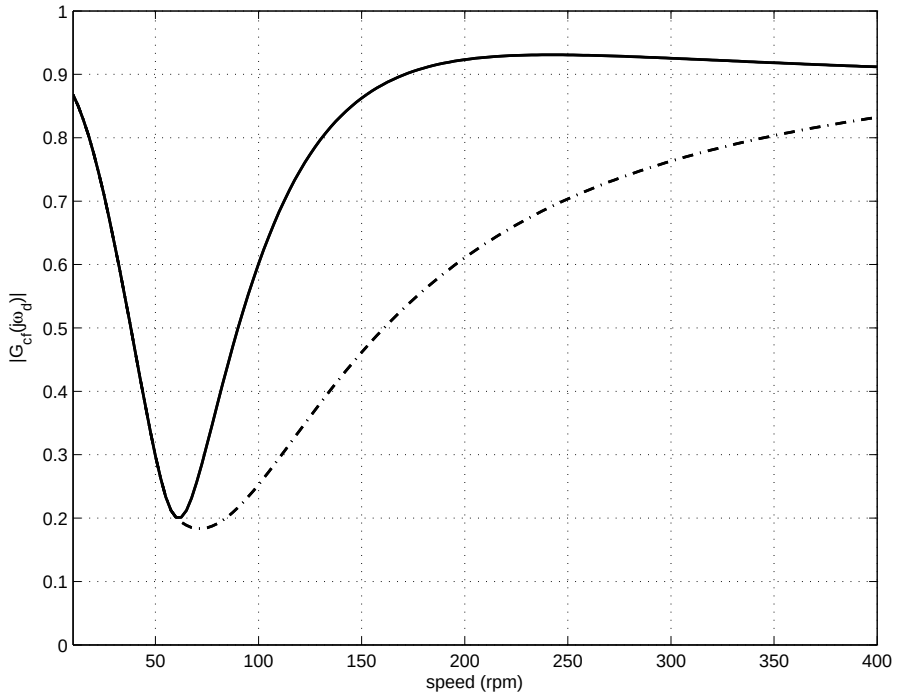

Figure 3.17: Convergence speed of the main harmonic component of angle-based repetitive controller with fixed parameters (solid line) and with variable parameters (dash dotted line) at different speeds.

in which k_d is already defined in Eq. 2.75 ($k_d = 24$ in our case).

The current feedback controller, with the second design approach presented in section 2.5.4, is used here as an example to illustrate, when the parameters K_{pi} and τ of the angle-based controller are fixed, how the disturbance rejection ratio and the convergence speed change with a varying speed. Fig. 3.16 and Fig. 3.17 show plots of $|H_{\text{cfd}}(j\omega_d)|$ and $|G_{cf}(j\omega_d)|$ for a speed varying between 10 and 400 rpm. These results show that at relative high speeds, the rejection ratio is weak and the convergence speed is slow, hence the performance obtained from the controller with fixed parameters is obviously inadequate.

This leads us to consider using another kind of repetitive controller, which is able to alter its parameters with respect to the speed so as to get better rejection capabilities, especially at high speeds. To design such kind of controller, primarily, we need to set a varying desire value of $|H_{\text{cfd}}(j\omega_d)|$ that changes with the speed. As we know, the goal of using the RC technique is to reduce $|P_2 D|$, which, in fact, is also a function of the speed. Owing to the chosen P_2, $|P_2 D|$ decreases with a rising speed. Hence, it is reasonable to set a relatively smaller rejection ratio (better reduction) at a low speed, and a relatively larger one (weaker reduction) at a high speed. Since under 60 rpm, as shown in Fig. 3.16, the rejection ratio obtained with the controller with fixed parameter is already smaller than 0.1, so it is sufficiently good. Then, the parameter variation only starts from 60 rpm. In this report, we hope

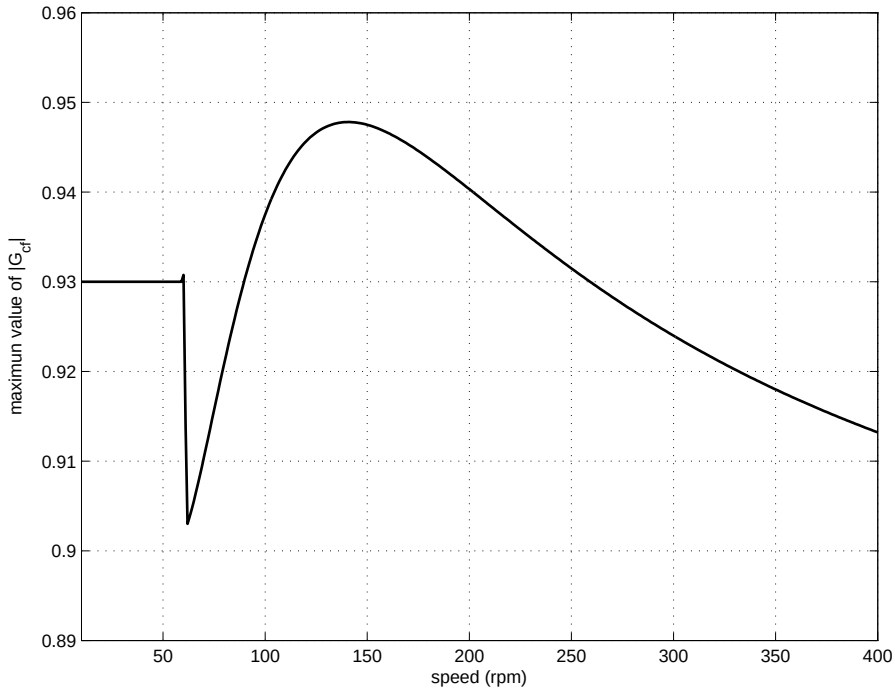

Figure 3.18: Maximum value of $|G_{cf}|$ at different speeds deduced from an angle-based controller with variable parameters (The maximum value of this curve, 0.9478, occurs at 140 rpm).

that when the speed exceeds 60 rpm, the proposed angle-based repetitive controller can keep the same $|H_{\text{cfd}}(j\omega_d)P_2(j\omega_d)D(j\omega_d)|$ as that at 60 rpm. For this, we use the proposed design rule with a speed dependent ω_d and $|H_{\text{cfd}}(j\omega_d)|$ defined as

$$|H_{\text{cfd}}(j\omega_d)| = R(V), \tag{3.28}$$

$$\text{with } R(V) = \begin{cases} R(60) & \text{if } V < 60, \\ R(60)\cdot V/60 & \text{if } V \geq 60, \end{cases} \text{ and } R(60) = 0.1.$$

As shown in Fig. 3.16, this choice leads to smaller values of $|H_{\text{cfd}}(j\omega_d)|$ than when using constant parameters. In this current feedback controller, the parameters of T_{ci} (the PI speed controller) are deduced from the SOM and will stay unchanged at different speeds, and the parameters of the angle-based repetitive process (the basic repetitive controller) with the proposed design rules (Eq. 2.77 and Eq. 2.78)

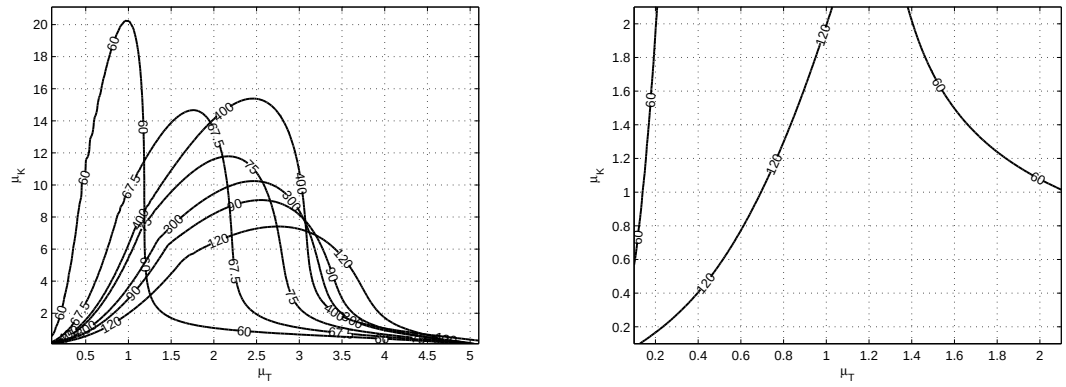

Figure 3.19: The stability robustness to the variation of process parameters. The left one is the global situation and the right is the zoomed situation.

are computed as

$$K_{pi}(V)=|Z(V)|,\ \theta_\tau=\omega_m\tau(V)=\frac{\mathrm{Arg}(Z(V))}{24},\ \text{and}\ \tau(V)=\frac{1}{\omega_d}\mathrm{Arg}(Z(V)), \quad (3.29)$$

$$\text{with}\ \ Z(V)=K_{pi}(V)e^{j\omega_d\tau(V)}=\frac{1-G_{cf}(j\omega_d)/T_u}{S_{ci}(j\omega_d)P(j\omega_d)}$$

$$\text{and}\ \ G_{cf}(j\omega_d)=1-(1-T_u)\frac{|S_{ci}(j\omega_d)|}{R(V)}.$$

As shown in Fig. 3.17, this choice also leads to a faster convergence speed than when using constant parameters only. Besides, we also need to check the stability of the this system, since the stability changes with the variation of the speed. The maximum value of stability of this controller at different speeds is shown in Fig. 3.18, in which the maximum is 0.9478, hence the design angle-based repetitive process can ensure the system stability in this speed range. In addition, to achieve the speed-based parameter variation, the speed information should be available for this repetitive controller, therefore it should become the controller input.

To guarantee the applicability of this angle-based controller, we also need to check its stability robustness to the uncertainty of both the process and the conventional controller (PI speed controller). Then according to Eq. 2.70, Eq. 3.18, Eq. 3.19 and the presented tuning methodology, the stability situation considering the uncertainty of the process and the conventional controller under different speeds are shown in Fig. 3.19 and Fig. 3.20 respectively. As shown in these figures, in both situations the stable regions of this angle-based controller under any considered speed are encircled by the curves obtained from 60 rpm and 120 rpm. As confirmed in the zoomed figures, with $50\,\%$ uncertainty of both the process and the conventional controller, the proposed angle-based repetitive controller is still able to keep the stability, showing a good stability robustness given by this design.

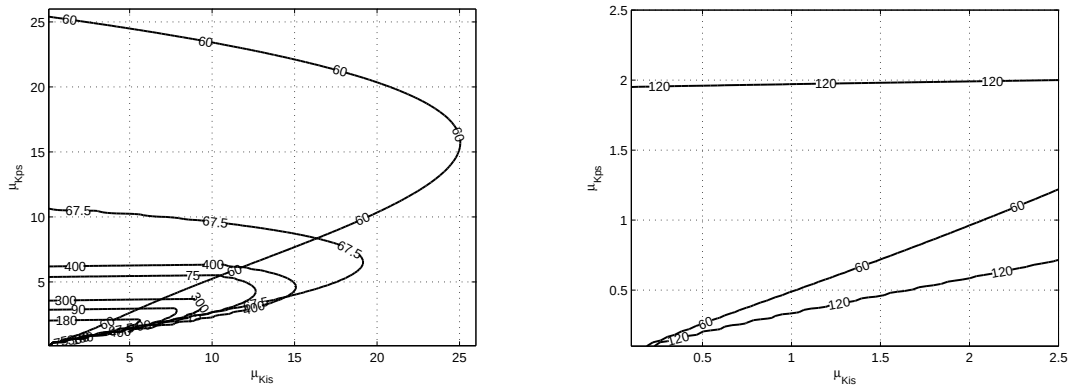

Figure 3.20: The stability robustness to the variation of process parameters. The left one is the global situation and the right is the zoomed situation.

3.2.4 Tracking performance improvements

The bad tracking behavior of RC systems has already raised the discussion in Chapter 2, in which a special repetitive controller, the NOSR repetitive controller, was proposed to fix this problem. However due to the particular structure of the NOSR RC system, other RC systems cannot directly copy its success. Hence, two other simple solutions are proposed to improve their tracking performance.

As shown in Fig. 2.44, the realization of the NOSR repetitive controller needs a replacement of the PI controller by an IP one in order to smooth the step signal. As we know, modifying the existing controller is not so easy, correspondingly, changing the PI controller by an IP controller is also difficult. Fortunately, a low-pass reference filter can be also used to get a smooth signal, hence is considered as a possible solution to improve the tracking performance. However, the use of a low-pass reference gains a better tracking transient at the cost of a slower system response. In order to balance the tracking transient and the system rapidity, it is recommended to choose the low-pass reference filter as [25],

$$T_{lp} = \frac{K_{is}}{K_{is} + sK_{ps}}. \tag{3.30}$$

Using this filter is then equivalent to replacing the PI controller by an IP one.

Another possible solution is to take a symmetric saturation function to limit the input of the repetitive controller (process), as shown in Fig. 3.21. The magnitude of the harmful oscillation is usually much larger than the amplitude of the error caused by the speed ripple. Once the limit of this saturation function is chosen to be an appropriate value that only keeps the useful error information go, the transient behavior can be improved without performance loss. The realization of this technique needs an observation, or at least an evaluation of $|P_2 D|$ is necessary so as to ind out an appropriate value of the limit of the saturation function.

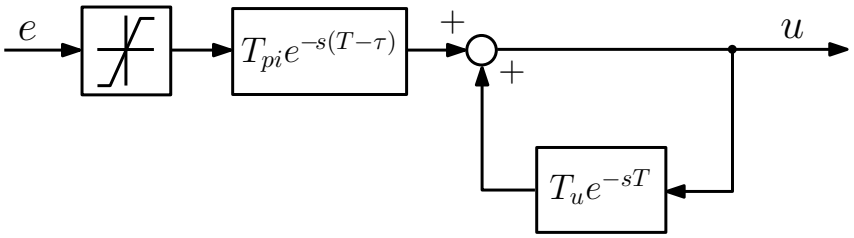

Figure 3.21: The integration of a symmetric saturation function into a repetitive controller.

The possible solutions presented here obviously can be used for almost all studied current RC systems, hence is much more adaptable than the NOSR repetitive controller. In conventional RC systems, the implementation of the low-pass reference filter or the saturation still requires a little knowledge and a slight modification of the existing controller. For the repetitive smart sensor systems, the saturation function is directly added into the smart sensor.

3.3 Experimental results

In this section, the proposed practical repetitive smart sensor and the angle-based RC technique together are implemented in the test bench, so as to verify the correctness of these techniques and the efficiency of the angle-based repetitive controller. In order to provide comparative results, an angle-based current feedback repetitive controller is also implemented.

The realization of the angle-based current feedback RC system and the angle-based smart sensor system are shown in Fig. 3.22 and Fig. 3.23. In both figures, a low-pass reference filter and a saturation function are used to improve the reference tracking performance.

The size of the memory used in the angle-based repetitive process is 1080, so according to the sampling rate of the dSPACE board ($10\,$kHz) and Eq. 3.25, until $555\,$rpm, no skipped index will occur in this case. Meanwhile, regarding to Fig. 1.19, the highest important torque ripple component is $35\,$th harmonic, then this memory size also fulfills Eq. 3.26, hence guarantees that the rejection capability can cover all important torque ripple components. The parameters of this repetitive process are computed from Eq. 3.29. The low-pass reference filter is deduced by Eq. 3.30 and the limit of the saturation function is chosen as 3 rpm. Besides, the parameters of the PI speed controller and the PI current controller are the same as in section 1.8.

Fig. 3.24, Fig. 3.25 and Fig. 3.26 show amplitude spectrums of the measured speed obtained in steady-state with the PI controller alone, the current feedback controller and the repetitive smart sensor at three speed references: 40, 60 and

80 rpm. These figures clearly show that in the three cases, the speed ripple reduction achieved by the current feedback controller and the repetitive smart sensor are quite similar. This is because T_{hp} is chosen as shown in Eq. 3.15. When the speed is 40 rpm, the main disturbance component, as shown in Fig. 3.24, is at 16 Hz. The theoretical value of $|S_{ci}(j\omega_d)|$ and $|H_{\text{rcd}}(j\omega_d)|$ are 0.4467 and 0.0651, therefore, according to Eq. 2.53 and the equivalence between both repetitive systems, the expected value of $|H_{\text{ssd2}}(j32\pi)| = |H_{\text{cfd2}}(j32\pi)|$, which indicates the extra reduction gained from using RC technique, is 0.1447. As shown in Fig. 3.24, the amplitude of the 16 Hz speed ripple obtained with the PI controller, the current feedback controller and the repetitive smart sensor is 0.428, 0.071 and 0.066 rpm respectively, so the achieved values of $|H_{\text{cfd2}}(j32\pi)|$ and $|H_{\text{ssd2}}(j32\pi)|$ are 0.1658 and 0.1552 respectively, which are both close to the desired value. A similar analysis has also been done for the other speeds, and the corresponding results are presented in Table. 3.1. This table not only confirms that the rejections of the main speed ripple component brought by both systems are similar, but also shows that the difference between the theoretical value of $|H_{\text{cfd2}}(j\omega_d)|$ and its experimental value is lower than 15 %.

In order to evaluate the global reduction, the peak-to-peak values of the speed ripple obtained in the nine cases are shown in Table. 3.2. This table shows that with the current feedback controller or with the repetitive smart sensor, nearly 80 % of the speed ripple can be removed at the three speeds.

Therefore, the analysis above draws two important conclusions: the first one is that once T_{hp} is chosen as in Eq. 3.15, the current feedback controller and the repetitive smart sensor can provide a similar speed ripple reduction capability; the other one is that the two proposed angle-based controllers are able to meet the rejection requirement at different speeds. In addition, from these figures and Table. 3.2, we can also conclude that the use of the RC technique does not amplify the sensor noise, as the resonances of $|H_{\text{cfd}}|$ (see Fig. 2.25) may let it fear.

The second group of experimental results is devoted to highlighting the interest of the low-pass reference filter and the saturation function. These results show the reference tracking behavior of four systems, using either a repetitive controller or a repetitive smart sensor, either with or without a reference filter associated to a saturation function. In these 60-second long experiments, the speed reference changes twice, firstly at 30 s, from 60 to 70 rpm, and secondly at 40 s, from 70 to 80 rpm. The repetitive processes are switched on at $t = 10$ s and switched off at $t = 50$ s. The results obtained with the current feedback repetitive controller and the repetitive smart sensor are shown in Fig. 3.27 and Fig. 3.28 respectively. Without filter and saturation function, reference steps lead to transients with overshoots and damped oscillations. The magnitude of the first few oscillations is close to the overshoot resulting from the PI controller, and even 8 s after a reference step, both systems

cannot reach their steady-state, since the residual oscillations are still large. With a low-pass filter and a saturation function together, in both systems, the overshoot stemming from the PI controller can be successfully avoided and the magnitude of the oscillations become nearly ignorable, as well as the disturbance reduction remains the same. As a result, the current repetitive controller and the repetitive smart sensor using the proposed low-pass reference filter and the saturation can provide a much better reference tracking behavior without losing their disturbance reduction capability.

Table 3.1: Reduction of the 24th harmonic of the speed ripple

speed reference (rpm)	$\lvert H_{\text{cfd2}}(j\omega_d)\rvert$		
	theoretical value	current feedback	smart sensor
40	0.1447	0.1658	0.1552
60	0.1298	0.1352	0.1400
80	0.1220	0.1275	0.1208

Table 3.2: Peak-to-Peak amplitude of the speed ripple

speed reference (rpm)	speed ripple (rpm)		
	conventional PI	current feedback	smart sensor
40	3.7957	0.7667	0.7832
60	3.4399	0.6511	0.6754
80	3.3084	0.7292	0.7188

3.4 Conclusion

In this section, we have presented two new RC techniques: the angle-based RC technique and the repetitive smart sensor technique.

The first part of this chapter shows that the repetitive smart sensor system is a current RC system, hence it is able to achieve the PMSM torque ripple reduction as other RC systems. The practical smart sensor with a special designed high-pass filter can provide the same stability and the same disturbance rejection as a current feedback repetitive controller, so the design methodology proposed for the current feedback repetitive controller can also be chosen for the repetitive smart sensor. We also notice that with this high-pass filter, the tracking behavior of the practical repetitive smart sensor system is still different from its current feedback counterpart. Besides, the robustness analysis confirms that the proposed repetitive smart sensor has an acceptable stability and performance robustness, hence it is a really applicable technique.

The second part of this chapter concludes that the angle-based RC technique is an effective solution that can extend the periodic disturbance rejection capability of the repetitive controllers to varying speeds. However, only the current repetitive controllers can adopt this technique to enhance their rejection capability. This technique, thanks to the proposed rounding rule, is achievable in conventional PMSM drive systems. The analysis shows that the stability and the performance of the angle-based repetitive controller can be studied as a particular case of the time-based repetitive controller, and the angle-based controller with varying parameters was designed to preserve the system stability and the rejection capability at different speeds. In addition, the low-pass reference filter and the saturation function are two simple and useful approaches that can improve the reference tracking.

Finally, the experimental results show that a well-designed repetitive smart sensor can achieve the same torque ripple reduction as a current feedback controller. These results show the feasibility of the angle-based technique in PMSM drives and confirm the disturbance reduction capability of the angle-based repetitive controller, as well as prove that the reference tracking performance of the RC system indeed benefits from the use of the low-pass reference filter and the saturation function.

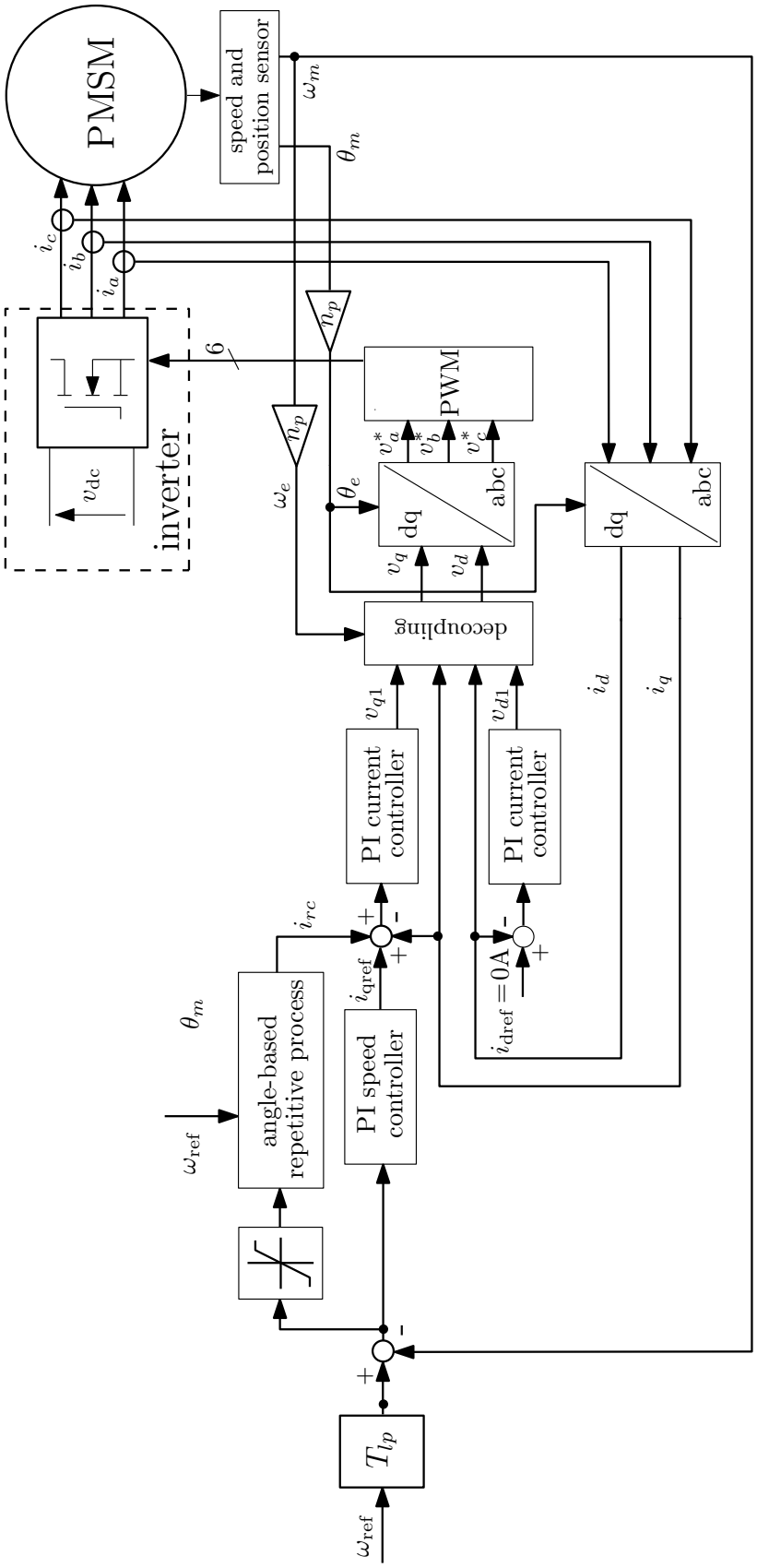

Figure 3.22: The block diagram of a field oriented PMSM drive using a current feedback controller implemented in the test bench (T_{lp} is the reference low-pass filter).

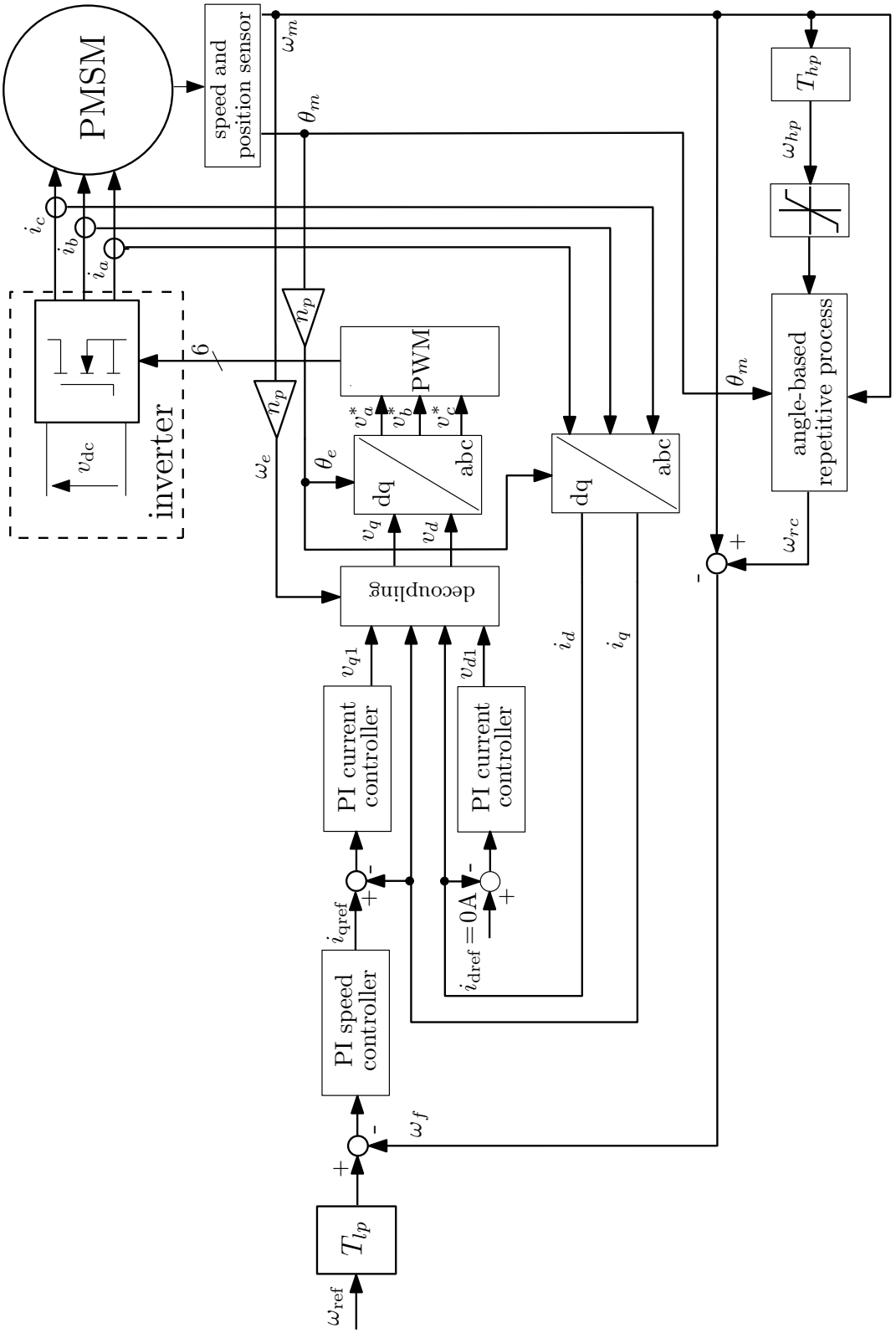

Figure 3.23: The block diagram of a field oriented PMSM drive using a practical repetitive smart sensor implemented in the test bench (T_{lp} is the reference low-pass filter and T_{hp} is the high-pass filter).

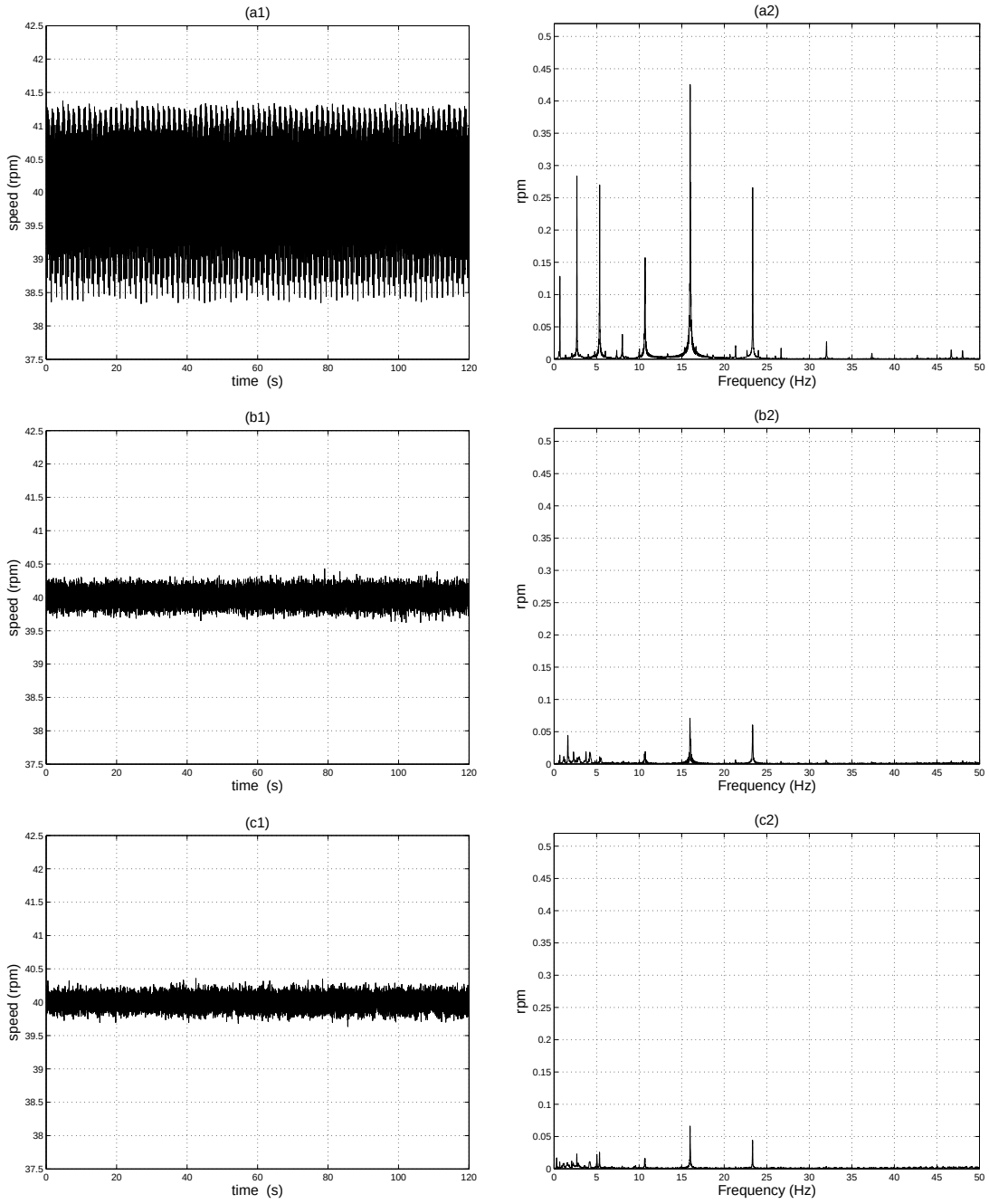

Figure 3.24: Time response and amplitude spectrum (plot of the sine wave amplitude versus frequency) of the measured speed in steady-state for (a) the PI controller alone, (b) the current feedback repetitive controller and (c) the repetitive smart sensor. The speed reference is is $\omega_m = 4\pi/3$ rad/s (40 rpm) and the torque load is $T_l = 1$ N·m.

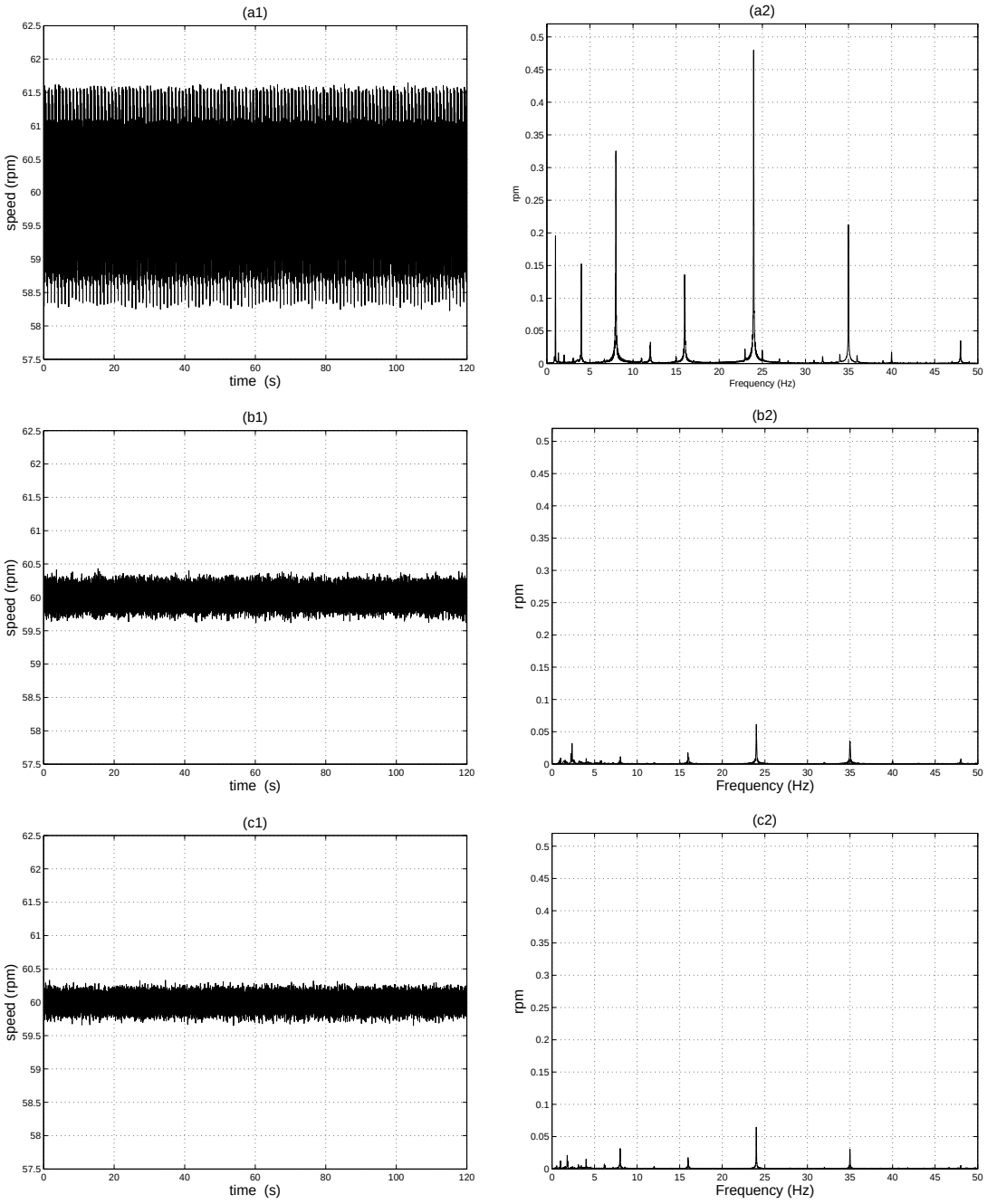

Figure 3.25: Time response and amplitude spectrum (plot of the sine wave amplitude versus frequency) of the measured speed in steady-state for (a) the PI controller alone, (b) the current feedback repetitive controller and (c) the repetitive smart sensor. The speed reference is is $\omega_m = 2\pi$ rad/s (60 rpm) and the torque load is $T_l = 1\,\mathrm{N{\cdot}m}$.

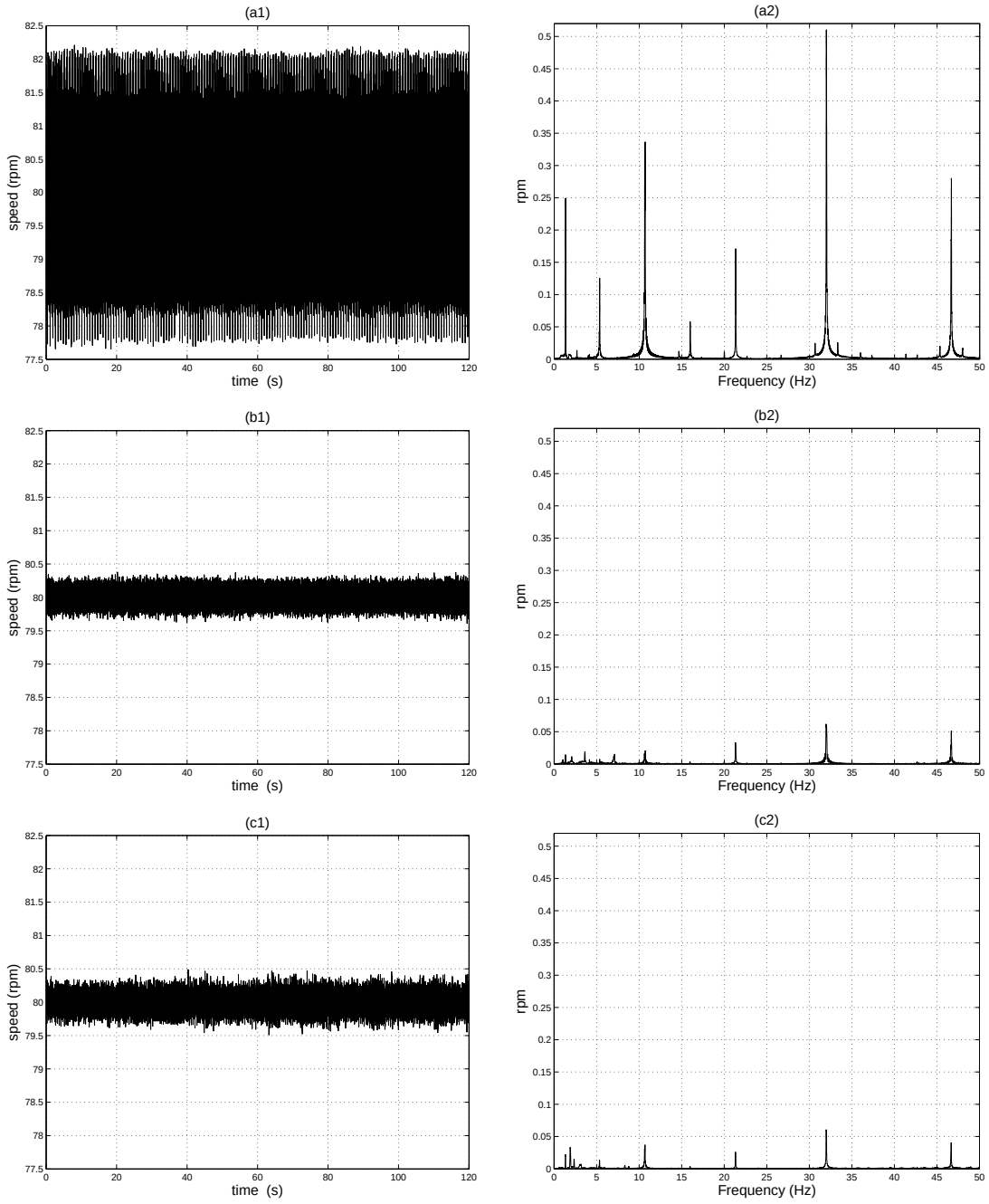

Figure 3.26: Time response and amplitude spectrum (plot of the sine wave amplitude versus frequency) of the measured speed in steady-state for (a) the PI controller alone, (b) the current feedback repetitive controller and (c) the repetitive smart sensor. The speed reference is is $\omega_m = 8\pi/3\,\text{rad/s}$ $(80\,\text{rpm})$ and the torque load is $T_l = 1\,\text{N}\cdot\text{m}$.

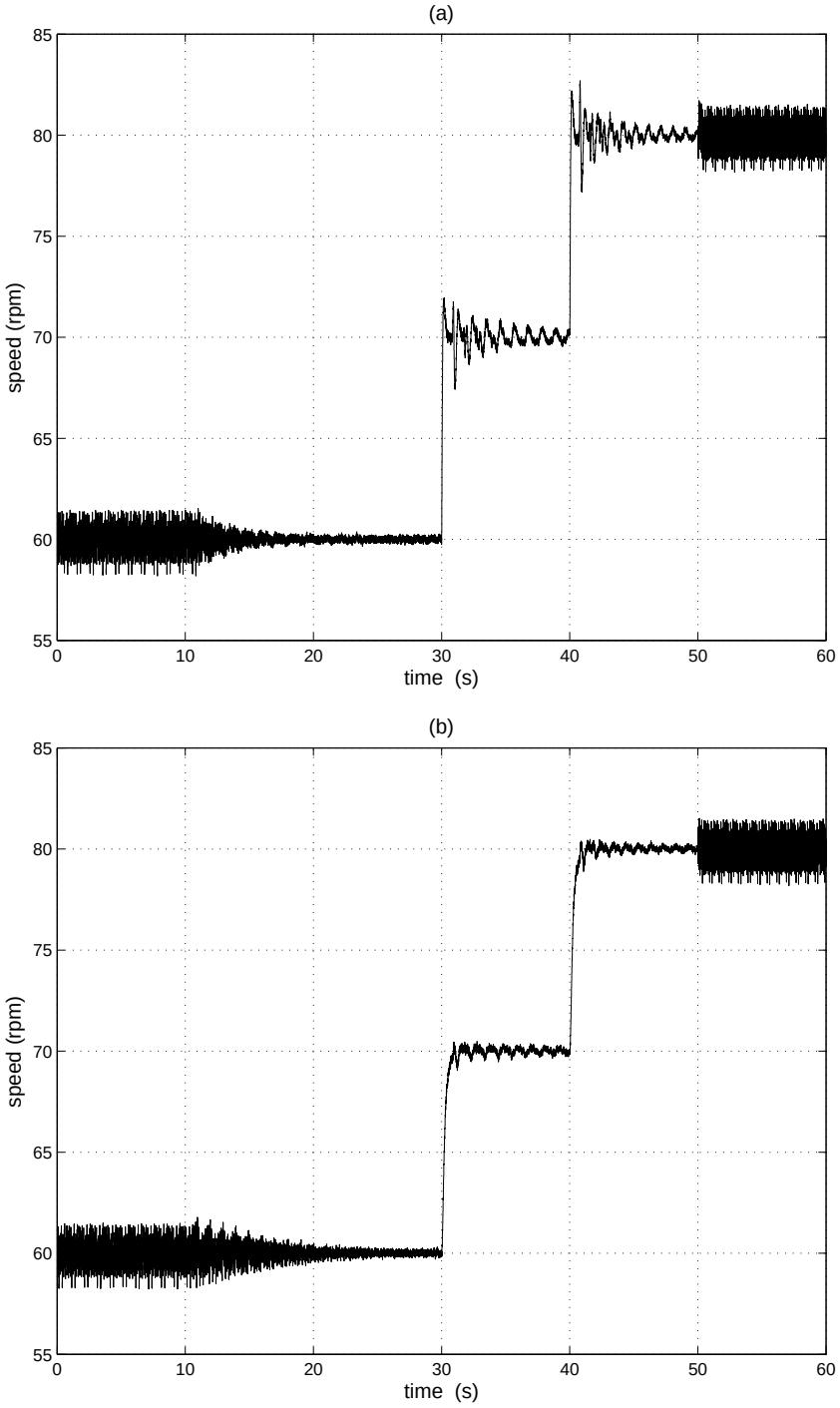

Figure 3.27: Time response of the angle-based current feedback RC system without (a) and with (b) the low-pass filter and the saturation.

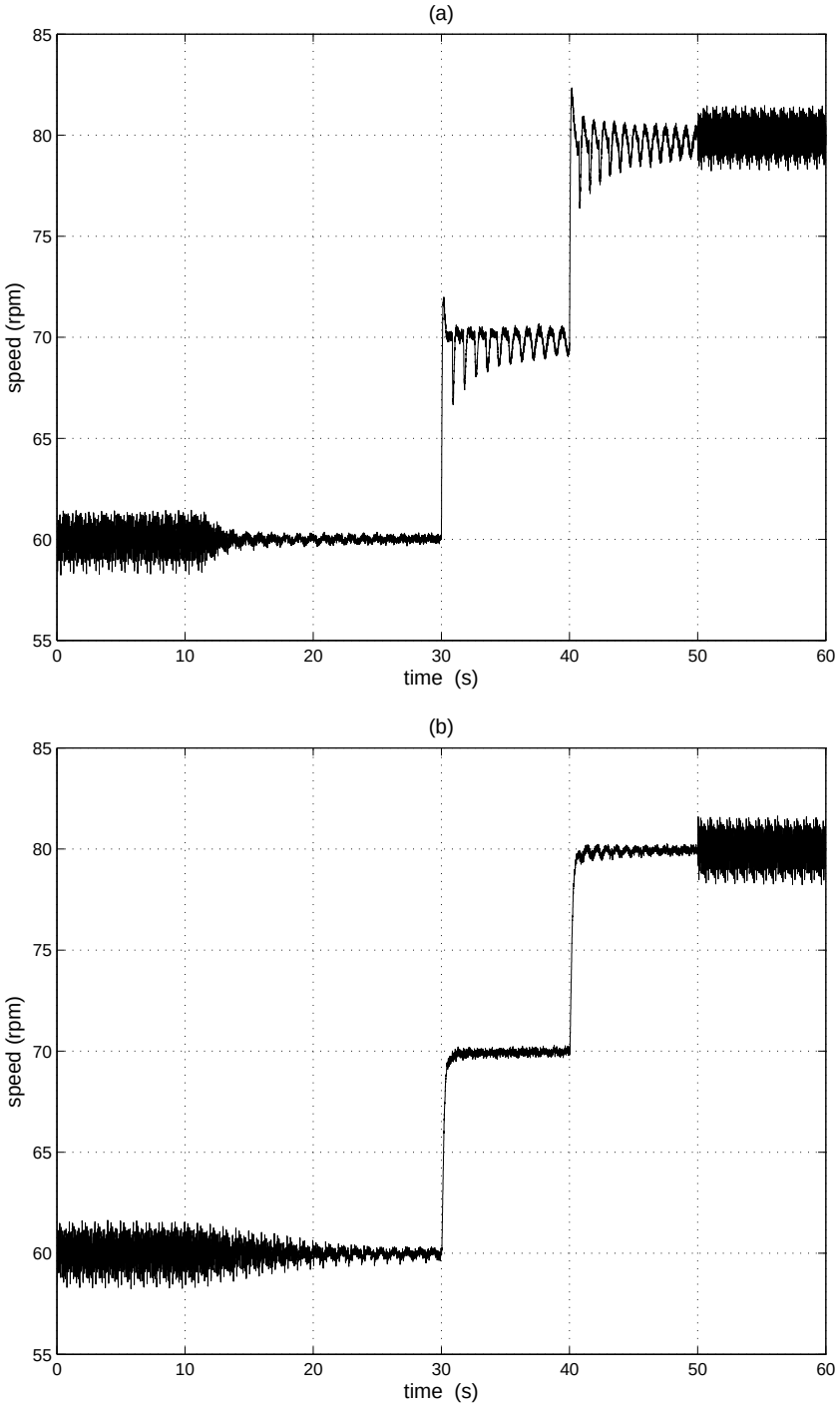

Figure 3.28: Time response of the angle-based repetitive smart sensor system without (a) and with (b) the low-pass filter and the saturation.

4

Conclusions and Perspectives

4.1 General conclusions

The objective of this thesis was to use the RC technique to achieve torque ripple reduction in PMSMs. In this work, we not only reviewed the basis of the PMSM and its torque ripples, but also studied and developed the RC technique, and finally implemented this technique in the test bench and successfully obtained the desired reduction.

In Chapter 1, a significant fact that torque ripples of the PMSM are functions of the mechanical angle was presented after studying the characteristics of each torque ripple. Consequently, the torque ripple reduction in PMSMs can be regarded as a periodical disturbance rejection problem. Based on a review of the current torque ripple reduction techniques, the RC, because of its particular capability in periodic disturbance rejection and obvious compatibility with common PMSM drives, was chosen for the PMSM torque ripple reduction problem.

Chapter 2 was mainly dedicated to enhancing the understanding of the RC technique so as to enable its use for our problem. The theoretical analysis proved that the small gain theorem was a useful tool to derive a sufficient stability condition for various repetitive controllers, and also showed that the basic RC system, owing to the unavoidable tracking error and delay, as well as the weak constant disturbance rejection capability, was not suitable for the PMSM torque ripple reduction. Because of this, this chapter introduced the current RC technique and presented two typical current repetitive controllers: the current iteration controller and the current feedback controller, which, under certain conditions, are equivalent to each other. The simulation results confirmed that both current repetitive controllers with

proper designs could achieve the desired reduction. The results also showed that the tracking performance of the RC systems would be impaired by the damped oscillations, which were due to the particular structure of the repetitive controllers. The IP repetitive controller, as an original repetitive controller, was used to eliminate the overshoot. The simulation results confirmed that the PMSM with a well-tuned NOSR repetitive controller could not only give a good periodic disturbance rejection capability but also bring a bumpless tracking behavior.

Two original RC techniques, the smart sensor technique and the angle-based RC technique, were proposed and studied in Chapter 3 so as to pave the way for common PMSM drives to use the RC technique. The repetitive smart sensor indeed simplifies the use of the RC technique in PMSM drives, because it no longer requires the modification of the controller. A closed-loop control system using a repetitive smart sensor is no more than a current RC system, so the repetitive smart sensor is capable of dealing with the torque ripple reduction. In fact, once the high-pass filter of the repetitive smart sensor is correctly designed, the current feedback controller and the repetitive smart sensor can provide similar speed ripple reduction capability. On the other hand, the conventional RC techniques, due to their nature, can perform the torque ripple reduction only when the rotor speed is constant. Thanks to the feature of the torque ripples, the angle-based repetitive controller is able to keep its reduction capability at varying speeds. The stability and the efficiency of this angle-based controller at different speeds can be guaranteed by a design methodology that is directly borrowed from the time-based repetitive controller design. The experimental results showed that the RC with the two proposed techniques becomes a really feasible solution to the PMSM torque ripple problem.

4.2 Perspectives

During this work, the RC technique with the smart sensor technique and the angle-based technique can be successfully applied to a common PMSM drive for the desired disturbance rejection. However, there are still some spaces available for improvements. Therefore, this work will continue not only on the theoretical side but also on the practical side.

Although the repetitive controller with the proposed design is already able to provide an attractive periodic disturbance rejection capability, there is no denying that to guarantee its efficiency, the repetitive controller needs to tune its parameters according to the characteristics of the machine. Hence, a designed repetitive controller unfortunately is only suitable for a very few machines. An adaptive repetitive controller, which is able to automatically adjust its parameters according to the variation of the machine parameters, may be is a promising solution to this limitation,

and therefore it will be the emphasis of the future work.

On the other hand, we have mentioned that, when the machine speed exceeds the set maximum value, linear interpolation will be used to maintain the efficiency of the angle-based repetitive controller. As a matter of fact, we did not get very far on this topic. However, it is very interesting and important to know what will happen when the angle-based controller uses the interpolation technique. According to this, a serious study that focuses on the system performance after using the interpolation probably should be considered in the future work.

Besides, in [122], the authors studied a new kind of repetitive controller, which, compared with conventional repetitive controllers, has two extra delays. Consequently, this controller is not only able to use the error and control information from one delay ago, but with these additional delays, can also use the information from two delays ago. The author in [122] investigated the behavior of the basic repetitive controller and current iteration one with additional delays, and concluded that this new kind of repetitive controller can provide a better disturbance rejection capability and a reference tracking performance. Hence, it seems also interesting to know whether the performance of the current feedback controller and the repetitive smart sensor can benefit from these extra delays.

On the practical side, until now, the function of the repetitive process of the repetitive smart sensor is achieved inside a dSPACE DS5202. In the next step, it will be put into a FPGA chip; then this chip will be embedded into a SKF position sensor unit in order to develop an industrial prototype. Meanwhile, all experimental results presented in this report are obtained only from the 1kW machine at relative low speeds, which, more or less, is insufficient to get a solid judgment about our techniques. Therefore, in the near future, we will test the repetitive smart sensor with various PMSMs and also with wider speed ranges. Furthermore, the similar test will expand to other machines. Hence, the proposed repetitive smart sensor, theoretically, is suitable for all the rotating machines suffering from torque ripples.

5

Résumé en Français

Pour se conformer aux conditions de l'Université de Nantes, ce mémoire rédigé en langue anglais s'achève par un résumé en langue française. Ce résumé peut permettre à un lecteur non anglophone de prendre aisément connaissance du contenu de cette thèse.

5.1 Introduction

Le travail présenté résulte d'une collaboration entre SKF France, "Automotive Development Centre (ADC), Sensor Integration (SI) department" et le laboratoire IREENA (Institut de Recherche en Énergie Électrique de Nantes Atlantique) de l'Université de Nantes. L'objectif de cette thèse est de développer un capteur intelligent basé sur la commande répétitive (CR) et capable de réaliser une réduction des oscillations de vitesse des machines synchrones à aimants permanents (MSAPs).

La MSAP, grâce à son rendement élevé, son excellente fiabilité et ses performances élevées, gagne rapidement de la popularité dans de nombreuses applications comme la robotique, les machines-outils et la propulsion de véhicules électriques, etc. Malheureusement, en raison de sa structure particulière, elle peut produire de fortes oscillations de vitesse, qui est un problème pour de nombreuses applications, en particulier pour les applications à basse vitesse et fort couple.

Par conséquent, depuis les dernières décennies, de nombreux articles techniques et scientifiques ont été consacrés à la réduction des oscillations de vitesse des MSAPs. Les solutions proposées dans ces articles peuvent être généralement classées en deux groupes : le premier réalise cette réduction par l'optimisation de la conception de la machine; le second exploite des contrôles actifs. Il faut noter que les

conceptions particulières compliquent la structure des machines. Leur réalisation est donc plus coûteuse. Par ailleurs, puisque le contrôleur est un élément nécessaire, l'utilisation d'algorithmes de commande plus sophistiqués apporte rarement des coûts supplémentaires.

Les oscillations de vitesse des MSAPs sont dues aux oscillations de couple, qui viennent de différentes sources, telles que le couple de denture, le couple harmonique etc. Presque toutes ces oscillations sont fonction de la position angulaire du rotor. Par conséquent, la diminution des oscillations de vitesse peut être considérée comme un problème de rejet des perturbations périodiques.

De ce fait, la CR est choisie pour sa forte capacité à réduire des perturbations périodiques et pour la simplicité de son intégration aux systèmes de commande des MSAPs. L'utilisation de la CR pour réduire les oscillations de couple a été publiée dans plusieurs articles [7, 8, 9, 10, 11, 12, 119]. L'analyse théorique et les résultats expérimentaux présentés dans ces publications montrent bien la capacité de diminution des perturbations périodiques. Néanmoins, ils révèlent une limitation inacceptable de cette technique qui ne peut être utilisée que si la vitesse de la machine est constante. Or, en pratique, la plupart des MSAPs sont utilisées pour des systèmes à vitesse variable. Par conséquent, le développement d'une nouvelle technique capable de réaliser une réduction des oscillations à vitesse variable est l'un des principaux défis de cette thèse.

De plus, habituellement l'application de la CR à une MSAP demandent le changement, ou au moins, la modification du contrôleur. Malheureusement, cela peut-être difficile pour des systèmes industriels, parce que les régulateurs sont bien souvent fournis par d'autres entreprises. Par conséquent, une autre partie importante de notre travail a pour objectif de simplifier l'application de la CR aux MSAPs, en intégrant la CR dans la chaîne de mesure.

Ce chapitre est organisé comme suit. Dans la section 5.2, la MSAP et ses oscillations de couple seront revus et une commande de la MSAP classique sera étudiée. En même temps, cette étude montrera l'état actuel des techniques de réduction des oscillations de vitesse. Pour finir, une introduction du banc d'essai sera effectuée pour servir de base aux études qui suivantes.

La section 5.3 rappellera le principe de la CR. Elle présentera le régulateur répétitif élémentaire et plusieurs régulateurs répétitifs avancés, appellés "current repetitive controller". Elle présentera également le théorème du petit gain, qui est un outil efficace pour analyser la stabilité des CR. Par ailleurs, plusieurs conceptions originales seront présentées afin de trouver un compromis entre la simplicité des régulateurs, la stabilité et les performances. Enfin, un nouveau régulateur répétitif sera proposé pour améliorer les performances de suivi de consigne de la CR.

Dans la section 5.4, deux nouvelles techniques : un régulateur répétitif basé sur la position angulaire et un capteur répétitif intelligent seront présentés. Le cap-

teur répétitif intelligent introduit un processus itératif dans un capteur de vitesse classique. Par conséquent, l'utilisation de ce capteur peut faciliter l'intégration de la CR. Pour étendre sa capacité de réduction des oscillations avec des fréquences variables, nous proposons une nouvelle technique de régulateur répétitif basé sur la position angulaire. Une analyse de la stabilité et des performances sera fournie. À la fin de la section, les deux techniques seront implémentées et validées sur notre banc d'essai.

5.2 MSAPs et oscillations de couple

Cette section a pour objectif de rappeler les principes de base, avant d'entamer une étude plus approfondie. Les caractéristiques des MSAPs dépendent de la conception de leur rotor et de leur stator. Donc, afin de comprendre les MSAPs, nous devons étudier d'abord leur rotor et leur stator. Ensuite, pour réaliser un actionneur électrique à base de MSAP, il est nécessaire de tenir compte de trois aspects : la machine, la stratégie de contrôle et la méthodologie de réglage du contrôleur. Un système typique comprend généralement des capteurs, un onduleur, un contrôleur et une MSAP. Une bonne compréhension de tous ces éléments est importante. Ils sont présentés ensemble dans cette section. La commande vectorielle, grâce à sa simplicité, est couramment utilisée. Par conséquent, elle est également choisie dans cette thèse. Avec la transformation de Park, le modèle de la machine développé dans le repère d-q est présenté. D'autre part, il existe plusieurs types d'oscillations de couple d'une MSAP. Pour réaliser la réduction des oscillations de vitesse, leurs caractéristiques doivent être connues. Beaucoup de méthodes ont été proposées pour réduire les oscillation de couple des MSAPs. Une présentation brève des méthodes utilisées est accomplie afin de trouver la méthode idéale pour notre projet. Finalement, cette section introduit aussi notre banc d'essai qui sera utilisé pour vérifier les études théoriques.

5.2.1 Architecture de MSAP et son système

Les MSAPs sont des machines synchrones polyphasées qui comportent des aimants permanents au rotor. En tant que machine synchrone, le flux magnétique du stator généré par le courant du stator et le flux magnétique généré par les aimants permanents doivent tourner à la même vitesse.

Les caractéristiques et la disposition des aimants permanents influencent fortement les performances de la machine. Il existe principalement trois types de MSAP [13] : la MSAP à aimants déposés en surface, la MSAP à aimants insérés et la MSAP à aimants enterrés. Dans cette étude, la MSAP choisie est une MSAP à aimants déposés en surface. Cette machine est fréquemment utilisée, car sa réa-

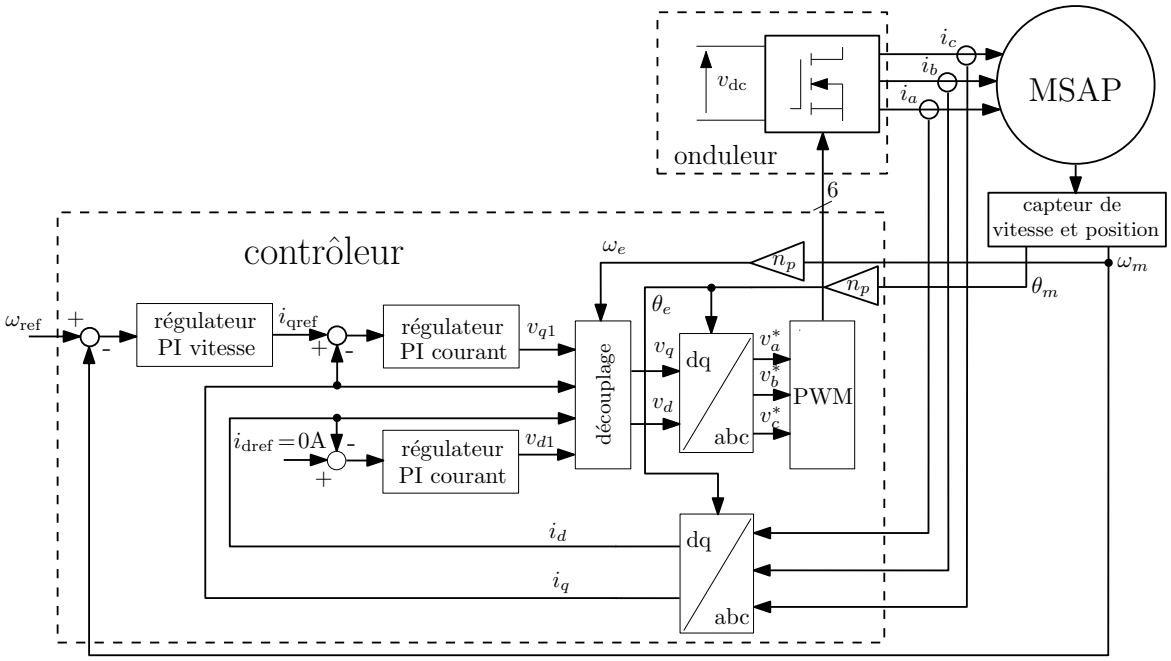

Figure 5.1: Schéma d'un système de commande vectorielle standard de MSAP.

lisation est relativement simple. En général, en raison de sa faible robustesse, ce montage ne convient pas pour les applications à vitesse rapide. Comme la perméabilité magnétique des aimants permanents est presque égale à celle de l'air, les inductances directes et en quadrature sont presque égales.

Généralement, le stator de la MSAP ressemble à celui des machines asynchrones. Le courant de stator est le résultat de la tension de l'onduleur et de la fem induite. Nous supposons que le flux magnétique généré par l'aimant permanent ψ_r est sinusoïdal [1] :

$$\psi_r(t) = \Psi_{rn} \sin(\omega_e t). \tag{5.1}$$

Dans cette équation, Ψ_{rn} est la valeur nominale de flux magnétique, ω_e est la vitesse angulaire électrique et t est le temps. Si nous supposons que le nombre de bobine par phrase est N_c, alors la force contre-électromotrice peut être calculée par [13]

$$e_{\text{fem}}(t) = -N_c \frac{d\psi_r(t)}{dt} = -N_c \, \Psi_{rn} \, \omega_e \cos(\omega_e t). \tag{5.2}$$

Il existe un autre type de machine à aimants permanents : la machine trapézoïdale qui présente une fem trapézoïdale [17]. La commande d'une MSAP est un peu plus compliquée que celle d'une machine trapézoïdale. Le couple de la MSAP est plus lisse que celui de la machine trapézoïdale, parce que cette dernière est affectée par une oscillation de couple supplémentaire : le couple de commutation. En outre, avec les mêmes pertes Joule, la puissance de sortie d'une machine trapézoïdale est $15.4\,\%$ supérieure à celle d'une MSAP [1]. L'architecture typique d'une

commande de MSAP est représentée par la Fig. 5.1. Le contrôleur calcule les commandes envoyées à l'onduleur pour piloter la MSAP et surveille l'état du système pour le protéger. L'onduleur convertit les ordres de contrôle en tensions à fréquence variable pour alimenter la machine. Les capteurs sont utilisés pour fournir les informations afin de réaliser la commande en boucle fermée. Dans ce système, les informations nécessaires sont les courants stator, la position du rotor et sa vitesse. Donc, ce système a besoin de deux types des capteurs : des capteurs de courant et un capteur de position et de vitesse.

5.2.2 Modélisation et commande d'une MSAP

La commande vectorielle est souvent choisie pour les systèmes à hautes performances. La réalisation d'une commande vectorielle repose sur la transformation de Park, défini par [18]

$$\begin{aligned} [x_d\, x_q]^T &= T\,[x_a\, x_b\, x_c]^T, \\ \text{avec } T &= \frac{2}{3}\begin{bmatrix} \cos(\theta) & \cos(\theta-2\pi/3) & \cos(\theta+2\pi/3) \\ -\sin(\theta) & -\sin(\theta-2\pi/3) & -\sin(\theta+2\pi/3) \end{bmatrix}. \end{aligned} \tag{5.3}$$

Dans le système étudié, le courant et la vitesse sont contrôlés par des régulateurs proportionnel-intégral (PI). Par conséquent, le réglage de ces régulateurs PI détermine les performances du système.

Une commande de MSAP typique présentée dans le repère synchrone d-q est représentée par la Fig. 5.2. Sous les hypothèses que la MSAP est non-saturée et que les courants de Foucault et les pertes par hystérésis sont négligeables, l'équation électrique de la MSAP, dans le repère d-q est donnée par [27] :

$$v_d = R_s i_d + \frac{d\psi_d}{dt} - \omega_e \psi_q \;\text{ et }\; v_q = R_s i_q + \frac{d\psi_q}{dt} + \omega_e \psi_d, \tag{5.4}$$

où $\psi_d = L_d i_d + \Psi$ et $\psi_q = L_q i_q$ sont les composantes d-q de flux, Ψ est le flux du rotor, ω_e est la vitesse angulaire électrique, v_d et v_q sont les tensions d-q, i_d et i_q sont les courants d-q, L_d et L_q sont les inductances d-q et R_s est la résistance du stator. La MSAP choisie pour ce projet est une MSAP à aimants montés en surface. Par conséquent, nous pouvons supposer que $L_d = L_q = L$. Si nous prenons en compte le découplage, la relation entre v_{d1} et i_d et celle entre v_{q1} et i_q sont :

$$\frac{I_d(s)}{V_{d1}(s)} = \frac{I_q(s)}{V_{q1}(s)} = \frac{1}{R_s + sL}. \tag{5.5}$$

La méthode de compensation de pôle est choisie pour régler les paramètres des régulateurs des boucles de courant. Donc, $K_{pc}/K_{ic} = L/R_s$, où K_{pc} et K_{ic} sont

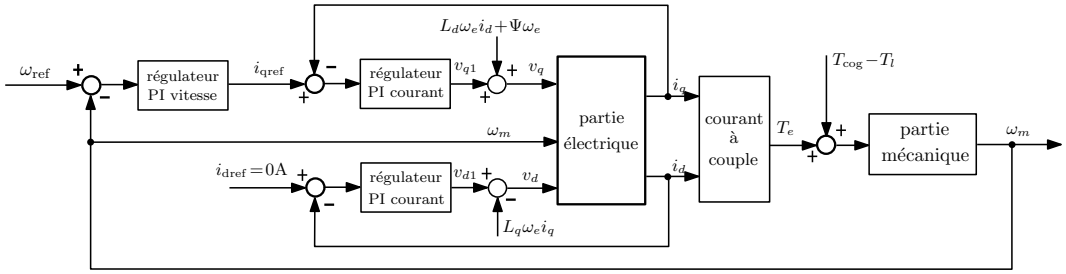

Figure 5.2: Le schéma simplifié d'un système de commande vectorielle standard d'une MSAP.

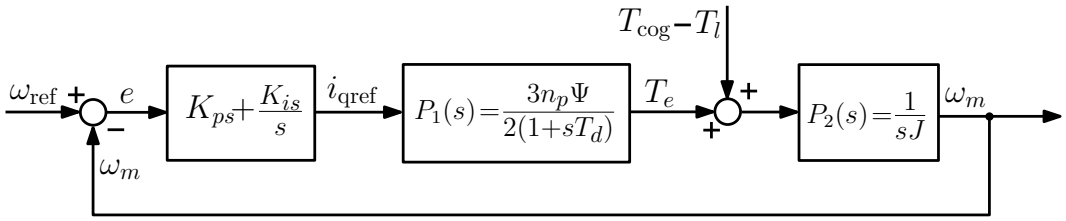

Figure 5.3: Le schéma simplifié de la commande d'une MSAP.

le gain proportionnel et le gain intégral du regulateur courant. Les fonctions de transfert en boucle fermée sont alors

$$\frac{I_d(s)}{I_{\text{dref}}(s)} = \frac{I_q(s)}{I_{\text{qref}}(s)} = \frac{\frac{K_{ic}+sK_{pc}}{s}\frac{1}{R_s+sL}}{1+\frac{K_{ic}+sK_{pc}}{s}\frac{1}{R_s+sL}} = \frac{1}{1+sT_d}, \tag{5.6}$$

où $T_d = R_s/K_{ic}$ est la constante de temps de la fonction de transfert du système. Sa bande passante peut être calculée par $f_b = 1/(2\pi T_d)$. Puis, K_{pc} et K_{ic} peuvent être calculés par

$$K_{pc} = 2\pi f_b L \;\text{ et }\; K_{ic} = 2\pi f_b R_s. \tag{5.7}$$

Le couple électromagnétique T_e est

$$T_e = \frac{3}{2}\, n_p(\psi_d\, i_q - \psi_q\, i_d) = \frac{3}{2} n_p\left(\Psi\, i_q + (L_d - L_q)\; i_d\, i_q\right), \tag{5.8}$$

où n_p est le nombre de paires de pôles. Grâce à $L_d = L_q$, l'Eq. 5.8 peut être simplifié en

$$T_e = \frac{3}{2} n_p \Psi\, i_q. \tag{5.9}$$

Si nous négligerons le couple de friction, l'équation mécanique de la MSAP peut être écrite comme

$$J\frac{dw_m}{dt} = (T_e + T_{\text{cog}} - T_l), \tag{5.10}$$

où J est l'inertie du rotor, $\omega_m = \omega_e/n_p$ est la vitesse mécanique angulaire, T_{cog}

représente le couple de denture et T_l représente le couple de charge. Cette équation indique que les oscillations de couple provoquent des oscillations de vitesse. Finalement, le système représenté par la Fig. 5.2 peut être organisé comme le montre la Fig. 5.3, avec :

$$P(s) = P_1(s)P_2(s) = \frac{K}{sT_d(1+sT_d)}, \tag{5.11}$$
$$\text{avec } P_1(s) = \frac{3n_p\Psi}{2(1+sT_d)},\ P_2(s) = \frac{1}{sJ} \text{ et } K = \frac{3n_pT_d\Psi}{2J}.$$

5.2.3 Oscillations de couple

Les oscillations de couple de la MSAP, parce qu'elles produisent des oscillations de vitesse, dégradent sérieusement les performances de la machine, en particulier à basse vitesse. Les oscillations de couple peuvent avoir différentes origines, telles que le couple de denture, le couple harmonique, ou le biais mécanique [1].

Le couple de denture provient de l'interaction entre le flux magnétique et les encoches du stator. Par conséquent, seules les machines à stator lisse sont à l'abri de ce type de couple. Dans de nombreuses machines du commerce, l'amplitude du couple de denture représente 5% à 10% du couple nominal. Parfois cette valeur peut augmenter jusqu'à 25% du couple nominal. Le couple de denture peut être écrit comme [35] :

$$T_{\text{cog}}(\theta_m) = \frac{\pi N_l\, l_{\text{eff}}}{4\mu_0}\left(R_o^2 - R_i^2\right)\sum_{n=1}^{\infty} n\, G_{nN_l} B_{nN_l} \sin(nN_l\theta_m), \tag{5.12}$$

où N_l est le plus petit multiple commun du nombre d'encoches du stator z et du nombre de pôle $2n_p$, l_{eff} est la longueur utile de la machine, μ_0 est la perméabilité de l'air, R_o et R_i sont respectivement les rayons intérieur et extérieur de l'entrefer. G est la perméabilité relative de l'entrefer et les coefficients de sa décomposition en série Fourier sont G_k et B est la densité du flux magnétique et les coefficients de sa décomposition en série Fourier sont B_k.

Une autre oscillation du couple importante est appelée couple harmonique. Comme le laisse entendre son nom, cette oscillation du couple est issue des harmoniques du flux magnétique. Le couple peut être exprimé sous la forme [36] :

$$T_e(\theta_e) = T_{\text{e,dc}} + T_{\text{e,harm}}(\theta_e),$$
$$\text{avec le couple principal } T_{\text{e,dc}} = \frac{3}{2}n_p\psi_m i_q \tag{5.13}$$
$$\text{et le couple harmonique } T_{\text{e,harm}}(\theta_e) = \frac{3}{2}n_p\left(\sum_{i=1}^{\infty}\psi_{rd,6i}\cos(6i\theta_e)\right)i_q. \tag{5.14}$$

Outre le couple de denture et le couple harmonique, il existe aussi le couple de décalage du courant [36] ou de l'erreur de gain [37] qui proviennent des imperfections du capteur de courant et des circuits analogiques. Les autres couples de perturbations sont d'ordre mécanique : par exemple, les déséquilibres de la machine et les défauts des roulements.

Selon l'analyse ci-dessus et la relation entre l'angle mécanique et électrique, on constate que les oscillations de couple de la MSAP sont des fonctions de l'angle mécanique. Du fait de l'Eq. 5.10, les oscillations de vitesse de MSAP sont des fonctions de l'angle mécanique aussi, en conséquence, leur réduction peut être considérée comme un problème de rejet de perturbations périodiques.

5.2.4 État de l'art des techniques de réduction

Au cours des dernières décennies, un grand nombre de travaux ont été consacrés à la réduction des oscillations de couple de la MSAP. Généralement, les techniques proposées peuvent être classées en deux catégories. La première consiste à concevoir une MSAP, qui peut fournir un couple plus lisse par l'optimisation de sa structure. L'autre relève de l'automatique et utilise des méthodes de commande avancées pour modifier le courant d'excitation et réduire activement les oscillations de vitesse.

Comme le couple de denture est la principale cause des oscillations de couple d'une MSAP, la plupart des techniques de conception concentrent leur attention sur les liens entre la réduction des oscillations de couple et l'optimisation de la structure de machine. Le couple de denture dépend de la conception du stator et du rotor, et de la combinaison de nombre de pôles du rotor et du nombre de dents au stator. De nombreuses publications ont démontré que le couple de denture et le couple harmonique peuvent être efficacement réduits par une amélioration de la structure de la machine. Quelques méthodes populaires sont : les encoches et les dents factices [39], les enroulements fractionnaires et raccourcis [42], l'inclinaisons des encoches ou des aimants [32, 47] etc. Cependant, nous ne pouvons pas nier le fait que, bien que certaines conceptions particulières sont capables de résoudre le problème des oscillations de couple, elles compliquent la structure de la machine. Par conséquent, elles augmentent la complexité de fabrication. En outre, certaines fournissent la réduction souhaitée aux prix d'un rendement réduit.

Le couple électromagnétique est généré par l'interaction entre le champ magnétique et le courant d'excitation. Donc, il est possible de réduire l'oscillation de couple par des modifications du courant. Dans une commande de MSAP conventionnelle, la capacité du régulateur PI à réduire les oscillations de couple est limitée par sa bande passante. En conséquence, beaucoup de méthodes des commandes avancées ont été utilisées pour la réduction des oscillations de couple des MSAPs.

Par exemple, quelques techniques particulières comme le filtrage Kalman [59], le filtrage passif [48], le filtrage hybride [49] et le filtre adaptatif [50] ont été employées. Par ailleurs, beaucoup de méthodes de commande comme la commande adaptative [51], la commande floue [52] et les réseaux de neurones [53] ont déjà été réalisées également pour réduire les oscillations de couple. Néanmoins, les méthodes de commande les plus utilisées sont basées sur des formes d'onde programmées ("programmed current waveform control") [54], la commande instantanée en couple ("instantaneous torque control") [6] et les stratégies itératives basées sur la mémorisation des cycles précédents ("memory-based control") [63]. Ces dernières sont composées de trois membres : le contrôle par apprentissage itératif, la commande répétitive et le contrôle cycle à cycle ("run-to-run control"). Ce type de commande détermine à partir des expériences précédentes le moyen d'atteindre la réduction souhaitée. Dans cette thèse, nous nous concentrons uniquement sur la commande répétitive. La réalisation de la commande répétitive demande juste un peu de mémoire, ainsi il est très facile de l'appliquer à une commande de MSAP conventionnelle.

5.2.5 Banc d'essai

Un banc d'essai centré sur un système dSPACE est présenté par la Fig. 5.4. Ce système a été conçu dans le service "ADC-SI" de la société SKF. Ce banc d'essai est utilisé non seulement pour mettre en place la commande vectorielle, mais également pour tester diverses commandes répétitives qui seront présentées dans les prochains paragraphes. Ce système est composé des éléments suivants : une MSAP à aimants déposés en surface, qui est choisie comme l'objet de nos expérimentations; la carte processeur dSPACE DS 1005, complétée par une carte dSPACE DS5202 FPGA, reliée à un ordinateur; un dSPACE RapidPro power unit utilisé comme onduleur; un frein dynamométrique à hystérésis Magtrol utilisé comme charge et contrôlé par un contrôleur dynamométrique DSP 7000 ; enfin, un Meamwell PSP600 utilisé comme alimentation de puissance.

Par ailleurs, deux logiciels ont été utilisés pour réaliser les essais. L'un est le logiciel Matlab&Simulink 2010a, qui est utilisé pour effectuer des simulations numériques avant les expérimentations et aussi pour préparer et compiler les programmes. L'autre est le logiciel dSPACE Control Desk 4.3 capable de télécharger les programmes dans la carte dSPACE FPGA et de fournir une interface visuelle pour permettre à l'utilisateur de gérer les expériences.

La MSAP choisie est utilisée dans le système EPS de la Renault Mégane. Ses principaux paramètres sont obtenus par quelques mesures et observations simples, Ils sont présentés par le Tableau 5.1. Un résolver, qui est integré à la machine, est utilisé comme capteur de position. Son rôle est de fournir l'information de position

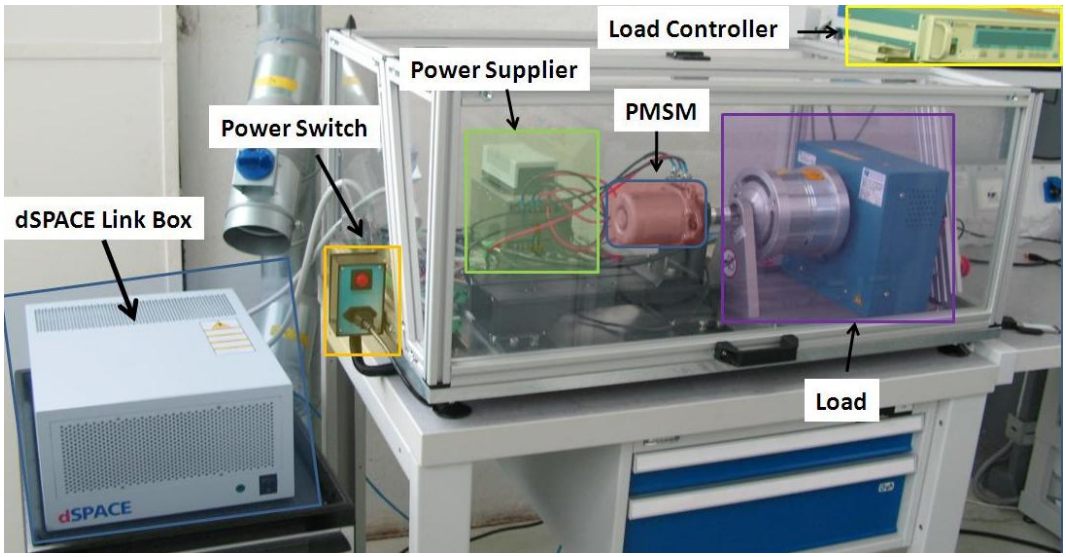

Figure 5.4: Le banc d'essai de SKF.

et de vitesse du rotor. De plus, un "encoder" incrémental est accouplé á la machine afin de vérifier les informations qui viennent du "resolver".

Le charge mécanique est un frein dynamométrique à hystérésis Magtrol. Cet appareil est composé de deux parties : un stator et un rotor [70]. Quand le courant passe dans les bobines du stator, il établit un champ magnétique, qui magnétise le rotor et génère un couple indépendant de la stator.

Table 5.1: Paramètres de la MSAP

Résistance du stator	0.013Ω
Inductance du stator	0.07 mH
Flux magnétique	0.017 Wb
Nombre de pôles	8
Nombre d'encoches	12
Puissance nominale	1 kW
Inertie de la machine et de la charge	0.012 kg.m^2

5.3 Commande répétitive

La commande répétitive (CR), grâce à sa capacité à réduire l'amplitude de perturbations périodiques, est choisie pour réaliser la réduction des oscillations de vitesse d'une MSAP. Une bonne connaissance de la CR est indispensable pour pouvoir l'utiliser avec succès. La compréhension approfondie de cette technique est l'un des premiers buts de cette section. Nous aboutirons alors à la conception de deux régulateur répétitif originaux, dont l'un est capable d'améliorer le suivi de consigne.

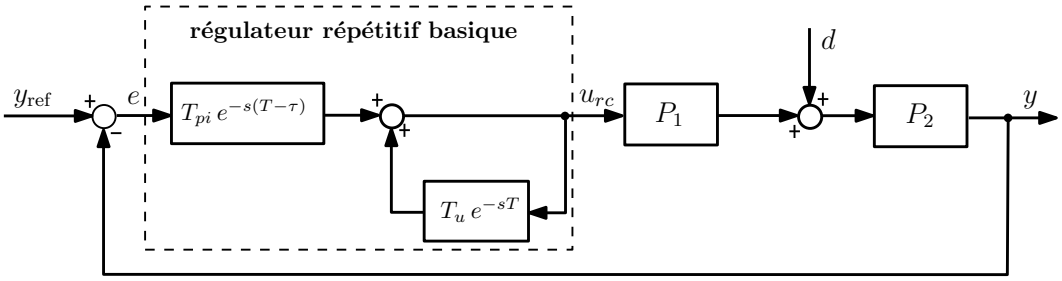

Figure 5.5: Schéma d'un système contrôlé par un régulateur répétitif élémentaire (dans notre cas, $y_{\text{ref}} = \omega_{\text{ref}}$, $y = \omega_m$, $u_{rc} = i_{\text{qref}}$, $d = T_{\text{cog}} - T_l$, et P_1 et P_2 sont définis par l'Eq. 5.11).

5.3.1 Principe de la commande répétitive

La commande répétitive est une technique basée sur le principe du modèle interne de Morari (PMI) [72]. C'est une méthode qui peut fournir des systèmes de contrôle ayant une bonne capacité de suivi des consignes périodiques ou de rejet des perturbations périodiques. Le PMI indique que, pour un système stable en boucle fermée, pour suivre ou rejeter un signal périodique sans erreur en régime permanent, un générateur autonome capable de générer ce signal répétitif, doit faire partie du système de contrôle. Ce type de générateur autonome peut être obtenu par une rétroaction positive avec un retard pur. Un système qui adopte ce principe peut être considéré comme un système de commande répétitive.

La structure typique d'un régulateur répétitif élémentaire est montrée par la Fig. 5.5. Dans cette figure, e^{-sT} est un retard, T_{pi} et T_u sont deux fonctions de transfert pour régler les performances du régulateur, e est l'entrée de ce régulateur et u_{rc} est sa sortie. La relation entre cette entrée et cette sortie est [63]

$$U_{rc}(s) = T_u(s)\, e^{-sT} U_{rc}(s) + T_{pi}(s)\, e^{-s(T-\tau)} E(s). \tag{5.15}$$

Selon la Fig. 5.5, la relation entre la sortie de système y, l'entrée de référence y_{ref} et la perturbation d est

$$\begin{aligned} Y &= \frac{T_{pi} P e^{-s(T-\tau)} Y_{\text{ref}} + (1 - T_u e^{-sT}) P_2 D}{1 - T_u e^{-sT} + T_{pi} P e^{-s(T-\tau)}} \\ &= H_{\text{rcr}}\, Y_{\text{ref}} + H_{\text{rcd}}\, P_2 D, \end{aligned} \tag{5.16}$$

$$\text{avec} \quad H_{\text{rcr}} = \frac{T_{pi} P e^{-s(T-\tau)}}{1 - G_{rc} e^{-sT}}, \quad H_{\text{rcd}} = \frac{1 - T_u e^{-sT}}{1 - G_{rc} e^{-sT}},$$

$$G_{rc} = T_u - T_{pi} P e^{s\tau} = T_u (1 - T_{pi2} P e^{s\tau}) \quad \text{et} \quad T_{pi2} = T_{pi}/T_u.$$

La relation entre l'erreur e et y_{ref} et d est

$$\begin{aligned} E &= \frac{1-T_u e^{-sT}}{1-T_u e^{-sT}+T_{pi}Pe^{-s(T-\tau)}}Y_{\text{ref}} - \frac{1-T_u e^{-sT}}{1-T_u e^{-sT}+T_{pi}Pe^{-s(T-\tau)}}P_2 D \\ &= H_{\text{rcd}}\,(Y_{\text{ref}}-P_2 D)\,. \end{aligned} \tag{5.17}$$

Ces deux équations sont à la base de l'étude approfondie du régulateur répétitif. Le processus utilisé ici est le modèle de la MSAP présenté par l'Eq. 5.11, où $P=P_1P_2$. Mais il faut noter que le modèle ci-dessus ignore intentionnellement les frottement visqueux de la machine. Si nous considérons ces frottements, l'Eq. 5.11 devient

$$P(s)=P_1(s)P_2(s)=\frac{3n_p\psi}{2(1+sT_d)}\frac{1}{f_b+sJ} = \frac{K}{T_d(f_b/J+s)(1+sT_d)}, \tag{5.18}$$

où $f_b=1.2\times10^{-4}$ N·m·s/rad est le coefficient des frottements visqueux. Ce nouveau modèle sera seulement utilisé pour l'étude de la stabilité et du rejet du couple de charge du régulateur répétitif élémentaire.

Une autre technique de commande itérative, le contrôle par apprentissage itératif (CAI), est très similaire à la CR. Par conséquent, il est nécessaire de distinguer la CR de son "frère jumeau" CAI [107]. Le CAI provient de l'idée que les compétences d'un être humain peuvent s'améliorer au fur et à mesure de la répétition des tâches. Donc, pour les machines, leurs performances peuvent aussi être améliorées par l'acquisition d'une expérience déduite des tâches précédentes. La distinction la plus importante entre les deux techniques est la suivante : le CAI est plutôt apte aux opérations discontinues, dont le processus est réinitialisé à chaque itération, par exemple en robotique; la CR est généralement apte aux opérations continues sans réinitialistion, par exemple la commande des disques durs et des machines tournantes.

5.3.2 Théorème du petit gain et stabilité du régulateur répétitif élémentaire

Le théorème du petit gain peut fournir une condition suffisante de stabilité pour un système en boucle fermée. Il est aussi un outil efficace d'analyse de la robustesse de la stabilité de ce type de système. À condition que $G_1(s)$ et $G_2(s)$ dans la Fig. 5.6 soient des fonctions de transfert stables, le théorème du petit gain dans un cas mono entrée-mono sortie peut être écrit comme

$$|\,G_1(j\omega)G_2(j\omega)\,| < 1, \quad \forall\omega \in [0,+\infty[\tag{5.19}$$

Le théorème du petit gain dérive du critère de stabilité de Nyquist. Selon l'Eq. 5.16, nous pouvons obtenir une autre représentation du système de régulateur répétitif

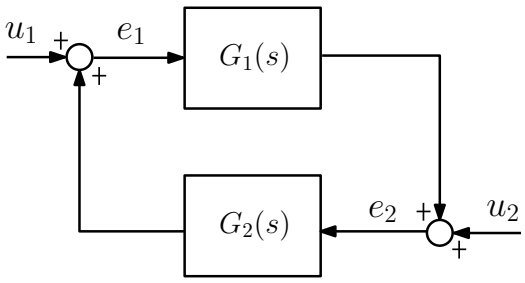

Figure 5.6: Une exemple simple de système rebouclé.

élémentaire, à partir des équations

$$\begin{aligned}\left(1-G_{rc}e^{-sT}\right)Y &= T_{pi}Pe^{-s(T-\tau)}Y_{\text{ref}} + (1-T_ue^{-sT})P_2D \\ Y &= G_{rc}e^{-sT}Y + T_{pi}Pe^{-s(T-\tau)}Y_{\text{ref}} + (1-T_ue^{-sT})P_2D,\end{aligned} \tag{5.20}$$

Par conséquent, le système présenté par la Fig. 5.5 peut être mis sous la forme représentée par la Fig. 5.7. Selon figure, le système de régulateur répétitif élémentaire est composé de trois parties : $T_{pi}Pe^{-s(T-\tau)}$, $(1-T_ue^{-sT})P_2$ et un système en boucle fermée avec un retard $G_{rc}e^{-sT}$. Il est facile de constater que la troisième partie est un cas particulier de la structure représentée par la Fig. 5.6. Sa stabilité peut donc être étudiée par le théorème du petit gain. Ensuite, comme

$$(1-T_ue^{-sT})P_2 = (1-e^{-sT})P_2 + (1-T_u)P_2e^{-sT}, \tag{5.21}$$

la stabilité du terme $(1-T_ue^{-sT})P_2$ est associée à deux parties : $(1-e^{-sT})P_2$ et $(1-T_u)P_2$. Nous supposerons que $(1-e^{-sT})P_2$, $(1-T_u)P_2$, $T_{pi}P$ et G_{rc} n'ont pas de pôles dans le côté droit du domaine de Laplace, selon le théorème du petit gain, une condition de la stabilité suffisante de ce système peut être [24, 114]

$$|G_{rc}(j\omega)| = \left|T_u(j\omega) - T_{pi}(j\omega)P(j\omega)e^{j\omega\tau}\right| < 1, \quad \forall\omega \in [0, +\infty[\tag{5.22}$$

Bien qu'elle ne soit qu'une condition suffisante, cette condition fournit avantageusement une condition de la stabilité qui implique seulement G_{rc} qui est indépendante de la période de la perturbation T.

5.3.3 Performance

L'étude de la performance du régulateur répétitif élémentaire est composée d'une part de la performance en suivi de consigne et d'autre part du rejet des perturbations périodiques et du couple de charge.

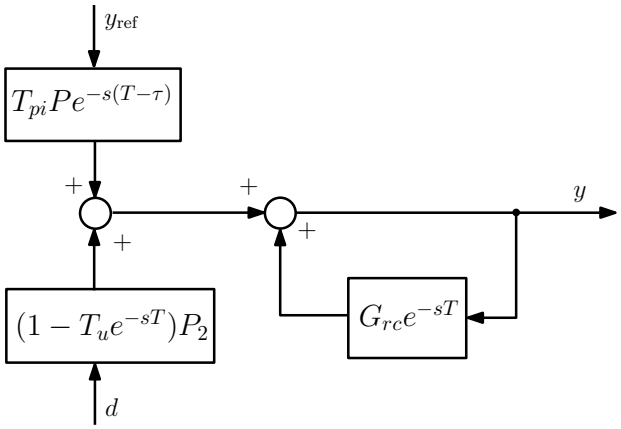

Figure 5.7: Représentation alternative du système avec régulateur répétitif élémentaire.

Performance en suivi de consigne

Selon le théorème de la valeur finale [118] et l'Eq. 5.17 et si nous supposons que la consigne est un échelon d'amplitude A, alors pour un système stable, l'erreur provoquée par le suivi de ce signal est

$$e_{\text{step}}(\infty) = \lim_{t\to+\infty} e_{\text{step}}(t) = \lim_{s\to 0} sH_{\text{rcd}}(s)\frac{A}{s} = H_{\text{rcd}}(0)A = \frac{1-T_u(0)}{1-G_{rc}(0)}A. \quad (5.23)$$

Par conséquent, lorsque $T_u(0)=1$, ce système peut suivre cet échelon de consigne sans erreur en régime permanent. Ensuite, si nous supposons que la consigne est une rampe de perte B, alors pour un système stable, l'erreur provoquée par le suivi de ce signal est

$$e_{\text{ramp}}(\infty) = \lim_{t\to+\infty} e_{\text{ramp}}(t) = \lim_{s\to 0} sH_{\text{rcd}}(s)\frac{B}{s^2} = \lim_{s\to 0} \frac{1-T_u(s)e^{-sT}}{s\left(1-G_{rc}(s)e^{-sT}\right)}B. \quad (5.24)$$

Ceci montre que pour ce système, le suivi d'une rampe provoque une erreur en régime permanent. Quand $\lim_{s\to 0} T_u(s)=1$, cette erreur est égale à $T/(1-G_{rc}(0))$, mais dans les autres cas, elle augmentera continuellement avec le temps.

Rejet des perturbations

À partir de l'Eq. 5.17, l'amplitude de l'erreur provoquée par une perturbation périodique est calculée par

$$|E_d(j\omega_k)| = \left|\frac{1-T_u(j\omega_k)}{1-G_{rc}(j\omega_k)}\right| |P_2(j\omega_k)D(j\omega_k)| = |H_{\text{rcd}}(j\omega_k)||P_2(j\omega_k)D(j\omega_k)|,$$

$$\forall \omega_k = k\omega_1 = k\frac{2\pi}{T}, \quad (5.25)$$

Dans cette équation, k est un nombre entier positif. L'Eq. 5.25 montre l'amplitude de l'erreur qui provient de la perturbation périodique est $|H_{\rm rcd}(j\omega_k)P_2(j\omega_k)D(j\omega_k)|$. Lorsque $|H_{\rm rcd}(j\omega_k)| < 1$, ce système est capable de rejet les perturbations périodiques.

Selon l'Eq. 5.17 et quelques publications existantes [11, 119], pour un régulateur répétitif, la capacité de rejet de perturbations périodiques provient du terme $1-T_u e^{-sT}$. Quand T_u est une constante proche de 1, nous avons $e^{-sT}=1$. Lorsque $\omega=2k\pi/T$, le terme $H_{\rm rcd}(j\omega)$ approche zéro. En conséquence, les perturbations de fréquence $\omega_k = 2k\pi/T$ peuvent être largement compensées. En revanche, quand T_u est une fonction de transfert, le terme $1-T_u(s)e^{-sT}$ peut être écrit comme $1-|T_u(j\omega)|e^{j\phi(\omega)-\omega T}$, où $\phi(\omega)$ est la phase de $T_u(s)$. C'est uniquement quand la fréquence du signal satisfait l'équation

$$\omega-\frac{\phi(\omega)}{T}=\frac{2\pi k}{T},$$

que le régulateur rejette la perturbation. Cependant, cette fréquence n'est plus un multiple entier de celle de la perturbation fondamentale ($2\pi/T$). Donc, il faut choisir T_u comme une constante proche d'un et désormais, T_u sera considéré comme une constante dans le reste du rapport.

Le rejet du couple de charge doit également être pris en compte aussi pour évaluer la performance de ce système. Selon l'Eq. 5.17, l'erreur causée par le couple de charge est

$$e_{\rm load}(\infty)=\lim_{t\to\infty} e_{\rm load}(t)=\lim_{s\to 0} sH_{\rm rcd}(s)P_2(s)\frac{B_d}{s}. \tag{5.26}$$

Si nous utilisons le modèle présenté par l'Eq. 5.18, il vient

$$e_{\rm load}(\infty)=\frac{1-T_u(0)}{1-G_{rc}(0)}P_2(0)B_d. \tag{5.27}$$

Il faut donc que $T_u = 1$, pour complètement supprimer l'erreur provoquée par le couple de charge.

En outre, la compensation des perturbations périodiques réalisée par une CR ne peut pas être obtenue instantanément. La vitesse de convergence du rejet doit aussi être considérée comme une performance importante. Pour le système de CR élémentaire, cette vitesse est déterminée par $|G_{rc}(j\omega)|$ [104].

5.3.4 "Current feedback repetitive controller"

L'utilisation du système de CR élémentaire sera sérieusement degradée par une mauvaise performance en suivi de consigne. Cette limitation est due à la non-utilisation de la valeur actuelle de l'erreur. L'amélioration de la performance en

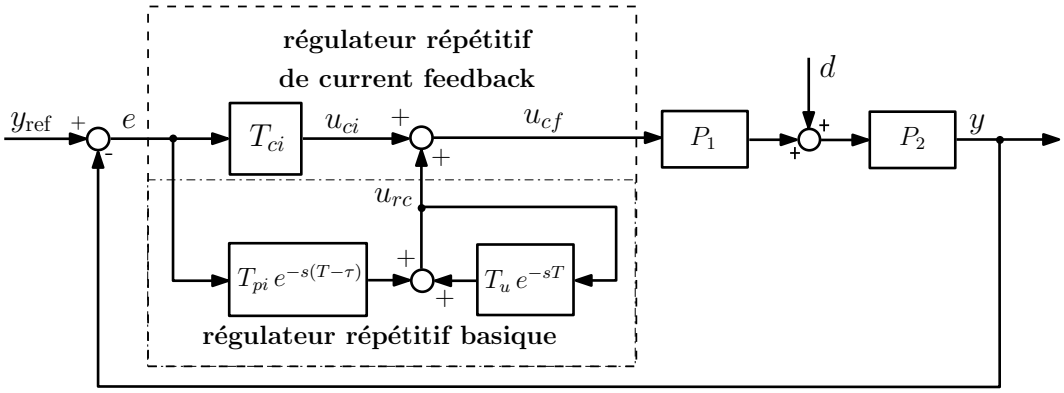

Figure 5.8: Représentation du système de current feedabck (dans notre cas, $T_{ci} = K_{ps}+K_{is}/s$, $u_{cf} = i_{\text{qref}}$, $T = 2\pi/\omega_m$ et y_{ref}, y, d et P_1 et P_2 sont définis par l'Eq. 5.5).

suivi de consigne peut être obtenu en ajoutant un terme déduit de l'erreur actuelle au régulateur répétitif. Ceci peut être réalisé en associant un contrôleur conventionnel au régulateur répétitif. De plus, nous espérons que l'utilisation de la CR ne bouleversera pas les structures existantes. Ceci demande que le régulateur répétitif ne remplace pas les contrôleurs (régulateurs) existants, mais coopère avec eux. En conséquence, une nouvelle sorte de régulateur répétitif, qui est constitué d'un régulateur répétitif élémentaire et d'un contrôleur (régulateur) conventionnel, est étudié. En raison de l'intégration du contrôleur conventionnel, la sortie de ce nouveau régulateur répétitif contient non seulement les informations passées, mais aussi les informations actuelles. Ce type de régulateur hybride est appelé "current repetitive controller" [107].

Il y a différentes manières de développer un "current repetitive controller" [107]. Cependant, du fait des objectifs de cette thèse, ainsi que de leur importance et de leur popularité, le "current feedback repetitive controller" et le "current iteration repetitive controller" sont considérés et étudiés dans ce mémoire.

D'abord, considérons le "current feedback repetitive controller". Ce régulateur a été d'abord étudié pour atteindre la minimisation des perturbations périodiques d'un onduleur PWM [120]. Dans cet article, un régulateur répétitif élémentaire et un régulateur PID prédictif fonctionnent ensemble. Les résultats montrés dans cet article prouvent que cette commande mixte peut fournir un bon suivi de consigne sans délai et une erreur statique nulle. La fonction de transfert du "current feedback repetitive controller" est

$$U_{cf}(s) = T_{ci}(s)E(s)+U_{rc}(s) = T_{ci}(s)E(s)+\frac{T_{pi}(s)e^{-s(T-\tau)}}{1-T_u e^{-sT}}E(s),$$

$$\text{donc } C_{cf}(s) = \frac{U_{cf}(s)}{E(s)} = \frac{T_{ci}(s)(1-T_u e^{-sT}) + T_{pi}(s)e^{-s(T-\tau)}}{1-T_u e^{-sT}}. \tag{5.28}$$

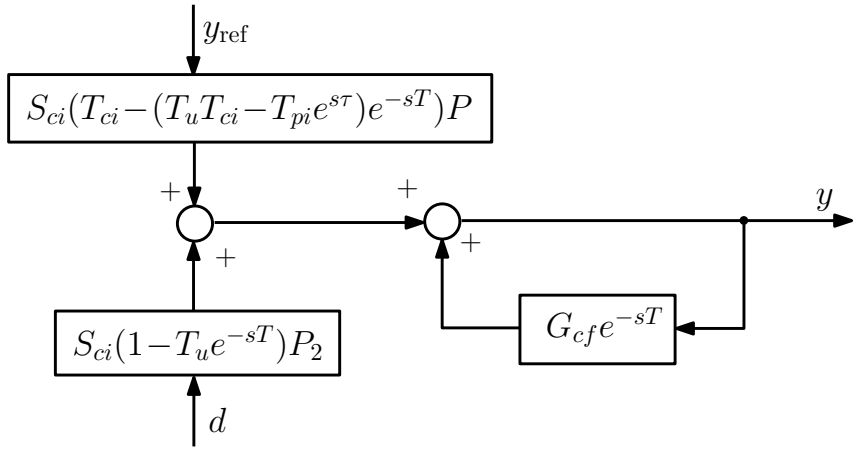

Figure 5.9: Présentation alternative du système de “current feedback”.

où T_{ci} représente le contrôleur (régulateur) conventionnel.

La structure typique du système en boucle fermée basée sur celle commande mixte est représentée par la Fig. 5.8. La fonction de transfert entre l'entrée y_{ref}, la sortie y et la perturbation d est [7]

$$\begin{aligned} Y &= \frac{(T_{ci}P-(T_uT_{ci}-T_{pi}e^{s\tau})Pe^{-sT})Y_{\text{ref}}+(1-T_ue^{-sT})P_2D}{(1+T_{ci}P)-((1+T_{ci}P)T_u-T_{pi}Pe^{s\tau})e^{-sT}} \\ &= H_{\text{cfr}}Y_{\text{ref}}+H_{\text{cfd}}P_2D, \end{aligned} \tag{5.29}$$

$$\text{avec}\ \ H_{\text{cfr}} = S_{ci}\frac{\left(T_{ci}-(T_uT_{ci}-T_{pi}e^{s\tau})e^{-sT}\right)P}{1-G_{cf}e^{-sT}},\ \ H_{\text{cfd}}=S_{ci}\,H_{\text{cfd2}},$$

$$H_{\text{cfd2}} = \frac{1-T_ue^{-sT}}{1-G_{cf}e^{-sT}},\ \ G_{cf}=T_u(1-T_{pi2}S_{ci}Pe^{s\tau})\ \text{ et }\ S_{ci}=\frac{1}{1+T_{ci}}.$$

S_{ci} est la fonction de sensibilité du système en boucle fermée lors de l'utilisation de la commande conventionnelle ($H_{\text{cid}} = S_{ci}$ quand $T_u = T_{pi} = 0$). À partir de l'Eq. 5.29, la relation entre e, y_{ref} et d est

$$E=\frac{1-T_ue^{-sT}}{(1+T_{ci}P)-((1+T_{ci}P)T_u-T_{pi}Pe^{s\tau})e^{-sT}}(Y_{\text{ref}}-P_2D)=H_{\text{cfd}}(Y_{\text{ref}}-P_2D). \tag{5.30}$$

Toutes les conclusions suivantes seront déduites des l'Eq. 5.29 et l'Eq. 5.30.

Stabilité et performances

Comme le cas du régulateur répétitif élémentaire, ici nous devons étudier la stabilité et les performances du “current feedback controller”. Tout d'abord, le système montré par la Fig. 5.8 peut être représenté comme la Fig. 5.9. À partir de cette figure, nous pouvons confirmer que la stabilité de ce système est aussi associée à trois termes : $S_{ci}(T_{ci}+T_{pi}e^{-s(T-\tau)})P$, $S_{ci}(1-T_ue^{-sT})P_2$ et un système en boucle

fermée qui contient $G_{cf}e^{-sT}$. T_{ci} est un régulateur PI, nous pouvons écrire

$$S_{ci}(s)=\frac{s^2T_d(1+sT_d)}{T_d^2s^3+T_ds^2+KK_{ps}s+KK_{is}}, \tag{5.31}$$

T_u était une constante, cet équation montre que la stabilité de $(1-T_ue^{-sT})S_{ci}P_2$ est liée seulement à S_{ci}. D'autre part

$$\begin{aligned} &S_{ci}(T_{ci}-(T_uT_{ci}-T_{pi}e^{s\tau})e^{-sT})P= \\ &(1-e^{-sT})T_{ci}PS_{ci}+(1-T_u)T_{ci}PS_{ci}e^{-sT}+T_{pi}PS_{ci}e^{-sT}, \end{aligned} \tag{5.32}$$

Selon l'équation ci-dessus, lorsque $(1-e^{-sT})T_{ci}PS_{ci}$, $(1-T_u)T_{ci}PS_{ci}$ et $T_{pi}PS_{ci}$ sont stables en même temps, la stabilité de $S_{ci}(T_{ci}-(T_uT_{ci}-T_{pi}e^{s\tau})e^{-sT})P$ peut être assurée. Parmi les trois termes, la stabilité de $(1-e^{-sT})T_{ci}PS_{ci}$ et $(1-T_u)T_{ci}PS_{ci}$ peut être garantie par un S_{ci} stable. Ensuite, afin d'utiliser le théorème du petit gain, on dois assurer aussi la stabilité de G_{cf}, qui, en effet, est aussi liée à le S_{ci} et $T_{pi}P$ ensemble. Selon l'analyse ci-dessus, nous pouvons conclure que quand S_{ci} et $T_{pi}P$ sont stables, une condition de la stabilité suffisante s'écrit

$$|G_{cf}(j\omega)|=\left|T_u-\frac{T_{pi}(j\omega)P(j\omega)e^{j\omega\tau}}{1+T_{ci}(j\omega)P(j\omega)}\right|=\left|T_u-S_{ci}(j\omega)T_{pi}(j\omega)P(j\omega)e^{j\omega\tau}\right|<1, \quad \forall\omega\in[0,+\infty[\tag{5.33}$$

La performance en suivi de consigne est examinée pour un signal échelon et un signal rampe. Nous supposons que le signal échelon est $A\cdot\Gamma(t)$ et le signal rampe est $B\cdot t\cdot\Gamma(t)$. Selon l'Eq. 5.30 et le théorème de la valeur finale, les erreurs qui proviennent du suivi des deux signaux pour un système stable sont

$$e_{\text{step}}(\infty) = S_{ci}(0)\frac{1-T_u}{1-G_{cf}(0)}A \tag{5.34}$$

$$\text{et}\quad e_{\text{ramp}}(\infty) = \lim_{s\to0}\frac{S_{ci}(s)}{s}\frac{1-T_ue^{-sT}}{1-G_{cf}(s)e^{-sT}}B. \tag{5.35}$$

Les équations ci-dessus indiquent que $S_{ci}(0)=0$ garantie la poursuite sans erreur en régime permanent. La composition d'une perturbation périodique est determinée par

$$|E_d(j\omega_k)|=|S_{ci}(j\omega_k)H_{\text{cfd2}}(j\omega_k)|\,|P_2(j\omega_k)D(j\omega_k)|. \tag{5.36}$$

$|H_{\text{cfd2}}(j\omega_k)|$ représente la différence entre un système de "current feedback" et un système avec un contrôleur (régulateur) conventionnel seulement. Ensuite, la vitesse de convergence est reliée à $|G_{cf}(j\omega)|$ [104].

Enfin, le rejet du couple de charge est calculée par

$$e_{\text{load}}(\infty)=\lim_{t\to+\infty} e_{\text{load}}(t) = \lim_{s\to 0} sS_{ci}(s)\frac{1-T_u e^{-sT}}{1-G_{cf}(s)e^{-sT}}P_2(s)\frac{B_d}{s}.$$
$$= \left(\lim_{s\to 0} S_{ci}(s)P_2(s)\right)\frac{1-T_u}{1-G_{cf}(0)}B_d. \tag{5.37}$$

Ceci montre que l'élimination de l'influence du couple de charge peut être réalisée par $\lim_{s\to 0} S_{ci}(s)P_2(s)=0$ ou $T_u=1$.

Conception du régulateur répétitif

Nous allons essayer de concevoir un "current feedback repetitive controller" afin d'obtenir un équilibre entre la complexité de conception, la robustesse de la stabilité, le rejet de perturbation et la vitesse de convergence. Pour cela, nous pouvons choisir T_u et T_{pi} comme constantes. La condition de stabilité de l'Eq. 5.33 peut être écrite comme

$$|G_{cf}(j\omega)|=|T_u|\left|1-K_{pi}e^{j\omega\tau}S_{ci}(j\omega)P(j\omega)\right|<1, \quad \forall\omega\in[0,+\infty) \tag{5.38}$$

Dans cette équation, $K_{pi}=T_{pi}/T_u$. Alors, selon l'Eq. 5.38, nous pouvons trouver que

$$G_{cf}(0)=T_u \text{ et } \lim_{\omega\to+\infty} G_{cf}(j\omega)=T_u, \tag{5.39}$$

ce qui indique que $|T_u|<1$ est une condition nécessaire pour assurer la stabilité. À partir de l'Eq. 5.30, le niveau de réduction de la perturbation périodique peut être écrit comme

$$|H_{\text{cfd}}(j\omega_d)|=(1-T_u)\frac{|S_{ci}(j\omega_d)|}{|1-G_{cf}(j\omega_d)|}, \tag{5.40}$$

$$\text{et donc } |1-G_{cf}(j\omega_d)|=(1-T_u)\left|\frac{S_{ci}(j\omega_d)}{H_{\text{cfd}}(j\omega_d)}\right|. \tag{5.41}$$

L'Eq. 5.41 montre que l'ensemble des valeurs complexes résultant de $|H_{\text{cfd}}(j\omega_d)|$ et T_u choisis est un cercle centré sur (1, 0) avec un rayon $(1–T_u)|S_{ci}(j\omega_d)|/|H_{\text{cfd}}(j\omega_d)|$, conformément à la Fig. 5.10. Si $|G_{cf}(j\omega_d)|$ devient plus petit, la convergence deviendra plus rapide. Car $|G_{cf}(j\omega_d)|$ est liée à la position de M, qui est située sur l'axe réel, comme montré par la Fig. 5.10. Cela demande

$$G_{cf}(j\omega_d)=1-(1-T_u)\frac{|S_{ci}(j\omega_d)|}{|H_{\text{cfd}}(j\omega_d)|}$$

$$\text{avec } G_{cf}(j\omega_d)=T_u(1-K_{pi}e^{j\omega_d\tau}S_{ci}(j\omega_d)P(j\omega_d)). \tag{5.42}$$

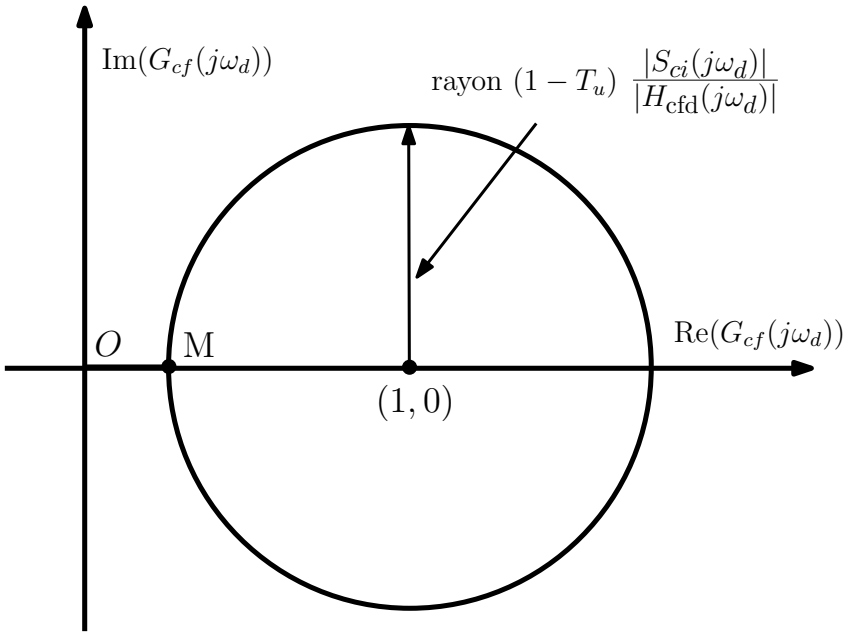

Figure 5.10: Valeurs possibles de $|G_{cf}(j\omega_d)|$ permettant d'obtenir une valeur de $|G_{cf}(j\omega_d)|$ désirée.

Ce sera possible si K_{pi} et τ sont choisis comme

$$K_{pi} = |Z|, \text{ et } \tau = \frac{1}{\omega_d}\text{Arg}(Z),$$
$$\text{avec } Z = K_{pi}e^{j\omega_d\tau} = \frac{1}{S_{ci}(j\omega_d)P(j\omega_d)}\left(1 - \frac{G_{cf}(j\omega_d)}{T_u}\right). \tag{5.43}$$

Ici, $|H_{\text{cfd}}(j\omega_d)|$ ne peut pas être choisi trop petit, puisque la condition $|G_{cf}(j\omega_d)| < 1$ indique que

$$|H_{\text{cfd}}(j\omega_d)| > \frac{1-T_u}{2}|S_{ci}(j\omega_d)|. \tag{5.44}$$

Finalement, avec le contrôleur conventionnel choisi comme un régulateur PI, on peut obtenir $S_{ci}(0) = 0$. Donc ce système est capable de suivre un échelon et une rampe sans erreur statique. De même, il n'y aura pas d'erreur statique venu du couple de charge.

La méthodologie de conception proposée est appliquée à une MSAP et testée d'abord par des simulations. La vitesse nominale $V = 60$ rpm, conduit à $T = 1$ s. Pour équilibrer la stabilité et les performances, nous choisirons $T_u = 0.9$. La principale composante de perturbation est la 24ème harmonique ($k_d = 24$, $\omega_d = 48\pi$) et nous voulons réduire de 90 % cette composante ($|H_{\text{cfd}}(48\pi)| = 0.1$). Les Eq. 5.8 et Eq. 5.43, conduisent à $K_{pi} = 17.74$ A·s/rad et $\tau = 841$ μs.

Grâce à la SOM, S_{ci} et $S_{ci}P$ sont stables, alors, selon l'Eq. 5.38, G_{cf} est également stable. Par conséquent, la stabilité du système peut être présentée par un dia-

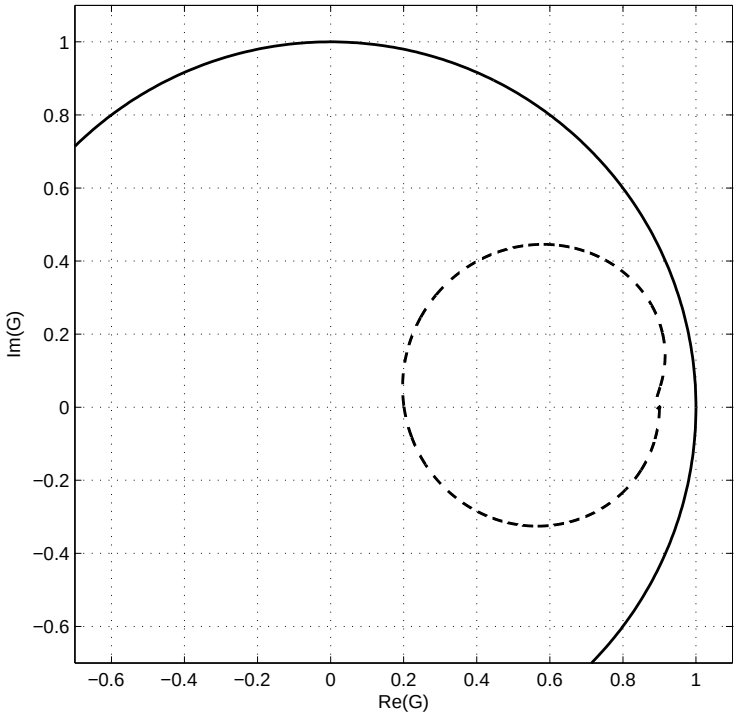

Figure 5.11: Diagramme de Nyquist de G_{cf} comparée au cercle unité. La valeur maximale de $|G_{cf}|$ est 0.93 et se situe à $96.8\,$Hz.

gramme de Nyquist de G_{cf}, ce qui est montré par la Fig. 5.11. La valeur maximale de $|G_{cf}|$ est 0.93. Ce chiffre confirme que le système en boucle fermée est stable, car G_{cf} satisfait l'Eq. 5.38.

La Fig. 5.12 montre l'analyse de la stabilité de la robustesse du régulateur proposé. Avec les valeurs supposées des K et de T_d, nous pouvons obtenir un régulateur répétitif. Ce diagramme montre la stabilité du système de ce régulateur répétitif lorsque les valeurs réelles sont $K_{\text{real}} = \mu_k K$ et $T_{\text{d,real}} = \mu_T T_d$. Plus précisément, cette figure montre si Max$|G_{\text{cf,real}}|$ est inférieure (zones blanches) ou supérieure (zones noires) à 1, avec

$$|G_{\text{cf,real}}(j\omega)| = |T_u| \left| 1 - K_{pi} e^{j\omega\tau} \frac{P_{\text{real}}(j\omega)}{1 + T_{ci}(j\omega) P_{\text{real}}(j\omega)} \right| \tag{5.45}$$

$$\text{et} \quad P_{\text{real}}(j\omega) = \frac{\mu_K K}{j\omega\mu_T T_d (1 + j\omega\mu_T T_d)}, \qquad \forall\omega \in [0, +\infty)$$

Comme il est montré par la Fig. 5.12, ce système reste stable même avec $\pm 50\,\%$ d'incertitude sur K et T_d. Par conséquent, le régulateur répétitif proposé apporte une bonne robustesse de stabilité au système.

Les performances en suivi de consigne et en rejet des perturbations sont présentées par la Fig. 5.13. La courbe supérieure montre que $|H_{\text{cfr}}(j\omega)|$ est presque constant jusqu'à $6\,$Hz et comporte ensuite plusieurs résonances à des fréquences plus

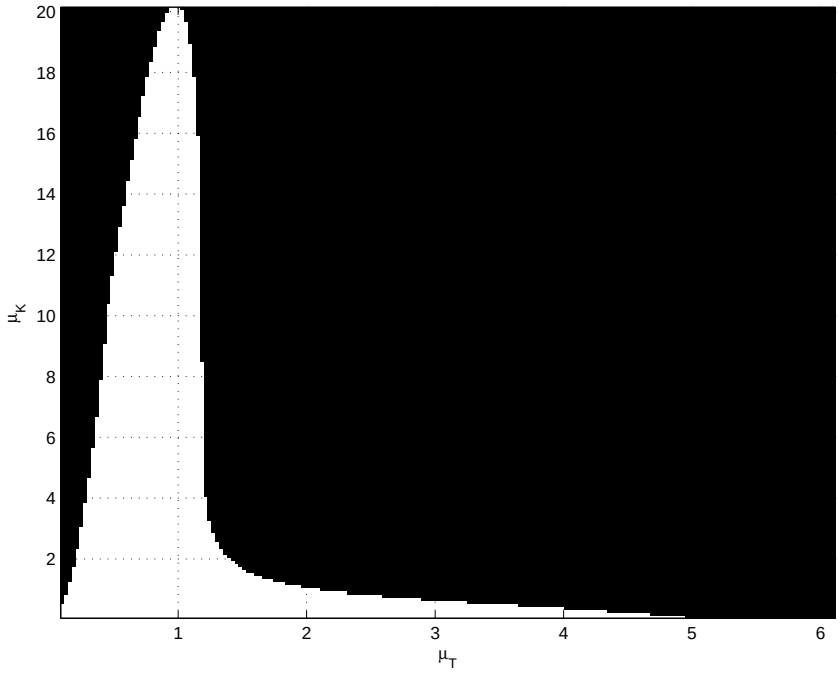

Figure 5.12: Analyse de la robustesse de la stabilité du système de current feedback.

élevées. Ces résonances peuvent causer des dépassements et des oscillations pendant les transitoires lorsque la référence est un échelon. Aux très basses fréquences, les perturbations sont complètement rejetées (car $S_{ci}(j\omega) = 0$ et $|H_{\text{cfd2}}(0)| = 1$, donc $|H_{\text{cfd}}(0)| = 0$). Comme spécifié dans la conception, la réduction des perturbations est meilleure que 20 dB jusqu'à la 24ème harmonique. Comme $|S_{ci}(48\pi)| \approx -2$ dB, cette figure montre clairement l'avantage apporté par le régulateur répétitif. Aux fréquences plus élevées, $|H_{\text{cfd}}(j\omega_k)|$ tend vers un (car $|S_{ci}(j\omega_k)|$ et $|H_{\text{cfd}}(j\omega_k)|$ tendent vers un), mais les perturbations hautes fréquences seront réduites par le processus P_2.

La Fig. 5.14 montre la courbe entre 0 et 30 Hz de $|G_{cf}(j\omega)|$, qui indique la vitesse de convergence pour une perturbation sinusoïdale. Le minimum de cette fonction est situé à environ 24 Hz, où sa valeur est d'environ 0.2. Par conséquent, la convergence de cette perturbation peut être accomplie en 5 itérations. La valeur de la convergence la plus mauvaise dans cette gamme est de 0.9, ce qui conduit à une convergence qui durera près de 65 itérations.

La réponse temporelle de ce système est testée par simulation. Au cours des 50 secondes de simulation, la référence (consigne) change trois fois. Elle évolue à 1 et à 25 s aux échelons et de 44 à 50 s comme une rampe. Pendant ce temps, un couple de charge de 20 N·m influe sur le système entre 16 et 25 s et entre 35 et 50 s. La perturbation périodique commence à 6 s. Elle est composée d'une seule sinusoïde de 24 Hz jusqu'à 27 s. Ensuite, une sinusoïde de 8 Hz est également ajoutée.

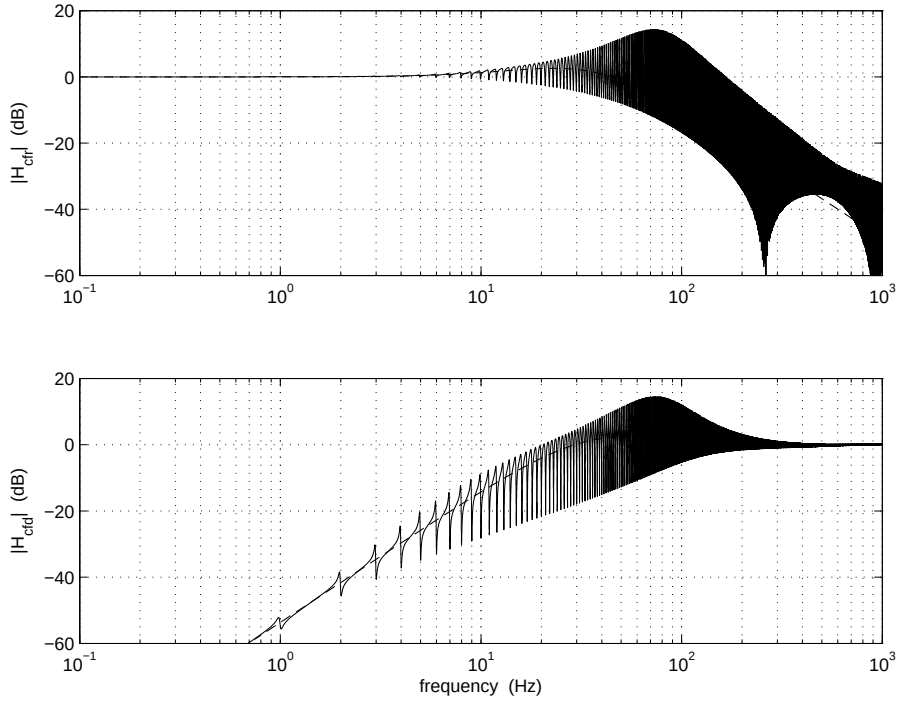

Figure 5.13: Diagrammes de Bode de H_{cfr} et H_{cfd}, comparés à ceux obtenus avec le régulateur PI seulement.

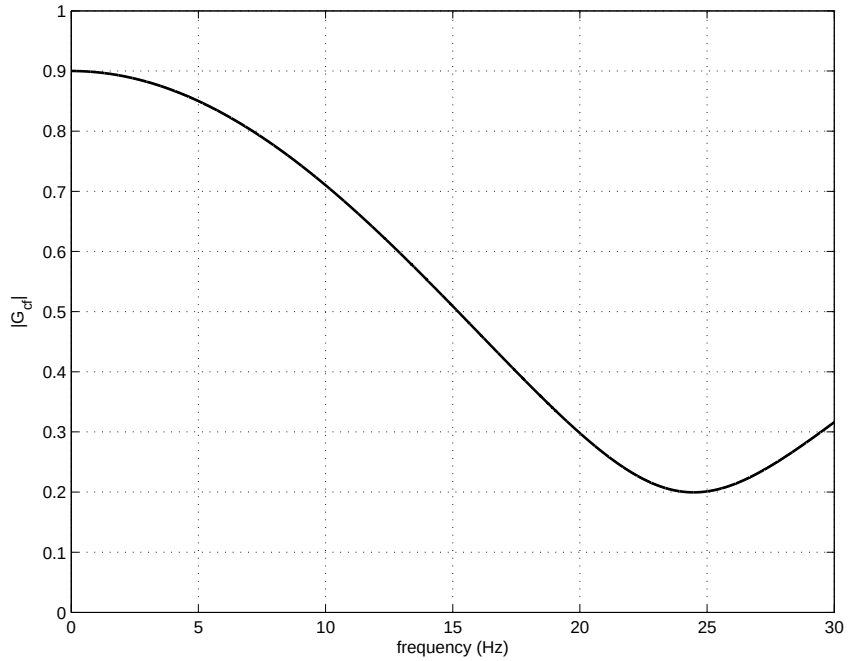

Figure 5.14: Diagramme de $|G_{cf}(j2\pi f)|$ indiquant les vitesses de convergence de signaux sinusoïdaux avec le "current feedback repetitive controller" proposé.

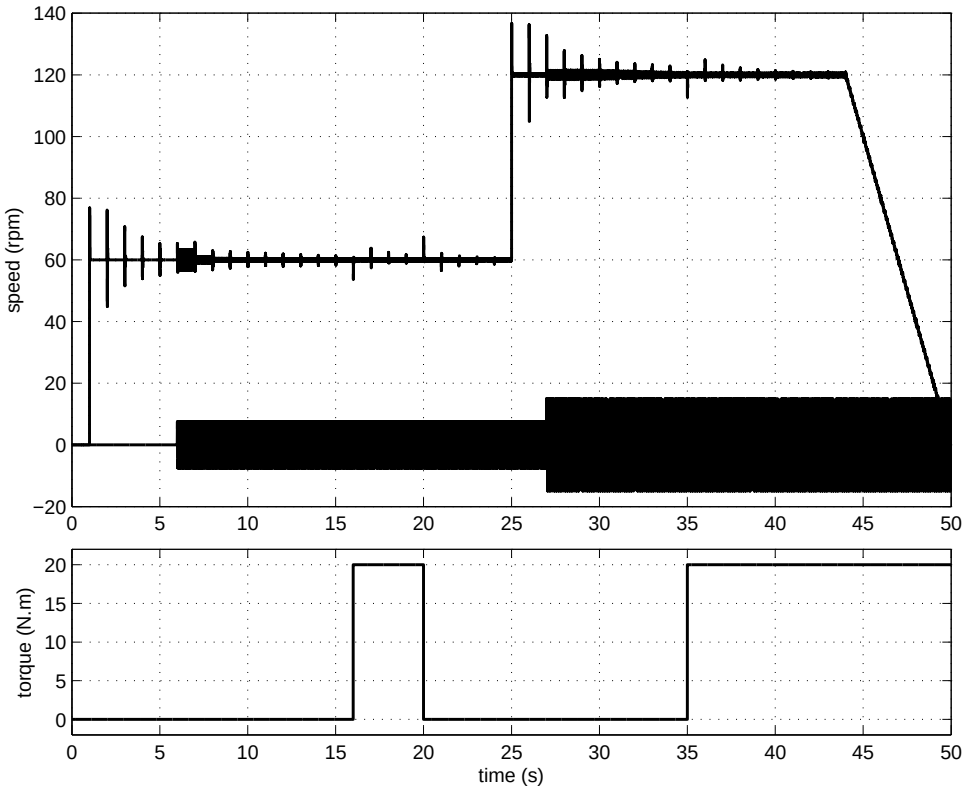

Figure 5.15: Résultats de simulation du système de “current feedback” proposé.

Les résultats obtenus par le système de “current feedback” sont présentés à la Fig. 5.15. Un système contrôlé par un régulateur PI seul, est utilisé comme élément de comparaison et est également testé par la même simulation, dont les résultats sont présentés par la Fig. 5.16. Le couple de charge, la perturbation et l'entrée sont également visualisées sur ces figures afin de faciliter l'analyse. Ces figures montrent que les deux systèmes ont presque la même réponse au couple de charge. En raison du régulateur PI, une référence en échelon provoque le même dépassement dans les deux systèmes. Cependant, dans le système de CR, à cause de la transmission directe de la référence à T_{pi} et aussi du délai, une série d'oscillations supplémentaires faisant écho au premier dépassement apparaît, comme le monte la Fig. 5.15. Ces oscillations durent plusieurs itérations et dégradent considérablement la performance en suivi de consigne. La réduction présentée par la Fig. 5.15 coïncide exactement avec l'analyse théorique précédente. La valeur crête-à-crête des oscillations de vitesse provoquée par la 24ème harmonique a diminué de 3.312 à 0.438 rpm en seulement 4 s, donc 86.7 % de l'amplitude de cette oscillation peut être éliminé dans une courte période. Ce résultat confirme une capacité de réduction excellente sur la perturbation principale. En outre, après 27 s, en raison de l'arrivée de la 8ème harmonique, la convergence de la perturbation mélangée de la 8ème et de la 24ème harmonique est plus lente que celle de la 24ème harmonique seule. Les résultats ci-dessus montrent que la capacité de réduction des perturbations périodiques apportée

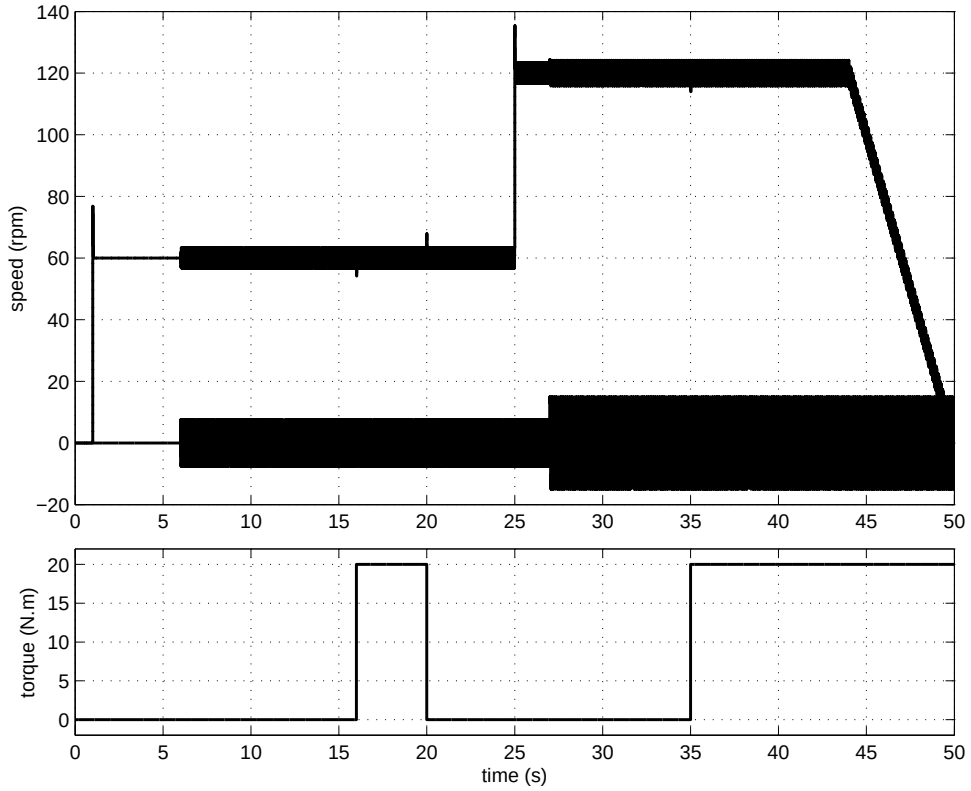

Figure 5.16: Résultats de simulation du système conventionnel (avec le régulateur PI seulement).

par le régulateur répétitif est bien meilleure que celle d'un régulateur PI. Cependant, nous devons constater que le dépassement produit par le régulateur répétitif dégradent sérieusement les performances de suivi de consigne de ce système.

5.3.5 "Current iteration repetitive controller"

Cette sous-section est consacrée à la présentation d'un autre "current repetitive controller" important : le "current iteration repetitive controller". Une structure typique d'un système en boucle fermée contrôlé par un "current iteration repetitive controller" est montrée par la Fig. 5.17. Elle montre que la réalisation de ce système est assez similaire à celle du système de "current feedback". La distinction entre les deux est que l'entrée du "current iteration repetitive controller" comprend la sortie de T_{ci}. En revanche, l'entrée du "current feedback repetitive controller" ne contient pas cette sortie, ce qui conduit à des différences entre les deux systèmes.

La raison d'étudier ce régulateur est qu'il est développé à partir d'un régulateur répétitif largement utilisé, appelé "plug-in repetitive controller" [75, 79, 80]. La structure basique d'un "plug-in repetitive controller" est représentée par la Fig. 5.18. Elle montre que le "plug-in repetitive controller" ne contient qu'un seul délai. Pour montrer plus clairement la relation entre ces deux systèmes, le système de "plug-in

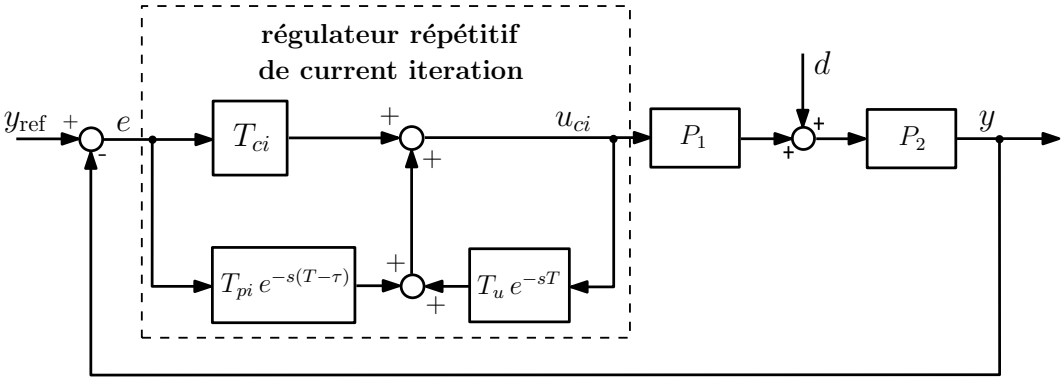

Figure 5.17: Représentation du système de current iteration (dans notre cas, $u_{ci} = i_{\text{qref}}$ et les autres symboles ont les mêmes définitions que dans la Fig. 5.8.

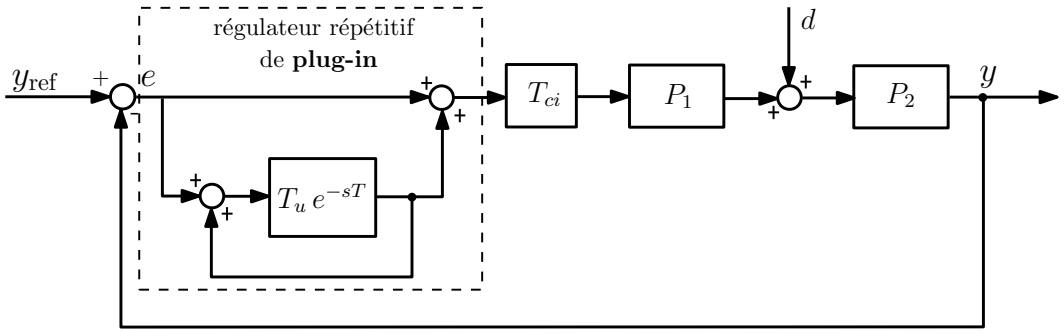

Figure 5.18: Schéma d'un système "plug-in RC system".

repetitive controller" peut être représenté de manière équivalente par la Fig. 5.19. Ensuite, la comparaison entre la Fig. 5.17 et la Fig. 5.19 montre que le "plug-in repetitive controller" n'est qu'un cas particulier ($T_{pi} = 0$ et $T_{ci} = 1$) du "current iteration repetitive controller". Par conséquent, les conclusions obtenues par le "current iteration repetitive controller" sont également valables pour le "plug-in repetitive controller". D'après la Fig. 5.17, la relation entre la sortie de système y, l'entrée du système y_{ref} et la perturbation d est

$$\begin{aligned} Y &= \frac{(T_{ci}+T_{pi}e^{-s(T-\tau)})PY_{\text{ref}}+(1-T_u e^{-sT})P_2 D}{(1+T_{ci}P)\left(1-\frac{T_u-T_{pi}Pe^{s\tau}}{1+T_{ci}P}e^{-sT}\right)} \\ &= H_{\text{cir}}\, Y_{\text{ref}} + H_{\text{cid}}\, P_2 D, \end{aligned} \tag{5.46}$$

$$\text{avec}\quad H_{\text{cir}} = S_{ci}\,\frac{(T_{ci}+T_{pi}\,e^{-s(T-\tau)})P}{1-G_{ci}\,e^{-sT}},\quad H_{\text{cid}} = S_{ci}H_{\text{cid2}},$$

$$H_{\text{cid2}} = \frac{1-T_u e^{-sT}}{1-G_{ci}e^{-sT}}\quad \text{et}\quad G_{ci} = S_{ci}\,G_{rc}.$$

Par ailleurs, la relation entre l'erreur e, y et y_{ref} est

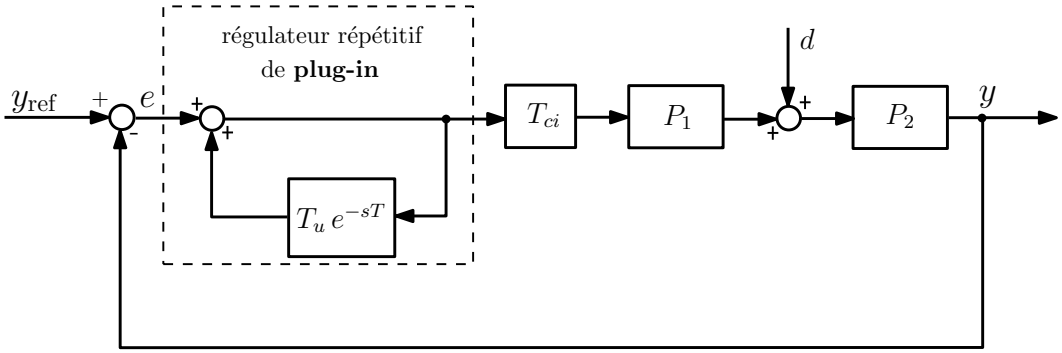

Figure 5.19: Schéma d'un système "plug-in RC system".

$$E = \frac{1-T_u e^{-sT}}{(1+T_{ci}P)(1-G_{ci}e^{-sT})} Y_{\text{ref}} - \frac{1-T_u e^{-sT}}{(1+T_{ci}P)(1-G_{ci}e^{-sT})} P_2 D = H_{\text{cid}}\,(Y_{\text{ref}} - P_2 D). \tag{5.47}$$

La similitude entre le "current feedback repetitive controller" et le "current iteration repetitive controller" a été mentionnée au début de cette sous-section. Ce paragraphe est dédié à analyser leur relation. Nous supposons que P, T_{ci}, T_u et τ sont identiques. T_{pi} dans le "current feedback repetitive controller" est noté T_{pi}^{cf}. Dans le "current iteration repetitive controller", il est noté T_{pi}^{ci}. La comparaison entre l'Eq. 5.46 et l'Eq. 5.29 indique que la relation

$$T_{pi}^{ci} = T_{pi}^{cf} - T_{ci}T_u e^{-s\tau}. \tag{5.48}$$

implique que $G_{ci} = G_{cf}$, $H_{\text{cid}} = H_{\text{cfd}}$ et $H_{\text{cir}} = H_{\text{cfr}}$. Alors, avec l'Eq. 5.48 et les hypothèses précédentes, le "current iteration repetitive controller" et le "current iteration repetitive controller" peuvent fournir la même robustesse de stabilité, la même performance de poursuite et la même capacité de réduction. Par conséquent, l'Eq. 5.48 est la condition qui peut rendre identiques le système de "current feedback" et le système de "current iteration".

Avec une conception présentée dans la section 2.6.3, la réponse temporelle du système de "current iteration" est montrée par la Fig. 5.20. Cette figure démontre que le "current iteration repetitive controller" offre une réduction de la perturbation périodique meilleure que son homologue qui est contrôlé par un régulateur PI. Mais, malheureusement, l'utilisation de ce régulateur, comme le "current feedback repetitive controller" apporte aussi des dépassements et des oscillations amorties gênants qui limitent sérieusement son application aux MSAPs.

5.3.6 "Non-overshooting step response repetitive controller"

Les résultats précédents montrent que la performance en suivi de consigne de tous les systèmes de CR présentés est dégradée en raison des dépassements et des

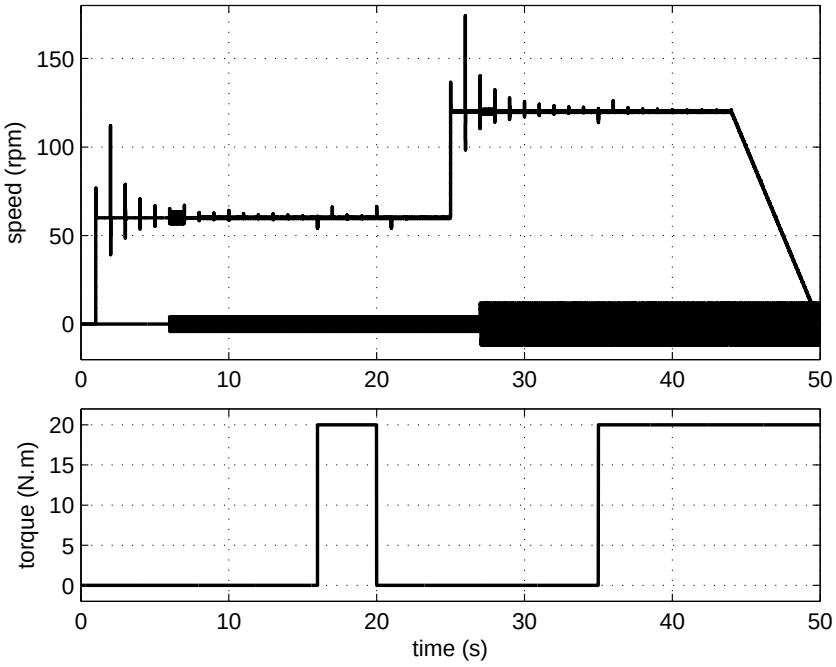

Figure 5.20: Résultats de simulation du système de "current iteration" proposé.

oscillations considérables. Par conséquent, dans cette sous-section, nous allons proposer un nouveau régulateur répétitif qui permet une amélioration significative de la performance en suivi de consigne, à tout en gardant la même réduction des perturbations périodiques que les autres régulateurs répétitifs. Avant de présenter ce nouveau régulateur, d'abord, nous devons expliquer pourquoi ces systèmes de CR souffrent de mauvaises performances de poursuite.

Le dépassement qui apparaît dans les systèmes précédents, en effet, est le résultat du zéro de T_{ci} (T_{ci} est choisi comme un régulateur PI dans les cas précédents). Les oscillations qui se produisent dans ces cas sont dus à la transmission directe de la référence à T_{pi} et la boucle fermée.

En conséquence, pour les éviter, on peut d'abord choisir un régulateur IP, au lieu d'un régulateur PI, comme contrôleur conventionnel [26], et ensuite part connecter T_{pi} à la sortie du processus seulement. La Fig. 5.21 montre un système, ou l'entrée de T_{pi} change de e à y_{ref}, mais l'entrée de T_u est inchangée. Dans le même temps, un régulateur de IP est utilisé en tant que contrôleur conventionnel. Le but de ce nouveau régulateur répétitif est de fournir une capacité de rejet des perturbations similaires aux autres systèmes de CR et une meilleure performance de poursuite. Parce que ce nouveau régulateur répétitif peut éliminer le dépassement et les oscillations produit par l'échelon, il est appelé le "non-overshooting step response (NOSR) repetitive controller". Selon la Fig. 5.21, la relation entre la sortie de système y, l'entrée de système y_{ref} et la perturbation d est

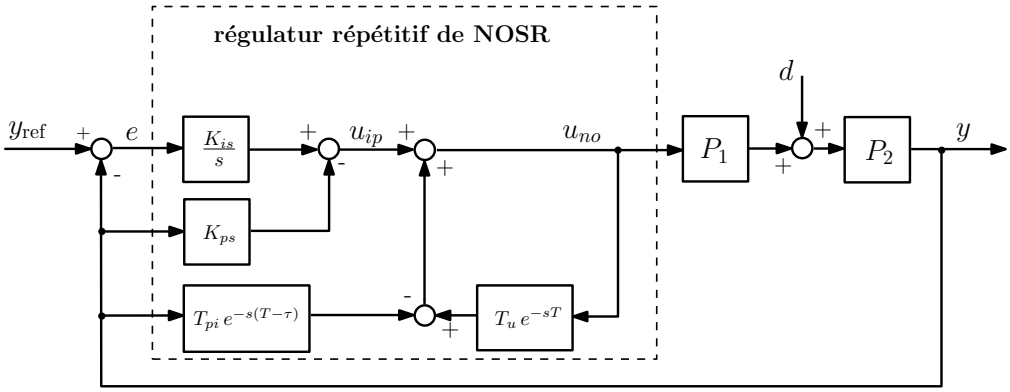

Figure 5.21: Schéma du système “NOSR” (dans notre cas, $u_{no} = i_{\text{qref}}$ et les autres symboles ont les mêmes définitions que dans la Fig. 5.17).

$$Y = \frac{K_{is}s^{-1}PY_{\text{ref}} + (1-T_u e^{-sT})P_2 D}{(1+K_{ps}P + K_{is}s^{-1}P) - (T_u - T_{pi}Pe^{s\tau})e^{-sT}} = H_{\text{nor}}\,Y_{\text{ref}} + H_{\text{nod}}\,P_2\,D,$$

$$\text{avec } H_{\text{nor}} = \frac{S_{ci}\,K_{is}\,P}{s}\,\frac{1}{1-G_{no}\,e^{-sT}},\quad H_{\text{nod}} = S_{ci}H_{\text{nod2}},\quad H_{\text{nod2}} = \frac{1-T_u\,e^{-sT}}{1-G_{no}\,e^{-sT}},$$

$$G_{no} = G_{ci} \text{ et } T_{pi} = K_{ps} + \frac{K_{is}}{s}. \tag{5.49}$$

La relation entre l’erreur e, y et y_{ref} est

$$\begin{aligned} E &= \frac{((1+K_{ps}P) - (T_u - T_{pi}Pe^{s\tau})e^{-sT})Y_{\text{ref}} + (1-T_u e^{-sT})P_2 D}{(1+K_{ps}P + K_{is}s^{-1}P) - (T_u - T_{pi}Pe^{s\tau})e^{-sT}} \\ &= H_{\text{nod}}\,(Y_{\text{ref}} - P_2\,D) + H_{\text{noe}}\,Y_{\text{ref}}, \end{aligned} \tag{5.50}$$

$$\text{avec } H_{\text{noe}} = S_{ci}\,\frac{(K_{ps} + T_{pi}\,e^{-s(T-\tau)})\,P}{1-G_{no}\,e^{-sT}}.$$

Les équations ci-dessus montrent $H_{\text{nod}} = H_{\text{cid}}$ et $G_{no} = G_{ci}$. En conséquence, ce système de “NOSR” proposé a la même capacité de réduction de perturbation que le système de "current iteration" en utilisant T_{ci} comme un régulateur PI. La conception proposée pour le système de "current iteration" peut être réutilisée pour le système de "NOSR".

Dans ce cas, avec le même réglage que celui utilisé dans le cas de "current iteration repetitive controller", la réponse temporelle d’un système “NOSR" est montrée par la Fig. 5.22. Les résultats présentés dans cette figure indiquent que la performance en suivi de consigne de ce système est presque égale au système conventionnel avec le régulateur de IP. La comparaison entre la Fig. 5.22 et la Fig. 5.20 prouve que le "NOSR" repetitive controller" peut fournir la même réduction des perturbations périodiques que le "current feedback repetitive controller".

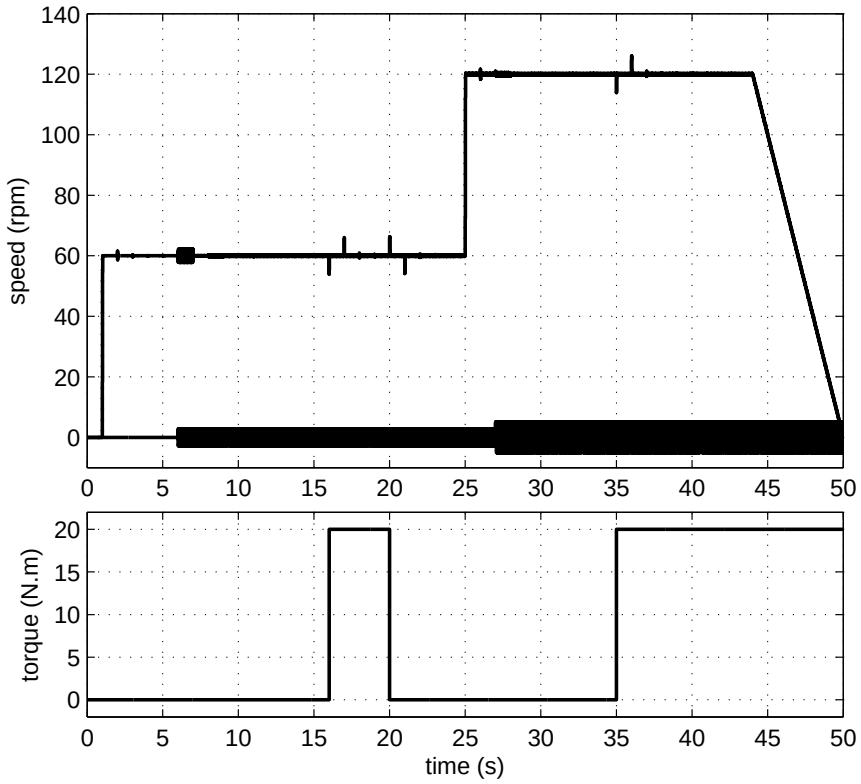

Figure 5.22: Résultats de simulation du système "NOSR" proposé.

5.4 Capteur répétitif intelligent et régulateur répétitif basé sur la position angulaire

Les paragraphes précédents ont déjà confirmé la capacité de la commande répétitive à réduire des oscillations de vitesse périodiques. Cependant, il est très difficile d'appliquer cette technique directement à une MSAP industrielle. Dans cette section, nous allons mettre en évidence certaines limitations de cette technique. Nous présenterons et étudierons aussi deux nouvelles techniques : le capteur répétitif intelligent et le régulateur répétitif basé sur la position angulaire, pour contribuer à l'utilisation d'une CR avec un actionneur industriel.

5.4.1 Capteur répétitif intelligent

Dans la section précédente, nous avons étudié le régulateur répétitif élémentaire et plusieurs régulateurs répétitifs avancés. Afin d'appliquer cette technique, nous constatons que les régulateurs existants doivent être remplacés. Ou, au moins, être modifiés. Malheureusement, dans certains cas, le contrôleur d'une MSAP vient d'une autre entreprise et est configuré à l'avance. Donc, le changement du con-

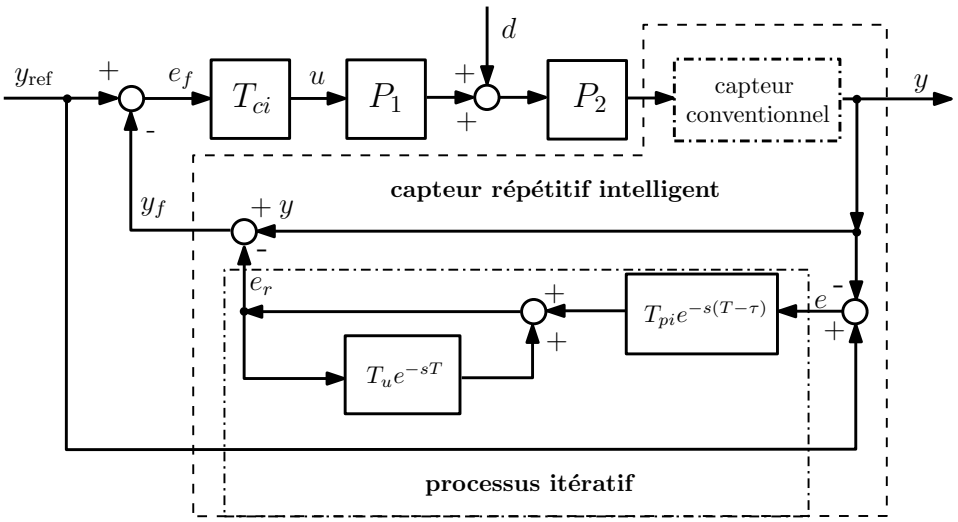

Figure 5.23: Schéma d'un système équipé d'un capteur répétitif intelligent.

trôleur est irréalisable et sa modification est également une tâche très compliquée.

Dans les MSAPs, la sortie du régulateur conventionnel est généralement déduite de l'erreur de vitesse, donc la modification de cette sortie peut être obtenue non seulement par la modification du régulateur, mais aussi par la modification de la mesure du vitesse, qui est une entrée du régulateur. Selon ce principe, nous proposons de mettre un processus itératif (un régulateur répétitif élémentaire) dans un capteur de vitesse conventionnel pour éviter la modification du contrôleur. Le capteur de vitesse avec un processus itératif est appelé capteur répétitif intelligent. Une fois l'efficacité de ce capteur répétitif intelligent garantie, la réduction souhaitée est obtenue sans modifier ou changer le contrôleur existant.

La structure de système en boucle fermée basé sur un capteur répétitif intelligent est représentée par la Fig. 5.23 [69]. Il faut noter que le capteur répétitif intelligent présenté ici est une première version de cette technique. Nous verrons un autre capteur intelligent plus avancé. Ce système, comme le montre la Fig. 5.23 contient deux parties : un capteur conventionnel et un processus itératif. Elles sont liées par une connexion quasi série.

Parce que dans le système de capteur répétitif intelligent, le processus itératif est intégré au capteur, la structure de ce système semble tout à fait différente des autres CR. Mais la vérité est que ce système de CR est seulement une sorte de système de CR avancée.

Pour mieux comprendre cela, dans un premier temps, le capteur intelligent présenté par la Fig. 5.23 peut être réarrangé comme selon la Fig. 5.24, dans laquelle le capteur intelligent répétitif apparait une CR avancée. Plus précisément, la comparaison entre la Fig. 5.24 et la Fig. 5.8 montre que la structure du capteur répétitif intelligent est très proche de celle d'un "current feedback".

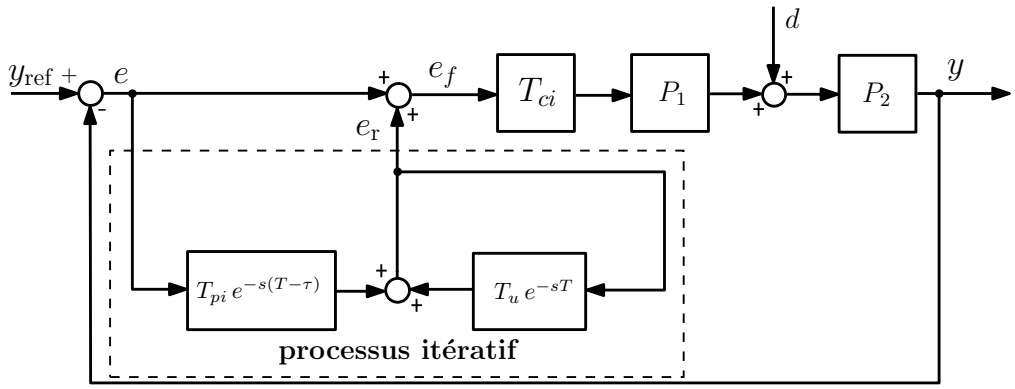

Figure 5.24: Représentation alternative du système équipé d'un capteur répétitif intelligent.

Capteur répétitif intelligent

L'analyse ci-dessus montre que le système proposé obtient les oscillations de vitesse directement de $y_{\text{ref}} - y$. Cela signifie que pour utiliser le capteur répétitif intelligent, un lien direct entre ce capteur intelligent et l'entrée de référence est nécessaire. Cependant, dans un système de MSAP commercial, ce type de connexion ne peut généralement pas être réalisé. Afin d'èliminer de cette connexion gênante, nous proposons une nouvelle version du capteur répétitif intelligent, capable d'obtenir l'information d'oscillation de vitesse de la sortie mesurée uniquement.

Lorsqu'un système de MSAP tourne à vitesse constante sans erreur statique, la vitesse mesurée est généralement constituée de deux composantes : la première est une composante constante qui doit être égale à la vitesse de référence et l'autre est une oscillation provoquée par les oscillations de couple. Par conséquent, l'information d'oscillation de vitesse peut être obtenue par un filtre passe-haut sans la connexion directe. Ce nouveau capteur intelligent peut alors être très facilement implanté dans un système de MASP industriel.

La structure typique de ce capteur intelligent est représentée par la Fig. 5.25, ou T_{hp} représente le filtre passe-haut. La sortie y_f inclut e_r et la sortie originale de processus. Afin de distinguer cette nouvelle version de l'ancienne, nous l'appelons capteur répétitif intelligent réaliste. La comparaison entre la Fig. 5.23 et la Fig. 5.25 montre que la différence entre les deux capteurs intelligents proposés est leur façon d'obtenir l'information de perturbation. Sur la Fig. 5.25, nous pouvons également observer que, avec ce nouveau capteur intelligent répétitif, l'implémentation de la CR n'aura plus besoin de modifier la commande du système actuel. Il suffira de remplacer le capteur conventionnel par un capteur répétitif intelligent. Cependant, sa réalisation demande un circuit numérique qui peut mettre en œuvre les fonctions de filtre passe-haut et de processus itératif. Selon la Fig. 5.23, la relation entre la

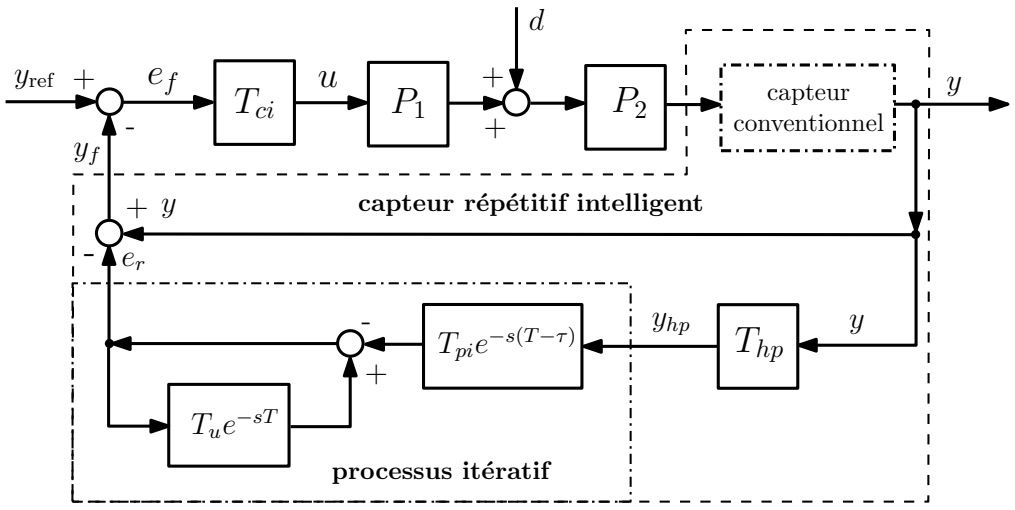

Figure 5.25: Schéma d'un système équipé d'un capteur répétitif intelligent avancé.

sortie de système y, l'entrée de système y_{ref} et la perturbation d est

$$\begin{aligned} Y &= \frac{(1-T_u e^{-sT})(T_{ci}PY_{\text{ref}}+P_2D)}{(1+T_{ci}P)-(T_u(1+T_{ci}P)-T_{pi}T_{ci}Pe^{s\tau})e^{-sT}} \\ Y &= H_{\text{psd}}\,(T_{ci}PY_{\text{ref}}+P_2D)=H_{\text{psr}}Y_{\text{ref}}+H_{\text{psd}}P_2D, \qquad (5.51) \\ \text{avec}\;\; H_{\text{psr}} &= H_{ci}H_{\text{psd2}},\;\; H_{\text{psd}}=S_{ci}H_{\text{psd2}},\;\; H_{\text{psd2}}=\frac{1-T_u e^{-sT}}{1-G_{ps}e^{-sT}} \\ \text{et}\;\; G_{ps} &= T_u-H_{ci}\,T_{pi}\,T_{hp}\,e^{s\tau}, \end{aligned}$$

Par ailleurs, la relation entre l'erreur e, y et y_{ref} est

$$\begin{aligned} E &= \frac{(1-T_u e^{-sT}+T_{pi}\,T_{hp}\,T_{ci}P\,e^{-s(T-\tau)})Y_{\text{ref}}-(1-T_u e^{-sT})P_2D}{(1+T_{ci}P)(1-G_{ps}e^{-sT})} \\ E &= H_{\text{psd}}(Y_{\text{ref}}-P_2D)+\frac{H_{\text{psr}}\,T_{pi}\,T_{hp}\,e^{-s(T-\tau)}}{1-T_u e^{-sT}}Y_{\text{ref}}. \qquad (5.52) \end{aligned}$$

Deux équations montrent les similarités entre le capteur répétitif intelligent et le "current feedback controller".

Conception du capteur répétitif intelligent

Afin d'utiliser cette technique, il est nécessaire de fournir une méthodologie de conception pour ce capteur intelligent qui peut garantir la stabilité et les performances du système. Les sections précédentes ont etudié la relation entre le système de "current feedback" et la première version du système de capteur répétitif intelligent. De plus, nous savons que la différence entre les deux systèmes de capteurs intelligents vient seulement de T_{hp}. Par conséquent, il est intéressant de savoir si la méthode de conception du système de "current feedback" est toujours adaptée

à ce nouveau capteur répétitif intelligent. Dans un premier temps, pour obtenir la réponse, nous supposons que le capteur répétitif intelligent est appliqué au même système "current feedback repetitive controller", donc T_{ci} et P sont les mêmes. En outre, nous supposons que T_{pi}, T_u et τ sont également identiques dans les deux systèmes. Alors, à partir d'une comparaison entre l'Eq. 5.29 et l'Eq. 5.51, nous pouvons déduire que

$$H_{\text{psd}} = \frac{1-G_{cf}e^{-sT}}{1-G_{ps}e^{-sT}} H_{\text{cfd}}, \quad \text{avec} \;\; G_{ps} = (1-T_{ci}T_{hp})T_u + T_{ci}T_{hp}G_{cf}, \tag{5.53}$$

ceci montre que généralement les deux système ont des conditions de stabilité, des capacités de réduction de perturbation différentes et des vitesses de convergence, sauf si

$$T_{hp} = \frac{1}{T_{ci}}. \tag{5.54}$$

Dans ce cas, $G_{ps} = G_{cf}$ et $H_{\text{psd}} = H_{\text{cfd}}$: le capteur répétitif intelligent et le "current feedback repetitive controller" partagent la même stabilité, la même réduction de perturbation et la même vitesse de convergence. Par conséquent, la règle de conception choisie pour le "current feedback repetitive controller" peut être réutilisée pour le capteur répétitif intelligent. Dans notre cas, T_{ci} est un régulateur PI, donc d'après l'Eq. 5.54

$$T_{hp} = \frac{s}{K_{is} + sK_{ps}}. \tag{5.55}$$

T_u et T_{pi} sont choisis comme des constantes, $K_{pi} = T_{pi}/T_u$ et τ sont issus d'une valeur souhaitée de $|H_{\text{psd}}(j\omega_d)|$ par l'Eq. 5.43. Pour le même processus et le même objectif de réduction, les paramètres du capteur répétitif intelligent devraient être les mêmes que pour le "current feedback repetitive controller".

Cependant, même si l'Eq. 5.54 est satisfaite, H_{cfr} et H_{psr} les performances de suivi de consigne seront encore différents. De l'analyse qui précède, il n'est pas difficile d'en déduire que $\lim_{s\to 0} S_{ci}(s)/s = 0$ et $S_{ci}(0) = 0$. Par conséquent, ce système de capteur répétitif intelligent, comme son homologue , le "current feedback", peut suivre une consigne en échelon ou en rampe sans erreur en régime permanent.

Afin d'étudier les performances de suivi de consigne du capteur répétitif intelligent proposé, les diagrammes de Bode de H_{psr} et H_{psd} pour les paramètres choisis sont présentés par la Fig. 5.26. De l'Eq. 5.51, nous pouvons déduire que

$$H_{\text{psd2}}(0) = 1 \;\; \text{et} \;\; \lim_{\omega\to+\infty} H_{\text{psd2}}(j\omega) = 1. \tag{5.56}$$

Par conséquent, H_{psr} et H_{ci} ont les mêmes caractéristiques à fréquences basses et hautes, comme clairement montrés dans cette figure. Des résonances supplémentaires apparaissent entre 1 et 200 Hz, qui peuvent probablement provoquer des

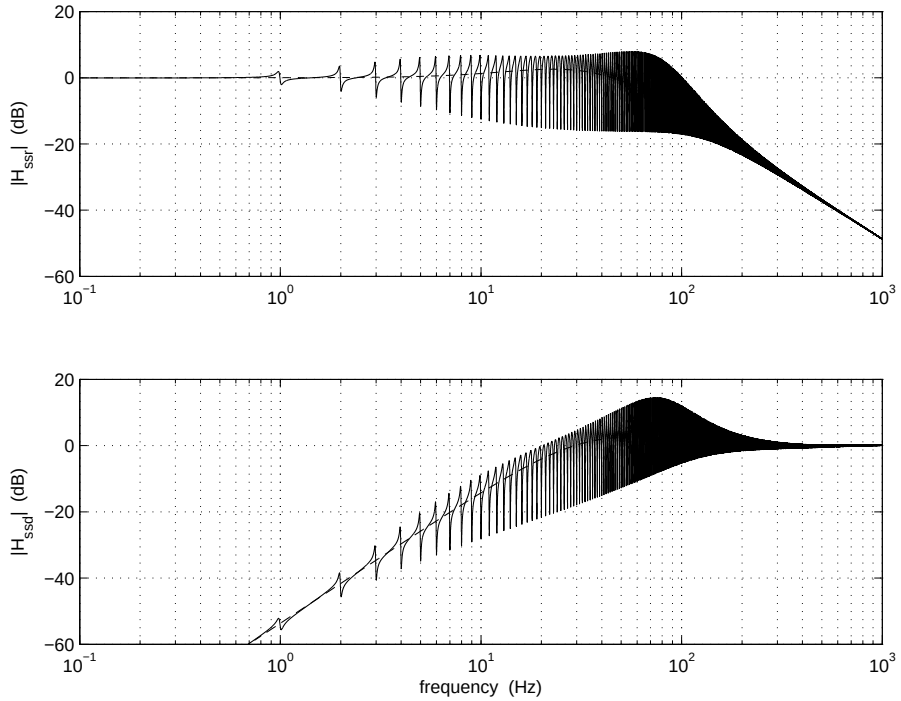

Figure 5.26: Diagrammes de Bode de H_{psr} et H_{psd}, comparés à ceux obtenu avec le régulateur PI seul.

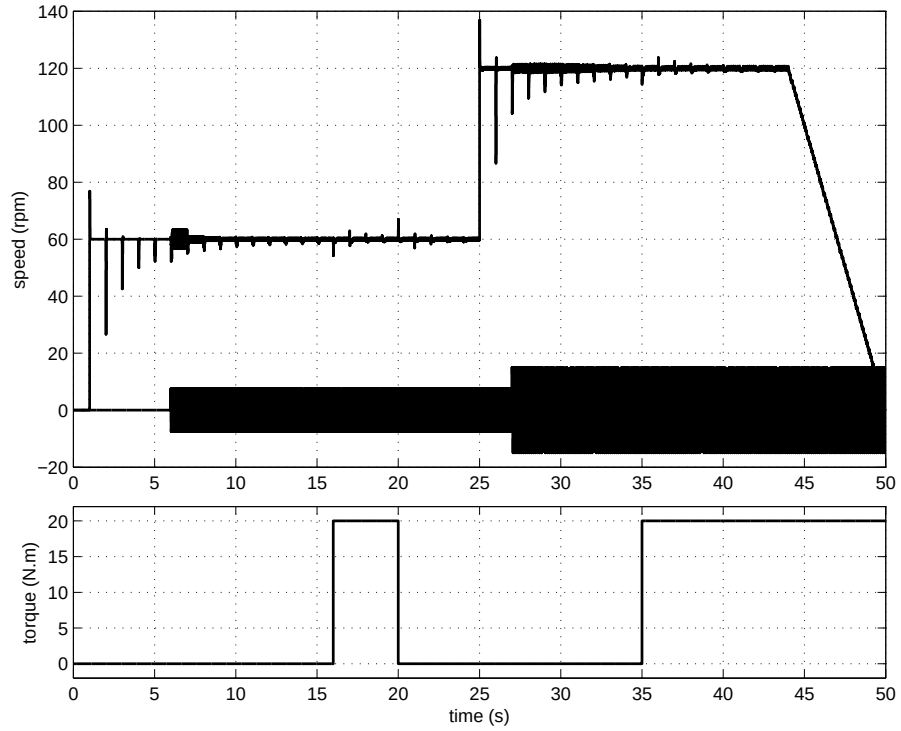

Figure 5.27: Résultats de simulation d'un système équipé du capteur répétitif intelligent proposé.

dépassements en transitoire.

La réponse temporelle de ce système est montrée par la Fig. 5.27. Nous pouvons voir que la compensation de perturbation pèriodique de ce système est exactement la même que celle du “current feedback”. Cependant, ils ont évidemment des réponses transitoires différentes. Cela peut être expliqué par la relation entre H_{psr} et H_{cfr}, lorsque $G_{cf}=G_{ps}$,

$$H_{\mathrm{psr}}=H_{\mathrm{cfr}}-\frac{S_{ci}T_{pi}e^{-s(T-\tau)}P}{1-G_{cf}e^{-sT}}. \tag{5.57}$$

Le terme complémentaire $H_{\mathrm{psr}}-H_{\mathrm{cfr}}$ est responsable des dépassements négatifs apparaissant dans la Fig. 5.27.

5.4.2 Régulateur répétitif basé sur la position angulaire

Le début de ce rapport a déjà mentionné que la vitesse variable est un obstacle inévitable qui exclut presque toutes les possibilités d'utilisation de la CR pour les MASP industrielles. Le régulateur répétitif basé sur la position angulaire capable d'adapter la CR aux vitesses variables.

Limitation du Régulateur répétitif conventionnel

Avant de présenter la technique basée sur l'angle, nous avons besoin de comprendre pourquoi les techniques de CR existantes ne peuvent pas être appliquées aux machines à vitesse variable. L'expression de la commande répétitve de base est d'abord rappelle

$$u_{rc}(t)=\mathcal{L}^{-1}\{T_u(s)\}*u_{rc}(t-T)+\mathcal{L}^{-1}\{T_{pi}(s)\}*e(t-(T-\tau)). \tag{5.58}$$

Cette équation montre que la commande répétitive à deux délais. Donc, elle utilise l'information de la commande du passé et l'information d'erreur du passé pour générer sa sortie. Il faut noter que l'utilisation des informations passées est la différence essentielle entre la CR et la plupart des autres techniques de contrôle. La capacité de réduction des perturbations périodiques de cette technique a été étudiée et vérifiée dans l'analyse précédente. En fait, cette capacité est due à l'utilisation des délais. Pour une perturbation périodique, la même valeur réapparaît à chaque période, ainsi l'information de perturbation obtenue à partir des périodes précédentes est utile pour le contrôle actuel. Grâce à l'utilisation des délais, l'information précédente peut être utilisée pour la tâche en cours. Cela demande que le délai soit exactement égal ou un multiple entier de la période de perturbation.

Régulateur répétitif basé sur la position angulaire

Le paragraphe précédent montre que, théoriquement, la capacité de réduction de la CR peut être garantie que si la perturbation est strictement répétitive en temps. Pratiquement, cette répétitivité parfaite est rarement obtenue dans de nombreuses applications, par exemple, la réduction des oscillations de vitesse des MASP.

Cependant, la périodicité et la répétitivité traitée dans la CR ne sont pas seulement limitées à une fonction du temps, mais peuvent aussi être fonction de l'état, de l'angle ou de la trajectoire. D'autre part, seulement lorsque la vitesse est constante, les oscillations de vitesse de MSAP peuvent être considérées comme des fonctions de temps. En effet, selon l'analyse précédente, ces oscillations sont fonction de l'angle mécanique essentiellement. Plus important encore, la variation de vitesse ne peut pas changer la relation entre l'angle et les oscillations de vitesse. Pour utiliser la CR, cette technique devrait être associée à l'angle mécanique. Afin de développer un contrôleur basé sur l'angle, ce contrôleur dois choisir l'angle mécanique comme variable courante et il s'appelle le régulateur répétitif basé sur la position angulaire.

Pour montrer comment obtenir un régulateur répétitif basé sur la position angulaire, prenons un MSAP qui fonctionne à vitesse constante ω_m. Pour cette machine, nous pouvons écrire $\theta_m = \omega_m\, t$, alors

$$t = \frac{\theta_m}{\omega_m} \text{ et } T = \frac{2\pi}{\omega_m}.$$

Un régulateur répétitif basé sur le temps avec T_u et T_{pi} constants peut être réécrit comme

$$u_{rc}\left(\frac{\theta_m}{\omega_m}\right) = T_u u_{rc}\left(\frac{\theta_m - 2\pi}{\omega_m}\right) + T_{pi} e\left(\frac{\theta_m + \omega_m \tau - 2\pi}{\omega_m}\right). \tag{5.59}$$

À condition que

$$u_a(\theta_m) = u_{rc}\left(\frac{\theta_m}{\omega_m}\right),\ e_a(\theta_m) = e\left(\frac{\theta_m}{\omega_m}\right) \text{ et } \theta_r = \omega_m \tau.$$

un régulateur répétitif basé sur la position angulaire peut être réécrit comme

$$u_a(\theta_m) = T_u u_a\left(\theta_m - 2\pi\right) + T_{pi}\, e_a\left(\theta_m + \theta_\tau - 2\pi\right). \tag{5.60}$$

Cette expression montre que la période de ce régulateur angulaire est 2π. l'Eq. 5.60 illustre les similitudes entre le régulateur répétitif basé sur la position angulaire et le régulateur répétitif classique basé sur le temps. Ainsi, comme son homologue basé sur le temps, le régulateur répétitif basé sur la position angulaire devrait être capable de gérer la réduction des perturbations périodiques. Il est très important de noter que le régulateur répétitif basé sur la position angulaire doit prendre l'angle

mécanique comme l'une de ses entrées obligatoires, car l'information angulaire est devenue la variable courante du régulateur.

Pour enregistrer u_a et e_a dans des tableaux (mémoires), la position angulaire est quantifiée

$$k = \text{round}\left(\frac{N\theta_m}{2\pi}\right) \bmod N. \tag{5.61}$$

N est la taille des tableaux, qui devrait être plus petit ou égal à la résolution du capteur de position. Il n'y aura pas d'index sauté dans les tableaux si la vitesse du rotor satisfait

$$V_{\max} < \frac{60F_s}{N}. \tag{5.62}$$

$V_{\max}$ (rpm) est la vitesse maximale possible et F_s est la fréquence d'échantillonnage de contrôleur numérique. Lorsque la vitesse dépasse $V_{\max}$, une technique d'interpolation linéaire peut être utilisée pour maintenir l'efficacité de régulateur répétitif basé sur la position angulaire. L'Eq. 5.62 indique qu'un F_s plus grand avec un N fixé permet un $V_{\max}$ plus élevé.

D'autre part, si $k_{\max}$ est l'ordre le plus grand des harmoniques des oscillations de vitesse, afin d'éviter une altération, selon du théorème d'échantillonnage de Nyquist-Shannon, N doit vérifier

$$N \geq 2k_{\max}. \tag{5.63}$$

En conséquent, seulement si le choix de N peut satisfaire l'Eq. 5.62 et l'Eq. 5.63 simultanément, le régulateur répétitif basé sur la position angulaire peut réaliser la réduction des oscillations de vitesse correctement.

Il est intéressant de savoir que tous les systèmes de CR présentés peuvent bénéficier de l'utilisation de cette technique. Nous considérons d'abord le système de CR élémentaire. Dans un système utilisé le régulateur répétitif basé sur le temps, il existe un délai entre l'entrée et la sortie du régulateur répétitif.

Pour un système utilisé le régulateur répétitif basé sur la position angulaire, ce délai n'est plus un intervalle de temps, mais un intervalle angulaire (égal à 2π). En conséquence, le régulateur répétitif basé sur la position angulaire ne peut pas fournir un signal de commande jusqu'à la fin de la première rotation mécanique. Cependant, sans la sortie du régulateur, dans le système de CR, la machine n'est pas capable d'accomplir cette rotation nécessaire. Par conséquent, il est impossible d'appliquer cette technique au système qui utilise le régulateur répétitif élémentaire.

À l'inverse, pour les systèmes, qui utilisent les régulateurs répétitives avancés, la machine peut démarrer et fonctionner avec le régulateur conventionnel, grâce au lien direct entre la référence et le processus. Puis, dans les rotations suivantes, avec les informations enregistrées de la première rotation, le processus itératif peut offrir la réduction souhaité. La technique basée sur la position angulaire ne peut donc être

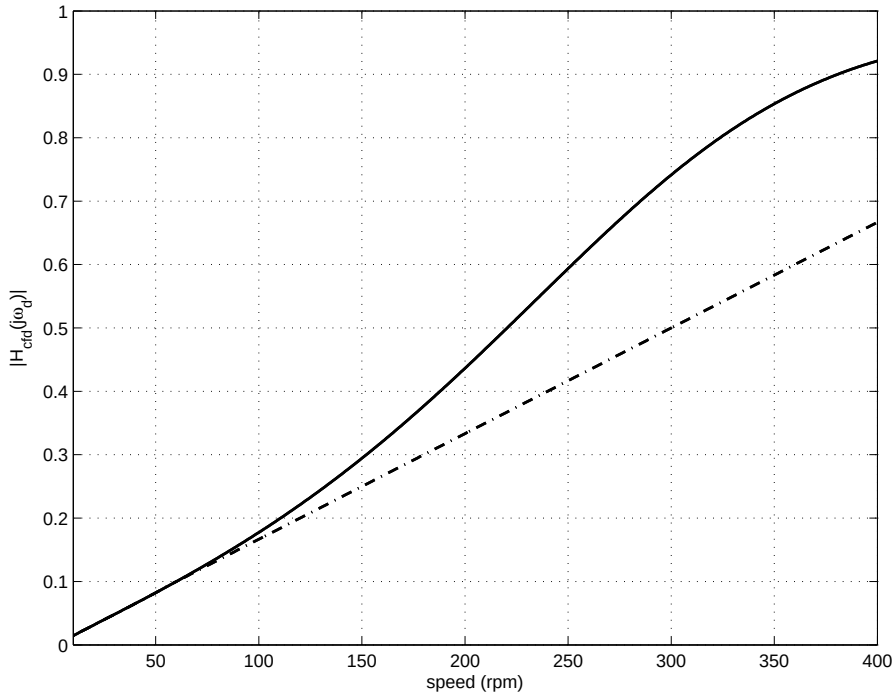

Figure 5.28: Niveau de réduction du régulateur répétitif avec les paramètres fixes ou variables à la fréquence principale de la perturbation, en fonction de la vitesse de rotation.

appliquée que pour les régulateurs répétitifs avancés.

Stabilité, performances et conception

Pour maintenir l'efficacité du régulateur basé sur la position angulaire, tout d'abord, sa stabilité et ses performances doivent être étudiées. Alors, un régulateur, qui peut ajuster ses paramètres en fonction de la vitesse, doit être mis au point.

L'Eq. 5.59 montre qu'un régulateur basé sur la position angulaire en régime permanent, a un homologue du régulateur basé sur le temps. En conséquence, la condition de la stabilité et les équations qui sont utilisées pour déterminer les performances sont encore valables pour le régulateur basé sur la position angulaire. Avec une vitesse variable (V), une série du régulateurs répétitifs équivalents basés sur le temps peut être déduite et la seule distinction entre eux est la durée de leur délai ($T = 60/V$). Étant donné que le théorème du petit gain est indépendant du délai, il n'y donc pas de relation avec la vitesse. Ces systèmes de RC équivalents basés sur le temps se partagent la même condition de la stabilité. Cependant, la réduction de perturbation de la vitesse périodique et la vitesse de convergence sont des fonctions de la fréquence. Par concéquent, elles changent avec la variation de vitesse.

Le réglage régulateur de "current feedback" proposé dans la la section 5.3.4 est réutilisé ici pour montre si les paramètres de régulateur sont fixés, étant donné que

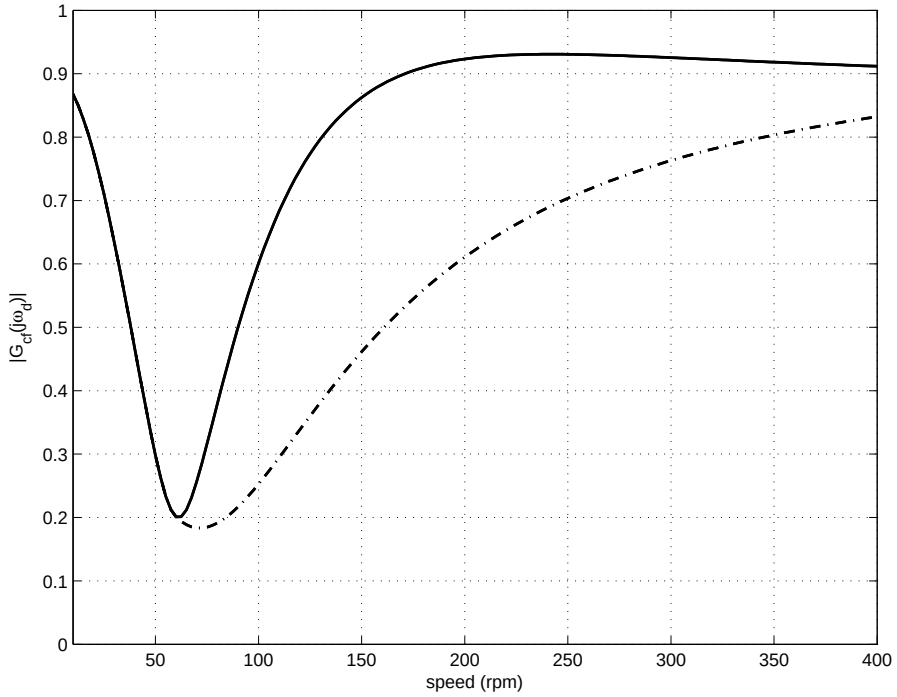

Figure 5.29: Vitesse de convergence du régulateur répétitif avec les paramètres fixes ou variables à la fréquence principale de la perturbation, en fonction de la vitesse de rotation.

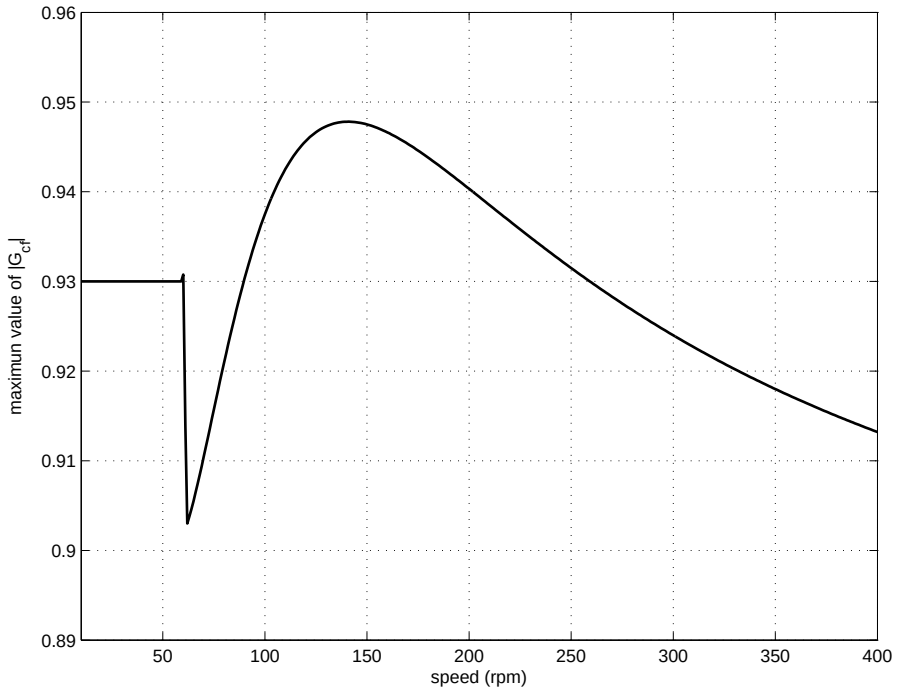

Figure 5.30: Valeurs maximales de $|G_{cf}|$ à des vitesses différentes déduites du régulateur répétitif basé sur la position angulaire avec paramètres variables. (La valeur maximale est 0.9478 et est obtenue à 140 rpm).

les performances concernés changent avec la variation de la vitesse. Les Fig. 5.28 et Fig. 5.29 montrent $H_{\text{cfd}}(j\omega_d)$ et $G_{cf}(j\omega_d)$ en fonction de la vitesse variée. Ces résultats montrent que, à des vitesses relativement élevées, la réduction est faible et la vitesse de convergence est lente. Les performances obtenues à partir du régulateur avec des paramètres fixes soit donc insuffisantes.

Cela nous amène à envisager d'utiliser un autre type de régulateur répétitif, capable de modifier ses paramètres par rapport à la vitesse pour obtenir de meilleures capacités de réduction, surtout à des vitesses élevées. Afin de développer ce type du régulateur, nous devons tout d'abord définir un $|H_{\text{cfd}}(j\omega_d)|$ souhaité variable en fonction de la vitesse. Le but de la CR est de réduire l'amplitude de $|P_2D|$. En effet, l'amplitude de $|P_2D|$ est aussi fonction de la vitesse. Grâce au choix de P_2, $|P_2D|$ diminue quand la vitesse augmente. Par conséquent, il est raisonnable de fixer une réduction relativement forte (meilleure réduction) à vitesse faible et une réduction relativement grande (réduction plus faible) à vitesse élevée. Lorsque la vitesse est inférieure de 60 rpm, comme montré dans la Fig. 5.28, la réduction obtenue à partir du régulateur répétitif avec paramètres fixés est déjà inférieur à 0.1, donc, il est correcte. Par conséquent, la variation des paramètres commence à partir de la vitesse 60 rpm. Dans ce rapport, nous espérons que lorsque la vitesse dépasse 60 rpm, le régulateur répétitif proposé basé sur la position angulaire peut garder le même $|H_{\text{cfd}}(j\omega_d)P_2(j\omega_d)D(j\omega_d)|$. Par conséquent, nous utilisons que la conception proposée avec ω_d et $|H_{\text{cfd}}(j\omega_d)|$ variable avec la vitesse, selon les équations suivantes

$$|H_{\text{cfd}}(j\omega_d)| = R(V),$$
$$\text{avec } R(V) = \begin{cases} R(60) & \text{si } V < 60, \\ R(60)\cdot V/60 & \text{si } V \geq 60, \end{cases} \quad \text{et } R(60) = 0.1. \tag{5.64}$$

La Fig. 5.28 montre que l'utilisation des paramètres variables donner $|H_{\text{cfd}}(j\omega_d)|$ plus petit que lors de l'utilisation des paramètres constants. Pour ce régulateur, les paramètres de T_{ci} (le régulateur PI de vitesse) sont déduites de la MOS et resteront inchangés aux vitesses différentes. Les paramètres du régulateur répétitif basés sur la position angulaire avec les règles de conception proposées (l'Eq. 5.42 et l'Eq. 5.43) sont calculés de la faÃ§on suivante

$$K_{pi}(V) = |Z(V)|,\ \theta_\tau = \omega_m \tau(V) = \frac{\text{Arg}(Z(V))}{24} \text{ et } \tau(V) = \frac{1}{\omega_d}\text{Arg}(Z(V)),$$
$$\text{avec } Z(V) = K_{pi}(V)e^{j\omega_d\tau(V)} = \frac{1 - G_{cf}(j\omega_d)/T_u}{S_{ci}(j\omega_d)P(j\omega_d)}$$
$$\text{et } G_{cf}(j\omega_d) = 1 - (1 - T_u)\frac{|S_{ci}(j\omega_d)|}{R(V)}. \tag{5.65}$$

Comme montré dans la Fig. 5.28, une vitesse de convergence plus rapide peut être atteinte que lors de l'utilisation des paramètres constants. Par ailleurs, nous avons également besoin de vérifier la stabilité de ce système, puisque la stabilité change avec la variation de la vitesse. La valeur maximale de la stabilité de ce régulateur à des vitesses différentes est montrée dans la Fig. 5.30. Son maximum est 0.9478, donc le processus répétitif basé sur la position angulaire peut assurer la stabilité du système pour ces vitesses. En outre, pour réaliser la variation des paramètres, l'information de vitesse doit être disponible pour ce régulateur répétitif. La vitesse doit donc devenir une entrée de ce régulateur.

Amélioration de la performance en suivi de consigne

La mauvaise performance de poursuite des systèmes de CR a déjà été abordée dans la section 5.3. Un régulateur répétitif de "NOSR". Cependant, étant donné la structure particulière du "NOSR" est un peu , les autres systèmes répétifs ne peuvent pas copier son succès directement. Ainsi, deux autres solutions relativement simples sont proposées pour améliorer les performances de poursuite.

Comme montré par la Fig. 5.17, le "NOSR" a besoin de remplacer le régulateur PI par un régulateur IP afin de lisser un signal d'échelon. Néanmoins, la modification du contrôleur existant n'est pas si facile. Par conséquent, le changement du régulateur PI par un régulateur IP est également difficile. Un filtre de référence passe-bas peut également être utilisé pour obtenir un signal plus lissé. Une solution possible pour améliorer la performance en suivi de consigne. Cependant, l'utilisation d'un filtre de référence passe-bas ralentit la réponse du système. Afin d'équilibrer la performance en régime transitoire et de la rapidité de système, il est recommandé de choisir le filtre de référence passe-bas suivant :

$$T_{lp} = \frac{K_{is}}{K_{is} + sK_{ps}}. \tag{5.66}$$

L'utilisation de ce filtre est alors équivalente au remplacement du régulateur PI par un régulateur IP [25].

L'autre solution possible consiste à prendre une fonction de saturation symétrique pour limiter l'entrée du régulateur répétitif, comme montré dans la Fig. 5.31. L'amplitude d'oscillation causée par le dépassement est généralement beaucoup plus grande que l'amplitude d'erreur causée par les oscillations de vitesse. Ainsi, une fois la limite de cette fonction de saturation choisie, elle permet de ne laisser passer sur les informations d'erreur utiles. La performance en régime transitoire peut donc être améliorée sans dégrader la rapidité de système. Il faut noter qu'une observation ou, au moins, une évaluation de $|P_2 D|$ est nécessaire pour la réalisation de cette technique.

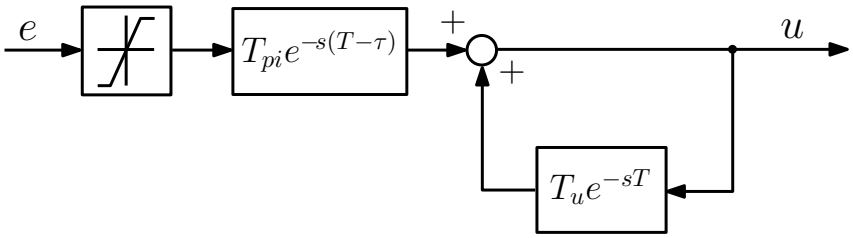

Figure 5.31: Intégration d'une fonction de saturation symétrique dans un régulateur répétitif.

Les solutions possibles présentées ici peuvent évidemment être utilisés pour tous les systèmes répétitifs étudiés. Ainsi, ils sont beaucoup plus adaptables que le régulateur répétitif de "NOSR". Dans les systèmes de CR conventionnels, l'implémemtation du filtre de référence passe-bas ou la saturation ont encore besoin d'un peu de connaissance et une légère modification de la commande existante. Pour les systèmes équipés du capteur intelligent répétitif, la fonction de saturation est ajoutée directement au capteur.

5.4.3 Résultats expérimentaux

Dans cette section, le capteur répétitif intelligent proposé et le régulateur répétitif basé sur la position angulaire sont mis en œuvre sur le banc d'essai pour vérifier l'efficacité de ces techniques. Afin de fournir des résultats comparatifs, un "current feedback repetitive controller" proposé dans la section 5.3 est également implémenté avec le banc d'essai.

La réalisation des deux régulateurs est présentée dans la Fig. 5.32 et la Fig. 5.33. Dans les deux cas, un filtre passe-bas de référence et une fonction de saturation sont utilisées pour améliorer la performance en suivi de consigne. La période d'échantillonnage de système est 10 kHz et la taille de la mémoire est $N = 1080$.

La Fig. 5.34, la Fig. 5.35 et la Fig. 5.36 montrent les spectres d'amplitude de la vitesse mesurée en régime permanent avec le régulateur PI seulement, avec le "current feedback repetitive controller" et avec le capteur répétitif intelligent à trois vitesses : 40, 60 et 80 rpm. Les 3 figures présentent clairement que dans tous les cas, les réductions d'oscillation de vitesse obtenues à partir du "current feedback repetitive controller" et du capteur répétitif intelligent sont presque pareilles. Lorsque la vitesse est de 40 rpm, la Fig. 5.34 montre que la composante principale de la perturbation est de 16 Hz. Les valeurs théoriques de $|S_{ci}(j\omega_d)|$ et $|H_{\mathrm{rcd}}(j\omega_d)|$ sont 0.4467 et 0.0651. Selon l'Eq. 5.29 et l'équivalence entre deux systèmes répétitifs, $|H_{\mathrm{ssd2}}(j32\pi)| = |H_{\mathrm{cfd2}}(j32\pi)|$. Ceci indique que la réduction supplémentaire apportée par la CR est de 0.1447. Comme montré dans la Fig. 5.34, l'amplitude d'oscillation 16 Hz de vitesse obtenue avec le régulateur PI, avec le "current feed-

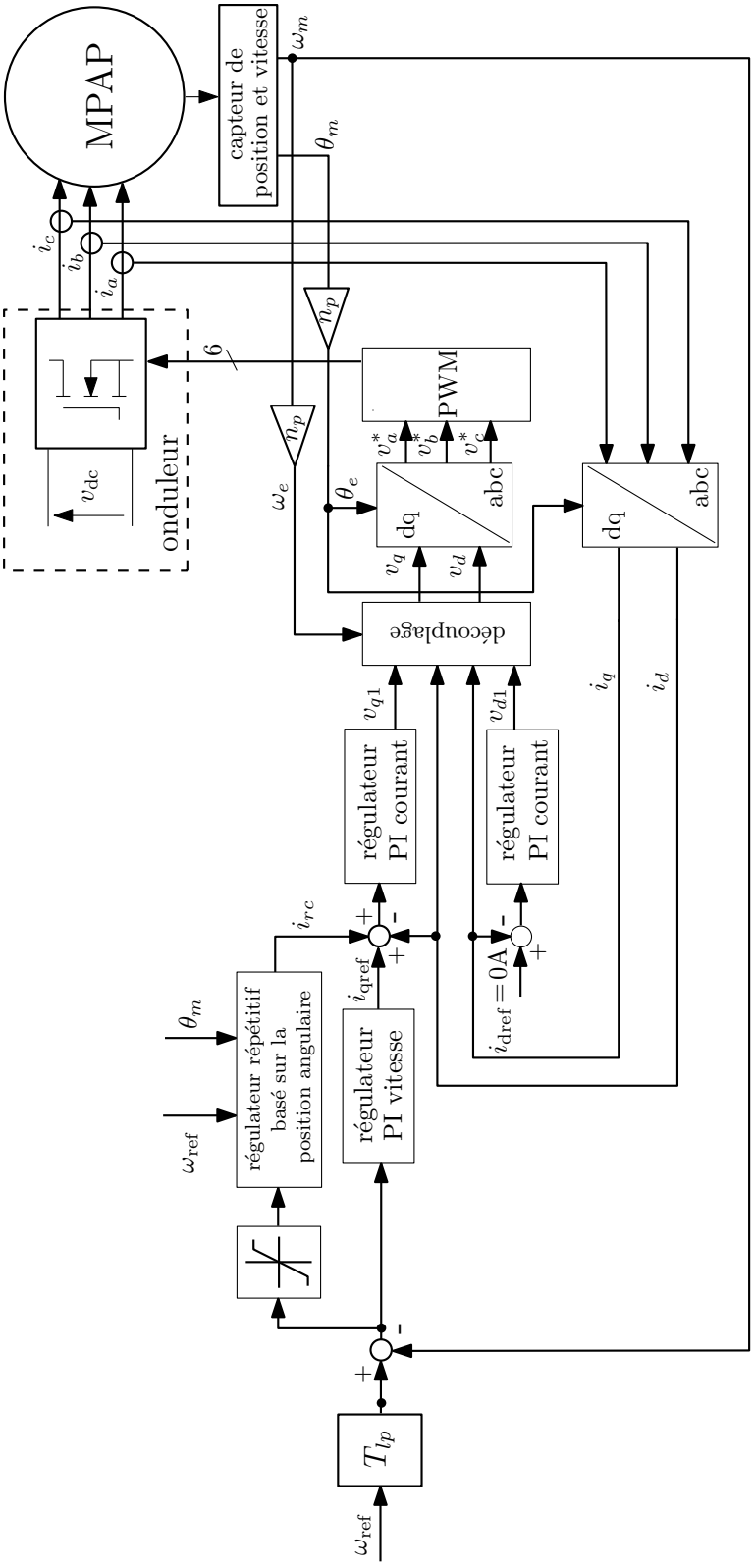

Figure 5.32: Réalisation d'un "current feedback repetitive controller" (T_{lp} est le filtre passe-bas).

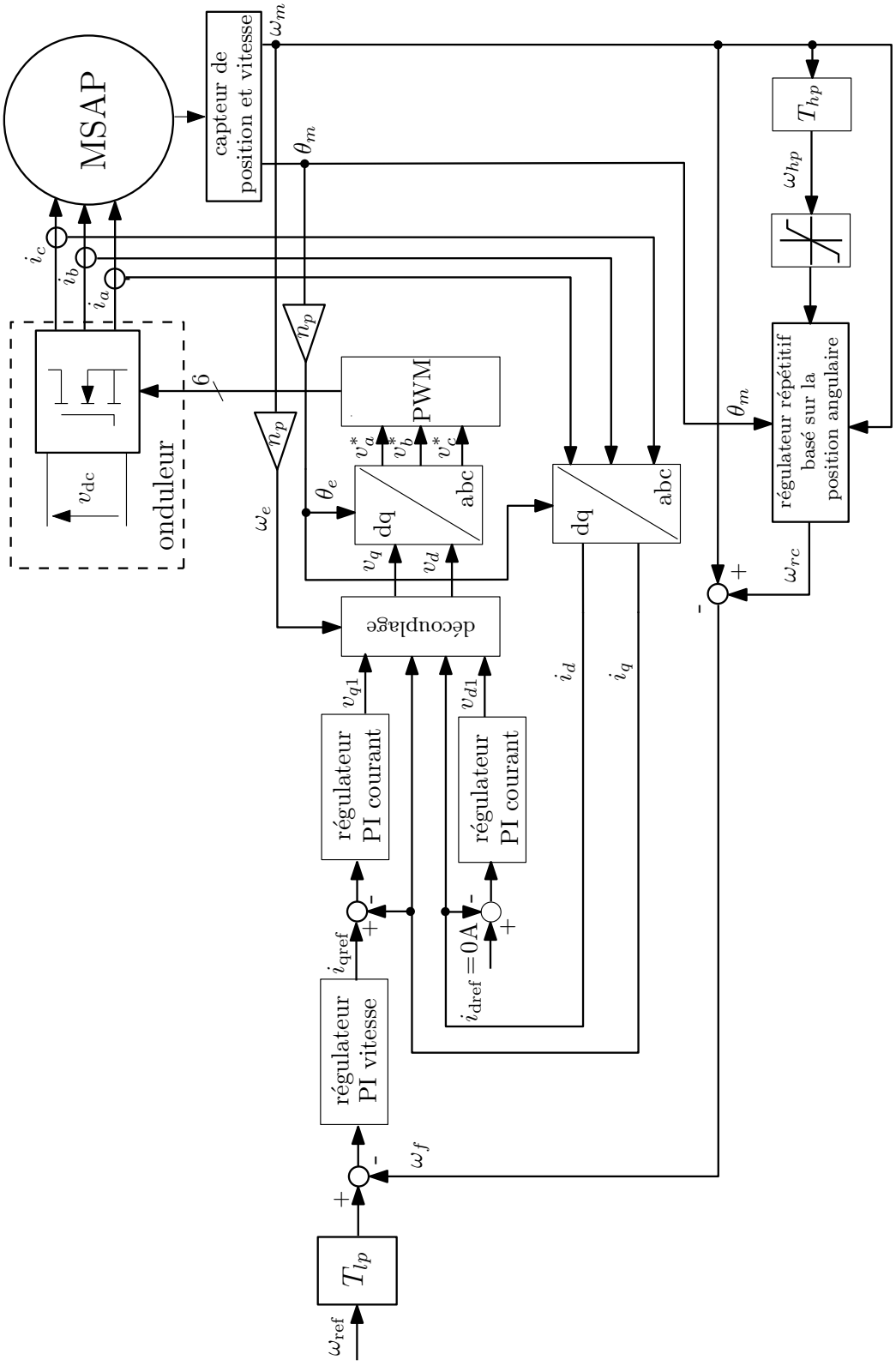

Figure 5.33: Réalisation d'un capteur répétitif intelligent (T_{lp} est le filtre passe-bas).

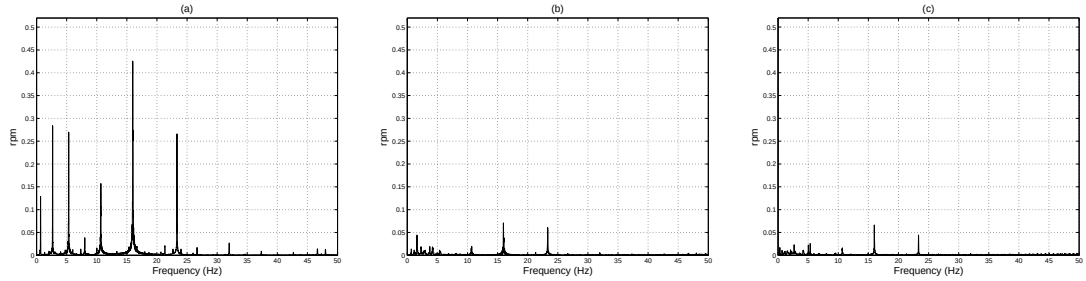

Figure 5.34: Spectre d'amplitudes des vitesses mesurées à l'état d'équilibre pour (a) le régulateur PI, (b) le current feedback repetitive controller et (c) le capteur répétitif intelligent. La référence de vitesse est $\omega_m = 4\pi/3$ rad/s (40 rpm) et le couple de charge est $T_l = 1$ N·m.

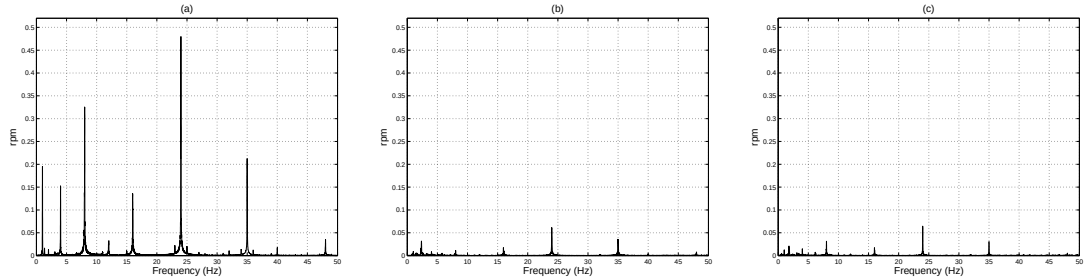

Figure 5.35: Spectre d'amplitudes des vitesses mesurées à l'état d'équilibre pour (a) le régulateur PI, (b) le current feedback repetitive controller et (c) le capteur répétitif intelligent. La référence de vitesse est $\omega_m = 2\pi$ rad/s (60 rpm) et le couple de charge est $T_l = 1$ N·m.

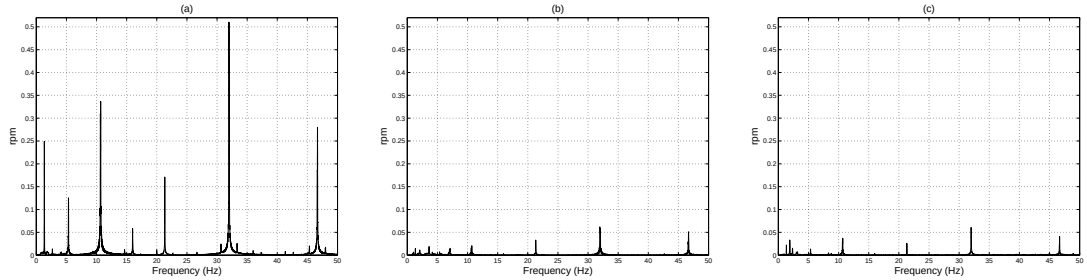

Figure 5.36: Spectre d'amplitudes des vitesses mesurées à l'état d'équilibre pour (a) le régulateur PI, (b) le current feedback repetitive controller et (c) le capteur répétitif intelligent. La référence de vitesse est $\omega_m = 8\pi/3$ rad/s (80 rpm) et le couple de charge est $T_l = 1$ N·m.

back repetitive controller" et avec le capteur répétitif intelligent sont respectivement de 0.428, 0.071 et 0.066 rpm. Les valeurs obtenues des $|H_{\text{cfd2}}(j32\pi)|$ et $|H_{\text{ssd2}}(j32\pi)|$ sont respectivement de 0.1658 et 0.1552, donc proches des valeurs souhaitées. Une analyse similaire a également été faite avec les autres vitesses. Les résultats sont présentés dans le Table. 5.2. Ce tableau confirme, non seulement que la réduction de la composante principale d'oscillation de vitesse apportée par deux systèmes est similaire, mais également que la différence entre la valeur théorique de $|H_{\text{cfd2}}(j\omega_d)|$ et sa valeur expérimentale est inférieure à $15\,\%$.

Afin d'évaluer la réduction générale, les valeurs crête-â-crête d'oscillation de vitesse obtenues dans les neuf cas sont montrés dans le Table. 5.3. Selon les résultats de ce tableau, presque 80% d'amplitude des oscillations de vitesse sont éliminées grâce à l'utilisation du "current feedback repetitive controller" et du capteur répétitif intelligent.

L'analyse ci-dessus permet de tirer deux conclusions importantes : 1) une fois que T_{hp} est choisi, le "current feedback repetitive controller" et le capteur répétitif intelligent peuvent fournir une réduction des oscillations des vitesses similaires; 2) le régulateur répétitif basé sur la position angulaire est capable de réaliser la réduction souhaitée à vitesse variable. En outre, à partir de ces résultats, nous pouvons également conclure que l'utilisation de la CR n'amplifie pas le bruit de capteur.

Le deuxième groupe de résultats expérimentaux est consacré à mettre en évidence l'intérêt d'utiliser le filtre de référence passe-bas et la fonction de saturation. Ces résultats montrent la performance en suivi de consigne de quatre systèmes, en utilisant soit un régulateur répétitif ou un capteur intelligent répétitif, avec ou sans filtre de référence associé à une fonction de saturation.

Dans ces expériences de 60 secondes, la vitesse de référence change deux fois, d'abord à 30 s, de 60 à 70 rpm, et ensuite à 40 s, de 70 à 80 rpm. Les processus répétitifs sont activés à $t = 10$ s et éteint à $t = 50$ s. Les résultats obtenus avec le "current feedback repetitive controller" et le capteur intelligent répétitif sont respectivement présentés par la Fig. 5.37 et la Fig. 5.38. Sans le filtre de référence ni la fonction de saturation, le signal échelon provoque des dépassements et des oscillations considérables. Avec un filtre passe-bas et une fonction de saturation, le problème de dépassement et des oscillations peuvent être reglés, car l'amplitude des oscillations devient presque négligeable, la réduction de la perturbation reste la même. En conséquence, dans les systèmes répétitifs, l'utilisation du filtre passe-bas de référence et de la fonction de saturation peuvent vraiment améliorer la performance en suivi de consigne sans perdre la compensation des perturbations périodiques.

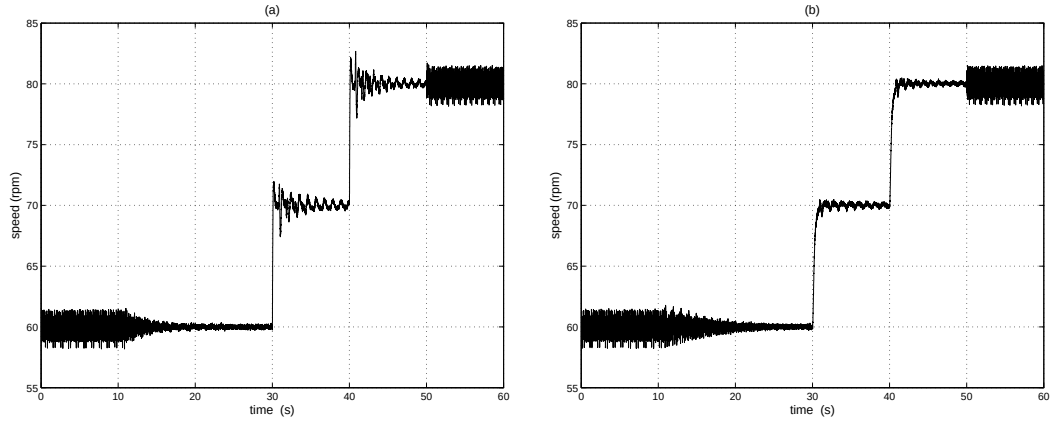

Figure 5.37: Réponse temporelle du système de “current feedback” sans (a) et avec (b) le filtre passe-bas et la saturation.

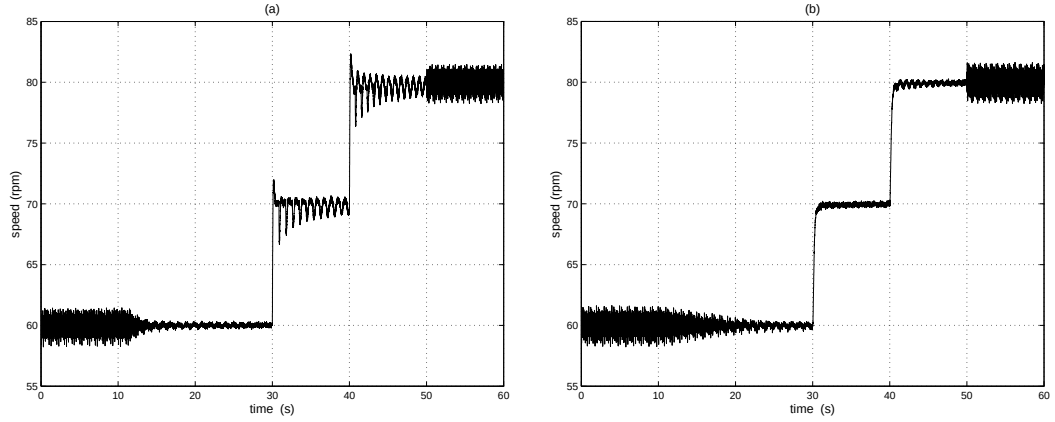

Figure 5.38: Réponse temporelle du système de capteur répétitif intelligent sans (a) et avec (b) le filtre passe-bas et la saturation.

Table 5.2: Réduction du 24ème harmonique des oscillations de vitesse

speed reference (rpm)	$\lvert H_{\mathrm{cfd2}}(j\omega_d)\rvert$		
	valeur théorique	current feedback	capteur intelligent
40	0.1447	0.1658	0.1552
60	0.1298	0.1352	0.1400
80	0.1220	0.1275	0.1208

Table 5.3: Amplitude crête-à-crête d’oscillation de vitesse

speed reference (rpm)	oscillation de vitesse (rpm)		
	PI conventionnel	current feedback	capteur intelligent
40	3.7957	0.7667	0.7832
60	3.4399	0.6511	0.6754
80	3.3084	0.7292	0.7188

5.5 Contribution et perspectives

5.5.1 Contribution

Dans ce travail, après avoir rappellé le principe de la MSAP et caractérisé ses oscillations de vitesse, mais nous avons étudié et développé plusieurs CR. Enfin, ces commandes ont été impliquées au banc d'essai pour obtenir la réduction souhaitée.

Dans la section 5.2, après avoir présenté le principe de MSAP et étudié les caractéristiques de chaque oscillation de couple, nous conclurons un point significatif : les oscillations de couple de MSAP sont fonction de l'angle mécanique. Donc, la réduction des oscillations de couple est devenue un problème du rejet des perturbations périodiques. Une enquête des techniques de la réduction des oscillations de vitesse indique la CR est approprié au but de cette thèse. Donc, elle est choisie pour réaliser la réduction souhaitée dans notre travail.

La section 5.3 a été principalement consacre à la compréhension de la CR afin de permettre son utilisation pour notre problème. L'analyse théorique a prouvé que, avec le théorème du petit gain, on peut facilement obtenir une condition de stabilité suffisante pour différents régulateurs répétitifs. Cette analyse montre aussi que le régulateur répétitif élémentaire ne peut pas être utilisé pour la MSAP, car ses délais et l'erreur statique sont inévitable et sa capacité de réduction du couple de charge extrême faible. Par conséquent, cette section présente deux régulateurs répétitifs avancés : le "current feedback repetitive controller" et le "current iteration repetitive controller", qui peuvent employer les informations directes (“current information”) pour améliorer ses performances. Nous montrons que ces deux régulateurs peuvent devenir équivalent sous certains ces conditions. Les résultats de simulations ont confirmé que les deux régulateurs répétitifs actuels avec des conceptions appropriées pourraient atteindre la réduction souhaitée. Le régulateur répétitif de "NOSR" a été utilisé pour éliminer le dépassement. Les résultats des simulations ont confirmé aussi que la MSAP avec le régulateur répétitif de "NOSR" peut, non seulement, avoir une bonne capacité de réduction de perturbation périodique, mais aussi fournir une performance de poursuite meilleure que ses homologues.

Deux nouvelles techniques de la CR, le capteur répétitif intelligent et le régulateur répétitif basé sur la position angulaire, ont été proposés et étudiés dans la section 5.4, afin de trouver le moyen d'appliquer cette technique aux MSAPs. Le capteur répétitif intelligent simplifie en effet l'utilisation de la CR dans les systèmes de MSAP, car il ne demande plus la modification du contrôleur. Nous prouvons aussi que le systéme de capteur répétitif intelligent avec un filtre passe-haut peut fournir une réduction identique à celle de son homologue de “current feedback”. D'un autre côté, en raison de leur nature, les CRs conventionnelles ne peuvent que permettre la réduction à vitesse constante. Grâce à la relation entre les oscillations et la po-

sition du rotor, le régulateur répétitif basé sur la position angulaire peut maintenir sa capacité de réduction à vitesse variable. La stabilité et l'efficacité de ce régulateur peuvent être garanties avec les différentes vitesses par une méthodologie de conception venue directement de la conception du "current feedback repetitive controller". Les résultats expérimentaux ont montré que la CR avec les deux techniques proposées est une solution, qui peut régler le problème d'oscillation de vitesse des MSAPs.

5.5.2 Perspectives

Bien que le régulateur répétitif avec la conception proposée soit déjà capable de fournir une capacité de réduction intéressante, il faut souligne que son efficacité est fortement liée à la connaissance des paramètres du régulateur PI. Par conséquent, la robustesse des performances et de la stabilité des régulateurs proposées sont absolument nécessaires. Parfois, la connaissance exacte des paramètres de ce type de la machine est difficile à acquérir. En conséquence, un régulateur répétitif adaptatif, qui peut ajuster automatiquement ses paramètres en fonction de la vitesse de machine, peut devenir une solution possible. Cette possibilité pourra être vérifiée dans le futur.

D'autre part, nous avons indiqué que, lorsque la vitesse de la machine est supérieure à la vitesse maximale, une interpolation linéaire pourrait être utilisée pour maintenir l'efficacité du régulateur répétitif basé sur la position angulaire. Toutes fois, nous l'avons insuffisamment l'étudiée. Il sera très intéressant et important de savoir ce qui va arriver, lorsque le régulateur utilise la technique d'interpolation.

Sur le côté pratique, jusqu'à maintenant, le capteur répétitif intelligent a été implémenté sur une carte dSPACE DS5202. Dans la prochaine étape, nous allons essayer d'intégrer les algorithmes dans un FPGA qui pourra être implanté dans le capteur de position afin d'obtenir un prototype industriel. Tous les résultats expérimentaux présentés dans ce rapport proviennent d'une machine de 1 kW, à des vitesses relativement faibles, ce qui, en quelque sorte, est insuffisant pour juger notre travail. Donc, dans un avenir proche, nous testerons le capteur répétitif intelligent avec plusieurs MSAPs et aussi avec des gammes de vitesse plus larges. En outre, des tests similaires seront étendus à d'autres types des machines tournantes. Théoriquement, cette technique peut en effet être utilisée avec tout type de machines tournantes pour réduire leur problème d'oscillations de vitesse.

Bibliography

[1] R. Krishnan, *Permanent magnet synchronous and brushless DC motor drives*, CRC Press, USA, 2009.

[2] R. Le Doeuff and M.E.H. Zaim, *Rotating electrical machines*, Wiley, UK, 2009.

[3] K.J. Binns, F.B. Chaaban, and A.A.K. Hameed, "Major design parameters of a solid canned permanent magnet motor with skewed magnets," *Electric Power Applications, IEE Proceedings B*, vol. 140, no. 3, pp. 161–165, May 1993.

[4] T.M. Jahns and W.L. Soong, "Pulsating torque minimization techniques for permanent magnet AC motor drives-a review," *IEEE Trans. on Industrial Electronics*, vol. 43, no. 2, pp. 321–330, Apr. 1996.

[5] E. Favre, L. Cardoletti, and M. Jufer, "Permanent-magnet synchronous motors: A comprehensive approach to cogging torque suppression," *IEEE Trans. on Industry Applications*, vol. 29, no. 6, pp. 1141–1149, Nov. 1993.

[6] T.S. Low, K.J. Tseng, T.H. Lee, K.W. Lim, and K.S. Lock, "Strategy for the instantaneous torque control of permanent-magnet brushless DC drives," *IEE Proceedings B, Electric Power Applications*, vol. 137, no. 6, pp. 355–363, Nov. 1990.

[7] P. Mattavelli, L. Tubiana, and M. Zigliotto, "Torque-ripple reduction in PM synchronous motor drives using repetitive current control," *IEEE Trans. on Power Electronics*, vol. 20, no. 6, pp. 1423–1431, Nov. 2005.

[8] T. Nakai and H. Fujimoto, "Harmonic current suppression method of PMSM based on repetitive perfect tracking control," in *33rd Annual Conf. of the IEEE Industrial Electronics Society, IECON 2007*, China, Nov. 2007, pp. 1049–1054.

[9] F. Kobayashi, S. Hara, and H. Tanaka, "Reduction of motor speed fluctuation using repetitive control," in *29th Int. Conf. on Decision and Control, CDC 1990*, USA, Dec. 1990, vol. 3, pp. 1697–1702.

[10] M. Ishida, S. Higuchi, and T. Hori, "Reduction control of mechanical vibration of an induction motor with fluctuated torque load using repetitive

controller," in *Proc. IEEE Int. Conf. on Industrial Technology, 1994*, China, Dec. 1994, pp. 533–537.

[11] S. Hattori, M. Ishida, and H. Takamasa, "Vibration suppression control method for PMSM utilizing repetitive control with auto-tuning function and fourier transform," in *27th Aunnal Conf. of the IEEE Industrial Electronics Society, IECON 2001*, USA, Nov. 2001, vol. 3, pp. 1673–1679.

[12] J.S. Kim, S. Doki, and M. Ishida, "Suppression of harmonic current in vector control for IPMSM by utilizing repetitive control," in *Proc. IEEE. Int. Conf. on Industrial Technology, ICIT 2002*, USA, Sept. 2002, vol. 1, pp. 264–267.

[13] A.E. Fitzgerald, C. Kingsley, and S.D. Umans, *Electric machinery (6th Editon)*, McGraw-Hill Press, USA, 2003.

[14] Microchip Technology, *Brushless DC (BLDC) motor fundamentals*, 2003.

[15] O. Wallmark, *Control of permanent-magnet synchronous machines in automotive application*, Ph.D. thesis, Chalmers University of Technology, Sweden, 2006.

[16] S. Carrière, *Synthèse croisée de régulateurs et d'observateurs pour le contrôle robuste de la machine synchrone (in French)*, Ph.D. thesis, Institut National Polytechnique de Toulouse, France, 2010.

[17] S. Kuttler, *Optimal design of synchronous machines for hybrid vehicles applications (in French)*, Ph.D. thesis, University of Technology of Compiégne, France, May 2005.

[18] Z.B. Zhou, "Control of a non-sinusoidal permanent magnet synchronous machine," M.S. thesis, University of Nantes, 2008.

[19] dSPACE, *dSPACE AC motor control solution*, 2011.

[20] C. Ebbesson, "Comparative study of different rotary position sensors for electrical machines used in an hybrid electric vehicle application," M.S. thesis, Lund University, 2011.

[21] J. Bocker and S. J. Mathapati, "State of the art of induction motor control," in *Proc. IEEE Int. Electric Machine and Drives Conference, IEMDC 2007*, Turkey, May 2007, vol. 2, pp. 1459–1464.

[22] J. Li, *AC motor control (in Chinese)*, Mechanical Industrial Press, China, 2005.

[23] M. Machmoun, *Modeling of electrical machine*, University of Nantes, France, 2010.

[24] W.S. Levine, Ed., *The control handbook*, CRC Press/IEEE Press, USA, 1999.

[25] T. Ane and L. Loron, "Easy and efficient tuning of PI controllers for electrical drives," in *32nd Annual Conf. of the IEEE Industrial Electronics Society, IECON 2006*, France, Nov. 2006, pp. 5131–5136.

[26] S.N. Vukosavic, *Digital control of electrical drives*, Springer, Germany, 2006.

[27] N.P. Quang and J.A. Dittrich, *Vector control of three-phase AC machines*, Springer, Germany, 2008.

[28] G.H. Cohen and G.A. Coon, "Theoretical considerations of retarded control," *Transaction of the ASME*, vol. 65, no. 4, pp. 827–834, 1953.

[29] C. Kessler, "Das symmetrische optimum (in German)," *Regelungstechnick*, vol. 1, no. 6, pp. 48–54, 432–436, 1958.

[30] W.Z. Qian, S.K. Panda, and J.X. Xu, "Reduction of periodic torque ripples in PM synchronous motors using learning variable structure control," in *28th Annual Conf. of the IEEE Industrial Electronics Society, IECON 2002*, Spain, Nov. 2002, vol. 2, pp. 1032–1037.

[31] C. Studer, A. Keyhani, T. Sebastian, and S.K. Murthy, "Study of cogging torque in permanent magnet machines," in *32th Annual Conf. of the IEEE Industry Applications Society, IAS 1997*, USA, Oct. 1997, vol. 1, pp. 42–49.

[32] X.H. Wang, *Permanent magnet machines (in Chinese)*, China Electrical Power Press, China, 2007.

[33] L. Zhu, S.Z. Jiang, Z.Q. Zhu, and C.C. Chan, "Analytical methods for minimizing cogging torque in permanent-magnet machines," *IEEE Trans. on Magnetics*, vol. 45, no. 4, pp. 2023–2031, Apr. 2009.

[34] S.M. Hwang, J.B. Eom, G.B. Hwang, W.B. Jeong, and Y.H. Jung, "Cogging torque and acoustic noise reduction in permanent magnet motors by teeth pairing," *IEEE Trans. on Magnetics*, vol. 36, no. 5, pp. 3144–3146, Sept. 2000.

[35] Z.Q. Zhou, S. Ruangsinchaiwanich, N. Schofield, and D. Howe, "Reduction of cogging torque in interior-magnet brushless machines," *IEEE Trans. on Magnetics*, vol. 39, no. 5, pp. 3238–3240, Sept. 2003.

[36] W.Z. Qian, S.K. Panda, and J.X. Xu, "Torque ripple minimization in PM synchronous motors using iterative learning control," *IEEE Trans. on Power Electronics*, vol. 19, no. 2, pp. 272–279, Mar. 2004.

[37] D.W. Chung and S. K. Sul, "Analysis and compensation of current measurement error in vector-controlled AC motor drives," *IEEE Trans. on Industry Applications*, vol. 34, no. 2, pp. 340–345, Mar. 1998.

[38] M.A. Jabbar, W.L. Aye, Z.J. Liu, and M.A. Rahman, "Computation of force and torque in electric machines," in *2000 Canadian Conf. on Electrical and Computer Engineering*, Canada, Mar. 2000, vol. 1, pp. 370–374.

[39] W. Hua and M. Cheng, "Cogging torque reduction of flux-switching permanent magnet machines without skewing," in *IEEE Int. Conf. on Electrical Machines and Systems, ICEMS 2008*, China, Oct. 2008, pp. 3020–3025.

[40] H.F. Lu, L. Zhang, and W.L. Qu, "A new torque control method for torque ripple minimization of BLDC motors with un-ideal back EMF," *IEEE Trans. on Power Electronics*, vol. 23, no. 2, pp. 950–958, Mar. 2007.

[41] K. Abbaszadeh and M. Jafari, "Optimizing cogging torque reduction in slot opening shift method for BLDC motor by RSM," in *2nd IEEE Electronics, Drive Systems and Technologies Conference, PEDSTC 2011*, Iran, Feb. 2011, pp. 62–66.

[42] J.B. Sun, S.H. Wang, and Z. Kuang, "Torque ripple comparison of short-pitched and fully-pitched winding switched reluctance machine," in *2012 15th Int. Conf. on Electrical Machines and Systems*, Oct. 2012, pp. 1–6.

[43] L. Casc, *Conception d'un actionneur à aimants permanents à faibles ondulations de couple pour assistance de direction automobile (in French)*, Ph.D. thesis, l'Institut National Polytechnique de Toulouse, France, 2004.

[44] A.M. Walker and K.R. Pullen, "An axial flux machine design with an air-gap winding using flat conductors," in *Proc. 3rd. IET Int. Conf. on Power Electronics, Machines and Drives*, Irland, Apr. 2006, pp. 221–225.

[45] M. F. Hsieh and Y.S. Hsu, "An investigation on influence of magnet arc shaping upon back electromotive force waveforms for design of permanent-magnet brushless motors," *IEEE Trans. on Magnetics*, vol. 41, no. 10, pp. 3949–3951, Oct. 2005.

[46] B. Nogarede and M. Lajoie-Mazenc, "Torque ripple minimization methods in sinusoidal fed synchronous permanent magnet machines," in *5th. Int. Conf. on Electrical Machines and Drives*, UK, Sept. 1991, pp. 41–45.

[47] S.M. Hwang, J.B. Ecom, Y.H. Jung, D.W. Lee, and B.S. Kang, "Various design techniques to reduce cogging torque by controlling energy variation in permanent magnet motors," *IEEE Trans. on Magnetics*, vol. 37, no. 4, pp. 2806–2809, July 2001.

[48] K. Gulez, A.A. Adam, I.E. Buzcu, and H. Pastaci, "Using passive filters to minimize torque pulsations and noises in surface PMSM derived field oriented control," *Simulation Modelling Practice and Theory*, vol. 15, no. 8, pp. 989–1000, Sept. 2007.

[49] A.A. Adam and K. Gulez, "Torque ripples and EMI noise minimization in PMSM using hybrid filter," in *SICE, 2007 Annual Conference*, Japan, Sept. 2007, pp. 2978–2983.

[50] M.N. Uddin, "An adaptive-filter-based torque-ripple minimization of a fuzzy-logic controller for speed control of IPM motor drives," *IEEE Trans. on Industry Applications*, vol. 47, no. 1, pp. 350–358, Jan. 2011.

[51] Y.A.I. Mohamed and E.F. El-Saadany, "A current control scheme with an adaptive internal model for torque ripple minimization and robust current regulation in PMSM drive systems," *IEEE Trans. on Energy Conversion*, vol. 23, no. 1, pp. 92–100, Mar. 2008.

[52] Y.B. Sun, G.X. Liu, C.Y. Wang, and J.K. Xia, "Fuzzy iterative learning control of ring permanent magnet torque motor," in *2010 Int. Conf. on Digital Manufacturing and Automation, ICDMA 2010*, China, Dec. 2010, vol. 1, pp. 761–765.

[53] K. Gulez and A.A. Adam, "Adaptive neural network based controller for direct torque control of PMSM with minimum torque ripples," in *SICE, 2007 Annual Conference*, Japan, Sept. 2007, pp. 174–179.

[54] G. Heins, F.G. De Boer, J. Wouters, and R. Bruns, "Experimental comparison of reference current waveform techniques for pulsating torque minimization in PMAC motors," in *IEEE Int. Conf. on Elctric Machines and Drives, IEMDC 2007*, Turkey, May 2007, vol. 2, pp. 1031–1036.

[55] P. Kshirsagar and R. Krishnan, "Efficiency improvement evaluation of non-sinusoidal back-EMF PMSM machines using field oriented current harmonic injection strategy," in *IEEE Energy Conversion Congress and Exposition, 2010*, USA, Sept. 2010, pp. 471–478.

[56] M. Rahimi, K. Abbaszadeh, and A. Radan, "Torque ripple suppression of surface mounted permanent magnet synchronous motor using harmonic injected currents," in *1st Power Electronic and Drive Systems and Technologies Conference, PEDSTC 2010*, Iran, Feb. 2010, pp. 279–283.

[57] M. Rahimi, M. Momeni, and K. Abbaszadeh, "A new approach to minimize torque pulsations in PMSM driven by field oriented control," in *2010 Int. Symp.on Power Electronics Electrical Drives Automation and Motion, SPEEDAM 2010*, Italy, June 2010, pp. 490–494.

[58] H.Y. Jia, M. Cheng, W. Hua, W.X. Zhao, and W.L. Li, "Torque ripple suppression in flux-switching PM motor by harmonic current injection based on voltage space-vector modulation," *IEEE Trans. on Magnetics*, vol. 46, no. 6, pp. 1527–1530, June 2010.

[59] F. Parasiliti, R. Petrella, and M. Tursini, "Torque ripple compensation in permanent magnet synchronous motors based on Kalman filter," in *Proc. 1999 IEEE. Int. Symp. on Industrial Electronics, ISIE 1999*, Slovenia, July 1999, vol. 3, pp. 1333–1338.

[60] N. Matsui, T. Makino, and H. Satoh, "Auto-compensation of torque ripple of DD motor by torque observer," in *IEEE Industry Applications Society Annual Meeting, 1991*, USA, Sept. 1991, vol. 1, pp. 305–311.

[61] S.K. Chung, H.S. Kim, C.G. Kim, and M.J. Youn, "A new instantaneous torque control of PM synchronous motor for high performance direct drive applications," *IEEE Trans. on Power Electronics*, vol. 13, no. 3, pp. 388–400, May 1998.

[62] T.S. Low, T.H. Lee, K.J. Tseng, and K.S. Lock, "Servo performance of a BLDC drive with instantaneous torque control," *IEEE Trans on, Industry Applications*, vol. 28, no. 2, pp. 455–462, Mar. 1992.

[63] Y.Q. Wang, F. Gao, and J.D. Francis, "Survey on iterative learning control, repetitive control, and run-to-run control," *Journal of Process Control*, vol. 19, no. 10, pp. 1589–1600, Dec. 2009.

[64] Y. Sato, M. Ishida, and T. Hori, "Speed control method of an induction motor with fluctuated load torque using repetitive controller," in *Int. Session Records of 1991 National Convention IEE Japan/Industry Applications Society*, July 1991, pp. 124–129.

[65] J.S. Kim, S. Doki, and M. Ishida, "Harmonics suppression of PMSM using repetitive control and application to improvement of sensorless control performance," in *29th Annual Conf. of the IEEE Industrial Electronics Society, IECON 2003*, Nov. 2003, vol. 1, pp. 908–912.

[66] B.H. Lam, S.K. Panda, and J.X. Xu, "Torque ripple minimization in PM synchronous motors using an iterative learning control approach," in *Proc. IEEE Int. Conf. on Power Electronics and Drive Systems, PEDS 99*, Hong Kong, July 1999, vol. 1, pp. 144–149.

[67] J.X. Xu, S.K. Panda, Y.J. Pan, T.H. Lee, and B.H. Lam, "Improved PMSM pulsating torque minimization with iterative learning and sliding mode observer," in *Proc. 26th Annual Conf. of the IEEE Industrial Electronics Society, IECON 2000*, Japan, Oct. 2000, vol. 3, pp. 1931–1936.

[68] G. Jayabaskaran, B. Adhavan, and V. Jagannathan, "Torque ripple reduction in permanent magnet synchronous motor driven by field oriented control using iterative learning control with space vector pulse width modulation," in *2013 Int. Conf. on Computer Communication and Informatics, ICCCI 2013*, India, Jan. 2013, pp. 1–6.

[69] Y. Yuan, F. Auger, L. Loron, F. Debrailly, and M. Hubert, "Design of a lying sensor for permanent magnet synchronous machine torque ripple reduction using the iterative learning control technique," in *Proc. IEEE Int. Conf. on Power Electronics and Drive Systems*, Singapore, Dec. 2011.

[70] Magtrol, *Hysteresis Brakes and Clutches*, 2013.

[71] dSPACE, *dSPACE RapidPro hardware*, 2012.

[72] C.Y. Li, D.Z. Zhang, and X.Y. Zhuang, "A survey of repetitive control," in *Proc. IEEE/RSJ Int. Conf. on Intelligent Robots and Systems, 2004*, China, Sept. 2004, vol. 2, pp. 1160–1166.

[73] B.A. Francis and W.M. Wonham, "The internal model principle for linear multivariable regulators," *Applied Mathematics and Optimization*, vol. 2, no. 2, pp. 170–193, 1975.

[74] T. Inoue, M. Nakano, and S. Iwai, "High accuracy control of servomechanism for repeated contouring," in *Proc. 10th Annual Symposium on Incremental Motion, Control System and Devices*, 1981, pp. 285–292.

[75] S. Hara, T. Omam, and M. Nakano, "Synthesis of repetitive control systems and its applications," in *24th IEEE Int. Conf. on Decision and Control, CDC 1985*, USA, Dec. 1985, vol. 24, pp. 1387–1392.

[76] S. Hara and Y. Yamamoto, "Stability of repetitive control systems," in *24th IEEE Int. Conf. on Decision and Control, CDC 1985*, USA, Dec. 1985, vol. 24, pp. 326–327.

[77] Y. Yamamoto, "Learning control and related problems in infinite-dimensional systems," in *2nd European Control Conference*, Netherlands, June 1993.

[78] S. Hara, Y. Yamamoto, T. Omata, and M. Nakano, "Repetitive control system: A new type servo system for periodic exogenous signals," *IEEE Trans. on Automatic Control*, vol. 33, no. 7, pp. 659–668, July 1988.

[79] M.C. Tsai and W.S. Yao, "Design of a plug-in type repetitive controller for periodic inputs," *IEEE Trans. on Control Systems Technology*, vol. 10, no. 4, pp. 547–555, July 2002.

[80] R.W. Longman, J.W. Yeol, and Y.S. Ryu, "Placing the repetitive controller inside or outside the feedback loop: simultaneously achieving the feedback and repetitive control objectives," in *Proc. AAS/AIAA 17th Space Flight Mechanics*, USA, Jan. 2007, vol. 127, pp. 1703–1722.

[81] K. Srinivasan and F.R. Shaw, "Analysis and design of repetitive control systems using the regeneration spectrum," in *Proc.1990 American Control Conference, ACC 1990*, USA, May 1990, pp. 1150–1155.

[82] T. Peery and H. Ozbay, "On $\mathcal{H}^\infty$ optimal repetitive controller," in *1993 IEEE. Conf. Decision and Control, CDC 1993*, USA, Dec. 1993, pp. 1146–1151.

[83] M. Nakano and S. Hara, "Microprocessor based repetitive control," in *D.Reidel Publication Corp*, 1986.

[84] M. Tomizuka, T. C. Tsao, and K. K. Chew, "Analysis and synthesis of discrete-time repetitive controllers," *ASME Trans. Journal of Dynamic Systems, Measurement, and Control*, vol. 111, pp. 353–358, Mar. 1989.

[85] M. Steinbuch, "Repetitive control for systems with uncertain period-time," *Automatica*, vol. 38, pp. 2103–2109, Sept. 2002.

[86] S.H. Yu and J.S. Hu, "Asymptotic rejection of periodic disturbance with fixed or varying period," *ASME Trans. Journal of Dynamic Systems, Measurement and Control*, vol. 123, no. 3, pp. 324–329, 2001.

[87] M.C. Tsai, G. Anwar, and M. Tomizuka, "Discrete time repetitive control for robot manipulators," in *Proc. 41st IEEE Int. Conf. on Robotics and Automation, 1988*, USA, Apr. 1988, vol. 3, pp. 1341–1346.

[88] R. Horowitz and W. W. Kao, "Digital implementation of repetitive controllers for robotic manipulators," in *IEEE Int. Conf. on Robotics and Automation, 1989*, USA, May 1989, vol. 3, pp. 1497–1503.

[89] G. Hillerstrom and J. Sternby, "Application of repetitive control to a peristaltic pump," *ASME Journal of Dynamic Systems, Measurement, and Control*, vol. 116, no. 1, pp. 786–789, 1994.

[90] K.K. Chew and M. Tomizuka, "Digital control of repetitive errors in disk drive systems," *IEEE Control Systems Magazine*, vol. 10, no. 1, pp. 16–20, Jan. 1990.

[91] T. Katayama, M. Ogawa, and M. Nagasawa, "High-precision tracking control system for digital video disk players," *IEEE Trans. on Consumer Electronics*, vol. 41, no. 2, pp. 313–321, May 1995.

[92] H.L. Broberg and R.G. Molyet, "Correction of periodic errors in a weather satellite servo using repetitive control," in *1st IEEE Conf. on Control Application*, USA, 1992, vol. 2, pp. 382–383.

[93] Y.Y. Tzou, S.L. Jung, and H.C. Yeh, "Adaptive repetitive control of PWM inverters for very low THD AC-voltage regulation with unknown load," *IEEE Trans. on Power Electronics*, vol. 14, no. 5, pp. 973–981, Sept. 1999.

[94] K. Zhang, Y. Kang, J. Xiong, and J. Chen, "Direct repetitive control of SPWM inverters for UPS purpose," *IEEE Trans. on Power Electronics*, vol. 18, no. 3, pp. 784–792, May 2003.

[95] B. Zhang, D.W. Wnng, K.L. Zhou, and Y.G. Wang, "Linear phase lead compensation repetitive control of a CVCF PWM inverter," *IEEE Trans. on Industry Electronics*, vol. 55, no. 4, pp. 1596–1602, Apr. 2008.

[96] S. Cong, "An innovative repetitive control system," in *1997 IEEE, Int. Conf. on Intelligent Processing Systems, ICIPS 1997*, China, Oct. 1997, vol. 1, pp. 640–644.

[97] K. Toyama, H. Ohtake, S. Matsuda, S. Kobayashi, and M. Morimoto, "Repetitive control of current for residential photovoltaic generation system," in *26th Annual Conf. of the IEEE Industrial Electronics Society, IECON 2000*, Japan, Oct. 2000, vol. 2, pp. 741–745.

[98] M. Wu, B. Xu, W. Cao, and J. She, "Aperiodic disturbance rejection in repetitive-control systems," *IEEE Trans. on Control System Technology*, vol. 99, no. 3, pp. 1–8, July 2013.

[99] Y.S. Lu and C.M. Cheng, "Disturbance-observer-based repetitive control with sliding modes," in *Proc. 2005 IEEE/ASME Int. Conf. on Advanced Intelligent Mechatronics*, USA, July 2005, pp. 1360–1365.

[100] E. Kurniawan, Z. Cao, and Z. Man, "Adaptive repetitive control of system subject to periodic disturbance with time-varying frequency," in *1st Int. Conf. Informatics and Computational Intelligence*, Indonesia, Dec. 2011, pp. 185–190.

[101] Y.P. Sun and Z. Li, "Adaptive repetitive control for nonlinear systems with time-varying parameters uncertainty," in *Symposium on ICT and Energy Efficiency and Workshop on Information Theory and Security, CIICT 2012*, Ireland, July 2012, pp. 232–237.

[102] J.Y. Wang, X.J. Liu, and X. Xue, "Nonlinear model predictive iterative learning control for robotic system," in *2012 Int. Conf. on System Science and Engineering*, China, June 2012, pp. 258–263.

[103] C.Y. Lin and Y.C. Liu, "Precision tracking control and constraint handling of mechatronic servo systems using model predictive control," *IEEE/ASME Trans. on Mechatronics*, vol. 17, no. 4, pp. 593–605, Aug. 2012.

[104] R.W. Longman, "Iterative learning control and repetitive control for engineering practice," *International Journal of Control*, vol. 73, no. 10, pp. 930–954, Oct. 2000.

[105] M. Uchiyama, "Formulation of high-speed motion pattern of a mechanical arm by trial," *Trans. SICE (Soc. Instrum. Contr. Eng.)*, vol. 14, no. 6, pp. 706–712, 1978.

[106] S. Arimoto, S. Kawamura, and F. Miyazaki, "Bettering operation of robots by learning," *Journal of Robot System*, vol. 1, pp. 123–140, 1984.

[107] D.A. Bristow, M. Tharayil, and A.G. Alleyne, "A survey of iterative learning control," *IEEE Control System Magazine*, vol. 26, no. 3, pp. 96–114, June 2006.

[108] T. Kavli, "Frequency domain synthesis of trajectory learning controllers for robot manipulators," *Journal of Robotic Systems*, vol. 9, no. 5, pp. 663–680, Oct. 1992.

[109] B. Bukkems, D. Kostic, B. de Jager, and M. Steinbuch, "Learning-based identification and iterative learning control of direct-drive robots," *IEEE Trans. on Control System Technology*, vol. 13, no. 4, pp. 537–549, July 2005.

[110] M.H.A. Verwoerd, *Iterative learning control – a critical review*, Ph.D. thesis, University of Twente, Netherlands, 2005.

[111] I. Maruta and T. Sugie, "Reset-free iterative identification based on the finite-dimensional signal subspace," in *47th. IEEE. Conf. on Decision and Control, CDC 2008*, Mexico, Dec. 2008, pp. 2368–2373.

[112] K. L. Moore, M. Dahleh, and S. P. Bhattacharyya, "Iterative learning control: A survey and new results," *Jounal of Robotic Systems*, vol. 9, no. 5, pp. 563–594, Mar. 1992.

[113] M. Green and D.J.N. Limebeer, *Linear robust control*, Pearson Education, USA, 1999.

[114] Q.C. Zhong, *Robust control of time-delay systems*, Springer, Germany, 2006.

[115] E.D. Solomentsev, "Encyclopedia of mathematics," *Dynamics and Control*, 2001.

[116] Y.J. Na, R. Grino, R. Costa-Castello, X. Ren, and Q. Chen, "Repetitive controller for time-delay systems based on disturbance observer," *IET Control Theory and Applications*, vol. 4, no. 11, pp. 2391–2404, Nov. 2010.

[117] K. Srinivasan, L.S. Ozbay, and S. Jung, "Stable inversion for nonminimum phase sampled-data systems and its relation with the continuous-time counterpart," in *Proc. ASME Dynamic System and Control Division*, USA, 1995, vol. 57, pp. 581–593.

[118] A.V. Oppenheim, A.S. Willsky, and S.H. Nawab, *Signals and systems*, Prentice Hall, USA, 1997.

[119] F. Kobayashi, H. Tanaka, and S. Hara, "Reduction of motor speed fluctuation using repetitive control," in *29th IEEE Int. Conf. on Decision and Control, CDC 1990*, USA, dec 1990, vol. 3, pp. 1697–1702.

[120] C. Rech, H. Pinheiro, H.A. Grundling, H.L. Hey, and J.R. Pinheiro, "Analysis and design of a repetitive predictive-PID controller for PWM inverters," in *32ed IEEE Power Electronics Specialist Conference, PESC 2001*, USA, June 2001, vol. 2, pp. 986–991.

[121] Y. Yuan, F. Auger, L. Loron, S. Moisy, and M. Hubert, "Torque ripple reduction in permanent magnet synchronous machines using angle-based iterative learning control," in *38th Annual Conf. of the IEEE Industrial Electronics Society, IECON 2012*, Canada, Oct. 2012, pp. 2518–2523.

[122] I. Touati, "Stabilité et robustesse des processus contrôlés à l'aide de régulateurs à temps continu conçus en utilisant les principes de commande par apprentissage itératif ou de commande répétitive (in French)," M.S. thesis, Nantes University, 2013.

6

Appendix

6.1 Derivation of the machine d-q model

6.1.1 Proof of Eq. 1.25

According to Eq. 1.6 and Eq. 1.7, the magnetic flux generated from the permanent magnet can be expressed as

$$\psi_{r,abc} = \begin{bmatrix} \psi_{r,a} \\ \psi_{r,b} \\ \psi_{r,c} \end{bmatrix} = \begin{bmatrix} \psi_{r,a}(\theta_e) \\ \psi_{r,a}(\theta_e - \frac{2\pi}{3}) \\ \psi_{r,a}(\theta_e + \frac{2\pi}{3}) \end{bmatrix}.$$

The Park transformation can be written

$$\begin{aligned} T_{23} &= \frac{2}{3} \begin{bmatrix} \cos(\theta) & \cos\left(\theta - \frac{2\pi}{3}\right) & \cos\left(\theta + \frac{2\pi}{3}\right) \\ -\sin(\theta) & -\sin\left(\theta - \frac{2\pi}{3}\right) & -\sin\left(\theta + \frac{2\pi}{3}\right) \end{bmatrix} \\ &= \frac{2}{3} \begin{bmatrix} \cos(\theta) & \sin(\theta) \\ -\sin(\theta) & \cos(\theta) \end{bmatrix} \begin{bmatrix} 1 & -\frac{1}{2} & -\frac{1}{2} \\ 0 & \frac{\sqrt{3}}{2} & -\frac{\sqrt{3}}{2} \end{bmatrix}. \end{aligned} \tag{6.1}$$

Since

$$\psi_{r,a}(\theta_e) = \sum_{i=1}^{\infty} \psi_{r,2i-1} \cos((2i-1)\theta_e),$$

then the magnetic flux in three phases can be represented as

$$\begin{aligned}
\psi_{ra} &= \sum_{i=1}^{\infty} \psi_{r,2i-1} \cos((2i-1)\theta_e), \\
\psi_{rb} &= \sum_{i=1}^{\infty} \psi_{r,2i-1} \cos\left((2i-1)\left(\theta_e - \frac{2\pi}{3}\right)\right) \\
&= \cos((2i-1)\theta_e)\cos\left((2i-1)\frac{2\pi}{3}\right) + \sin((2i-1)\theta_e)\sin\left((2i-1)\frac{2\pi}{3}\right), \\
\psi_{rc} &= \sum_{i=1}^{\infty} \psi_{r,2i-1} \cos\left((2i-1)\theta_e + \frac{2\pi}{3}\right) \\
&= \cos((2i-1)\theta_e)\cos\left((2i-1)\frac{2\pi}{3}\right) - \sin((2i-1)\theta_e)\sin\left((2i-1)\frac{2\pi}{3}\right).
\end{aligned}$$

Then if $i = 3k$, where k is an integer, so $2i-1=6k-1$, then

$$\begin{aligned}
\cos\left((6k-1)\left(\theta_e - \frac{2\pi}{3}\right)\right) &= -\frac{1}{2}\cos((6k-1)\theta_e) - \frac{\sqrt{3}}{2}\sin((6k-1)\theta_e), \\
\cos\left((6k-1)\left(\theta_e + \frac{2\pi}{3}\right)\right) &= -\frac{1}{2}\cos((6k-1)\theta_e) + \frac{\sqrt{3}}{2}\sin((6k-1)\theta_e).
\end{aligned}$$

As a result, we can get

$$\psi_{r,6k-1} = \begin{bmatrix} 1 & 0 \\ -\frac{1}{2} & -\frac{\sqrt{3}}{2} \\ -\frac{1}{2} & \frac{\sqrt{3}}{2} \end{bmatrix} \begin{bmatrix} \cos((6k-1)\theta_e) \\ \sin((6k-1)\theta_e) \end{bmatrix},$$

then

$$T_{23} \sum_{k=1}^{\infty} \psi_{r,6k-1} = \sum_{k=1}^{\infty} \psi_{r,6k-1} \begin{bmatrix} \cos(6k\theta_e) \\ -\sin(6k\theta_e) \end{bmatrix}.$$

On the other hand, if $i=3k+1$, so $2i-1=6k+1$, then

$$\begin{aligned}
\cos\left((6k+1)\left(\theta_e - \frac{2\pi}{3}\right)\right) &= -\frac{1}{2}\cos((6k+1)\theta_e) + \frac{\sqrt{3}}{2}\sin((6k+1)\theta_e), \\
\cos\left((6k+1)\left(\theta_e + \frac{2\pi}{3}\right)\right) &= -\frac{1}{2}\cos((6k+1)\theta_e) - \frac{\sqrt{3}}{2}\sin((6k+1)\theta_e).
\end{aligned}$$

So we can get

$$\psi_{r,6k+1} = \begin{bmatrix} 1 & 0 \\ -\frac{1}{2} & \frac{\sqrt{3}}{2} \\ -\frac{1}{2} & -\frac{\sqrt{3}}{2} \end{bmatrix} \begin{bmatrix} \cos((6k+1)\theta_e) \\ \sin((6k+1)\theta_e) \end{bmatrix}.$$

By using the Park transformation, we can get

$$T_{23}\sum_{k=0}^{\infty}\psi_{r,6k+1}=\sum_{k=0}^{\infty}\psi_{r,6k+1}\begin{bmatrix}\cos(6k\theta_e)\\ \sin(6k\theta_e)\end{bmatrix}.$$

On the other side, if $i=3k+1$, so $2i-1=6k+3$, then

$$\cos\left((2i-1)\left(\theta_e-\frac{2\pi}{3}\right)\right)=\cos((2i-1)\theta_e),$$
$$\cos\left((2i-1)\left(\theta_e+\frac{2\pi}{3}\right)\right)=\sin((2i-1)\theta_e).$$

So,

$$\psi_{r,6k+1}=\begin{bmatrix}1&0\\1&0\\1&0\end{bmatrix}\begin{bmatrix}\cos((2i-1)\theta_e)\\ \sin((2i-1)\theta_e)\end{bmatrix}=\begin{bmatrix}0\\0\end{bmatrix}.$$

Finally, $\psi_{r,dq}$ can be written as

$$\psi_{r,dq}=\begin{bmatrix}\psi_{rd}\\ \psi_{rq}\end{bmatrix}=\begin{bmatrix}\psi_m+\sum_{k=1}^{\infty}\psi_{rd,6k}\cos(6k\theta)\\ \sum_{k=1}^{\infty}\psi_{rq,6k}\sin(6k\theta)\end{bmatrix},\tag{6.2}$$

where $\psi_m=\psi_{r,1}$, and

$$\psi_{rd,6k}=\psi_{r,6k-1}+\psi_{r,6k+1}$$
$$\psi_{rq,6k}=-\psi_{r,6k-1}+\psi_{r,6k+1},$$

which proves Eq. 1.25.

6.1.2 Proof of Eq. 1.28 and Eq. 1.32

The inverse-Park transformation can be rewritten as

$$\begin{aligned}T^{-1}&=\begin{bmatrix}\cos(\theta)&-\sin(\theta)&1\\ \cos(\theta-2\pi/3)&-\sin(\theta-2\pi/3)&1\\ \cos(\theta+2\pi/3)&-\sin(\theta+2\pi/3)&1\end{bmatrix}\\&=\begin{bmatrix}1&0&1\\ -\frac{1}{2}&\frac{\sqrt{3}}{2}&1\\ -\frac{1}{2}&-\frac{\sqrt{3}}{2}&1\end{bmatrix}\begin{bmatrix}\cos(\theta)&-\sin(\theta)&0\\ \sin(\theta)&\cos(\theta)&0\\ 0&0&1\end{bmatrix}.\end{aligned}\tag{6.3}$$

Differential calculation of the inverse-Park transformation can be calculated as

$$\begin{aligned}\frac{dT^{-1}}{d\theta} &= \begin{bmatrix} 1 & 0 & 1 \\ -\frac{1}{2} & \frac{\sqrt{3}}{2} & 1 \\ -\frac{1}{2} & -\frac{\sqrt{3}}{2} & 1 \end{bmatrix} \begin{bmatrix} -\sin(\theta) & -\cos(\theta) & 0 \\ \cos(\theta) & -\sin(\theta) & 0 \\ 0 & 0 & 1 \end{bmatrix} \\ &= \begin{bmatrix} 1 & 0 & 1 \\ -\frac{1}{2} & \frac{\sqrt{3}}{2} & 1 \\ -\frac{1}{2} & -\frac{\sqrt{3}}{2} & 1 \end{bmatrix} \begin{bmatrix} \cos(\theta) & -\sin(\theta) & 0 \\ \sin(\theta) & \cos(\theta) & 0 \\ 0 & 0 & 1 \end{bmatrix} \begin{bmatrix} 0 & -1 & 0 \\ 1 & 0 & 0 \\ 0 & 0 & 1 \end{bmatrix} \\ &= T^{-1} \begin{bmatrix} 0 & -1 & 0 \\ 1 & 0 & 0 \\ 0 & 0 & 1 \end{bmatrix}. \end{aligned} \tag{6.4}$$

From this derivation, and provided that $\theta = \omega t$,

$$\begin{aligned}\frac{dT^{-1}}{dt} &= \begin{bmatrix} 1 & 0 & 1 \\ -\frac{1}{2} & \frac{\sqrt{3}}{2} & 1 \\ -\frac{1}{2} & -\frac{\sqrt{3}}{2} & 1 \end{bmatrix} \omega \begin{bmatrix} -\sin(\theta) & -\cos(\theta) & 0 \\ \cos(\theta) & -\sin(\theta) & 0 \\ 0 & 0 & 1 \end{bmatrix} \begin{bmatrix} 0 & -1 & 0 \\ 1 & 0 & 0 \\ 0 & 0 & 1 \end{bmatrix} \\ &= T^{-1}\omega \begin{bmatrix} 0 & -1 & 0 \\ 1 & 0 & 0 \\ 0 & 0 & 1 \end{bmatrix}. \end{aligned} \tag{6.5}$$

Therefore,

$$T\frac{dT^{-1}}{dt} = \omega \begin{bmatrix} 0 & -1 & 0 \\ 1 & 0 & 0 \\ 0 & 0 & 1 \end{bmatrix}, \tag{6.6}$$

which proves Eq. 1.28.

The transpose of the inverse-Park transformation is

$$(T^{-1})^T = \begin{bmatrix} \cos(\theta) & \sin(\theta) & 0 \\ -\sin(\theta) & \cos(\theta) & 0 \\ 0 & 0 & 1 \end{bmatrix} \begin{bmatrix} 1 & -\frac{1}{2} & -\frac{1}{2} \\ 0 & \frac{\sqrt{3}}{2} & -\frac{\sqrt{3}}{2} \\ 1 & 1 & 1 \end{bmatrix}, \tag{6.7}$$

then

$$(T^{-1})^{-T}T^{-1} = \frac{3}{2} \begin{bmatrix} 1 & 0 & 0 \\ 0 & 1 & 0 \\ 0 & 0 & 2 \end{bmatrix}. \tag{6.8}$$

Hence,

$$(T^{-1})^{-T}\frac{dT^{-1}}{d\theta}=\frac{3}{2}\begin{bmatrix}1&0&0\\0&1&0\\0&0&2\end{bmatrix}\begin{bmatrix}0&-1&0\\1&0&0\\0&0&1\end{bmatrix}=\frac{3}{2}\begin{bmatrix}0&-1&0\\1&0&0\\0&0&2\end{bmatrix}, \tag{6.9}$$

which proves Eq. 1.32.

6.1.3 Proof of Eq. 1.33 and Eq. 1.34

Differential calculation of the Park transformation can be written as

$$\begin{aligned}\frac{dT}{d\theta}&=\frac{2}{3}\begin{bmatrix}\cos(\theta)&\sin(\theta)&0\\-\sin(\theta)&\cos(\theta)&0\\0&0&1\end{bmatrix}\begin{bmatrix}1&-\frac{1}{2}&-\frac{1}{2}\\0&\frac{\sqrt{3}}{2}&-\frac{\sqrt{3}}{2}\\\frac{1}{2}&\frac{1}{2}&\frac{1}{2}\end{bmatrix}\\&=\begin{bmatrix}0&1&0\\-1&0&0\\0&0&1\end{bmatrix}\frac{2}{3}\begin{bmatrix}\cos(\theta)&\sin(\theta)&0\\-\sin(\theta)&\cos(\theta)&0\\0&0&1\end{bmatrix}\begin{bmatrix}1&-\frac{1}{2}&-\frac{1}{2}\\0&\frac{\sqrt{3}}{2}&-\frac{\sqrt{3}}{2}\\\frac{1}{2}&\frac{1}{2}&\frac{1}{2}\end{bmatrix}\\&=\begin{bmatrix}0&1&0\\-1&0&0\\0&0&1\end{bmatrix}T.\end{aligned} \tag{6.10}$$

The deduction of Eq. 1.33 is shown here

$$\begin{aligned}(T^{-1})^{T}\frac{d(T^{-1}L_{dq0}T)}{d\theta}T^{-1}&=(T^{-1})^{T}\left(\frac{dT^{-1}}{d\theta}L_{dq0}T+T^{-1}L_{dq0}\frac{dT}{d\theta}\right)T^{-1}\\&=(T^{-1})^{T}\frac{dT^{-1}}{d\theta}L_{dq}TT^{-1}+(T^{-1})^{T}T^{-1}L_{dq}\frac{dT}{d\theta}T^{-1},\end{aligned}$$

considering Eq. 6.9 and Eq. 6.10, this equation can changed as

$$=\frac{3}{2}\begin{bmatrix}0&-1&0\\1&0&0\\0&0&2\end{bmatrix}L_{dq0}+\frac{3}{2}\begin{bmatrix}1&0&0\\0&1&0\\0&0&2\end{bmatrix}L_{dq0}\begin{bmatrix}0&1&0\\-1&0&0\\0&0&1\end{bmatrix}. \tag{6.11}$$

If neglecting the zero sequence, the above equation can be simplified as

$$\begin{aligned}&=\frac{3}{2}\left(\begin{bmatrix}0&-1\\1&0\end{bmatrix}\begin{bmatrix}L_d&0\\0&L_q\end{bmatrix}+\begin{bmatrix}L_d&0\\0&L_q\end{bmatrix}\begin{bmatrix}0&1\\-1&0\end{bmatrix}\right)\\&=\frac{3}{2}(L_d-L_q)\begin{bmatrix}0&1\\1&0\end{bmatrix},\end{aligned} \tag{6.12}$$

which proves Eq. 1.33.

Eq. 1.31 can be rewritten here, as

$$T_e(\theta_m) = n_p \left(\frac{1}{2} i_{dq0}^T (T^{-1})^T \frac{d(T^{-1} L_{dq0} T)}{d\theta_m} T^{-1} i_{dq0} + i_{dq0}^T (T^{-1})^T \frac{dT^{-1}}{d\theta_m} \psi_{rdq0} \right)$$

According to above analysis, this electromagnetic torque in d-q reference frame can be deduced as

$$\begin{aligned} T_e &= n_p \left(\frac{3}{4}(L_d - L_q) i_{dq}^T \begin{bmatrix} 0 & 1 \\ -1 & 0 \end{bmatrix} i_{dq} + \frac{3}{2} i_{dq}^T \begin{bmatrix} 0 & -1 \\ 1 & 0 \end{bmatrix} \begin{bmatrix} \psi_m \\ 0 \end{bmatrix} \right) \\ &= n_p \left(\frac{3}{2}(L_d - L_q) i_d i_q + \frac{3}{2} \psi_m i_q \right) \\ &= \frac{3}{2} n_p \left(L_d i_d i_q - L_q i_q i_d + \psi_m i_q \right) \\ &= \frac{3}{2} n_p \left(\psi_{sd} i_q - \psi_{sq} i_d + \psi_m i_q \right) \\ &= \frac{3}{2} n_p \left((\psi_{sd} + \psi_m) i_q - \psi_{sq} i_d \right) \\ &= \frac{3}{2} n_p \left(\psi_d i_q - \psi_q i_d \right) \end{aligned} \tag{6.13}$$

which proves Eq. 1.34

Symbols Table

Symbols

A	Magnitude of step reference
B	Magnetic flux density & Slope of ramp reference
B_d	Magnitude of load torque
B_i	Coefficient of the magnetic flux density harmonic
C	Transfer function of the repetitive controller
D	Disturbance and the load torque
E	Error or the input of the system controller
E_d	Error caused by the periodic disturbance
E_r	Error caused by the reference tracking
e_{back}	Back EMF
e_f	Input of the conventional controller in repetitive smart sensor systems
e_{load}	Error caused by load torque
e_{ramp} e_{step}	Error caused by tracking a ramp and a step
e^{-sT}	Time delay presented in frequency domain
F_s	Sampling rate of the digital controller
$f_{\max}$	Frequency of the maximum value of $\|G_{rc}\|$
f_b	Friction coefficient of PMSM mechanical part
f_d	Bandwidth of the open-loop transfer function of PMSM electrical part
f_k	Frequency of the harmonic component
G	Regeneration spectrum of RC systems
H_{bo}	Transfer function used for SOM
i	Phase current
J	Machine+Load Inertia
K_{hp}	Gain of high-pass filter
K_i	Integral gain of PI and IP controller
K_p	Proportional gain of PI and IP controller
$K_{abc,s}$	Scaling factors of three-phase current
$k_{\max}$	Order of the highest torque ripple component
L	Inductance
l_{ef}	Effective length of the stator

N	Volume of the memory used in repetitive controllers (processes)
N_c	Number of coils turns per phase
N_l	Least common multiple of slot number and permanent magnet number
n	Location in an array of the repetitive controller
n_p	Pole pair number
P	Process
P_{real}	Uncertainty model
R	Resistance
R_{in}	Inner radius of the stator
S_{ci}	Sensitivity function of the conventional control system
T	One mechanical rotation duration and the delay length in repetitive controller (Pr
T & T^{-1}	Park transformation and Inverse Park transformation
T_{cog}	Cogging torque
T_d	Time constant of the open-loop transfer function of PMSM electrical part
T_e	Electromagnetic torque
T_{fric}	Friction torque
T_{harm}	Harmonic torque
T_i	Inverse of the integral action
T_{hp}	High-pass filter used in the practical repetitive smart sensor
T_l	Load torque
T_{lp}	Low-pass reference filter
T_{rc}	Parameter of the periodic signal generator
T_u, T_{pi}	Parameter of the repetitive controller
T_s	Sampling period of the digital controller
t	Instantaneous time
u	Controller action (output)
V	Speed of PMSM (in RPM)
V_{max}	Maximum speed supported by interpolation technique
v_{dc}	DC source voltage
v_m	Inverter midpoint voltage
$v_{abd,n}$	Three-phase voltages
Y	System (process) output
y_f	Output of the repetitive smart sensors
y_{hp}	Input of the repetitive process in repetitive smart sensor
e_r	Output of the repetitive process in repetitive smart sensors
y_{ref}	Reference input
W_{mag}	Magnetic energy
W_{cog}	Magnetic energy of the cogging torque
z_n	Damping factor of the T_{pi2}

α	Static gain
Δi	DC off-set current
η	SOM coefficient calculated from the desired phase margin
θ_e	Electrical angular position of the rotor
θ_c	Mechanical angular position locating at the center of one tooth
θ_m	Mechanical angular position of the rotor
θ_r	Electrical angle between an assumptive position P and the axis of rotor
θ_s	Electrical angle between an assumptive position P and the axis of stator
κ	DC offset torque calculation coefficient
μ	Divergence between the real value of the parameters and their supposed value
μ_0	Magnetic permeability of air
μ_{Fe}	Magnetic permeability of the iron core
μ_{PM}	Magnetic permeability of the permanent magnet
τ	Leading-time component
Ψ	Phase of the regeneration function in repetitive controller
Ψ_{rn}	Nominal value of the magnetic flux
ϕ_r	Magnetic flux linkage generated from magnet permanents
ψ_i	Coefficient of the magnetic flux linkage harmonic
ψ_m	Constant component of the magnetic flux linkage
ψ_s	Magnetic flux linkage generated by conducting current
φ_m	Desired phase margin in SOM
ω_e	Electrical angular speed
ω_k	Angular frequency of the harmonic component
ω_i	Integral action
ω_m	Mechanical angular speed
ω_n	Natural frequency of the T_{pi2}
ω_d	Frequency of the main disturbance
ω_q	Inverse of system constant

Subscript & Superscript

AD	Measured
A, B, C	One phase of machine or inverter in three phase reference frame
a, b, c	One phase of machine or inverter in three phase reference frame
cf	Current feedback repetitive controller
ci	Current iteration repetitive controller
d, q	One phase of machine in two phase reference frame
ip	IP repetitive controller
m	Mutual (Inductance) and mechanical and measured
pi	Previous information
r	Rotor
ref	Reference
rc	Basic repetitive controller
s	Stator, self (Inductance) or speed
ss	Repetitive smart sensor
ps	Practical repetitive smart sensor

Abbreviation

AC	Alternating current
A/D	Analogue digital converter
BIBO	Bound-input bound-output
CFRC	Current feedback RC system
D	Diode
D/A	Digital analogue converter
DC	Direct current
DSP	Digital signal processor
EMF	Electromagnetic force
EPS	Electric power steeling
FEM	Finite-element method
FPGA	Field-programmable gate array
I/O	Input/output
ILC	Iterative learning control
IMP	Internal model principle
IP	Integral-proportional
LTI	Linear time-invariant
LSM	Least-square method
MIMO	Multiple-input multiple-output
PCM	Pole cancellation method
PI	Proportional-integral
PID	Proportional-integral-derivative
PM	Permanent magnet
PMSM	Permanent magnet synchronous machine
PWM	Pulse-width modulation
R2R	Run-to-run control
RC	Repetitive control
RR	Reduction Ratio
RSSS	Repetitive smart senor system
SISO	Single-input single-output
SOM	Symmetry optimum method

Contents

List of Tables

List of Figures

l'université nantes angers le mans
COMMUNAUTÉ D'UNIVERSITÉS ET ÉTABLISSEMENTS

UNIVERSITÉ DE NANTES

Thèse de Doctorat

Yi YUAN

Reduction des oscillations de vitesse des machines synchrones à aimants permanents par des commandes répétitives (version provisoire)

Torque Ripple Reduction in a Permanent Magnet Synchronous Machine Using Repetitive Control Techniques (Drift)

Résumé

Les machines synchrones à aimants permanents (MSAP) sont de plus en plus utilisées dans de nombreuses applications grâce à leur efficacité, fiabilité et performances. Cependant, les oscillations de couple peuvent provoquer des oscillations de la vitesse qui sont considérées comme un problème majeur dans certaines applications à faible vitesse. Par conséquent, la commande répétitive (CR) est choisie pour sa forte capacité à réduire ces perturbations périodiques et réduire les oscillations de couple. Il existe deux problèmes principaux lors de l'application de la CR à une MSAP. D'abord, la CR ne peut réaliser la réduction souhaitée que dans le cas d'une vitesse constante. Grâce à la relation fixe entre ces oscillations et la position du rotor, nous proposons de prendre l'angle mécanique comme la nouvelle variable du fonctionnement de la CR. Ce nouveau régulateur est appelé régulateur répétitif basé sur la position angulaire. L'avantage de ce contrôleur est sa capacité de réduction même dans le cas d'une vitesse variable. Le deuxième inconvénient de l'application de la CR est sa difficulté d'implantation dans les systèmes industriels. Ainsi, nous proposons d'ajouter le contrôleur répétitif dans un capteur de vitesse et de développer une nouvelle technique appelée capteur répétitif intelligent. Avec ce capteur, l'application de la technique de CR ne requiert aucune modification du contrôleur, mais il est nécessaire de remplacer le capteur normal par le capteur répétitif intelligent. Finalement, ces deux nouvelles techniques sont réalisées ensemble sur un banc d'essais et leur efficacité est validée par des résultats expérimentaux.

Mots clés

machines synchrones à aimants permanents, oscillations de couple, rejet de perturbations périodiques, commande répétitive, capteur intelligent, commande indexée sur la position.

Abstract

Permanent magnet synchronous machines (PMSMs), due to their attractive efficiency, reliability and performance, are rapidly gaining popularity in many applications. However, torque ripples of PMSM generally cause speed ripples, which are considered as an important hindrance in some low speed applications. The repetitive control (RC), which is particularly suitable for the reduction of periodic disturbance, is chosen to achieve the torque ripple reduction, because torque ripples of PMSM can be considered as periodic disturbances. The use of the RC for machine torque ripple reduction is not new. However, the reduction is always achieved at a given speed. This is due to the nature of the RC. So as to extend the use of the RC to varying speeds, the angle-based RC technique, which takes the mechanical angle as the running variable, is considered in this work. Thanks to the fixed relationships between the torque ripples and the mechanical angle, the angle-based repetitive controller can keep its rejection capability, whether the speed is constant or not. Besides, applying the RC in a PMSM drive requires to implement a new controller, which is hardly achievable for commercial systems. In order to apply the RC for PMSM drives, this paper proposes to include the RC into a speed sensor, forming a particular speed sensor called repetitive smart sensor. Accordingly, the torque ripple reduction can simply be accomplished by changing a conventional speed sensor for a repetitive smart one. Finally, the efficiency of the proposed angle-based repetitive smart sensor is verified through experimental results.

Key Words

permanent magnet synchronous machines, torque ripple, periodic disturbance rejection, repetitive control, repetitive smart sensor technique, angle-based technique.